KINETICS OF STRUCTURE FORMATION OF COMPLEX NANOPARTICLES IN MODEL FLOW REACTORS

Von der Fakultät für Ingenieurwissenschaften
Abteilung Elektrotechnik und Informationstechnik
der Universität Duisburg-Essen

zur Erlangung des akademischen Grades

Doktor der Ingenieurwissenschaften

genehmigte Dissertation

von

Thore Lars Rosenberger
aus
Duisburg

Gutachter: Prof. Dr.-Ing Einar Kruis
Prof. Dr. rer. nat. Markus Winterer

Tag der mündlichen Prüfung: 17.01.2023

"Yesterday is history, tomorrow is a mystery, and today is a gift...
that's why it is called the present".

— Alice Morse Earl —

For my beloved wife Miriam and my beautiful daughter Karla.

ABSTRACT

The structure formation of particles in the gas phase, eg. by coagulation, sintering, nucleation, can be described by structure formation models. These models are needed to simulate structure formation mechanisms in aerosol reactors and to improve the yield of defined particle structures. The precise investigation of the structure formation mechanisms is in aerosol reactors for production processes not possible or lead to very inaccurate results. The reason for this is that the various mechanisms leading to structure formation often occur very rapidly or simultaneously, and the process conditions usually cannot be defined well enough. In order to obtain precise kinetic data, the mechanisms have to be isolated from each other and well-defined conditions with defined particle properties have to be provided. Coagulation and sintering are the two main important mechanisms leading to the particle morphology and growth. Whereas coagulation is well described in models, sintering is due to its dependency on various particle properties (e.g., size, shape, agglomerate structure), material properties, as well as process conditions (temperature–time history of the particles) a more complex mechanism.

The emphasis of this thesis is placed on determining precise kinetic data for structure formation mechanism, especially sintering, of aerosol nanoparticles. Defined initial particles structures in the size range from 20 to 200 nm are provided by classifying a polydisperse aerosol into monodisperse size fractions. Therefore, a custom-built medium-flow differential mobility analyzer (MF-DMA) was designed and optimized for larger aerosol flow rates and longer runtime. A model flow reactor (MFR) was designed for the precise examination of structure formation mechanism by providing a narrow temperature-residence time distribution of the particles. A computational fluid dynamics (CFD) model of the MFR was validated by comprehensive temperature measurements to optimize the flow field in the reaction zone where the structure formation takes place. The validated CFD model is needed to calculate the temperature-residence time distribution from simulated particle trajectories as function of different operation temperatures, which are used as input conditions for the numerical determination of the kinetic data. Monitoring the particle size and mass distribution with online aerosol instrumentation allows the calculation of structure properties or characteristics via structure models (like particle surface area, primary particle size, effective density, number of primary particles per agglomerate) to

describe the structure or its changes.
A sintering model describing the decrease in surface area with a kinetic term in form of an Arrhenius expression, including an activation energy and a pre-factor, is assumed. The activation energy and pre-factor are determined numerically by error minimization between modeled and measured particle size, considering the temperature-residence time history of the particles. The application and validation of the sintering model to aerosol reactors in the pilot scale or production plant is challenging. Besides of the complexity of the setups and the simultaneously occurring structure formation mechanisms, some of the reactors are also operated at low pressure. Thereby, the use of standard online aerosol measurement techniques, such as scanning mobility particle sizer (SMPS), centrifugal particle mass analyzer (CPMA) and electrical low-pressure impactor (ELPI), is not possible or require comprehensive calibrations for a specific pressure range. One solution to this is the use of a commercial vacuum ejector as a simple tool for continuous sampling from low pressure areas. Vacuum ejectors are usually designed to create a low pressure by a accelerated driving gas over a converting nozzle. This effect can be also used to transfer aerosol particles from a low pressure to atmospheric pressure. For this study, a test aerosol was synthesized to determine the transfer behavior of two different commercially available vacuum ejectors. The applicability of the ejectors to a low-pressure microwave plasma reactor and a flame reactor with high production rates was tested using a combination of standard online instruments.

ZUSAMMENFASSUNG

Die Strukturbildung von Partikeln in der Gasphase, z. B. durch Koagulation, Sinterung, Nukleation usw., kann durch Strukturbildungsmodelle beschrieben werden. Diese Modelle werden benötigt, um die Strukturbildungsmechanismen in Aerosolreaktoren zu simulieren und die Ausbeute an definierten Partikelstrukturen zu verbessern. Die genaue Untersuchung der Strukturbildungsmechanismen ist in Aerosolreaktoren für Produktionsprozesse nicht möglich oder führt zu sehr ungenauen Ergebnissen. Das liegt daran, dass die verschiedenen Mechanismen, die zur Strukturbildung führen, oft sehr schnell oder gleichzeitig ablaufen und die Prozessbedingungen meist nicht gut genug definiert werden können. Um genaue kinetische Daten zu erhalten, müssen die Mechanismen voneinander isoliert und wohldefinierte Bedingungen mit definierten Partikeleigenschaften bereitgestellt werden. Koagulation und Sinterung sind die beiden wichtigsten Mechanismen, die zu Morphologie und Wachstum der Partikel führen. Während die Koagulation in Modellen gut beschrieben werden kann, ist die Sinterung aufgrund ihrer Abhängigkeit von verschiedenen Partikeleigenschaften (z. B. Größe, Form, Agglomeratstruktur), Materialeigenschaften sowie Prozessbedingungen (Temperatur-Zeit-Verlauf der Partikel) ein komplexerer Mechanismus.
Der Schwerpunkt dieser Arbeit liegt auf der Ermittlung präziser kinetischer Daten für den Mechanismus der Strukturbildung, insbesondere der Sinterung, von Aerosol-Nanopartikeln. Durch die Aufteilung eines polydispersen Aerosols in monodisperse Größenfraktionen werden definierte Ausgangspartikelstrukturen im Größenbereich von 20 bis 200 nm bereitgestellt. Hierzu wurde ein sonderangefertigter differentieller Mobilitätsanalysator für den mittleren Durchflussbereich (MF-DMA) entwickelt und für größere Aerosolflussraten und längere Laufzeiten optimiert. Ein Modellströmungsreaktor (MFR) wurde für die genaue Untersuchung des Strukturbildungsmechanismus konzipiert, indem eine enge Temperatur-Verweilzeit-Verteilung der Partikel bereitgestellt wird. Ein numerisches Strömungsmodell (CFD-Modell) des MFRs wurde durch umfassende Temperaturmessungen validiert, um das Strömungsfeld in der Reaktionszone, in der die Strukturbildung stattfindet, zu optimieren. Das validierte CFD Modell wird benötigt, um die Temperatur-Verweilzeit-Verteilung aus simulierten Partikeltrajektorien in Abhängigkeit von verschiedenen Betriebstemperaturen zu berechnen, die als Eingangsbedingungen für die numerische Bestimmung der Kinetikdaten verwendet werden. Die

Überwachung der Partikelgrößen- und -massenverteilung mit Online Aerosolmessgeräten ermöglicht die Berechnung von Struktureigenschaften oder -merkmalen über Strukturmodelle (wie Partikeloberfläche, Primärpartikelgröße, effektive Dichte, Anzahl der Primärpartikel pro Agglomerat), um die Struktur oder ihre Veränderungen zu beschreiben. Es wird ein Sintermodell angenommen, das die Abnahme der Oberfläche mit einem kinetischen Term in Form eines Arrhenius-Ausdrucks beschreibt, der eine Aktivierungsenergie und einen Vorfaktor enthält. Die Aktivierungsenergie und der Vorfaktor werden numerisch durch Fehlerminimierung zwischen modellierter und gemessener Partikelgröße bestimmt, unter Berücksichtigung des Temperatur-Verweilzeit-Verlaufs der Partikel. Die Anwendung und Validierung des Sintermodells auf Aerosolreaktoren im Pilotmaßstab oder in Produktionsanlagen ist eine Herausforderung. Neben der Komplexität der Aufbauten und der gleichzeitig auftretenden Strukturbildungsmechanismen werden einige der Reaktoren auch bei Niederdruck betrieben. Dadurch ist der Einsatz von Standard Online Aerosolmessverfahren wie Scanning Mobility Particle Sizer (SMPS), Centrifugal Particle Mass Analyzer (CPMA) und Electrical Low-Pressure Impactor (ELPI) nicht möglich oder erfordert umfangreiche Kalibrierungen für einen bestimmten Druckbereich. Eine Lösung hierfür ist die Verwendung eines kommerziellen Vakuumejektors als einfaches Hilfsmittel für die kontinuierliche Probenahme aus Niederdruckbereichen. Vakuumejektoren sind in der Regel so konstruiert, dass sie einen Niederdruckbereich durch ein beschleunigtes Antriebsgas über eine konvergierende Düse erzeugen. Dieser Effekt kann auch genutzt werden, um Aerosolpartikel von einem Niederdruckbereich auf Atmosphärendruck zu übertragen. Zur Bestimmung des Übertragungsverhaltens verschiedener kommerzieller Vakuumejektoren wird ein Testaerosol synthetisiert und die Anwendbarkeit der Ejektoren in Kombination mit Standard Online Instrumenten an einem Niederdruck-Mikrowellenplasmareaktor und Flammenreaktor mit hohen Produktionsraten getestet.

Die besten Dinge im Leben sind nicht die,
die man für Geld bekommt.

— Albert Einstein —

DANKSAGUNG

Ich hatte eine wunderbare und interessante Zeit am Institut für Nanostrukturotechnik (NST) an der Universität Duisburg-Essen. Meine Forschungsarbeit wäre ohne die finanzielle Unterstützung der Forschungsgruppe 2284 *"Model-based scalable gas-phase synthesis of complex nanoparticles"* durch die Deutsche Forschungsgemeinschaft (DFG) unter der Projektnummer 262219004 nicht möglich gewesen. Die Herausforderungen und Aufgaben dieses Projekts haben mir viel Freude bereitet, ebenso wie die Zusammenarbeit mit den Projektpartnern, die Diskussionen und die informativen Reisen zu Konferenzen.

Zuallererst spreche ich *Prof. Dr.-Ing. F. Einar Kruis* meinen tiefsten Dank für die Möglichkeit in seiner Gruppe zu arbeiten aus. Seine beharrliche Unterstützung und seine umfangreiche wissenschaftliche Erfahrung haben meine Forschungsarbeit erheblich bereichert. Er hat wesentlich zum Erfolg dieser Arbeit beigetragen. Ich bedanke mich für die anregenden Diskussionen, das Vertrauen und die wissenschaftliche Freiheit, die mir gegeben wurde.

Bedanken möchte ich mich auch bei *Prof. Dr. rer. nat. Roland Schmechel* für seine Unterstützung in seiner Funktion als Institutsleiter, für Einblicke in verschiedene Themen der Thermoelektrik und organischen Photovoltaik und für das angenehme Arbeitsumfeld.

Des Weiteren bedanke ich mich bei *Prof. Dr. rar. nat. Markus Winterer* für seine Unterstützung und Expertise bei der Analyse der Eisenphasen, für unsere hilfreichen Diskussionen und Kooperationen, sowie für seine Bereitschaft diese Dissertation als Zweitprüfer zu begutachten.

Ich bedanke mich bei allen *Kolleginnen* und *Kollegen* der NST für die schöne Zeit am Institut und für die Hilfe bei Experimenten. Ein besonderer Dank geht hierbei an *Dipl. Phys. Dennis Kiesler* für seine Leidenschaft für die Wissenschaft. Er hat durch sein Fachwissen und sein Enthusiasmus für die Forschung meine Arbeit grundlegend beeinflusst. Es hat mir sehr viel Spaß gemacht mit ihm zu arbeiten und ich bedanke mich herzlich für die lehrreiche Zusammenarbeit.

Die Realisierung der technischen Aufbauten wäre ohne *Felix Bensel* nicht möglich gewesen, der mir mit technischen Zeichnungen und der Montage der Modellströmungsreaktoren geholfen hat. Daran anschließend bedanke ich mich bei den *Universitätswerkstätten* für die schnelle und präzise Herstellung der technischen Geräte, Vakuumanschlüsse und Adapter für meine Aufbauten.
Abschließend bedanke ich mich bei meinen Eltern *Beate* und *Hans-Joachim*, meinen Brüdern *Brian*, *Marvin* und *Marcel*, meinen *Freunden* und natürlich meiner Ehefrau *Miriam* und meiner Tochter *Karla* für die unnachgiebige Unterstützung und Motivation, meine Arbeit erfolgreich abzuschließen.

CONTENTS

LIST OF FIGURES

LIST OF TABLES

AP-PMS	ambient-pressure particle mass spectrometer
APM	aerosol particle mass analyzer
BET	Brunauer, Emmett and Teller
C-DMA	cylindrical differential mobility analyzer
CFD	computational fluid dynamics
CMD	count median diameter
CO	critical orifice
CPC	condensation particle counter
CPMA	centrifugal particle mass analyzer
DAPS	differential aerodynamic particle sizer
DBD	dielectric barrier discharge
DMA	differential mobility analzyer
DMPS	differential mobility particle sizer
DO	discrete ordinate
EDX	energy-dispersive X-ray
EELS	electron energy loss spectroscopy
ELPI	electrical low-pressure impactor
ESP	electrostatic precipitator
FCE	Faraday cup with electrometer
GDF	gas dilution factor
HAB	height above burner
HEPA	high-efficiency particulate absorbing
HF-DMA	high-flow differential mobility analyzer
HMDSO	hexamethyldisiloxane
HTR	high-temperature reactor
LCF	linear combination fitting
LII	laser-induced incandescence
LP-DMA	low-pressure differential mobility analyzer

LPSD	low-pressure sampling device
MD	molecular dynamics
MF-DMA	medium-flow differential mobility analyzer
MFC	mass flow controller
MFM	mass flow meter
MFR	model flow reactor
MRI	magnetic resonance imaging
NDF	numerical differentiation formula
NP	nanoparticle
NPMR	nanoparticle microreactor
PBMS	particle beam mass spectrometer
PDF	particle dilution factor
PDF	probability density function
PMS	particle mass spectrometer
PSD	particle size distribution
PSL	polystyrene latex
R-DMA	radial differential mobility analyzer
SMPS	scanning mobility particle sizer
SSA	specific surface area
TAO	tube after the orifice
TEM	transmission electron microscope
TEOS	tetraethoxysilane
TF	transfer function
TOF	time of flight
TTIP	titanium tetraisopropoxide
UCPC	ultrafine condensation particle counter
VSVO	variable step size and variable order
XAFS	X-ray absorption fine structure
XANES	X-ray absorption near edge structure
XRD	X-ray diffraction

LATIN SYMBOLS

A	slip correction parameter
a, A	surface area
A_s	pre-exponential factor
b	distance, spacing
C_C	Cunningham correction
D_x	diffusion coefficient of the sintering mechanism
d, D	diameter
D_α	scaling exponent
D_{fm}	mass–mobility exponent
E	electrical field
e	elementary charge
E_a	activation energy
E_{loss}	electron energy loss
f	non-uniformities in the electric field
F_B	Brownian force
F_c	centrifugal force
f^{charge}	charge propability distribution
F_D	drag force
f_D	friction coefficient
F_{el}	Coulomb force
$FWHM$	full width at half maximum
G_c	geometry parameter
GDF	gas dilution factor
I+, I-	positive or negative ion
i	index for size channel
j	numerical control variable
k_α	pre-factor

k_B	Boltzmann constant
k_{fm}	pre-factor
Kn	Knudsen number
L	length
x_M	length of the shock cell
M	Mach's number
m	mass
N	number or number concentration
n	ion concentration
N_A	Avogadro constant
N_{agglo}	number of primary particles per agglomerate
P	penetration
p	pressure
PDF	particle dilution factor
Pe	Péclet number
Q	gas flow rate
q	number of charges
$\mathcal{R}$	resolution
r	radius
Re	Reynolds number
r_{radial}	radial coordinate
St'	modified Stokes number
St_0	Stokes number
T	temperature
t	time
TF	transfer function
U	voltage
u	numerical factor
U_{i}	average flow velocity in the inlet tube
U_{o}	average flow velocity in the orifice
u, v	velocity of the object
v, V	volume

w	grain boundary width
X	mole fraction
x, m	exponential factor
Z	electrical mobility
z_{axial}	axial coordinate

GREEK SYMBOLS

α, β, γ	Millikans's pre-factor
α	height of a DMA transfer function
β	aerosol to sheath gas flow ratio
γ	specific heat ratio
γ_s	surface tension
δ	ratio of in- and outflowing gas flow rates
ϵ	numerical error parameter
ϵ_0	dielectric constant
ζ	Gaussian distributed random number
η	dynamic viscosity of the gas
η^{CPC}	counting efficiency
η	particle losses
Θ	angle between the incident beam and the crystallographic reflecting plane
λ, λ_{mfp}	mean free path
μ	dimensionless deposition parameter
ρ	density
ρ_0	standard-density
ΣSQR	sum of square root
σ	dimension variance
$\tilde{\sigma}$	dimensionless variance
σ_g	geometric standard deviation
τ	residence time
τ_r	relaxation time
τ_s	characteristic sintering time
ω	angular velocity

SUBSCRIPT

aero, a	aerodynamic
aerosol, A	aerosol
approx	approximation
axial	axial direction
B	Bubbler
BET	Brunauer Emmett and Teller
bulk	bulk properties
calc	calculation
c	centerline
CO	critical orifice
CPC	condensation particle counter
D	dilution
DMA	differential mobility analyzer
eff	effective
excess	excess
exit	outlet of the capillary
exp	experimental
FCE	Faraday cup with electrometer
g	geometric
gas	gas
i	inner
in	inflow
m, B, mobil,p	mobility
va	surface area equivalent
max	maximum value
min	minimum value
mode	mode or modal value
mono	monodisperse

neut	neutral
o, S0, 0	orifice
O2	oxygen
o	outer
out	outflow
p	particle
poly	polydisperse
prim	primary
radial	radial direction
s	Stokes
scan	scan or measurement time
setp	setpoint
sheath, S	sheath gas
SMPS	scanning mobility partice sizer
sph	spheres
t	tube
UCPC	ultrafine condensation particle counter
vac	vacuum/low-pressure region
mol	molar

Part I

SYNOPSIS

1

INTRODUCTION

The investigation of the structure formation mechanisms of complex nanoparticles is classified as fundamental research and aims to give insight into the formation and evolution of nanoscale aerosol particles. The determination of kinetic data to model the formation processes and their validation is required to simulate structure formation mechanisms and predict the development of specific particle structures. These models are needed to optimize the synthesis of nanoparticles with defined structures and properties in aerosol reactors. This research is part of nanotechnology, which deals with applications and phenomena on the nanoscale, in particular with nanoscale structures with at least one dimension smaller than 100 nm. The production of nanoscaled structures can be divided into two approaches, the production from a solid material (top-down) or the assembly of individual components to form a superordinate nanostructure (bottom-up). Very small particulate structures, liquid or solid, somewhat larger than gas molecules, show slow sedimentation and can be transferred to and transported in the gas phase. Larger particles of the order of a few micrometers are mainly affected by gravitational and inertial forces and have a much shorter residence time in the gas phase. The mixture of gas and solid or liquid particles is technically classified as an aerosol (*Greek* aero = air, *Latin* solutio = solution). Aerosol technology is the study of the properties, behavior, and physical principles of aerosols and the application of this knowledge to their measurement and control (Hinds, 1999). It is concerned, among many other things, with the efficient synthesis of specific or functionalized particle structures and properties and with measuring aerosol particle, describing their structures using suitable models. The ability to create specific structures opens up another dimension for functionalizing material properties. The synthesis of ultrafine and pure particle structures with defined material properties, such as electrical, magnetic or optical, is in the gas phase possible. It also allows the modification and combination of different material properties as well as the creation of new properties on the nanoscale, such as quantum effects, optical or superparamagnetic properties (Gupta and Gupta, 2005). The morphology of the particles, e.g. the surface or volume structure, plays a key role in this regard. Wolfgang Pauli is reported to have once said *"God created the volume, the devil created the surface"*, and emphasizes with his statement the challenges that come with the surfaces. This is

already evident in the difficulty of describing the structure in terms of a model. The particle structure or morphology usually consists of a primary structure or primary particle size (substructure), which by combination or agglomeration leads to a superordinate/hierarchical structure, the so-called agglomerate structure. The combination of different primary structures, their modifications by e.g. coatings, crystallinity etc. and the fractal dimension of the agglomerates (compact/open structure), leads to a variety of possible combinations. These degrees of freedom allow to create almost any structure or specific material properties and thereby the use in different applications.

1.1 INFLUENCE OF PARTICLE STRUCTURE ON PRODUCT PROPERTIES

Nanoparticles with large specific surface areas or open structures are particularly suitable for catalysis (Lu, Salabas, and Schüth, 2007), energy storage (Frey et al., 2009), gas sensors (Miller, Akbar, and Morris, 2014) and thermoelectric generators (Hülser et al., 2011) . The large interface of the particle surface to the surrounding fluid offers a large contact area for thermal, electrical or chemical interaction/reaction. Compact structures with larger volume approach the bulk material properties. Depending on their properties, these structures can be used in electronic and magnetic devices or as growth nuclei for other structures, e.g. nanowires (Heurlin et al., 2012). In this work, iron (Fe) and iron oxide (Fe_xO_y) nanoparticles (NPs) are synthesized to study the mechanisms of structure formation. Fe or Fe_xO_y NPs are widely used in catalysis, as pigments or as wave seals (as ferrofluids) and especially for a variety of biomedical applications. These areas of application arise from the possibility of being able to specifically influence the material properties on the nanoscale via the structure. In catalysis, Fe_xO_y is valuable due to its tunable catalytic activity (Liu et al., 2015), conductive coupling, porosity and substoichiometric oxide content. Ferrofluids consist of small magnetic Fe_xO_y nanoparticles dispersed in a liquid fluid and can be influenced in shape by an external magnetic field (Gazeau et al., 1998). Ferrofluids are used in loudspeakers as damping fluids or as sealants in rapidly rotating bearings. For certain applications, especially medical, more complex structures, e.g. encapsulating a core material with an inert/non-toxic shell (core-shell particle), might be useful. Iron oxide NPs can be modified with organic and inorganic agents, antibodies, nonionic detergents, starches, enzymes, proteins, drugs, nucleotides, and polyelectrolytes to enable further applications based on their broad surface chemical potential. Iron and iron oxides can have ferromagnetic properties that become magnetic when an external magnetic field is applied. This proves to be an advantageous property

when the aforementioned materials fit into the nanoscale. Iron oxide nanosized particles with ferromagnetic properties smaller than 20 nm can show superparamagnetic properties, at the same time having low toxicity and ease of separation. Iron oxide is the most common magnetic material and can be used as nanoparticles in organs, tumors and tissues by applying an external magnetic field for hyperthermic treatment purposes (Tong et al., 2017) and applications in medical diagnostics such as magnetic resonance imaging (MRI) (Park, 2017), protein immobilization in biomedicine, and drug delivery. Marcu et al. (2013) investigated the cytotoxicity and the anti-proliferation effects of Fe_xO_y-NPs in vitro on the breast adenocarcinoma cell line MCF-7 for application as drug delivery. They demonstrated that the particle structure and size of synthesized iron oxide particles with a diameter in the range of 8 to 10 nm by laser pyrolysis and coated with antracyclinic antibiotic Violamycine B1 showed a better performance by higher action on cell adhesion/proliferation than commercial pure $\gamma-Fe_2O_3$ (> 99 %) nanoparticles with a diameter of 20 nm. That the modification of particle morphology leads to a changes in material properties is also shown in the work of Chertok et al. (2008). They investigated commercial magnetic iron oxide nanoparticles (G100, chemicell GmbH, Berlin, Germany) and starch coated iron oxide NPs with hydrodynamic diameter of 100 ± 22 nm (mean$\pm$SD) for magnetic targeting. The extent of the in vivo effects and the selectivity of NP accumulation in rat tumors were studied by an intravenous injection of nanoparticles (12 mg/kg) under a magnetic field density of 0 T (control) or 0.4 T (experimental). A significant increase of the accumulation of iron oxide NPs in gliosarcoma was reached by magnetic targeting and could be successfully quantified by MR imaging. The success of magnetic targeting depends on the magnetic properties, which in turn depend on the size distribution of the nanoparticles and, to a large extent, on the crystal quality (Batlle et al., 2011). The excerpt from these works shows the complex requirements for the particle structure, which must be adapted to the specific application. Adding to the commercial application of functionalized nanoparticles, efficient and cost-effective production of larger particle quantities is required.

1.2 AEROSOL REACTORS

The synthesis and modification of aerosol nanoparticles is carried out and studied in aerosol reactors based on various synthesis methods, including plasma (Kunze et al., 2019; Münzer et al., 2017; Stein and Kruis, 2016), and flame processes (Ifeacho et al., 2007) or laser ablation (Kim, Osone, et al., 2017). These methods rely on an energy input to vaporize, ablate,

or decompose a material or precursor molecule. Once the gas phase is supersaturated with a material, the formation of small nanoparticles occurs by nucleation, condensation, coagulation and sintering. For the synthesis of certain particle structures or materials, some methods are more or less suitable than others due to the different process requirements/conditions. Flame reactors are long-term and high-temperature stable processes that require a fuel with oxidant (oxygen). The production rate is high and it is possible to decompose various materials, but the synthesis of pure particles of a material, especially materials susceptible to oxidation such as some metals or transition metals, is not directly possible. The synthesis of high-purity (transition) metal particles such as copper (Cu), zinc (Zn), titanium (Ti) or aluminum (Al) is possible with plasma reactors. These are more complex processes that can be difficult to control, as they can reach very high temperatures locally. Laser ablation requires a high-power laser and a light-absorbing material that can be vaporized by the energy of the laser pulse. The yield of nanoparticles can be adjusted by the operating parameters such as temperature, gas velocity, and pressure. A higher temperature leads often to a higher evaporation rate, operating the aerosol reactor at low pressure results in a higher gas velocity at a constant gas mass flow rate and thus a shorter residence time of the particles in the hot zones. This can have significant impact on particle size distribution and production rate (Granqvist and Buhrman, 1976).

The targeted generation of a desired structure or combinations thereof requires precise knowledge of the structure formation mechanisms as well as of the process conditions. In aerosol reactors, different processes such as sintering, coagulation, condensation can take place simultaneously or very quickly so that it is not possible to investigate the individual structure formation mechanisms separated from each other. Homogeneous condensation (nucleation) and heterogeneous condensation lead to the formation of primary particles from monomers, which then form a superordinate particle structure, agglomerates and aggregates, through the two main mechanisms, coagulation and sintering (Figure 1.1). Coagulation is well described in models, whereas sintering is a more complex mechanism due to its dependence on different particle properties, material properties and process conditions. The formulation and validation of a sintering model is therefore challenging. The investigation requires the isolation of this mechanism, providing well-defined process conditions, and accurate monitoring of the particle structure.

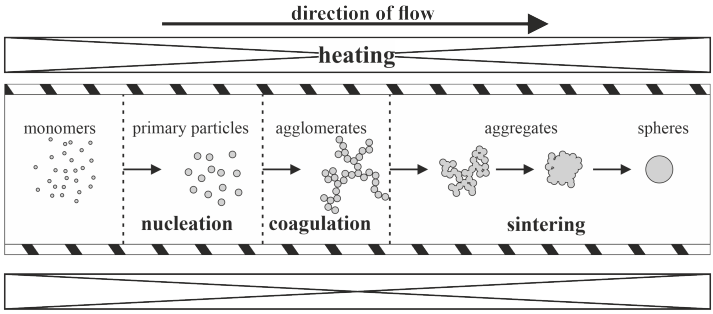

Figure 1.1: Schematic illustration of processes of particle formation and growth in aerosol reactors, adapted from Seto et al. (1997)

1.3 PROCESS CONTROL OF AEROSOL REACTORS

In addition to the theoretical description of the structure formation mechanisms, precise process control and monitoring is necessary to determine the process conditions on the one hand and to investigate their influence on particle production on the other hand. Aerosol reactors for the production of larger quantities of nanoparticles are usually in the pilot or production scale. Monitoring or process control of specific process parameters, like temperature, gas velocity and gas mixture, which strongly influence the formation of nanoparticles and their structure, is difficult due to the plant size and the complexity of the setups. Often, the process pressure is below atmospheric pressure in order to achieve higher gas velocities and thus a shorter residence time in the particle formation zone for a given gas mass flow. A higher temperature gradient is achieved, which leads to the formation of fine particle structures (Friedlander, 2000). In addition, sub-atmospheric pressure systems prevent particles from leaking out in an uncontrolled manner. The measurement and monitoring of particle formation and structure changes is particularly important to ensure high product quality. The measurement of particle size or mass distribution during the process is possible by means of online measuring devices and allows the optimization of process parameters. The measurement with standard aerosol instrumentation, such as scanning mobility particle sizer (SMPS), centrifugal particle mass analyzer (CPMA) or electrical low-pressure impactor (ELPI), in low pressure is not possible or requires extensive calibrations for a specific pressure range. Some instruments like the CPMA or aerosol particle mass analyzer (APM) are unsuitable for the operation under low pressure because of their complex design and fast rotating parts. A well-characterized continuous sampling

technique that transfers the aerosol from low pressure to atmospheric pressure and allows the use of online instrumentation on low-pressure aerosol reactors would be desirable. This would contribute to the use of the validated structure formation models in extensive simulations of more complex aerosol reactors and verify the results by using online measurement techniques. The findings from the simulations will contribute to the optimization of aerosol reactors for the synthesis of defined particle structures.

1.4 MODELS FOR AGGREGATE DYNAMICS

The study of particle formation and growth makes it possible to set up models for structure formation. Nanoparticle structures synthesized in the gas phase form mainly by coagulation and sintering. Sintering is only active in a narrow time window when the temperature is sufficiently high. Coagulation is dominant especially at very high nanoparticle concentrations and leads to the formation of fractal-like agglomerates (Friedlander, 2000). Lowering the particle number concentration reduces the collision rate between particles significantly and allows the separate study of coalescence and coagulation. Koch and Friedlander (1990) studied sintering and recognized that surface area reduction is limited by the overall size of the aggregates. They modeled the growth of primary particle size and considered the effect of coagulation on sintering for the free-molecule region. Kruis, Kusters, et al. (1993) describe the evolution of aggregate volume and surface area during simultaneous coagulation and sintering under non-isothermal conditions, assuming a monodisperse aggregate and primary particle size distribution. The aggregate structure is described using an exponential term, a fractal mass dimension of the aggregates. The individual models are used in population balances to describe particle formation (Kotalczyk, Skenderović, and Kruis, 2019). Here, volume-equivalent spheres or agglomerates with a constant fractal-like structure are assumed.

1.5 OPTIMIZATION OF AEROSOL REACTORS

The study of particle and structure formation processes allows the optimization of particle yield at defined particle properties. A high nanoparticle production rate of more than 1 kg/h is necessary to commercialize the particles in a wide range of products. Enhancing the particle yield with defined structure or properties requires validated structure formation models to simulate the particle formation occurring during the synthesis. Previous works have shown that coagulation is strongly dependent on

the particle number concentration while for sintering the temperature-residence time distribution of the particles is more important. The investigation and validation of structure formation models require accurate kinetic data, which can be determined under well-defined conditions for sintering in a narrow temperature-residence time distribution. Ideal process conditions can be set and monitored in a test reactor, a so called model flow reactor (MFR). MFRs designed to study specific reactions and mechanisms under controlled conditions. The flow pattern is simplified to guarantee a narrow and well-defined temperature-time distribution in the reaction zone. The process parameters can be controlled precisely and allow the investigation of even complex reactions and mechanisms.

In this thesis, a new MFR was designed and optimized to investigate structure formation mechanisms, e.g. sintering and coating, of nanoparticles (Publication D). It bases on a vertical high-temperature tube furnace with defined aerosol in- and outlets on the centerline. Monodisperse aerosol particles with a characterized structure are introduced into the reaction zone, can be mixed with a precursor, and structure formation can be investigated under well-defined temperature-residence time distribution, Figure 1.2.

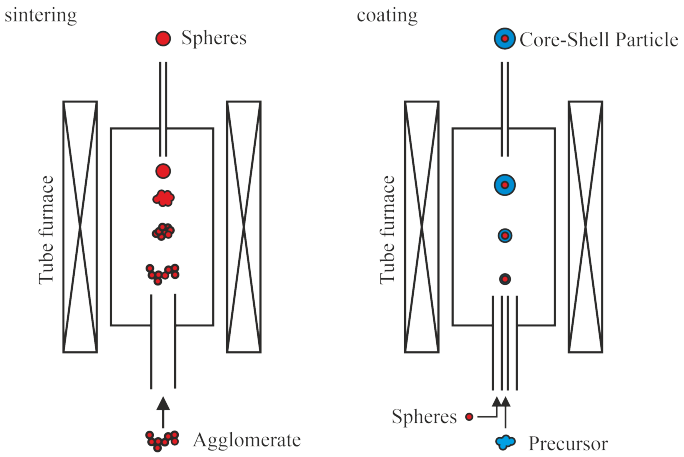

Figure 1.2: Concept of a model flow reactor

Computational fluid dynamics (CFD) simulations confirm well-defined conditions in a narrow temperature-residence time distribution of the particles, allowing to determine precise kinetic data. A longtime stable monodisperse aerosol with a narrowly distributed initial particle struc-

ture is provided by a new designed differential mobility analzyer (DMA) for higher aerosol flow rates up to 5 L/min (Publication B). This device is mandatory to measure the size-selected particle structures with different aerosol instruments, each requiring a certain sample flow rate with sufficient particle number concentration. Thereby, it is possible to measure different particle properties simultaneously and to determine the particle structure. The evaluation of particle structure change considering the particle temperature-residence time distribution and assuming a suitable structure formation model leads to precise kinetic data (Publication F). The model can be applied to random aerosol reactors with known temperature-residence time history of the particles. Verification of the structure models on low-pressure aerosol reactors is not directly possible using standard online measurement techniques, since these are generally calibrated or designed for atmospheric pressure. Continuous sampling from low pressure and transfer to atmospheric pressure is possible with vacuum ejectors and would allow the use of standard online instrumentation. For this purpose, two commercial vacuum ejectors differing in the working pressure are fully characterized and their operation is demonstrated on different aerosol reactors (Publication A, C and E).

2

MEASUREMENT METHODS

In measurement technology, different definitions of particle size and shape are used. Depending on the method, simplified properties (e.g. spherical particles) are assumed in order to determine the particle size distribution. The measured particle size is expressed as an equivalent diameter to assign a size to a particle that represents its specific property or behavior in a specific conditions (Figure 2.1). It is the diameter of the sphere, with the same physical property as the irregular shaped particle.

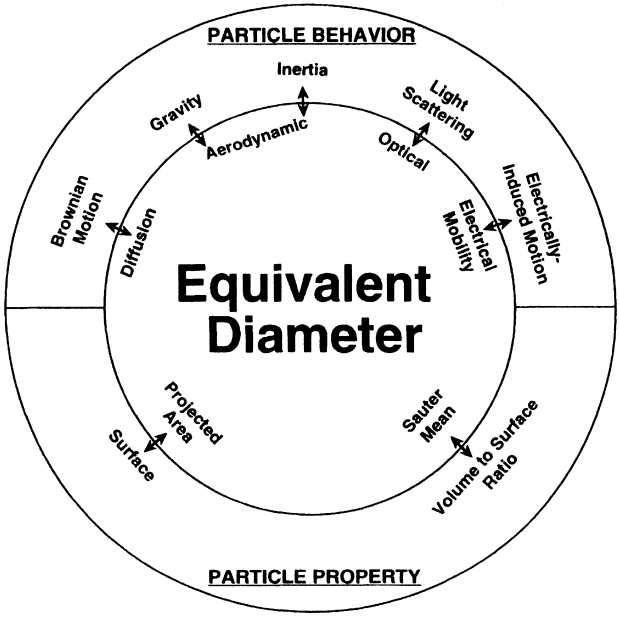

Figure 2.1: Definition of the particle size (equivalent diameter) depend on observations of particle properties or behavior (Kulkarni, Baron, and Willeke, 2011).

The aerodynamic equivalent diameter or Stokes diameter are defined as the diameter of a sphere of standard density of $1\,g/cm^3$ (aerodynamic diameter) or its bulk density of the material (Stokes diameter) that has the same terminal velocity on settling under gravity as the particle under

consideration. For extremely small particles, the aerodynamic diameter may not be relevant; instead, a mobility equivalent diameter is more often used. The mobility equivalent diameter is the diameter of a spherical particle with the same mobility (defined as the particle velocity generated by an external force unit) as the particle in question.

2.1 PROVIDING A MONODISPERSE AEROSOL

Aerosol particles can be synthesized by various bottom-up or top-down techniques. Most synthesis methods produce nanoparticles with a broad range of sizes due to simultaneous occurring mechanisms, such as nucleation, condensation, coagulation, evaporation, and sintering. Statistically, coagulation leads to an almost log-normally distributed polydisperse particle size distribution. The direct synthesis of an aerosol that is narrowly distributed in size is usually not possible or is very complicated because precise process conditions and control are required. The stability of the aerosol with only one size class is severely limited by the number concentration. As the number concentration increases, the probability of two or more particles colliding and sticking together (coagulation/agglomeration) increases, and an approximately lognormal size distribution arises.

A narrow distribution of a particle property is also described as monodisperse and is essential for precise detection of structural changes of an initial structure. For the diameter, it is characterized by a narrow size range, respectively by a narrow width of the particle size distribution (PSD). Statistically, the PSD arises an almost log-normal shape, so that the geometric standard deviation σ_g is used to describe its width. It is defined by Equation (2.1) with the number N of the particle diameter d in the size channel i and the geometric mean diameter d_g.

$$\ln \sigma_g = \left(\frac{\int \left(\ln d_i - \ln d_g \right)^2 \mathrm{d}N_i}{(\Sigma N_i) - 1} \right)^{1/2} \tag{2.1}$$

The geometric mean diameter is calculated by the Equation (2.2) and is for a lognormal distribution equal to the count median diameter (CMD).

$$\ln d_g = \frac{1}{\Sigma N_i} \int (\ln d_i)\, \mathrm{d}N \tag{2.2}$$

Monodisperse particle size distributions have a geometric standard deviation of $\sigma_g < 1.1$. A narrow particle size fraction can be extracted from a polydisperse particle size distribution by classifying the aerosol on the

basis of its properties. Integral classification methods are characterized by separating particles with an equivalent diameter larger or smaller than a cut-off diameter. Particle diameters larger than the cut-off diameter can be removed from the aerosol with an impactor or smaller particles with a diffusion battery. The combination of both methods allows the classification of an aerosol with a differential particle size distribution that is in the size range between the two cut-off diameters. This method is called differential classification and is used in differential electrical mobility analysis. It is one of the standard methods for classifying particles by its electrical mobility in an electrical field. This assumes that the particles are already electrical charged before the analysis. Depending on the charging method, particles can carry positive or negative polarity as well as multiple charges. The charge state of the particles is direct proportional to the electrical mobility and has to be known for the analysis. Radioactive sources or X-rays emitting bipolar ions can be used to achieve a defined state of charge equilibrium. This neutralization of the aerosol and the subsequent mobility analysis results in high particle loss, since on the one hand only one polarity is classified and on the other hand the probability of charging nanoparticles decreases with the particle size (Wiedensohler and Fissan, 1991). Nevertheless, mobility analysis outperforms other classification and deposition methods due to its narrow transfer function and the possibility to select the width of the classified particle fraction by the operation parameters.

2.1.1 *Electrical-mobility analysis*

The electric mobility of particles is defined by the drift velocity of a charged particle in an electric field $Z_\mathrm{p} = u/E$. In a laminar flow field, the electrical mobility can be calculated from the equilibrium of the drag force exerted by the gas F_D and the Coulomb force F_el, Equation (2.3).

$$\underbrace{qeE}_{F_\mathrm{el}} = \underbrace{\frac{3\pi\eta u d_\mathrm{m}}{C_\mathrm{C}(d_\mathrm{m})}}_{F_\mathrm{D}} \Rightarrow Z_\mathrm{p} = \frac{u}{E} = \frac{qeC_\mathrm{C}(d_\mathrm{m})}{3\pi\eta d_\mathrm{m}} \tag{2.3}$$

The Coulomb force F_el is defined by the number of charges q, the elementary charge e, and the electrical field E. The drag force F_D for a rigid sphere can be described by Stokes' law. It is calculated from the dynamic viscosity of the gas η, the velocity of the object u, and the diameter of the object d_p assuming spherical particles. The force equilibrium yields that the electric mobility Z_p is proportional to the ratio of the charge number to the particle diameter. For particle diameters

of the order of the mean free path in the gas λ, expressed by the Knudsen numbers $Kn = \lambda / d_p$, a slip correction factor C_C must be considered. In the Millikan experiment, it was noticed that very small oil droplets tend to sink faster than Stokes' law predicts. The introduced correction factor of Cunningham and Larmor (1910) takes into account that particles with small diameters experience slip at the particle surface (i.e., the relative velocity of the fluid at the surface is not zero). The slip correction parameter A as a function of Knudsen numbers Kn and describes the slip at the particle surface.

The slip correction function is determined by measuring the sedimentation velocity of small particles in an Millikan apparatus and fitting the pre-factors α, β, and γ of Equation (2.4) to the experimental data.

$$C_C\left(d_p\right) = 1 + Kn \underbrace{\left(\alpha + \beta \cdot \exp\left(-\gamma \cdot Kn\right)\right)}_{Parameter\,A} \tag{2.4}$$

A precise slip correction function with the pre-factors $\alpha = 1.165$, $\beta = 0.483$, and $\gamma = 0.997$ is given by Kim, Mulholland, et al. (2005), determined with polystyrene latex (PSL) particles. Figure 2.2 depicts the Cunningham correction factor C_C as function of the particle diameter d_p using the slip correction parameter A introduced by Kim, Mulholland, et al. (2005), assuming a mean free path λ of 67.4 nm. It can be seen that the Cunningham correction factor increase with decreasing particle diameter.

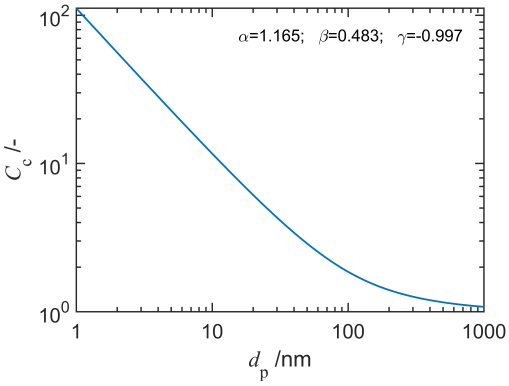

Figure 2.2: Cunningham correction factor C_C as function of the particle diameter d_p using the slip correction parameter A from Kim, Mulholland, et al. (2005) and a mean free path λ of 67.4 nm.

For the analysis of the particle mobility, a defined electrical field and laminar flow field, in which charged particles are classified by their electrical mobility, are provided by a differential mobility analyzer (DMA). The cylindrical DMA design of the classification zone is the most common, besides the radial or plate design, and is shown in Figure 2.3.

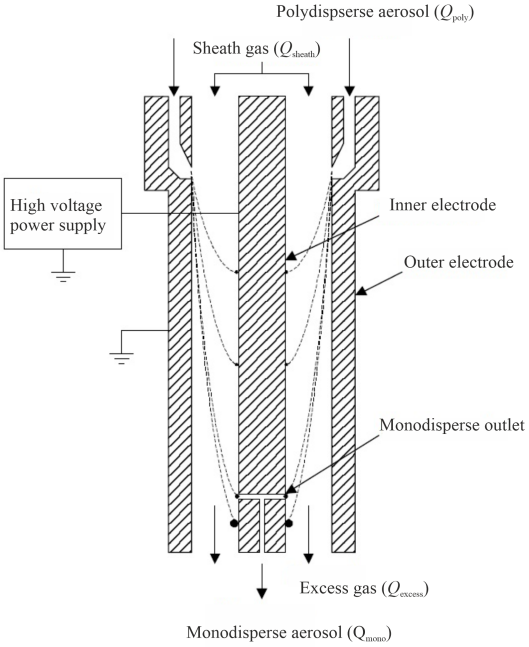

Figure 2.3: Schematic of a cylindrical differential mobility analyzer

It is defined by the geometry of the capacitor, the distance between the aerosol inlet and outlet, the length, and the gap between the cylindrical electrodes. The electrical field E is generated by applying an external voltage U to the capacitor. It is assumed that the electrical field is homogeneous and has only one component in radial direction. The flow field in the classification zone, between aerosol inlet and outlet, results from the aerosol flow rate Q_{aerosol} and a particle-free gas, called sheath gas Q_{sheath}. The polydisperse aerosol enters through the inlet Q_{poly} and flows tangential to the electrodes towards the sheath gas outlet. The flow field is assumed to be laminar and can be conveniently expressed as a plug flow, neglecting wall effects.

As soon as an external voltage is applied to the electrodes, an electrical field arises and charged particles get deflected according to their electrical mobility (based on polarity, charge state, and size) towards the electrodes. The mean electrical mobility Z_p^* of the particles passing through the outlet of the the DMA is a function of the classification zone design defined by the inner r_i and outer radii r_o and the length L, as well as of the operation parameters, the voltage U and the mean gas flow rate $1/2(Q_{sheath} + Q_{excess})$, Equation (2.5).

$$Z_p^* = \frac{Q_{sheath} + Q_{excess}}{U_{DMA}} \cdot \frac{\ln\left(\frac{r_o}{r_i}\right)}{4\pi \cdot L} \tag{2.5}$$

Particles with a higher electrical mobility are deposited on the electrode walls upstream, whereas lower mobilities deposit on the electrode walls downstream of the monodisperse outlet slit or leave the DMA via the excess outlet together with uncharged particles, as indicated by dashed lines in Figure 2.3. A consideration of the limits of the particle mobilities still classified in the monodisperse outlet ($Z_{p,max}$ and $Z_{p,min}$) can be defined by the two-dimensional stream function and calculating the particle trajectories in the DMA. Figure 2.4 depicts the typical triangular shaped transfer function (TF) without diffusional broadening. The triangular shape results from the convolution of two rectangularly shaped flow fields, here of the polydisperse and monodisperse aerosol flow field.

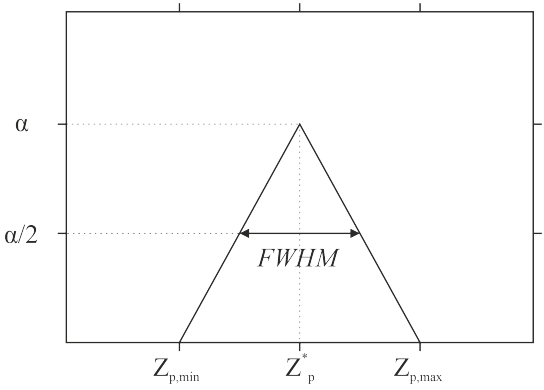

Figure 2.4: Non-diffusional transfer function of differential mobility analyzers

The full width at half maximum $FWHM$ of the TF is determined by the electrical maximal and minimal mobility passing through the monodisperse outlet at a given voltage U, Equation (2.6).

$$FWHM = \frac{Z_{p,max} - Z_{p,min}}{2Z_p^*} \tag{2.6}$$

$FWHM$ is proportional to 2β, the ratio of aerosol to sheath gas flow rate.

$$\beta = \frac{Q_{poly} + Q_{mono}}{Q_{sheath} + Q_{excess}} \tag{2.7}$$

and is a value for the monodispersity of the particle fraction, Equation (2.7). Flagan (1999) derived an approximate expression for the resolution of DMAs $\mathcal{R}_{approx} = 1/\sqrt{\beta^2 + 6\tilde{\sigma}^2}$ which is inversely proportional to β and to the dimensionless variance $\tilde{\sigma}$, taking diffusional broadening into account.

The diffusional broadening is more dominant for small particle diameters having longer residence times in the classification zone. This is the case, when the diffusive transport mechanism becomes more dominant than the electrophoretic transport mechanism, expressed by the Péclet number. Is the electrophoretic transport mechanism more dominant, the resolution can be estimated by β, the gas flow ratio $Q_{aerosol}/Q_{sheath}$ at constant sheath gas and aerosol flow rate $\left(\delta = \frac{Q_{mono} - Q_{poly}}{Q_{mono} + Q_{poly}} = 0\right)$. Usually, a sufficiently narrow particle size distribution, which can be defined as monodisperse ($\sigma_g < 1.1$), is achieved with a resolution higher than $\mathcal{R}_{approx} = 5$, respectively a flow ratio of $\beta = 0.2$. The modal value of the size distribution in the monodisperse outlet of the DMA is defined by $Z_p^* = Z_p$. Solving Equations (2.3) and (2.5) shows that the classified mobility-equivalent diameter d_m can be adjusted with the external voltage U, allowing differential analysis of the electrical mobility.

2.1.2 *Mass-mobility analysis*

The mass of aerosol particles is an important property and can be measured by their inertia, expressed in the relaxation time $\tau_r = \rho_p {d_p}^2 C_C / 18\eta$. The relaxation time depends on the particle density ρ_p and diameter d_p, the Cunningham correction C_C, and the dynamic viscosity of the gas η. The relaxation time characterizes the time required for a particle to adjust or relax its velocity to a new condition of forces (Hinds, 1999). This behavior can be used to measure the mass of aerosol particles. At a critical nozzle separating an atmospheric to a sub-atmospheric pressure region, drastic changes in streamlines occur. Particles differing in size or mass

will adapt to this flow change at different rates and are initially focused on defined trajectories in the low pressure (Babick et al., 2018). Small particle masses can also be measured by their deflection in a centrifugal field using a centrifuge with very high rotational speed.

Figure 2.5 shows the cross-section of the classification zone of a APM or CPMA. The classification zone consists of two rapidly rotating cylinders arranged coaxially to one another at a distance $r_o - r_i$. An electric field in this annular spacing is generated by applying an external voltage to the cylinders. Electrically charged aerosol particles flowing through

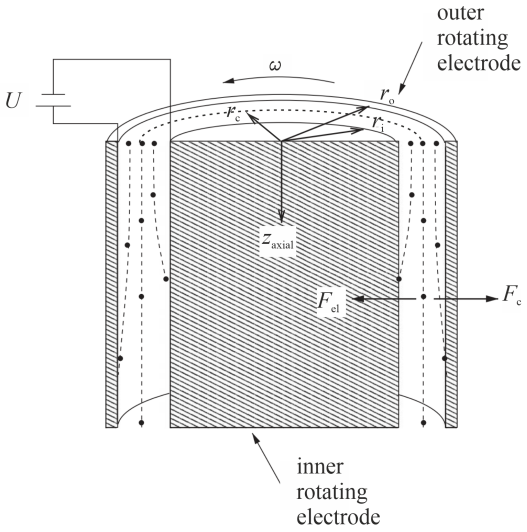

Figure 2.5: Cross-section of a cylindrical particle mass analyzer, adapted from Olfert and Collings (2005)

the classification zone are deflected from their initial trajectory as a function of their mass-charge ratio m_p/q. A force equilibrium between the centrifugal force F_c and the Coulomb force F_{el} for aerosol particles with a certain mass to charge ratio can be set by the operating parameters ω, the annular velocity of the cylinders and the applied voltage U, Equation (2.8).

$$\frac{m_p}{q} = \frac{eU}{\omega_c^2 r_c^2 \ln(r_o/r_i)} \tag{2.8}$$

Particles with a higher mass or opposite polarity will be deflected to the outer cylinder, whereas particles with a higher charge number will

be deflected to the inner cylinder, as shown in Figure 2.5 by dashed lines. The equilibrium of forces is only achieved in the center of the annular spacing gap r_c between the cylinders, since the Coulomb force increases towards the inner cylinder and the centrifugal force decreases. The CPMA uses in comparison to the APM different rotational speeds of the cylinders. The annular velocity of the inner cylinder is faster than the outer cylinder $\omega_o < \omega_i$ to achieve a force equilibrium independent from the radial position. This significantly improve the transfer behavior of the particles with the certain m_p/q ratio and allows the classification of low particle quantities. In the Publication F, the CPMA is used for the particle mass measurement in sintering experiments. Challenges that occur with the measurement of small nanoparticles are discussed.

2.2 SAMPLING FROM AEROSOL REACTORS

The application, verification, and adaption of the found sintering kinetics to aerosol reactors with broad temperature-residence time scattering is complicated by the fact that many aerosol reactors for nanoparticle production are operated at low pressure. The standard online measurement techniques that allow near real-time measurement of particle properties and study of the formation process can only be operated at atmospheric pressure or with a small deviation from it. SMPS, CPMA or ELPI cannot be operated at low pressure or require extensive calibration for a specific pressure range. Some instruments, such as the CPMA, are not suitable for low-pressure adjustment due to their complex design and rapidly rotating cylinders. A well-characterized continuous sampling technique that transfers the aerosol from low pressure to atmospheric pressure is required to use online instruments without extensive calibration. Time-efficient study of the influence of process conditions on particle characteristics with online instrumentation in low-pressure aerosol reactors would then be possible. Depending on the sampling method and sampling line, the transport efficiency of particles can be affected by the particles themselves (particle size, shape, or density) or by the process conditions (temperature, gas velocity, gas composition, etc.). Characterization of the sampling method and how the sample changes during sampling is necessary for adequate measurements. The time between sampling and measurement should be as short as possible to avoid alteration of the sample, especially for particles with reactive surfaces, such as those prone to oxidation.

A vacuum ejector or low-pressure ejector is a simple tool for creating a low-pressure area with a highly accelerated gas, based on the Venturi principle. Wang et al. (2005) showed that vacuum ejectors can be used to transfer aerosol particles from a certain low-pressure range to

atmospheric pressure. They synthesized nanoparticles in a low-pressure plasma reactor and used a two-stage ejector to measure particle size distribution with a SMPS at atmospheric conditions. However, the transfer function of the two-stage ejector was not characterized.

2.2.1 *Ejector-based sampling*

A vacuum ejector or low-pressure ejector consists of a smooth-walled tube with two cones directed towards each other, forming a converging nozzle with a small cross-section and at least one diffuser nozzle downstream, schematically depicted in Figure 2.6.

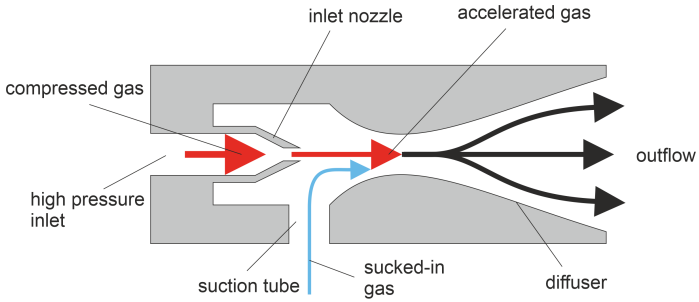

Figure 2.6: Schematic of a Venturi nozzle

When a compressed gas of several bars is applied to the converging nozzle, the fluid is accelerated according to the continuity law to velocities of the speed of sound (Mach number $M = 1$) in the narrowest cross-section. The high velocity of the gas results in a pressure drop, which can be used to suck in a gas flow rate by creating a small opening between the end of the converging nozzle and the diffuser, here suction tube. The driving gas from the converging nozzle entrains and mixes with the sucked-in gas flow, having enough velocity to be ejected into the diffuser. The diffuser is a tube with a steadily enlarging diameter, used to expand the volume of the gas mixture. Thereby, the gas velocity decreases and the external pressure increases up to atmospheric pressure. The suction effect of the vacuum ejector depends on the velocity and shape of the converging nozzle, as well as on the design of the diffuser. The suction flow of a single-stage ejector consisting of one converging nozzle with diffuser is limited, so is the lowest pressure in the suction tube, typically in the range of a 100 mbar. A higher suction flow rate or a lower pressure is achieved by combining more than one Venturi nozzle. A lower pressure is achieved when an upstream Venturi nozzle generates

a low pressure for the outflow of the downstream diffuser, allowing higher gas velocities. Separating the Venturi nozzles into stages separated by elastic flaps, so that the outflow of the downstream Venturi nozzle forms the driving gas for the upstream nozzle, allows higher suction flow rates for certain pressure ranges. The more detailed description of the design and operation of multi-stage ejectors, the commercial low-pressure ejectors (VIP-4 and VHP-5, Landenfeld, Kassel, Germany), is shown in Publication A and C.

3

EXPERIMENTAL SETUP

The experimental setup for the study of sintering kinetics shown in Figure 3.1 consists of c) particle synthesis and classification, b) structure transformation in the MFR and a) particle analysis with different measuring devices. Particles are synthesized by spark discharge and selected by its size using a medium-flow differential mobility analyzer (MF-DMA) (Publication B). The size-selected particles are monitored with a first SMPS before the particles flow into the MFR and undergo structure formation. Thereby, it can be ensured that the pre-selected particle size upstream of the MFR is maintained during sintering. The particle mass is measured with the CPMA and the aerodynamic particle diameter with the differential aerodynamic particle sizer (DAPS) simultaneously with the size measurement (second SMPS) downstream of the MFR. An electrostatic precipitator (ESP) is used to deposit particles for offline analysis, in particular to determine the chemical phase of the particles.

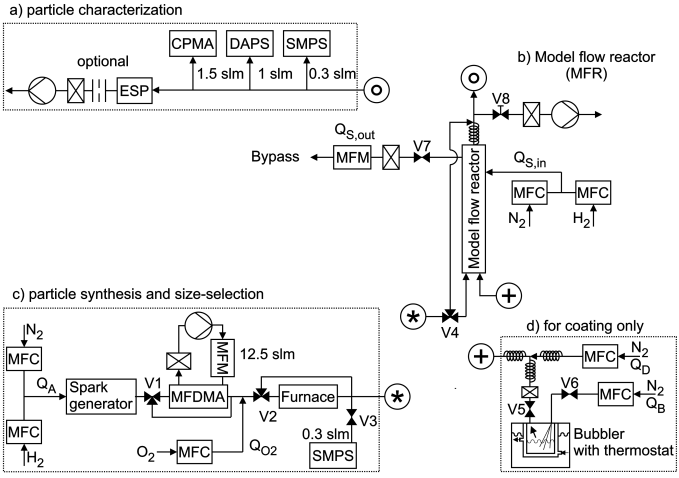

Figure 3.1: Experimental setup to measure structure formation used in Publication D and F)

This setup with modifications is also used to study particle coating mechanisms. A gas bubbler in a thermostat ($T = 300\,\mathrm{K}$), indicated by

d) in Figure 3.1, is filled with a liquid precursor and is used to transfer the precursor to the gas phase at precise conditions. The gas flow with precursor is directly quenched and tube walls are tempered to $T = 320\,\mathrm{K}$ to avoid supersaturation of the precursor and nucleation. Non-gaseous precursor are deposited in a HEPA-filter. A MFC connected to an oxygen gas bottle and tube furnace downstream of the MF-DMA are used to coalesce the particles into spherical Fe_xO_y-NP in a oxygen-rich atmosphere after size selection. Thus, the particle size/structure is well-defined and the increase in size and mass due to the structure formation in the upstream MFR can be attributed to surface growth by coating. The mixing of the spherical particles with the precursor takes place in the MFR through separate inlets in the injection probe (Publication D).

3.1 NANOPARTICLE SYNTHESIS BY SPARK DISCHARGE

A spark generator is used to synthesize small Fe and Fe_xO_y primary particles $d_{va} = 4\,\mathrm{nm}$ (surface area mean diameter) in a highly agglomerated structure. It is based on periodic electrical spark discharges between two electrodes, here iron. The high energy of the spark erodes the electrode material, resulting in the supersaturation of the gas and the formation of an aerosol, Figure 3.2.

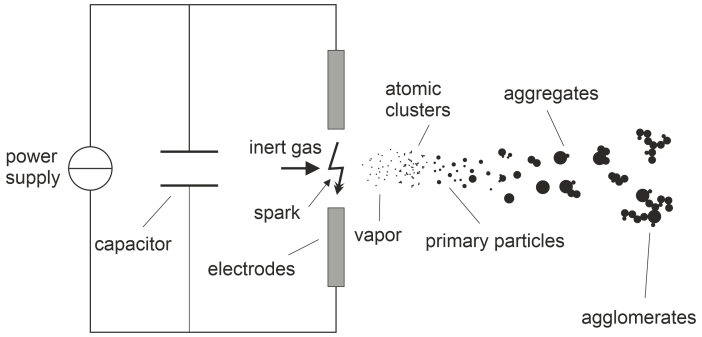

Figure 3.2: Synthesis of nanoparticles with a spark generator, adapted from Pfeiffer, Feng, and Schmidt-Ott (2014).

The aerosol formed includes smaller and larger particle structures, differing less by primary particle size but more in the number of primary particles per agglomerate. Small structures tend to have a more compact, less branched, structure. The particle structure of the aerosol can be slightly altered by the spark energy (Tabrizi et al., 2009). A stronger spark leads to a higher erosion rate of the electrode material and an increase of

the particle concentration, thus resulting in particles with a larger modal diameter. The spark energy per pulse depends on the breakdown voltage and the number of capacitors connected in parallel to the electrodes. The breakdown voltage is adjusted by the distance between the electrodes. The frequency of the pulses depends on the charging current of the capacitors at a constant breakdown voltage (Pfeiffer, Feng, and Schmidt-Ott, 2014). The kinetic energy of the electrons is created by the high voltage applied to the electrodes and accelerates the electrons from the cathode to the anode. The gas molecules between the electrodes are ionized (electrons are released from the molecular shell) by the collision with the accelerated electrons, creating a positively charged gas molecule that forms an electrically conductive path. The excess energy is released as heat or as photons, whose wavelengths are characteristic of the vaporized materials and the gas conditions. On the way from the cathode to the anode, the electrons ionize several gas molecules, which leads to an avalanche effect.

3.2 DESIGN OF THE MEDIUM-FLOW DIFFERENTIAL MOBILITY ANALYZER (MF-DMA)

For accurate analysis of the structure formation mechanisms, the aerosol is pre-selected into small particle size fractions (monodisperse size distribution) and measured using a combination of different online instrumentations. This procedure allows to determine the particle structures precisely via different particle properties, e.g. particle size and mass, and to calculate the structures by means of structure models. Each online technique requires a specific sample flow rate with a certain particle number concentration. The sample flow rate has to be highly diluted and cooled to prevent possible alteration of the sample (e.g., further sintering). Accordingly, a high total sample flow rate with a defined particle structure over the total measurement period must be provided for the characterization. A constant aerosol over days or at least 24 h to study the sintering kinetics at constant process conditions is needed. The operating time of DMAs is usually limited by the deposition of particles in the housing or in the filters over time. The particle deposits lead to changes in the flow field or to electrical breakdown between the inner and outer electrode in the case of electrically conductive particles. The classification of a monodisperse aerosol can no longer be guaranteed.

For the study of the sintering of nanoparticles (Publication D and F), a total sample flow rate of 2.5 L/min is needed. An increase of the aerosol flow rate requires an increase of the sheath gas flow rate to reach a sufficiently high resolution, Equation (2.7). Unfortunately, this leads

to a decrease in the maximum selectable particle size due to the higher sheath gas flow rate and the limitation of the applicable voltage until electrical discharges occur. The higher gas volume flow rate results in a faster gas velocity and thus shorter residence time of the particles in the classification zone. Classifying larger particle diameters using a higher aerosol flow rate is therefore only possible by extending the classification zone.

Table 3.1 shows a list of different radial and cylindrical DMA designs, which have been tested under different operation conditions.

DMA type	Reference	Geometric Parameters			Typical Operation Parameters	
		L (mm)	r_i (mm)	r_o (mm)	Flow ratio ($\frac{l/min}{l/min}$)	Diameter Range (nm)
Vienna-type (short)	Winklmayr et al. (1991)	110	25	33.5	2.0/20	3.5 – 65
Vienna-type (medium)		280	25	33.5	0.5/5	15 – 100
Vienna-type (long)		500	25	33.5	1.0/10	35 – 200
CIT Radial	Zhang et al. (1995)	-	-	-	0.5/5	8.0 – 75
RDMA	Nanda and Kruis (2014)	10	2	23.5	1.5/15	5 – 50
		10	2	35.5	1.5/15	7 – 75
		10	2	50.5	1.5/15	10 – 140
TSI Long	Model 3071a, TSI, St. Paul, MN	444	9.37	19.58	1.0/5.0	13 – 100
	Publication B				0.3/3	14 – 700
HF-DMA	Hontañón and Kruis (2009)	100	78	120	90/1100	3 – 30
MF-DMA (short)	Publication B	95	36	46	1.5/15	15 – 200
MF-DMA (long)		495	36	46	1.5/15	45 – 600

Table 3.1: Technical reference for the DMA types, extended from Birmili et al. (1997)

It can be seen that the diameter range is dependent on the length of the DMA classification zone, as well as on the sheath gas flow rate. A commercial Long DMA (3081, TSI, MN, US) operates with a sample to sheath flow ratio of 0.3 L/min to 3 L/min, having a maximum attainable particle size of 700 nm. If more measurement instruments behind a DMA should be applied, a higher sample flow rate is needed. Sample flow rates between 1 to 2 L/min have been tested with a Vienna-type, radial and TSI DMA with limitations to the resolution of the transfer function or largest selectable particle diameter. A high-flow differential mobility analyzer (HF-DMA) was developed for a high sample flow rate of 100 L/min and particle diameters up to 30 nm (Hontañón and Kruis, 2009). The HF-DMA is aimed for the pilot scale to select a monodisperse aerosol in a production process, which makes it oversized for smaller setups in the lab scale. A cylindrical DMA designed for medium flow rates and covering the full nanometer range is introduced in Publication B. Higher gas flow rates as used in conventional DMAs are possible due to the larger annulus space between inner ($r_i = 36$ mm) and outer ($r_o = 46$ mm) electrode, and

optimized aerosol in- and outlets. The classification zone of the MF-DMA can be extended from the short (95 mm) to the long version (495 mm). This makes the Short MF-DMA design more accurate for classifying smaller particle sizes, high electrical mobilities, and the Long MF-DMA for larger particle sizes. Figure 3.3 depicts the cross-section of the Short a) and Long MF-DMA b).

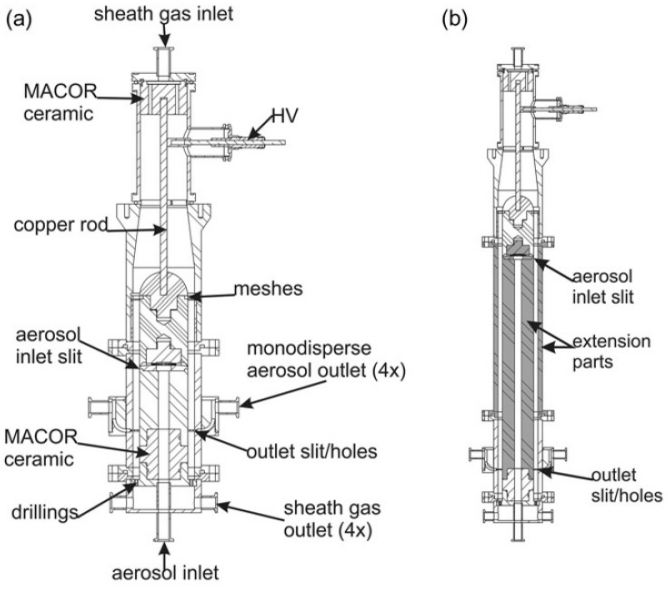

Figure 3.3: Cross-sections of the Short a) and Long MF-DMA b). Extensions parts for enlarge the classification zone are colored in gray (Publication B)

The polydisperse aerosol enters at the bottom of the MF-DMA and flows upwards in the inner electrode. It gets homogeneously distributed by small drillings before the particles flow through the aerosol inlet slit into the classification zone. The sheath gas flows from the top of the DMA through laminarization meshes to the classification zone. The classified aerosol leaves the classification zone through small drillings at the outer electrode whereas the excess gas leaves the annular space through the sheath gas outlets. The design of the MF-DMA is described in more detail in Publication B.

3.3 DESIGN OF THE MODEL FLOW REACTOR (MFR)

A MFR is designed to provide a reaction zone with well-defined conditions. For the investigation of structure formation mechanisms, e.g. sintering and coating, a certain temperature-residence time profile is required. While sintering is strongly influenced by temperature, residence time is more important for the formation of coatings (Post and Weber, 2019). Providing a long-term stable temperature-time history of the particles in the range of seconds is challenging due to diffusion, thermophoresis or other forces which could result in high particle losses or a broadening of the temperature-residence time profile. Previous studies have shown that radial temperature gradients occur in a horizontal tube furnace with laminar flow (Flynn and Dunlap, 1986) and that convection and condensation lead to the deposition of particles or precursors on the tube walls downstream of the heated zone (Park et al., 2001). Shrivastava, Gidwani, and Jung (2009) compared the particle trajectories in horizontally and vertically oriented tube furnaces and found out that the horizontal tube orientation leads to flow recirculation effects that result in more complex particle paths. The particles are forced by the buoyancy from the center to the upper hot tube walls, which causes radial mixing of the particles and broadening of the residence time distribution. Kirchhof, Schmid, and Peukert (2004) designed a vertical MFR, but used a turbulent flow field to achieve a more homogeneous temperature profile by turbulent mixing of a preheated sheath gas with a cold aerosol. This concept is inappropriate for achieving a narrowly distributed residence time distribution as a result of turbulent particle trajectories.

Therefore, a MFR with a laminar flow field in a vertical tube furnace was designed. Figure 3.4 depicts a schematic of the model flow reactor used in Publication D and F. Two concentric ceramic tubes are vertically arranged in the tube furnace with aerosol injection and sampling probes on the centerline. The inner ceramic tube is shorter than the outer tube and is suspended at the top. The lower end of the inner ceramic tube ends below the aerosol injection and allows the preheating of a sheath gas which is passed between the two ceramic tubes from top to bottom through the heating zone of the furnace. The aerosol enters the reaction zone, where the structure formation takes places, from the bottom and flows upwards together with the preheated sheath gas to the aerosol sampling outlet, respectively to the exhaust. The reaction zone is limited by the water-cooled aerosol injection and sampling probes (axial) and the preheated sheath gas (radial) (Gullett, Blom, and Gillis, 1988). In combination with thermophoretic forces caused by the heated tube walls, the preheated sheath gas stabilizes the aerosol particles on the centerline

and results in a much faster heating of the cold aerosol. An adjustment or extension of the reaction zone is possible by shifting the aerosol inlet and outlet. The design of the MFR is described in more detail in Publication D.

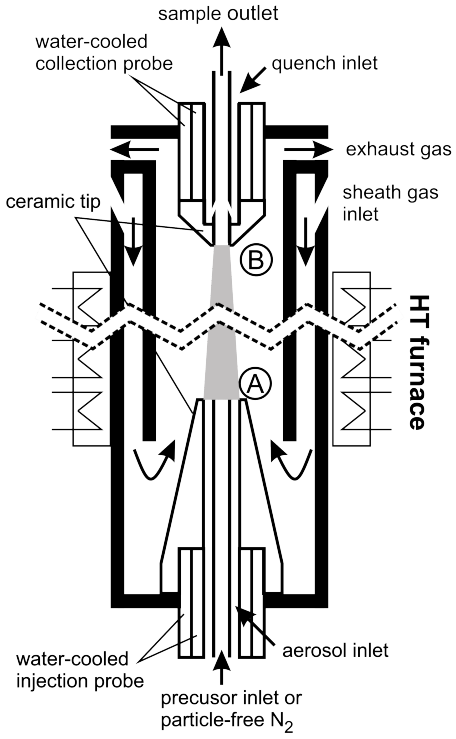

Figure 3.4: Schematic representation of the model flow reactor (MFR) (Publication D)

The ceramic tips on the probes converge with smooth surfaces toward the reaction zone, reducing the formation of a transient flow field at the aerosol inlet and outlet or high heat loss to the water-cooling. Particle losses at the cold probe walls, especially at the aerosol outlet, can be reduced by temperature control of the water cooling. A quench gas at the aerosol outlet allows rapid dilution and cooling of the hot aerosol from the reaction zone and reduces further losses. However, no quench gas was used in the experiments to avoid further reducing of the already low particle number concentration in the sampling probe. At the aerosol

inlet, an additional tube can be inserted and adjusted on the centerline and allows the separate inflow of a precursor, reactive gas, or particles into the reaction zone.

3.4 APPLICATION OF COMMERCIAL VACUUM EJECTORS FOR LOW-PRESSURE AEROSOL SAMPLING

It has already been demonstrated that ejectors are suitable for continuous sampling of aerosols from low-pressure areas (Wang et al., 2005), but a characterization of the transfer behavior of the ejector has not been carried out. Therefore, a change in the particle size distribution due to the sampling procedure can not be completely excluded. In Publication A and C, two different multi-stage ejectors differing in the working pressure were investigated. Multi-stage ejectors consist of more than one Venturi nozzle with diffuser in series, so that the outgoing gas from the diffuser, a mixture of sucked-in gas and compressed gas from the nozzle, is used as driving gas for the subsequent stages. Each of these nozzle stages has a larger nozzle diameter to cope with the falling gas pressure difference. The total extraction rate is then the sum of the individual nozzles, so that a significantly lower final pressure, compared to single ejectors, can be achieved (Ryans and Roper, 1986). Alternatively, the Venturi nozzles are arranged so that one Venturi nozzle lowers the pressure in the diffuser of another Venturi nozzle, allowing higher gas velocities and thus a lower pressure in the suction tube. After exiting the last Venturi nozzle, the exhaust gas is decelerated to reach atmospheric pressure.

Figure 3.5 shows a schematic of the interior of the VIP-4 and VHP-5 ejectors (Landefeld, Kassel, Germany). The housing of the two ejectors do not differ much and consists of an anodized aluminum box (67x182 mm) with a lid and rubber gasket. A high-pressure stage and four stages, each with a brass Venturi nozzle (indicator 1-4) are separated in chambers. Two elastic flaps are used to separate the stages 1 to 3, which are closed when the downstream pressure is significantly lower. Both ejectors consist of main Venturi nozzles, which are straight aligned and glued into the housing between the stages. The VHP-5 ejector uses a different nozzle design and an additional Venturi nozzle with small opening in parallel to the main nozzles between stages 1-2. As a result, two nozzles are supplied with the high pressure simultaneously and the first nozzle ejects the gas at 172 mbar in stage 2, reaches higher Mach numbers and reduces the pressure to 12 mbar in stage 1. The pressure is gradually increased from the lowest pressure in stage 1 to ambient conditions in stage 4. The low-pressure inlet and aerosol outlet are located in stages 1 and 4.

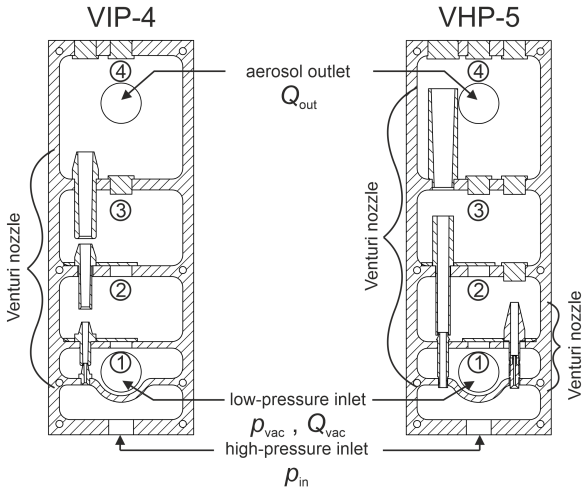

Figure 3.5: Schematic of the commercial vacuum ejectors VIP-4 and VHP-5 (Publication C)

4 PROVIDING WELL-DEFINED AEROSOLS

Precise kinetic data are needed to validate structure formation models (Kruis, Fissan, and Peled, 1998). The process conditions, especially the temperature-residence time profile of the particles during structure formation, have a dominant influence on the structure formation mechanisms besides the initial particle structure. A monodisperse aerosol with a defined particle structure is provided by using the MF-DMA (Publication B). Well-defined process conditions are achieved in a MFR (Publication D) that provides an adjustable narrow temperature-residence time distribution ($T(t)$) (Publication F). A narrowly distributed $T(t)$ profile, as well as PSD or particle structure, are essential for accurate measurements.

4.1 DETERMINING AND OPTIMIZING THE MF-DMA TRANSFER FUNCTION

The operation performance of the designed MF-DMA, expressed in the transfer function (TF), needs to be determined to find out if a narrow particle size distribution with defined particle structure can be provided. An approved method to measure the TF is the use of a tandem DMA setup, the configuration of two DMAs in series (Stratmann et al., 1997). The classified particle fraction leaving the first DMA at constant voltage is measured with a second DMA downstream by varying the voltage stepwise, known as the differential mobility particle sizer (DMPS) method, shown in Figure 4.1. The measured signal is then a result of both TFs and can be calculated by deconvolution (Hummes et al., 1996). For the mathematical solution, one of the two TFs must be known or both must be identical shaped.

The TF can be characterized by its width $FWHM$ and height α, assuming a triangular shape (§2.1.1). This is valid for the non-diffusional broadened TF, where in- and outflow rates of sheath gas and aerosol are constant ($\delta = 0$). The area of the TF represents the total amount of particles and gives information about the particle losses in the DMA. For the triangular-shaped TF, it is equal to the multiplication of α and $FWHM$. The diffusion increases with decreasing particle diameter and leads to a deviation from the ideal triangular function by a broadening and smoothing of the shape (Stolzenburg, 1988; Stolzenburg and McMurry, 2008).

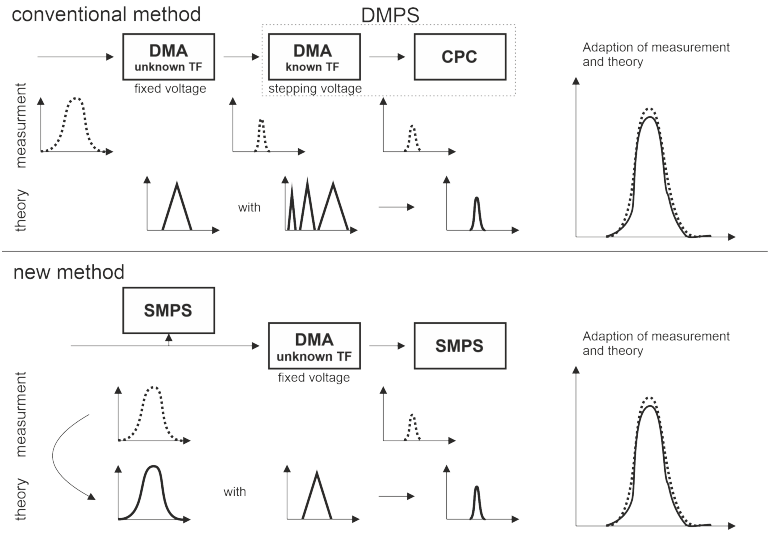

Figure 4.1: Method to determine the TF

A new method for faster, higher resolved, and versatile determination of the DMA transfer function is introduced and demonstrated in Publication B. It is based on the tandem DMA setup, but differs by the use of two SMPS systems with a Long DMA (3081, TSI) downstream and upstream of the DMA with unknown TF, here the MF-DMA. The simultaneous measurement of the in-flowing and out-flowing particle size distribution by scanning is a much faster measurement method, compared to the DMPS method. A constant sheath gas rate and aerosol flow rate is set to the MF-DMA with automatically altering the voltage for different size fractions. The published MATLAB script allows the computation of the TF directly from the SMPS data. All relevant parameters (TF of the Long DMA, particle losses in the SMPS system, counting efficiency, etc.) to calculate the unknown TF of the DMA precisely, have been determined and are considered in the computation.

In our experiments, the TF of the MF-DMA was determined for different resolutions ($\beta^{-1} = 10$, 5 and 3) with aerosol flow rates up to 8 L/min and sheath gas flow rates up to 24 L/min. During the investigation of the size selection performance of the MF-DMA, it was found that an optimization of the aerosol inlet leads to an improvement of the transfer characteristic, especially for higher aerosol flow rates > 2.5 L/min. The gas velocity was too high in the aerosol inlet area and led to an inhomo-

geneous distribution before entering the classification zone (B.3, within Publication B). This could be solved by doubling the amount of inlet drillings used to distribute the aerosol over the aerosol inlet slit, reducing the pressure over each drilling and the gas velocity. Adjusting the aerosol inlet slit from 1 and 2 mm further improves the TF for higher aerosol flow rates $> 5\,\mathrm{L/min}$.

Figure 4.2 a) and b) depict the TF of the Long MF-DMA for $\beta = 0.2$, experimentally characterized by the width $\mathcal{R}^{-1}$ and height α. The aerosol inlet is already optimized and an aerosol inlet gap of 1 mm was used. The TF is shown for particle diameters in the size range from 50 nm to 600 nm for aerosol flow rates of 1.5, 2.5 and 5 L/min. Theoretical values for diffusional $\mathcal{R}^{-1}_{\mathrm{approx}}$ (solid lines) and non-diffusional β (dashed line) broadened TF, as well as no loss, respectively a transfer efficiency of 100 % in the DMA (dotted line), are indicated. The non-diffusional TF describes the triangular-shaped TF and gives theoretical values for the minimum width at half maximum and maximum height. The transfer behavior of the DMA can be evaluated by comparing the diffusional with the experimentally determined TF.

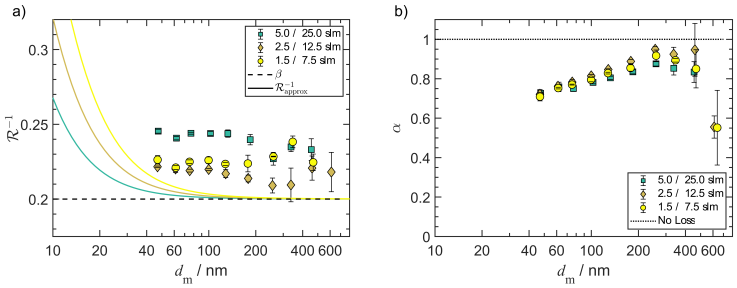

Figure 4.2: Width $\mathcal{R}^{-1}$ and height α of the Long MF-DMA transfer function for a flow ratio $\beta = 0.2$ and an aerosol inlet gap of 1 mm as function of the mobility equivalent particle diameter d_{m}, adapted from Publication B

The total particle losses in the DMA are calculated from the difference of the integrated incoming and outgoing particle size distributions. For the triangular TF, it is the multiplication of the height by $FWHM$ and should correspond to the ratio of aerosol to sheath gas flow rate β, since particle losses in the DMA classification zone are usually small. Non-ideal transfer behavior occurring in the classification zone leads to a broadening (increase of $\mathcal{R}^{-1}$) and at the same time to a decrease of the height α. This can be seen by comparing Figure 4.2 a) and b). The height α increases with the particle size from 0.7 to 0.9 and the width decreases.

For particle sizes larger than 200 nm, the standard deviation is large due to weak signals, which is due to insufficient particle concentration. Considering the theory, the broadening of the TF is a result of a still not ideal flow field in the classification zone and increasing diffusion losses with decreasing particle size. In Publication B, we demonstrated that a further opening of the aerosol inlet gap to 2 mm improves the transfer characteristic for aerosol flow rates $> 5\,\mathrm{L/min}$. For the investigation of the structure formation, described in §5, the Long MF-DMA is operated with an aerosol to sheath gas ratio of 2.5/12.5, with an aerosol inlet gap of 1 mm, and in a voltage range from 65 to 3620 V leading to monodisperse aerosols with modal diameters in the size range 25 to 250 nm.

4.2 DETERMINING THE TEMPERATURE-TIME PROFILES OF THE MFR

A MFR was designed to provide a narrow $T(t)$ distribution for accurate determination of the sintering kinetics. This is achieved by using a vertical high-temperature tube furnace with an defined aerosol in- and outlet on the centerline. A preheated sheath gas covers and forces the aerosol on the centerline so that nearly straight particle trajectories from aerosol inlet to outlet arise. Particles not reaching the aerosol outlet are removed via an exhaust and are not considered in the evaluation. Aerosol in- and outlet probes are water-cooled and covered with thermal isolation to separate the sample-line from the reaction zone, where structure formation takes place.

The design and optimization of the MFR is accompanied by CFD simulations. For the validation of the CFD model, the temperature along the outer ceramic tube through the heated zone (boundary condition) and in the reaction zone in radial and axial direction was experimentally determined. The simulated temperature profile, assuming a radiation model and using material values from the literature, resulted in good agreement of the measured profiles for temperatures 773, 1023 and 1273 K (D.5 within Publication D). The radiation model is required to calculate the interaction of surfaces with thermal radiation, especially the outer and inner ceramic tube, as well as metal parts introduced for the validation (thermocouples, tension wire, and positioning cross) and results in higher surface temperatures. With the validated CFD simulation it was found that the mixing of the sheath gas with a cold aerosol leads to an unsteady flow field. The reason for this is the difference in viscosity between the still cold aerosol from the injections probe and the already preheated sheath gas flow. Adjusting the gas flow rates, the length and the position of the heating zone led to a more effective heating of the aerosol and to a laminar flow field (D.6 b) within Publication D). On the basis of

the validated CFD simulations, particle trajectories in the reaction zone were calculated and the particle temperature-time histories determined accurately. For the three different temperatures used in the experimental validation, 1000 polydisperse particles randomly distributed over the aerosol inlet have been tracked. Figure 4.3 a) depicts the mean values of the simulated particle temperature-time profiles. The profiles resulting from the simulation of the particle trajectories are indicated by black lines with the standard deviation with gray areas. It can be seen that the residence time shortens with increasing temperature because the gas mass flow rate in the MFR is set constant, Figure 4.3 b). An increase of the temperature results in an expansion of the gas volume and thus in a higher gas velocity.

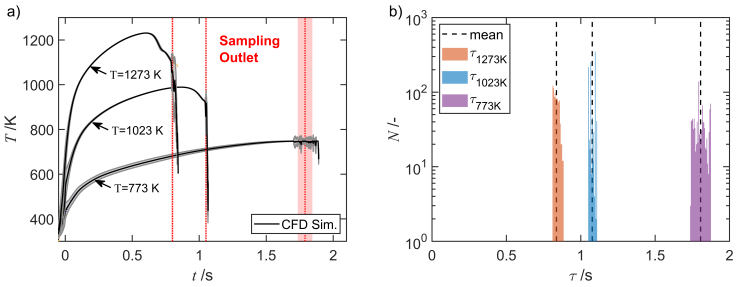

Figure 4.3: a) Mean temperature-time history $T(t)$ calculated from CFD simulation indicated as solid lines and b) residence time distribution of each 1000 particles with median residence time τ indicated as dash lines for the furnace temperatures of 773, 1023 and 1273 K. The standard deviation $T(t)$ in a) is shown as gray areas (Publication F)

The standard deviation becomes narrower at temperatures higher than 773 K. The reason for this is that the higher temperature leads to higher buoyancy, higher axial gas velocity and thus reduces the formation of a stagnation point or backflow areas near the aerosol inlet or endings of the heating zone.

4.3 APPLICATION OF THE MF-DMA AND MFR TO STUDY COATING BEHAVIOR

Coating experiments on monodisperse and spherical Fe_xO_y particles are carried out in the MFR with the precursor hexamethyldisiloxane (HMDSO) and tetraethoxysilane (TEOS). For this study, the modified experimental setup described in §3 was used. Monodisperse spherical iron oxides are provided by size selection with a DMA followed by densification in the sintering furnace. Oxygen is added to the sintering to ensure fully oxidized iron particles. By this, the measured change in particle size can be directly attributed to the coating of the particles. The liquid precursors are transferred into the gas phase and mixed with the Fe_xO_y particles at the tip of the injection probe of the MFR. The precursor was injected on the centerline, surrounded by the particles to get a good mixing. The coating experiments and the investigation of the thermal decomposition of the precursor were carried out at different precursor amount, for TEOS in the range of 1, 2, 4 and 6 ppm, at constant oxygen concentration by increasing the temperature of the MFR stepwise. An SMPS was used to measure the nucleation of the decomposed precursor, particle diameter > 3 nm, and the growth on the spherical Fe_xO_y particles by coating.

For TEOS, the residence time of the particles in the reactor is sufficient to detect layer thicknesses of about 1 nm for heterogeneous condensation without detectable nucleation, regarding the lower detection limit of the SMPS (Figure 4.4). Increasing the temperature above $T > 1073\,\mathrm{K}$ leads to the increased homogeneous nucleation of SiO_x-containing particles and growth of the added particles from 24 nm to approx. 27 nm for 1 to 2 ppm of the precursor TEOS. Higher temperatures in combination with higher precursor amounts (4 and 6 ppm) lead to the formation of particles in the size range of $> 5\,\mathrm{nm}$. In this case, the coating process is more dominated by coagulation, the collision between Fe_xO_y and SiO_x-containing particles, and leads to a significant increase of the Fe_xO_y particles up to 32 nm.

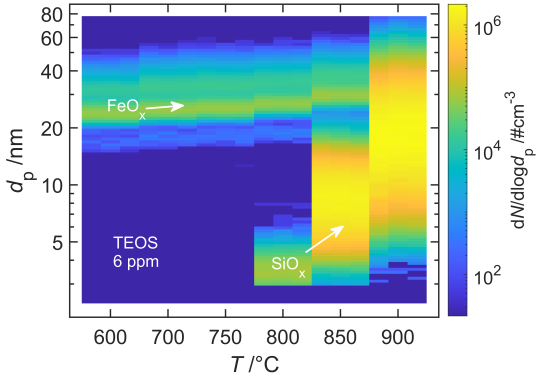

Figure 4.4: Particle growth by coating due to the thermal decomposition of TEOS as function of the temperature

A thermal decomposition of the precursor TEOS or HMDSO by pyrolysis, without adding oxygen, was not observed.

4.4 DETERMINING THE TRANSFER BEHAVIOR OF LOW-PRESSURE EJECTORS

The continuous sampling and transfer of aerosol particles from a low pressure to an atmospheric-pressure region is required to apply standard online instrumentation to low-pressure aerosol reactors. This enables the application of the found kinetic data and its verification by means of online measurement technology on low-pressure systems. The determination of the transfer behavior is necessary for accurate measurements. The characterization of the low-pressure ejectors is done in two ways, I) without particles to determine the gas dilution factor (GDF) and II) with particles to determine particle losses resulting in a particle dilution factor (PDF). Figure 4.5 shows a schematic illustration of a single-stage ejector consisting of an inlet nozzle, a diffuser and a suction tube. Flow and pressure meters are attached to the inlets and outlets of the ejector to measure the process parameters. The compressed gas is applied to the inlet nozzle to form the highly accelerated driving gas. Its mass flow rate Q_{in} and pressure p_{in} are measured with a mass flow controller (MFC) and a pressure gauge. The minimum pressure in the suction tube p_{vac} is determined as a function of the sucked-in mass flow rate Q_{vac}. For sampling, p_{vac} must be lower than the process pressure from which the sample is to be taken.

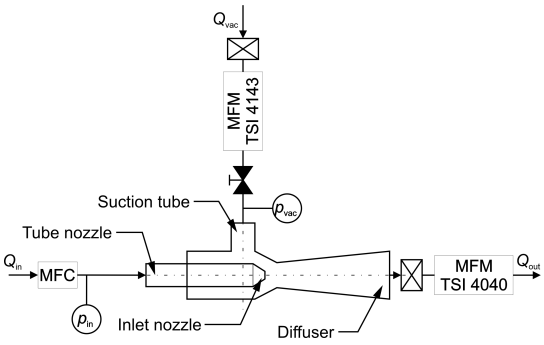

Figure 4.5: Setup for investigating a low-pressure ejector as described in Publication A

In Publication A and C, two different multi-stage ejectors are characterized to sample aerosol particles from low-pressure aerosol reactors.

For determining the ejector PDF, a monodisperse aerosol of spherical silver particles in the size range from 15 to 80 nm was generated as a test aerosol (Figure 4.6). Silver granulates filled in a ceramic boat are

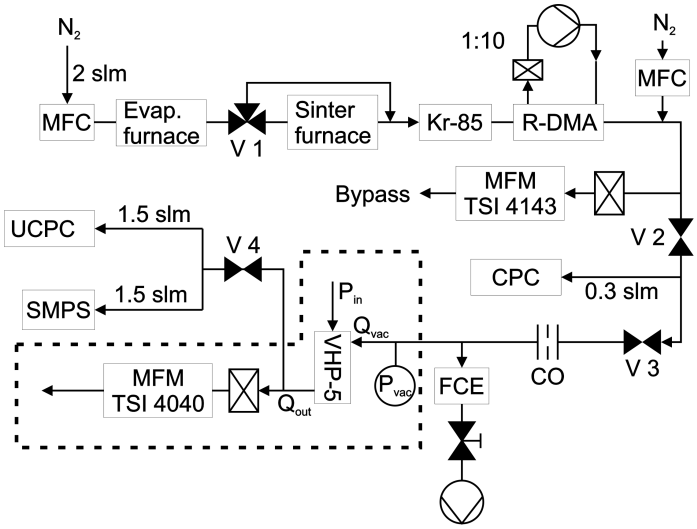

Figure 4.6: Experimental setup for measuring the particle dilution factor (PDF) of the VHP-5 ejector, the part within the dashed lines are used to determine the gas dilution factor (GDF) (Publication C)

transferred to the gas phase in a tube furnace at atmospheric pressure by an evaporation and condensation process. Downstream, a second tube furnace is used for the sintering of the silver agglomerates into spherical particles. Size selected particles via DMA are transferred to a low-pressure region via a critical nozzle before the particles are sucked-in by the ejector and brought back to atmospheric pressure. Measurement of the particle size distribution with online instrumentation (SMPS) are performed upstream and downstream the low-pressure region. The particle number concentration in the low pressure is measured via a Faraday cup with electrometer (FCE) and allows to distinguish and calculate particle losses at the critical nozzle and in the low-pressure ejector. In this way, changes to the particle size distribution can be attributed to the critical nozzle or the low-pressure ejector. It has been shown that the modal value of the classified particle size distribution does not change due to the transfer into and out of the low-pressure region by the ejector. However, particle losses occur as a function of particle size d_p and pressure p_vac (Publication A and C).

5 DETERMINING THE SINTERING KINETICS

Different mechanisms such as chemical reactions, surface growth, coagulation, condensation and sintering occur during the formation of nanoparticles, their structures and properties (Pratsinis, 1988). These mechanisms can occur very rapidly and simultaneously, making it difficult to describe the individual mechanisms. Besides coagulation, sintering is one of the most important mechanisms determining particle morphology (German, 1996). Sintering models depend on certain characteristic parameters which have to be determined from accurate experimental data for the validation of the models.

The sintering model by Koch and Friedlander (1991) for the coalescence of two identical particles is used to determine the sintering kinetics. They assume that the change of the surface area as function of the time $\mathrm{d}a/\mathrm{d}t$ of a single agglomerate is proportional to the deviation from the surface area of the fully coalesced particle a_{sph}, as shown in Equation (5.9). The driving force for the coalescence is the minimization of the surface energy resulting in a material transport to the sintering neck.

$$\frac{\mathrm{d}a}{\mathrm{d}t} = -\frac{1}{\tau_s} \cdot \left(a - a_{\mathrm{sph}}\right) \tag{5.9}$$

The characteristic sintering time τ_s is proportional to the change of the particle surface area (Friedlander and Wu, 1994). The sintering time can be calculated by an Arrhenius expression as function of the characteristic sintering parameters, activation energy E_{a} and pre-exponential factor A_{s} (Eq. 5.10). The sintering time is exponentially dependent on the sintering temperature T as well as on the primary particle diameter d_{prim} to the power of x.

$$\tau_s = A_{\mathrm{s}} \cdot d_{\mathrm{prim}}^{x} \cdot \exp\left(\frac{E_{\mathrm{a}}}{k_B T}\right) \tag{5.10}$$

The pre-exponential factor A_{s} includes the physical quantities, such as surface tension γ_{s}, diffusion coefficient D_{x} of the sintering mechanism, molar volume v_{mol}, grain boundary width w, of the structure to be sintered (Kruis, Kusters, et al., 1993).

During sintering, various mass transport mechanisms can occur, which can generally be divided into surface transport (surface diffusion and

vaporization/condensation) or mass transport (grain boundary diffusion, plastic flow, viscous flow and volume diffusion). In the coalescence of two spherical particles, surface transport contributes to the formation of the sintering neck or particle bonding, and mass transport processes contribute to the densification through the fusion of the two mass points (Fig. 5.1).

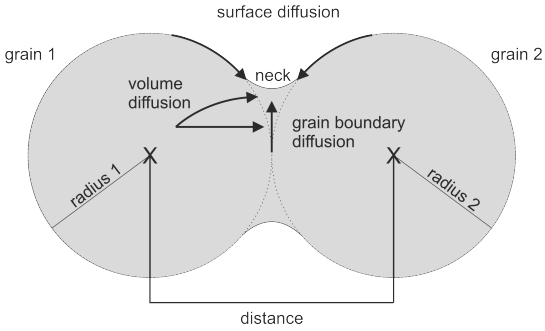

Figure 5.1: Illustration of the coalescence of two spherical particles

Early-stage sintering initiates bonding by surface transport, but as surface area is converted into grain boundary area the opportunity for densification increases. Smaller particles, longer sintering times, and higher sintering temperatures increase sintering densification. The dominant transport mechanism of the sintering process determines the exponent x of the primary particle size. As different transport mechanisms can occur during sintering, even simultaneously, the exponent x alone cannot identify the transport mechanism. It is introduced as a parameter showing the sensitivity of the sintering on the primary particle size. Since the activation energy and the pre-exponential factor might not be independent from each other and will depend on the sintering mechanism, a global minimum from the combination of all three parameters must be found in order to determine the sintering kinetics. The mathematical problem can be simplified by assuming a dominant sintering mechanism/exponent and calculating the kinetic parameters by error minimization between experiment and assumed sintering model. The numerical solution in MATLAB (2020a, MathWorks, Natick, MA, USA) introduced in Publication F is used to solve the sintering kinetics. It is based on the Nelder-Mead simplex algorithm for solving strictly convex functions with two dimensions (Lagarias et al., 1998). Equation (5.9) is solved by integration with a variable step size and variable order (VSVO) solver, based on the numerical differentiation formulas (NDFs), and leads

to the surface according to the temperature-time history and combination of E_a and A_s. The quality of the fit, as expressed by the ΣSQR, is evaluated by comparing the measured primary particle size $d_{prim,exp}$ and the calculated particle size $d_{prim,calc}$ considering the temperature-time histories for a given combination of E_a and A_s, Equation (5.11).

$$\Sigma SQR = \frac{\sum [d_{prim,exp} - d_{prim,calc}]^2}{d_{prim,exp}^2} \tag{5.11}$$

5.1 DETERMINING CHANGES OF THE PARTICLE STRUCTURE

The characterization of nanoparticles, their size, structure, or composition is difficult due to their small size and their different behavior compared to macro-sized objects. Smaller nanoparticles are less dominated by inertia under typical atmospheric conditions and undergo a random motion due to collision with gas molecules, called Brownian motion. Additionally, solid aerosol particles are usually irregularly shaped, making the description of their morphology complex. Equivalent diameters defined by different particle properties, such as mass, volume or surface area, are necessary for the description of particles with complex shapes and structures. The differences between the equivalent diameters allow the calculation of additional particle properties, like primary particle size, shape or density (Eggersdorfer, Kadau, et al., 2012). The use of equivalent diameters and other correction factors allows these theories to be applied to non-spherical particles. For example, the fractal dimension factor is a correction term used in Stokes' law that allows its application to non-spherical particles.

Only the knowledge of different equivalent diameters makes it possible to describe the particle structure based on structure models. A first indication of an non-spherical particle structure can be given metrologically by the effective density of the particles ρ_{eff}, the quotient of the particle mass m_p to the volume v_p. For spherical particles, the effective density is equal to the density of the solid. Agglomerate structures are usually open-pored structures with large voids, so that the effective density is much smaller than the bulk density.

5.1.1 *Measurement of the structure formation*

Before structure formation takes place in the MFR, the synthesized agglomerates are size-selected by their electrical mobility in a MF-DMA. The designed MF-DMA provides, compared to conventional DMAs, a

long-term stable monodisperse size distribution over the entire nanometer range in a larger aerosol flow rate. This allows the parallel measurement with different online instrumentation downstream of the DMA, which requires a specific sample flow rate and a certain particle number concentration. Measurements downstream and upstream of the MFR allow to attribute any changes in particle structure directly to the reaction zone, as shown in Figure 3.1. The modal diameter of the monodisperse particle size distribution is obtained by SMPS measurements. It is based on the analysis of the electrical particle mobility by using a neutralizer, DMA and particle counter in series. A defined charge state of the particles is provided by the neutralizer, assuming spherical structure. The particle size distribution is determined by changing the voltage applied to the DMA and counting the particle number concentration of the classified fraction. The particle mass is measured by the CPMA according to the equilibrium of the Coulomb force and the centrifugal force (§2.1.2). A rapidly rotating cylindrical capacitor forces particles on a specific trajectory according to their mass-to-charge ratio and allows the calculation of the particle mass. Adjusting the mobility-equivalent particle size distribution with aerodynamic particle size distributions from DAPS measurements also allows the calculation of the effective particle density and is thus an alternative method to determine the particle mass.

The particle structure model for agglomerates introduced by Eggersdorfer, Kadau, et al. (2012) is used to calculate advanced particle properties, like the primary particle diameter d_{prim}, the number of primary particles per agglomerate N_{agglo}, the effective density ρ_{eff} (ratio of agglomerate mass to its volume) and the fractal dimension D_α (self-similarity of the agglomerate structure) from the mobility diameter and particle mass. The Equation (5.12) is adapted in Publication A to express the primary particle diameter as function of the effective density $\rho_{\mathrm{eff}} = 6m_{\mathrm{p}} / \left(\pi d_{\mathrm{m}}^3\right)$.

$$d_{\mathrm{prim}} = d_{\mathrm{p}} \left(k_\alpha \cdot \frac{\rho_{\mathrm{bulk}}}{\rho_{\mathrm{eff}}} \right)^{\frac{1}{2D_\alpha - 3}} \tag{5.12}$$

The agglomerate structure descriptive parameters $k_\alpha = 0.99$ and $D_\alpha = 1.082$ are independent of the sintering mechanism and result from molecular dynamics (MD) simulations (Eggersdorfer and Pratsinis, 2013). The primary particle diameter d_{prim} is expressed as the volume to surface equivalent diameter and is comparable to the Brunauer, Emmett and Teller (BET) diameter. The bulk density is taken from literature for iron ($\mathrm{Fe} = 7.874\,\mathrm{g/cm^3}$) and iron oxide ($\mathrm{Fe_3O_4} = 5.2\,\mathrm{g/cm^3}$) after determining the main chemical phase of the particles with different offline

methods, X-ray absorption fine structure (XAFS) and electron energy loss spectroscopy (EELS) (Publication F).

5.2 DETERMINATION OF THE SINTERING PARAMETERS

In the experiment, size-selected agglomerates via DMA (20 different diameters, logarithmic distribution over the size range 25 to 250 nm) are measured with different online instrumentation down- and upstream of the MFR. The primary particle size and number per agglomerate are calculated from SMPS and CPMA measurements. These parameters can also be calculated with the combination of DAPS and SMPS, but lead to a lower accuracy due to the detection limit of the DAPS, smaller primary particles at low temperatures and low number concentration at high temperatures (Figure F.6, within Publication F). The growth of d_{prim} (circles) and the reduction of N_{agglo} (crosses) of different agglomerate sizes and as a function of the furnace temperature in N_2 atmosphere is depicted in Figure 5.2. The solid line represents the calculated values from the used sintering model with the found combination of E_{a} and A_{s}. The particle mass remains constant during sintering for the respective size-selected agglomerate so that coagulation, evaporation or condensation can be excluded. In addition, the particle synthesis in N_2 and $N_2 + 5\%H_2$ has no significant influence on the initial primary particle diameter (approx. 4 nm), nor does the mean primary particle size of the size-selected agglomerates differ. Large changes, increase of d_{prim} and decrease of N_{agglo} are observed at approx. 900 K leading to a more compact structure (Schmidt-Ott, 1988). In $N_2 + 5\%H_2$ atmosphere the sintering is slightly shifted to lower temperatures, the slope is much steeper and no further changes of N_{agglo} are observed for $T > 1100$ K (Figure F.7 b, within Publication F).

For the determination of sintering kinetics, 14 representative measurements, with three different initial agglomerate sizes, at 4 temperatures (298, 773, 1023 and 1273 K) were used from the experimental data. These measurements have sufficient signal and can be used to accurately determine the kinetics. Figure 5.3 shows the result of the numerical solution as sum of squares error (ΣSQR) as function of the activation energy and the sintering rate in N_2, assuming plastic and viscous flow as dominant transport mechanism $x = 1$. It can be seen that combinations of E_{a} and A_{s} lead to a valley of minima, which makes it necessary to specify a wide range of values in order to find a global minimum. Larger values of x show larger errors.

A global minimum with $\Sigma SQR = 0.52$ is found for an activation energy of 55.22 kJ/mol and a pre-factor of $2.54 \cdot 10^4$ s/m.

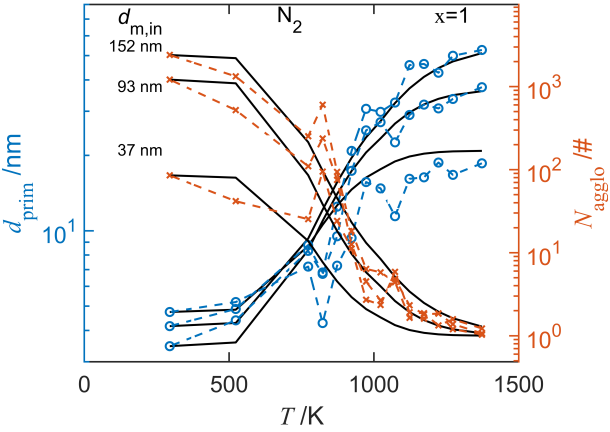

Figure 5.2: Primary particle diameter d_{prim} and number of primary particles per agglomerate N_{agglo} as function of the temperature T. The densification of three different agglomerate sizes before sintering $d_{\mathrm{m},in}$ are shown, adapted from Publication F.

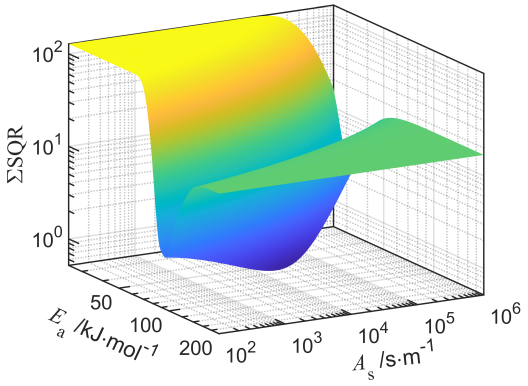

Figure 5.3: ΣSQR as function of the characteristic sintering parameters, activation energy E_{a} and sintering prefactor A_{s} (Publication F).

5.3 CHARACTERIZING THE LOW-PRESSURE EJECTORS

The characterization of the transfer performance of the commercial ejector is needed to determine in which way the sample is changed while transferred from low pressure to atmospheric pressure. Knowledge of the correction function, which takes the transfer behavior of the ejectors into account, allows precise measurements. The commercial availability of the low-pressure ejectors, together with the published correction functions (Publication A and C) allows an immediate external use of the sampling method at low-pressure processes. Figure 5.4 depicts the Q_{vac} and GDF as function of p_{vac} of the two commercial ejectors VIP-4 and VHP-5. The sample flow rate, being inversely proportional to the GDF decreases with pressure p_{vac}. The pressure p_{vac} defines the minimum pressure from which a sample can be taken. Lower pressure can be reached with the VHP-5 ejector compared to the VIP-4 ejector due to the different arrangement and dimensions of the Venturi nozzles. The GDF is a value for the dilution of the sample and reaches values from approx. 100 to 30,000. A sufficiently high particle concentration is therefore needed when working at lower pressures, which is usually the case in aerosol reactors.

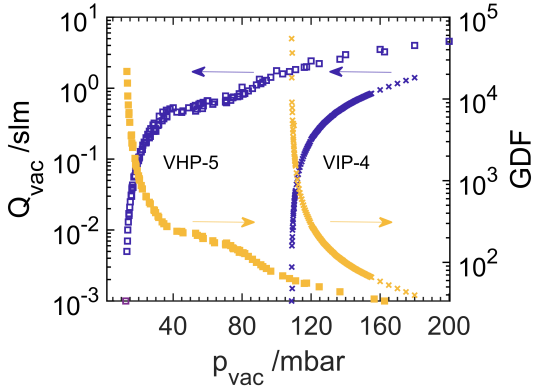

Figure 5.4: Q_{vac} and GDF as function of p_{vac} of VIP-4 and VHP-5 ejector (Publication C)

Figure 5.5 depicts the particle dilution factor of the commercial low-pressure ejector VHP5 (Landefeld, Kassel, Germany).

This commercial multi-stage ejector reaches a minimum pressure of 12.5 mbar and was successfully tested in the pressure range from 20 to 180 mbar. It can be seen that the PDF is higher for lower process pressure due to its dependence on the sample rate. The increase of PDF

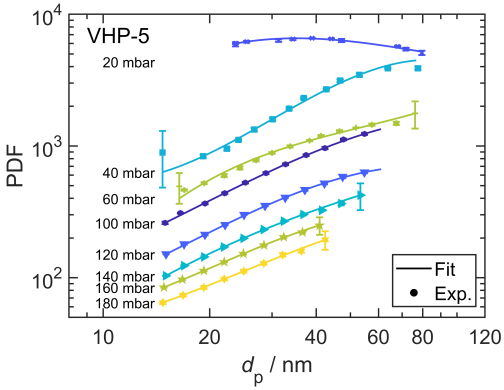

Figure 5.5: Particle dilution factor *PDF* of the VHP-5 ejector as function of the particle size for spherical particles (Publication C)

with increasing particle size is effected due to higher particles losses by impaction. At low process pressure (e.g 20 mbar) the sampling is still possible, but a *PDF* of approx. 7000 has to be taken into account. This requires a higher particle concentration at the entrance of the ejector to reach a sufficiently high signal in the measurement techniques. For standard online measurement techniques a particle concentration of 10^4 #/cm^3 is recommended. The high dilution of the aerosol is an advantage for sampling from aerosol reactors for production process, because the rapid quenching avoids changes of the particle size distribution in the sample line by e.g. coagulation, diffusion, thermophoresis. The use of the low-pressure ejector at aerosol reactors is simple and requires only a pressure of 4.5 bar at the high pressure inlet (Publication C). It operates nearly maintenance-free and can be variable applied to different types of reactors due to its compact design with standard vacuum component plugs. The low-pressure ejectors have been successfully used with a combination of different online instrumentations at a low-pressure microwave plasma reactors and a flame reactor for the synthesis of nanoparticles (Publication A and E).

6

SUMMARY

This thesis focuses on the precise determination of kinetic parameters for the characterization of structure formation mechanisms of complex nanoparticles, in particular the sintering of iron and iron oxides. Therefore, a medium-flow differential mobility analyzer (MF-DMA) was designed, tested and optimized to provide a long-term stable monodisperse aerosol with a defined initial particle structure. Well-defined conditions, a narrow temperature-residence time distribution, are provided by the model flow reactor (MFR) and allow the precise investigation of structure formation mechanisms. The development of the MFR was supported by computational fluid dynamics (CFD) simulation, based on a temperature validated two-dimensional model, and the flow field was characterized and optimized. It was demonstrated that the MFR is suitable for the precise determination of sintering kinetics in the temperature range from 773 to 1373 K within residence times of seconds. The kinetic data in terms of an activation energy and exponential pre-factor were obtained by error minimization of the primary particle diameters from numerical calculation and measurements. The primary particle diameter was calculated from online measurements of the particle mass and particle diameter, assuming a structure model. The application of this specific measurement procedure with used online instrumentation at low-pressure aerosol reactors is not directly possible. Therefore, the particle dilution factor of two commercial low-pressure ejectors was determined in order to investigate the particle structure formation at low-pressure aerosol reactors. The aerosol particles are transferred from low-pressure regions to atmospheric pressure and get directly quenched. This provides a lower number concentration of particles at atmospheric pressure and offers ideal conditions for online measurement instrumentation even at high-production rates. The application of the commercial low-pressure ejectors was tested with a combination of online instrumentations at a low-pressure microwave reactor and a flame reactor.

7 OUTLOOK

This work provides accurate kinetic data for the calculation of the structure formation of aerosol nanostructures, a clear validation of the found sintering mechanisms was not performed. A detailed knowledge of the sintering mechanisms is not essential for the calculation and simulation of structure formation, but will allow a deeper understanding of nanoparticle structure formation. This would require measurements of particle mass and particle size with changes in residence time at constant temperature. The higher ΣSQR of simulations in reducing gas atmosphere can be improved by considering temperature residence time profiles around about 900 K where phase transformation occurs, and by including a model to describe the phase transformation. An even more interesting investigation would be to compare the here found kinetic data with kinetic data from a model flow reactor with a broad temperature-residence time distribution. This may provide information on the extent to which accurate kinetic data are required. First coating experiments were performed and it could be shown that both the decomposition of hexamethyldisiloxane (HMDSO) and tetraethoxysilane (TEOS) can be investigated and the coating on nanoparticles can be detected. However, the study and determination of the coating kinetics has not been carried out.

REFERENCES

Babick, F. et al. (2018). "Multiparameter Characterization of Aerosols." In: *Chemie Ingenieur Technik* 90.7, pp. 923–936. ISSN: 0009286X. DOI: 10.1002/cite.201700094.

Batlle, X., Pérez, N., Guardia, P., Iglesias, O., Labarta, A., Bartolomé, F., García, L. M., Bartolomé, J., Roca, A. G., Morales, M. P., and Serna, C. J. (2011). "Magnetic nanoparticles with bulklike properties (invited)." In: *Journal of Applied Physics* 109.7, 07B524. ISSN: 0021-8979. DOI: 10.1063/1.3559504.

Birmili, W., Stratmann, F., Wiedensohler, A., Covert, D., Russell, L. M., and Berg, O. (1997). "Determination of Differential Mobility Analyzer Transfer Functions Using Identical Instruments in Series." In: *Aerosol Science and Technology* 27.2, pp. 215–223. ISSN: 0278-6826. DOI: 10.1080/02786829708965468.

Chertok, B., Moffat, B. A., David, A. E., Yu, F., Bergemann, C., Ross, B. D., and Yang, V. C. (2008). "Iron oxide nanoparticles as a drug delivery vehicle for MRI monitored magnetic targeting of brain tumors." In: *Biomaterials* 29.4, pp. 487–496. ISSN: 0142-9612. DOI: 10.1016/j.biomaterials.2007.08.050.

Cunningham, E. and Larmor, J. (1910). "On the velocity of steady fall of spherical particles through fluid medium." In: *Proceedings of the Royal Society of London. Series A, Containing Papers of a Mathematical and Physical Character* 83.563, pp. 357–365. ISSN: 0950-1207. DOI: 10.1098/rspa.1910.0024.

Eggersdorfer, M. L., Kadau, D., Herrmann, H. J., and Pratsinis, S. E. (2012). "Aggregate morphology evolution by sintering: Number and diameter of primary particles." In: *Journal of Aerosol Science* 46, pp. 7–19. ISSN: 00218502. DOI: 10.1016/j.jaerosci.2011.11.005.

Eggersdorfer, M. L. and Pratsinis, S. E. (2013). "Restructuring of aggregates and their primary particle size distribution during sintering." In: *AIChE Journal* 59.4, pp. 1118–1126. ISSN: 0001-1541. DOI: 10.1002/aic.14043.

Flagan, R. C. (1999). "On Differential Mobility Analyzer Resolution." In: *Aerosol Science and Technology* 30.6, pp. 556–570. ISSN: 0278-6826. DOI: 10.1080/027868299304417.

Flynn, J. H. and Dunlap, L. A. (1986). "Temperature gradients in horizontal tube furnaces." In: *Thermochimica Acta* 105, pp. 215–218. ISSN: 00406031. DOI: 10.1016/0040-6031(86)85238-8.

Frey, N. A., Peng, S., Cheng, K., and Sun, S. (2009). "Magnetic nanoparticles: Synthesis, functionalization, and applications in bioimaging and magnetic energy storage." In: *Chemical Society Reviews* 38.9, pp. 2532–2542.

Friedlander, S. K. (2000). *Smoke, dust, and haze: Fundamentals of aerosol dynamics*. 2. ed. Topics in chemical engineering. New York: Oxford Univ. Press. ISBN: 0195129997.

Friedlander, S. K. and Wu, M. K. (1994). "Linear rate law for the decay of the excess surface area of a coalescing solid particle." In: *Physical review. B, Condensed matter* 49.5, pp. 3622–3624. ISSN: 0163-1829. DOI: 10.1103/PhysRevB.49.3622.

Gazeau, F., Bacri, J. C., Gendron, F., Perzynski, R., Raikher, Y. L., Stepanov, V. I., and Dubois, E. (1998). "Magnetic resonance of ferrite nanoparticles: Evidence of surface effects." In: *Journal of Magnetism and Magnetic Materials* 186.1-2, pp. 175–187.

German, R. M. (1996). *Sintering theory and practice*. A Wiley-Interscience publication. New York [u.a.]: Wiley. ISBN: 047105786X.

Granqvist, C. G. and Buhrman, R. A. (1976). "Ultrafine metal particles." In: *Journal of Applied Physics* 47.5, pp. 2200–2219. ISSN: 0021-8979. DOI: 10.1063/1.322870.

Gullett, B. K., Blom, J. A., and Gillis, G. R. (1988). "Design and characterization of a 1200 °C entrained flow, gas/solid reactor." In: *Review of Scientific Instruments* 59.9, pp. 1980–1984. ISSN: 0001-1452. DOI: 10.1063/1.1140062.

Gupta, A. K. and Gupta, M. (2005). "Synthesis and surface engineering of iron oxide nanoparticles for biomedical applications." In: *Biomaterials* 26.18, pp. 3995–4021.

Heurlin, M., Magnusson, M. H., Lindgren, D., Ek, M., Wallenberg, L. R., Deppert, K., and Samuelson, L. (2012). "Continuous gas-phase synthesis of nanowires with tunable properties." In: *Nature* 492.7427, pp. 90–94. DOI: 10.1038/nature11652.

Hinds, W. C. (1999). *Aerosol technology: Properties, behavior, and measurement of airborne particles*. 2. ed. A Wiley-Interscience publication. New York: Wiley. ISBN: 9780471194101.

Hontañón, E. and Kruis, F. E. (2009). "A Differential Mobility Analyzer (DMA) for Size Selection of Nanoparticles at High Flow Rates." In: *Aerosol Science and Technology* 43.1, pp. 25–37. ISSN: 0278-6826. DOI: 10.1080/02786820802446812.

Hülser, T., Schnurre, S. M., Wiggers, H., and Schulz, C. (2011). "Gas-phase synthesis of nanoscale silicon as an economical route towards sustainable energy technology." In: *KONA Powder and Particle Journal* 29, pp. 191–207.

Hummes, D., Neumann, S., Fissan, H., and Stratmann, F. (1996). "Experimental Determination of the Transfer Function of a Differential Mobility Analyzer (DMA) in the nanometer size range." In: *Particle & Particle Systems Characterization* 13.5, pp. 327–332. ISSN: 09340866. DOI: 10.1002/ppsc.19960130513.

Ifeacho, P., Hülser, T., Wiggers, H., Schulz, C., and Roth, P. (2007). "Synthesis of SnO_{2-x} nanoparticles tuned between $0 \leqslant x \leqslant 1$ in a premixed low pressure $H_2/O_2/Ar$ flame." In: *Proceedings of the Combustion Institute* 31.2, pp. 1805–1812. ISSN: 15407489. DOI: 10.1016/j.proci.2006.07.083.

Kim, J. H., Mulholland, G. W., Kukuck, S. R., and Pui, D. Y. H. (2005). "Slip Correction Measurements of Certified PSL Nanoparticles Using a Nanometer Differential Mobility Analyzer (Nano-DMA) for Knudsen Number From 0.5 to 83." In: *Journal of Research of the National Institute of Standards and Technology* 110.1, pp. 31–54. ISSN: 1044-677X. DOI: 10.6028/jres.110.005.

Kim, M., Osone, S., Kim, T., Higashi, H., and Seto, T. (2017). "Synthesis of Nanoparticles by Laser Ablation: A Review." In: *KONA Powder and Particle Journal* 34.0, pp. 80–90. ISSN: 0288-4534. DOI: 10.14356/kona.2017009.

Kirchhof, M. J., Schmid, H.-J., and Peukert, W. (2004). "Reactor system for the study of high-temperature short-time sintering of nanoparticles." In: *Review of Scientific Instruments* 75.11, pp. 4833–4840. ISSN: 0001-1452. DOI: 10.1063/1.1809258.

Koch, W. and Friedlander, S. K. (1990). "The effect of particle coalescence on the surface area of a coagulating aerosol." In: *Journal of Colloid and Interface Science* 140.2, pp. 419–427. ISSN: 0021-9797. DOI: 10.1016/0021-9797(90)90362-R.

Koch, W. and Friedlander, S. K. (1991). "Particle Growth by Coalescence and Agglomeration." In: *Particle & Particle Systems Characterization* 8.1-4, pp. 86–89. ISSN: 09340866. DOI: 10.1002/ppsc.19910080115.

Kotalczyk, G., Skenderović, I., and Kruis, F. E. (2019). "Monte Carlo simulations of homogeneous nucleation and particle growth in the presence of background particles." In: *Tellus B: Chemical and Physical Meteorology* 71.1, p. 1554415. DOI: 10.1080/16000889.2018.1554415.

Kruis, F. E., Fissan, H., and Peled, A. (1998). "Synthesis of nanoparticles in the gas phase for electronic, optical and magnetic applications—a review." In: *Journal of Aerosol Science* 29.5, pp. 511–535. ISSN: 00218502. DOI: 10.1016/S0021-8502(97)10032-5.

Kruis, F. E., Kusters, K. A., Pratsinis, S. E., and Scarlett, B. (1993). "A Simple Model for the Evolution of the Characteristics of Aggregate Particles

Undergoing Coagulation and Sintering." In: *Aerosol Science and Technology* 19.4, pp. 514–526. ISSN: 0278-6826. DOI: 10.1080/02786829308959656.

Kulkarni, P., Baron, P. A., and Willeke, K., eds. (2011). *Aerosol measurement: Principles, techniques, and applications*. 3. ed. Hoboken, NJ: Wiley. ISBN: 978-0-470-38741-2.

Kunze, F., Kuns, S., Spree, M., Hülser, T., Schulz, C., Wiggers, H., and Schnurre, S. M. (2019). "Synthesis of silicon nanoparticles in a pilot-plant-scale microwave plasma reactor: Impact of flow rates and precursor concentration on the nanoparticle size and aggregation." In: *Powder Technology* 342, pp. 880–886. ISSN: 0032-5910. DOI: 10.1016/j.powtec.2018.10.042.

Lagarias, J. C., Reeds, J. A., Wright, M. H., and Wright, P. E. (1998). "Convergence Properties of the Nelder–Mead Simplex Method in Low Dimensions." In: *SIAM Journal on Optimization* 9.1, pp. 112–147. ISSN: 1052-6234. DOI: 10.1137/S1052623496303470.

Liu, C., Liu, R., Sun, Q., Chang, J., Gao, X., Liu, Y., Lee, S., Kang, Z., and Wang, S. (2015). "Controlled synthesis and synergistic effects of graphene-supported PdAu bimetallic nanoparticles with tunable catalytic properties." In: *Nanoscale* 7 (14), pp. 6356–6362. DOI: 10.1039/C4NR06855F.

Lu, A., Salabas, E. L., and Schüth, F. (2007). "Magnetic nanoparticles: Synthesis, protection, functionalization, and application." In: *Angewandte Chemie - International Edition* 46.8, pp. 1222–1244.

Marcu, A., Pop, S., Dumitrache, F., Mocanu, M., Niculite, C. M., Gherghiceanu, M., Lungu, C. P., Fleaca, C., Ianchis, R., Barbut, A., Grigoriu, C., and Morjan, I. (2013). "Magnetic iron oxide nanoparticles as drug delivery system in breast cancer." In: *Applied Surface Science* 281, pp. 60–65. ISSN: 01694332. DOI: 10.1016/j.apsusc.2013.02.072.

Miller, D. R., Akbar, S. A., and Morris, P. A. (2014). "Nanoscale metal oxide-based heterojunctions for gas sensing: A review." In: *Sensors and Actuators, B: Chemical* 204, pp. 250–272.

Münzer, A., Sellmann, J., Fortugno, P., Kempf, A., Schulz, C., and Wiggers, H. (2017). "Inline coating of silicon nanoparticles in a plasma reactor: Reactor design, simulation and experiment." In: *Materials Today: Proceedings* 4, S118–S127. ISSN: 2214-7853. DOI: 10.1016/j.matpr.2017.09.176.

Nanda, K. K. and Kruis, F. E. (2014). "A radial differential mobility analyzer for the size-classification of gas-phase synthesized nanoparticles at low pressures." In: *Measurement Science and Technology* 25.7, p. 075605. ISSN: 1361-6501. DOI: 10.1088/0957-0233/25/7/075605.

Olfert, J. S. and Collings, N. (2005). "New method for particle mass classification—the Couette centrifugal particle mass analyzer." In:

Journal of Aerosol Science 36.11, pp. 1338–1352. ISSN: 00218502. DOI: 10.1016/j.jaerosci.2005.03.006.

Park, K. Y. (2017). "The drug delivery field at the inflection point: Time to fight its way out of the egg." In: *Journal of controlled release: official journal of the Controlled Release Society* 267, pp. 2–14. DOI: 10.1016/j.jconrel.2017.07.030.

Park, K. Y., Ullmann, M., Suh, Y. J., and Friedlander, S. K. (2001). "Nanoparticle microreactor: Application to synthesis of titania by thermal decomposition of titanium tetraisopropoxide." In: *Journal of Nanoparticle Research* 3.4, pp. 309–319. ISSN: 1388-0764. DOI: 10.1023/A:1017906916427.

Pfeiffer, T. V., Feng, J., and Schmidt-Ott, A. (2014). "New developments in spark production of nanoparticles." In: *Advanced Powder Technology* 25.1, pp. 56–70. ISSN: 09218831. DOI: 10.1016/j.apt.2013.12.005.

Post, P. and Weber, A. P. (2019). "Coating of gasborne nanoparticles with silica and silica-organic shells in a post-plasma CVD process." PhD thesis. Universitätsbibliothek Der TU Clausthal. DOI: 10.21268/20190312-5.

Pratsinis, S. E. (1988). "Simultaneous nucleation, condensation, and coagulation in aerosol reactors." In: *Journal of Colloid and Interface Science* 124.2, pp. 416–427. ISSN: 0021-9797. DOI: 10.1016/0021-9797(88)90180-4.

Ryans, J. L. and Roper, D. L. (1986). *Process vacuum system design and operation*. New York: McGraw-Hill. ISBN: 0070543550.

Schmidt-Ott, A. (1988). "New approaches to in situ characterization of ultrafine agglomerates." In: *Journal of Aerosol Science* 19.5, pp. 553–563. ISSN: 00218502. DOI: 10.1016/0021-8502(88)90207-8.

Schneider, F., Suleiman, S., Menser, J., Borukhovich, E., Wlokas, I., Kempf, A., Wiggers, H., and Schulz, C. (2019). "SpraySyn-A standardized burner configuration for nanoparticle synthesis in spray flames." In: *Review of Scientific Instruments* 90.8, p. 085108. ISSN: 0001-1452. DOI: 10.1063/1.5090232.

Seto, T., Hirota, A., Fujimoto, T., Shimada, M., and Okuyama, K. (1997). "Sintering of Polydisperse Nanometer-Sized Agglomerates." In: *Aerosol Science and Technology* 27.3, pp. 422–438. ISSN: 0278-6826. DOI: 10.1080/02786829708965482.

Shrivastava, M., Gidwani, A., and Jung, H. S. (2009). "Modeling Oxidation of Soot Particles Within a Laminar Aerosol Flow Reactor Using Computational Fluid Dynamics." In: *Aerosol Science and Technology* 43.12, pp. 1218–1229. ISSN: 0278-6826. DOI: 10.1080/02786820903321716.

Stein, M. and Kruis, F. E. (2016). "Optimization of a transferred arc reactor for metal nanoparticle synthesis." In: *Journal of Nanoparticle Research* 18.9, p. 258. ISSN: 1388-0764. DOI: 10.1007/s11051-016-3559-y.

Stolzenburg, M. R. (1988). "An Ultrafine Aerosol Size Distribution Measuring System." Ph.D. Thesis. Minneapolis, MN, USA: University of Minnesota.

Stolzenburg, M. R. and McMurry, P. H. (2008). "Equations Governing Single and Tandem DMA Configurations and a New Lognormal Approximation to the Transfer Function." In: *Aerosol Science and Technology* 42.6, pp. 421–432. ISSN: 0278-6826. DOI: 10.1080/02786820802157823.

Stratmann, F., Kauffeldt, T., Hummes, D., and Fissan, H. (1997). "Differential Electrical Mobility Analysis: A Theoretical Study." In: *Aerosol Science and Technology* 26.4, pp. 368–383. ISSN: 0278-6826. DOI: 10.1080/02786829708965437.

Tabrizi, N. S., Ullmann, M., Vons, V. A., Lafont, U., and Schmidt-Ott, A. (2009). "Generation of nanoparticles by spark discharge." In: *Journal of Nanoparticle Research* 11.2, pp. 315–332. ISSN: 1388-0764. DOI: 10.1007/s11051-008-9407-y.

Tong, S., Quinto, C. A., Zhang, L., Mohindra, P., and Bao, G. (2017). "Size-Dependent Heating of Magnetic Iron Oxide Nanoparticles." In: *ACS nano* 11.7, pp. 6808–6816. DOI: 10.1021/acsnano.7b01762.

Wang, X., Hafiz, J., Mukherjee, R., Renault, T., Heberlein, J., Girshick, S. L., and McMurry, P. H. (2005). "System for In Situ Characterization of Nanoparticles Synthesized in a Thermal Plasma Process." In: *Plasma Chemistry and Plasma Processing* 25.5, pp. 439–453. ISSN: 1572-8986. DOI: 10.1007/s11090-005-4991-4.

Wiedensohler, A. and Fissan, H. J. (1991). "Bipolar charge distributions of aerosol particles in high-purity argon and nitrogen." In: *Aerosol Science and Technology* 14.3, pp. 358–364. ISSN: 0278-6826. DOI: 10.1080/02786829108959498.

Winklmayr, W., Reischl, G. P., Lindner, A. O., and Berner, A. (1991). "A new electromobility spectrometer for the measurement of aerosol size distributions in the size range from 1 to 1000 nm." In: *Journal of Aerosol Science* 22.3, pp. 289–296. ISSN: 00218502. DOI: 10.1016/S0021-8502(05)80007-2.

Zhang, S. H., Akutsu, Y., Russell, L. M., Flagan, R. C., and Seinfeld, J. H. (1995). "Radial differential mobility analyzer." In: *Aerosol Science and Technology* 23.3, pp. 357–372. ISSN: 0278-6826. DOI: 10.1080/02786829508965320.

Part II

PUBLICATIONS

PUBLICATIONS

A T. Rosenberger, A. Münzer, D. Kiesler, H. Wiggers, F. E. Kruis, "Ejector-based sampling from low-pressure aerosol reactors", J. Aerosol Sci. 123, DOI: 10.1016/j.jaerosci.2018.06.003 (2018)

- Thore Rosenberger did the design, set-up and execution of the experimental study, the evaluation, analysis and visualization of the data, and the writing of the manuscript.
- Adrian Münzer and Dennis Kiesler supported the work during the measurement campaign at the low-pressure microwave reactor, as well as in the evaluation and analysis of the resulting data.
- Hartmut Wiggers and Einar Kruis assisted in the research study and contributed to the interpretation of the results and the manuscript

B T. Rosenberger, D. Kiesler, E.r Hontañón, D. Fuentes and E. Ramiro, F. E. Kruis, "Design and optimization of a Medium Flow Differential Mobility Analyzer (MF-DMA) for classification of high-density particles", Aerosol Science and Technology 53(10), DOI: 10.1080/02786826.2019.1642443 (2019)

- Thore Rosenberger did the design, set-up and execution of the experimental study, the evaluation, analysis and visualization of the data, and the writing of the manuscript.
- Dennis Kiesler supported the evaluation, did the CFD simulations and provided the computational program to determine the transfer function.
- Esther Hontañón and Daniel Fuentes manufactured the MF-DMA and helped with technical problems.
- Emilio Ramiro and Einar Kruis assisted in the research study and contributed to the interpretation of the results and the manuscript.

C T. Rosenberger, J. Neises, D. Kiesler, and F. E. Kruis, "Ejector-based Nanoparticle Sampling from Pressures down to 20 mbar", J. Aerosol Sci. 144, DOI: 10.1016/j.jaerosci.2020.105531 (2020)

- Thore Rosenberger did the setup of the experimental study, extend the analysis and visualization of the data and the writing of the manuscript.
- Julian Neises did the evaluation, analysis and visualization of the data.
- Dennis Kiesler supported the data analysis.
- Einar Kruis assisted in the research study and contributed to the interpretation of the results and the manuscript.

D T. Rosenberger, J. Sellmann, I. Wlokas, F. E. Kruis, "A model flow reactor design for the study of nanoparticle structure formation under well-defined conditions", Rev. Sci. Instrum. 91(9), DOI: 10.1063/5.0018880 (2020)

- Thore Rosenberger did the design, setup and execution of the experimental study and CFD simulations in ANSYS Fluent; performed the evaluation, analysis and visualization of the data and wrote the manuscript.
- Johannes Sellmann and Irenäus Wlokas supported the simulations, helped with problems, and played a significant role in the evaluation of the simulation results.
- Irenäus Wlokas and Einar Kruis assisted in the research study and contributed to the interpretation of the results and the manuscript.

E S. Suleiman, M. Nanjaiah, I. Skenderović, T. Rosenberger, I. Wlokas, F. E. Kruis, H. Wiggers, C. Schulz, "Atmospheric-pressure particle mass spectrometer for particle growth in spray flames", J. Aerosol Sci. 158, DOI: 10.1016/j.jaerosci.2021.105827 (2021)

- Samer Suleiman designed the device, performed the setup and conducted the experimental study.
- Monika Nanjaiah did the CFD simulation.
- Ivan Skenderović calculated the population balance and assisted during the measurement campaign at the flame reactor.
- Frederik Kunze performed thermophoretic sampling and TEM analysis.
- Thore Rosenberger supported with conventional aerosol measurement techniques during a measurement campaign and analyzed recorded measurement data.
- Irenäus Wlokas, Einar Kruis, Hartmut Wiggers and Christof Schulz assisted in the research study and contributed to the interpretation of the results and the manuscript.

F T. Rosenberger, I. Skenderović, J. Sellmann, P. Wollny, A. Levish, I. Wlokas, A. Kempf, M. Winterer, F. E. Kruis, "Determining the Sintering Kinetics of Fe and Fe_xO_y-Nanoparticles in a Well-defined Model Flow Reactor", Aerosol Science and Technology 56(9), DOI: 10.1080/02786826.2022.2089011 (2022)

- Thore Rosenberger did the design, setup and execution of the experimental study and CFD simulations in ANSYS Fluent; performed the evaluation, analysis and visualization of the data and wrote the manuscript.
- Johannes Sellmann and Patrick Wollny extended the simulations and simulated the particle tracks, helped with problems, and played a significant role in the evaluation of the simulation results.
- Alexander Levish did the XRD and XANES measurements and investigated the chemical phase of the particle.
- Irenäus Wlokas, Andreas Kempf, Markus Winterer and Einar Kruis assisted in the research study and contributed to the interpretation of the results and the manuscript.

A

EJECTOR-BASED SAMPLING FROM LOW-PRESSURE AEROSOL REACTORS

Thore Rosenberger[1], Adrian Münzer[2], Dennis Kiesler[1], Hartmut Wiggers[2] and Frank Einar Kruis*[1]

[1]*Institute of Technology for Nanostructures (NST) and Center for Nanointegration Duisburg-Essen (CENIDE), University Duisburg-Essen, Duisburg, D-47057, Germany*

[2]*Institute for Combustion and Gas Dynamics, and Center for Nanointegration Duisburg-Essen (CENIDE), University Duisburg-Essen, Duisburg, D-47057, Germany*

Published in Journal of Aerosol Science, Volume 123, Pages 105-115 (2018)
DOI: 10.1016/j.jaerosci.2018.06.003

ABSTRACT

Online measurements of nanoparticles are necessary when rapid information about the particle size and mass distribution is needed. Currently, the application of online measurement techniques with commonly used instruments such as SMPS, CPMA and ELPI+ is not possible at low-pressure conditions. In this work, a commercial vacuum ejector is used as a simple tool to transfer nanoparticles from a low pressure region to atmospheric pressure. The vacuum ejector is investigated for different process pressures between 120 to 170 mbar to measure size-selected aerosols in the range from 10 to 100 nm. It was found that the sampling with the vacuum ejector does not change the particle size. The gas and particle dilution factors as well as the particle losses are determined, so that quantitative measurements of the aerosol size distribution can be obtained. Additionally, the applicability of the vacuum ejector is tested during particle synthesis in a low-pressure microwave plasma reactor with a combination of online instrumentation. The direct transfer of the aerosol to atmospheric pressure allows real-time measurements. The primary particle size, mass mobility exponent and effective density are calculated exemplary based on parallel online ELPI+, SMPS and CPMA measurements and are compared to offline TEM analysis.

1. INTRODUCTION

Aerosol instrumentation plays an important role in the study of aerosol reactors and process equipment where aerosols have relevance, such as semiconductor processing equipment. The instrumentation can be divided in online and in-situ measurements. In-situ measurements allow to obtain information of the evolution of the particle size inside the actual particle formation zone, usually by non-intrusive optical methods such as laser-induced incandescence (Eom et al., 2004), and laser-based diagnostics (Dreier and Schulz, 2016) which requires however relatively large particle number concentrations, light-absorbing particles and a substantial amount of information about the particle properties. Although, for online measurements the aerosol has to be sampled from a specific reactor zone and conditioned before size analysis can be performed, the advantage is the availability of a range of different measurement methods, which in combination can also be used to extract information about the particle morphology, such as agglomerate density, primary particle size and mass fractal dimension (Eggersdorfer, Kadau, et al., 2012). Common necessary conditioning steps are rapid cooling and dilution before the aerosol can be analyzed. When the reactor volume is large enough, the finite size of the sampling probe (usually 5 to 15 mm in diameter) does not disturb the process substantially.

A fundamental difficulty for the online measurement techniques is that the process pressure is often substantially below atmospheric pressure. In inert-gas evaporation of nonreactive metals, the process pressure is along with the type of carrier gas the main process parameter determining the particle size (Granqvist and Buhrman, 1976). In aerosol reactors, both low-pressure flame synthesis (Zhao, Liu, and Tse, 2009) as well as chemical vapor synthesis apply non-atmospheric process pressures, usually in the range 30 to 500 mbar. From a scientific viewpoint, low-pressure flames owe their popularity to the fact that the computational modeling is simplified due to a simpler axisymmetric velocity flow field, in which temperature and species profiles are one-dimensional (Janzen, Kleinwechter, et al., 2002; Janzen, Knipping, et al., 2003).

In chemical vapor synthesis of nanoparticles, the process pressure is one of the main factors determining particle size, size distribution, and production rate (Schilling and Winterer, 2014). Commercially available aerosol instrumentation is however not designed to operate at pressures below 500 mbar. Some studies have been performed in order to investigate the performance of specific aerosol instruments at lower pressures (Seifert et al., 2004) or have developed differential mobility analyzers adapted for lower pressures (Nanda and Kruis, 2014; Seto et al., 1997).

The drawbacks of these procedures is the requirement that all of the components have to be tested over the full pressure range of the process. Mobility analysis as being applied in commercial scanning mobility particle sizer (SMPS) is heavily dependent on the availability of experimentally evaluated charging probability. However, the precision of the charging probability measurements is at lower pressures not sufficient, as a result of the obligatory use of an electrometer as particle counter in lack of a low-pressure condensation particle counter. Other instruments such as the aerosol particle mass analyzer (APM) (Ehara, Hagwood, and Coakley, 1996) are – due to their intricate construction as a result of the very high rotational speeds – unsuitable for a low pressure adaption. Therefore, a more convenient route would be to bring the aerosol from the low-pressure reactor environment to ambient pressure to enable conventional aerosol measurements such as SMPS, ELPI and APM.

Bringing the aerosol back to ambient pressure can be done in a discontinuous way, e.g. by using a flexible evacuated bag which sucks in the low-pressure aerosol and letting the bag inflate to atmospheric pressure (Ober et al., 2002). This is a time-consuming and labor-intensive as well as slow sampling procedure. A continuous sampling procedure from low pressure into ambient pressure would be of great advantage for online methods to achieve real-time measurements. A first report on the technical feasibility of such a sampling was given by Wang et al. (2005), who extracted an aerosol from a low pressure environment using an ejector. Although they collected particles from the low-pressure reactor, they did not study the transfer behavior of the ejector. Ejectors are commonly used as a tool to generate low pressure regions on the basis of the Venturi principle. A high-velocity gas provides the driving force to entrain a side gas, usually the gas to be sampled, by the use of a converging nozzle where the pressure is locally decreased. When this local pressure is lower than the pressure of the gas to be sampled, the gas to be sampled will be sucked in. Then the gas mixture is slowed down in a diverging diffuser section and the final pressure of the mixed gas is in between that of the driving gas and the sampled gas, and usually at atmospheric pressure.

In this work, a vacuum ejector is investigated as a suitable transfer system for sampling nanoparticles from a low-pressure process. This study is divided in experiments with and without particle load to find optimal working conditions of the vacuum ejector as well as to determine the pressure dependency of the gas dilution factor (GDF) of defined sample flow rates. Changes in the incoming particle size distribution (PSD) are measured as function of pressure and size. Additionally, the vacuum ejector is assessed with a combination of online measurement

instrumentation in a case study of a low-pressure microwave plasma reactor with high production rates on the lab scale.

2. EXPERIMENTAL

2.1. Setup for measuring the gas dilution factor

The ejector used in this work is a commercial ejector designed to sample a gas from a low pressure region, specified for up to approx. 100 mbar (VIP-4, Landenfeld, Kassel, Germany) and a maximum flow rate of the driving gas Q_{out} of 63 slm (standard liter per minute). It contains three consecutive chambers, each with a Venturi nozzle which are separated from each other by elastic flaps. The Venturi nozzles are designed to deal with smaller to larger pressure regions in flow direction. The final pressure is reached quickly by closing the flaps successively when the final pressure of each Venturi nozzle is reached. In this work only the smallest Venturi nozzle is effectively in use. The ejector is driven by purified nitrogen gas having several bars of overpressure, thereby entraining the gas to be sampled which can be at a pressure lower than atmospheric, denoted by p_{vac}.

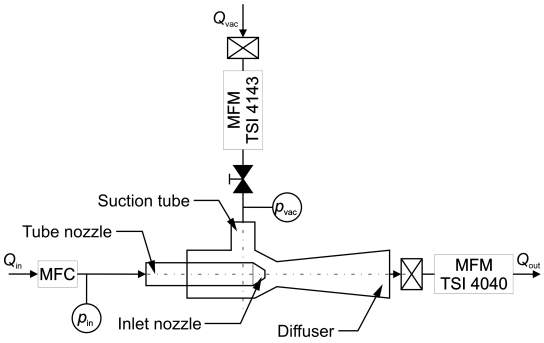

Figure A.1: Setup used to measure the gas dilution factor (GDF) of the low-pressure ejector.

The gas dilution factor (GDF) is defined as the ratio of the diluted gas flow rate after the ejector Q_{in} and the gas sampled from a low-pressure system Q_{vac}. Knowledge about the gas dilution factor is required when the particle losses are to be determined on the basis of the measured particle dilution factor (PDF). Therefore, a setup was built that allows to investigate the driving gas Q_{in}, the sampling flow rate Q_{vac} and the outflow rate Q_{out} in dependency of the driving gas pressure p_{in} and the

process pressure p_{vac} (Figure A.1). The system provides a gas at defined sub-atmospheric pressures by varying the needle valve opening. The flowrates Q_{out} and Q_{vac} are measured with flowmeters (Model 4040 and 4143, TSI, Minneapolis, US) as function of the system pressure p_{vac} with a vacuum gauge (TTR 101, Leybold, Cologne, Germany).

2.2. Setup for measuring the particle transfer efficiency of the ejector

In order to assess whether the aerosol remains unaffected by the vacuum transfer system and to experimentally establish the particle dilution factor, a system was built which provides a size-selected aerosol at atmospheric pressure, expands it via a critical orifice in a low pressure region and brings it back to atmospheric pressure by means of the low-pressure ejector (Figure A.2). Particle counters located before and after the low-pressure system allow to assess the change in particle number concentration (UCPC, 3025A, TSI, Minneapolis, US). The aerosol is generated by evaporating silver in a tube furnace at 1350 °C, then enlarged in size by passing it through a coagulation vessel with a volume of 12 L and sintered into spherical particles at a sintering temperature of 650 °C using a second tube furnace. Size-selected particles between 15 and 120 nm are obtained and measured using a home-built neutralizer containing ^{85}Kr and a cylindrical differential mobility analyzer (DMA, model 3081, TSI, Minneapolis, US). The sheath gas for the DMA is supplied by a gas recirculation system containing a critical orifice (diameter 1.1 mm), an oil-free pump (ACP 15, Pfeiffer Vacuum, Asslar, Germany), an expansion vessel, and a flow meter. The aerosol to sheath gas ratio is approx. 1:5. The size-selected aerosol is sucked into the low pressure region via a critical orifice having an inner diameter of 0.3 mm. The pressure p_{vac} is created by a vacuum pump (MD 8 C, vacuubrand, Wertheim, Germany) and adjusted by means of a needle valve. Thus the vacuum p_{vac} is independent from the pressure created by the vacuum ejector. The particle number concentration after the critical orifice is measured in the gas stream to this pump via a Faraday cup connected to an electrometer (Model 642, Keithley Instruments, Ohio, Cleveland, US). After being brought back to atmospheric pressure and dilution by the vacuum ejector, the aerosol is measured using a particle counter and a SMPS (3080, 3081, 3775, TSI, Minneapolis, US). Valve V 1 is used to decouple the particle synthesis from the measurement instrumentation, whereas valves V 2-3 are closed between the measurements to examine the outflow Q_{out} at the lowest pressure p_{vac} ($Q_{vac} = 0$).

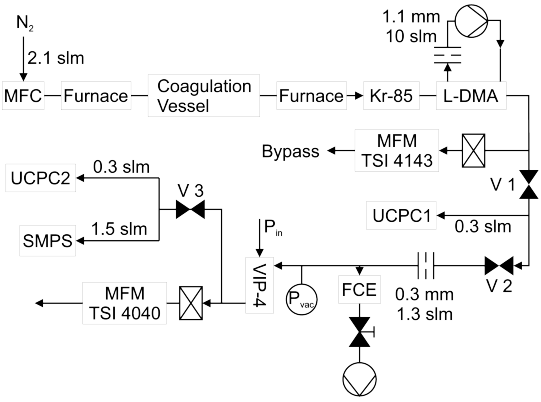

Figure A.2: Schematic setup used to determine the particle transfer efficiency of the vacuum ejector VIP-4.

2.3. *Particle synthesis setup*

The reactor setup is similar to that one we used for the formation and inline-coating of silicon nanoparticles described in our previous paper (Münzer et al., 2017) and is depicted in Figure A.3. This arrangement is based on the formation of a microwave-supported plasma ignited in a quartz tube. The plasma gases (argon and hydrogen) and the silicon precursor silane (10 vol.% SiH_4 in argon) are injected via a central nozzle at the bottom of the reactor. This axial gas flow is surrounded by a coaxial swirl consisting of argon and hydrogen to stabilize the central gas injection. Typical operation parameters are 6 to 10 slm to 10 slm argon, 0.4 to 0.8 slm hydrogen and 0.01 to 0.3 slm silane. Typically, the reactor is operated at a pressure between 10 and 200 mbar abs., for further details see Petermann et al. (2011).

For the online-measurement of the aerodynamic-, mobility- and mass-based particle size distribution of the as-synthesized silicon nanoparticles, the reactor pressure was set to 150 mbar to ensure a flow from the reactor into the ejector due to low pressure limitations of the ejector. Reactor mass flows were adjusted to the values given in Table A.1. The ejector-based sampling system and the subsequent online instrumentation is connected to the exhaust tube as shown in Figure A.3.

Similar to the experiments of Petermann et al. (2011), Si-NPs were continuously produced by thermal decomposition of gaseous SiH_4 in a non-equilibrium, high-temperature H_2/Ar plasma. The process conditions mentioned above allow for a production rate of more than two g/h of soft

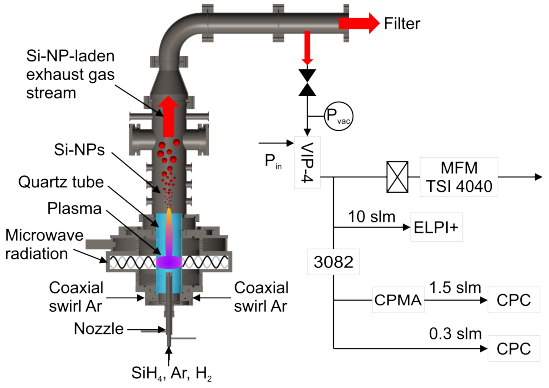

Figure A.3: Experimental setup of the microwave plasma reactor with sampling from the exhaust.

Synthesis parameter	Coaxial swirl gas	Nozzle gas
Mass flow / sccm	Ar: 6570, H_2: 500	Ar: 1670, H_2: 166, SiH_4: 30

Table A.1: Synthesis parameters for silicon nanoparticles.

agglomerates consisting of spherical silicon crystallites. The crystallites size can be tuned between 5 and 50 nm depending on the experimental settings.

The vacuum ejector is connected via a DN KF-16 ball valve to the exhaust pipe close to the reactor filter and equipped with a TTR 101 pressure gauge. The vacuum ejector works with a driving gas pressure of 3.5 bar so that a minimum pressure of 107 mbar abs. is reached. The ball valve is opened slowly and the aerosol is sucked in and transferred to atmospheric pressure through the vacuum ejector. On account of the driving gas, a diluted aerosol flow rate of approx. 55 slm is available for the case study after the ejector. Partial flow rates of 0.3 and 1.5 slm are used for SMPS (3082, 3081, 3775, TSI, Minneapolis, US) and CPMA (Cambustion, Cambridge, UK) measurements, respectively. Additionally, the Long DMA can be used to classify a specific particle size and its mass can be analyzed by the CPMA downstream. The aerodynamic diameter is measured simultaneously with the ELPI+ requiring a sample flow rate of 10 slm with a short measuring time. In this way, the process is controlled and comprehensive measurements can be started when constant conditions are reached.

3. EXPERIMENTAL ASSESSMENT OF LOW-PRESSURE EJECTOR WITH SIZE-SELECTED AEROSOLS

In this section, results for the gas dilution factor (GDF) and the particle dilution factor (PDF) and an assessment whether the aerosol remains unchanged by the sampling procedure are shown. Furthermore, the particle losses of two different critical orifices are measured to determine the particle losses in the vacuum ejector.

3.1. Gas dilution factor

The pressure generated locally inside the ejector should be lower than the pressure at the sampling position as otherwise no aerosol will be sucked in. In order to find out the required inlet pressure of the driving gas, the sample flow is switched off ($Q_{vac} = 0$) and the pressure at the entrance to the ejector has been measured. Figure A.4 depicts the pressure p_{vac} of the low-pressure region as a function of the driving gas pressure p_{in}. It can be seen that a pressure below 100 mbar is reached at inlet pressures above 3.4 bar. Therefore, a fixed inlet pressure of 3.5 bar was selected for the remainder of this study.

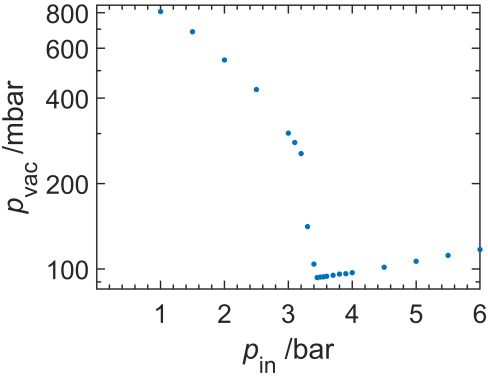

Figure A.4: Pressure at the sample inlet of the vacuum ejector as function of the pressure of the driving gas.

The knowledge of the gas dilution factor Q_{out}/Q_{vac} is mandatory since it is required to indicate particle losses during sampling. Using the procedure described in §2.1 for measuring the gas dilution factor and the setup from Figure A.1, the gas dilution factor was measured as function

of the pressure p_{vac} at the inlet of the low-pressure ejector (Figure A.1 and A.2) and the result is shown in Figure A.5. With decreasing pressure, the volume flow which is sampled (Q_{vac}) sharply decreases and becomes 0 at a pressure of 107 mbar. As a result, there is a strong increase in the gas dilution factor with decreasing pressure at the inlet. Especially below 110 mbar the dependency of the inlet pressure on the sample flow rate (Q_{vac}) is so strong that small pressure fluctuations will lead to unacceptable changes in the GDF.

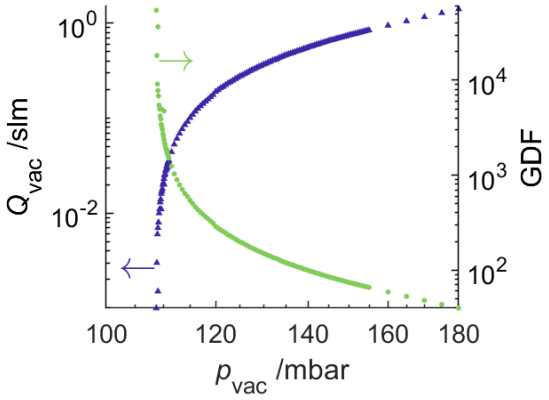

Figure A.5: The gas dilution factor (GDF) as function of the pressure p_{vac} and gas flow rate Q_{vac} at the inlet of the low-pressure ejector.

3.2. *Assessment of sampling effects on aerosol size distribution*

It is important to ensure that the aerosol size distribution is not changed during the passage through the low-pressure sampler. By sampling size-selected aerosols as described in §2.2 a possible change in aerosol size distribution can be measured using a SMPS after the low-pressure ejector. The comparison of the diameter d_{out} (modal value of the size distribution) sampled with the vacuum ejector with that of the incoming aerosol d_{in} (diameter selected with the DMA) indicates a shift of the PSD. The size-selected aerosol measurements shown in Figure A.6, specify that the low-pressure ejector does not lead to a change in particle diameter. A linear function with a slope of 1.016 and a slight offset of -0.067 can be fitted with an error square of 0.999 for the regarding pressure and size range. A study of possible breakage of agglomerates due to high shear

stresses in the ejector is out of the scope of this assessment, as the reactor specifically produces spherical (sintered) particles.

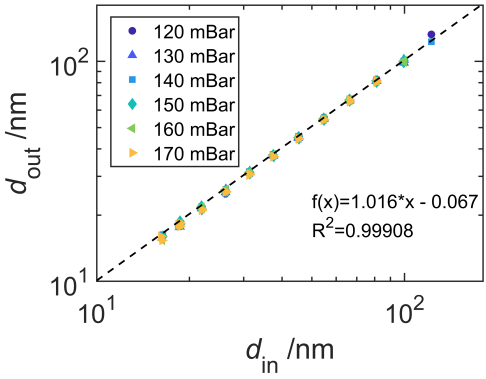

Figure A.6: Modal diameter of the sampled aerosol d_{out} as function of the selected diameter d_{in} by the DMA.

3.3. Particle dilution factor

In order to measure the effective dilution of the aerosol, the aerosol number concentration is measured at the entrance of the critical orifice placed before the low-pressure sampler as well as in the diluted aerosol transferred to atmospheric pressure coming from the low-pressure sampler. It is known that particle losses occur during the passage through a critical orifice, which has been shown experimentally and was denoted as deposition efficiency by Chen et al. (2007). In order to determine these particle losses precisely, the aerosol is size-selected and the number concentration in the low pressure area is measured with a FCE for different process pressures p_{vac}. In Figure A.7 and Figure A.8, the particle losses η are shown and calculated for the given pressures p_{vac} depending on the square root of a modified Stokes number $\sqrt{St'}$ on the lower and on the aerodynamic diameter d_{aero} on the upper X-axis as a comparison to Chen et al. (2007). The Stokes number St_0 is a dimensionless characteristic for the collection efficiency for impactors and is defined as the ratio of the particle stopping distance at the average nozzle exit velocity to the jet radius. The aerodynamic diameter d_{aero} is calculated by the mobility diameter selected by the DMA, assuming spherical particles with a density $\rho_{\text{Ag}} = 10.49\,\text{g/cm}^3$ of the bulk material used in §3 for

the experimental assessment. The particle losses η are determined by comparing the number concentration of N_{UCPC} and N_{FCE}:

$$\eta = \left(1 - \frac{N_{\mathrm{FCE}}}{N_{\mathrm{UCPC}}}\right) * 100\% \tag{A.1}$$

The number concentration is defined by the ratio of the count rate and the sample flow rate into the counter. While the sample flow rate into the UCPC is constant, the flow rate into the FCE is pressure dependent and has to be calculated by the flow rate sucked into the vacuum ejector and the flow rate over a critical orifice. The critical orifice between atmospheric and low pressure area with a diameter of 0.3 mm provides a critical aerosol flow rate of 1.3 slm which is then separated in a DN KF-16 tee before getting sucked into the vacuum ejector or the FCE. The sample flow rate into the FCE is calculated by the total aerosol flow rate of the critical orifice Q_{CO} and Q_{vac} from Figure A.5.

$$Q_{\mathrm{CO}} = Q_{\mathrm{vac}} + Q_{\mathrm{FCE}} \tag{A.2}$$

It seems that the particle losses are independent from the pressure and increase significantly with the square root of a modified Stokes number $\sqrt{St'}$ above 0.1, which is calculated by:

$$\sqrt{St'} = \sqrt{\frac{St_0 U_{\mathrm{o}}}{U_{\mathrm{i}}} \left(\frac{D_{\mathrm{o}}}{D_{\mathrm{t}}}\right)^{1.16}} \tag{A.3}$$

where U_{o} and U_{i} are the average flow velocity in the orifice and inlet tube, D_{o} and D_{t} the diameter of the orifice and the tube after the orifice. This behavior is related to the measurements of the deposition efficiency in the tube after the orifice (TAO) (Chen et al., 2007).

The experimental data align with an exponential fit function and are used to adjust the aerosol number concentration entering the vacuum ejector. It can be seen that in comparison to the experimental data from Chen et al. (2007) and Pui, Ye, and Liu (1988) a steeper gradient is reached. However, these results are only partly comparable due to a different critical orifice geometry and inner diameter of the tubing after the critical orifice as well as a different measurement methodology, which have an influence on the collection efficiency. In this work, a single critical orifice with a two-step reduction of the inner diameter from 1 mm to the critical one of 0.3 mm with a total channel length of 8 mm, is used. The 0.3 mm orifice is drilled with a 2 mm hole depth and chamfered with an angle of 45° in downstream direction followed by a DN KF-16 tubing. It is

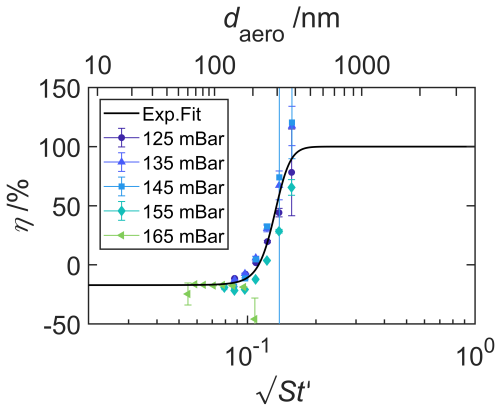

Figure A.7: Particle losses after a CO with an aspect ratio of 3 : 20 followed by a DN KF-16 tubing at different pressure as a function of $\sqrt{St'}$ and d_{aero}

conspicuous that negative particle losses result for smaller particles and the deviation increases for large particles (Figure A.7). The reason for this is the recharging of the particles in the orifice channel due to collisions between particles and wall. A change of the polarization is observed for particles larger than 100 nm from positive to negative. As a result, the current measured with the FCE by selecting small to large particles becomes zero first and then negative. Thereby, the calculated number concentration from the FCE data for small particles as well as the particle losses for large particles are overestimated. If the channel of the critical orifice is reduced from an aspect ratio of 3:20 to an aspect ratio of 3:1 the deviation and the negative particle losses disappear, also the real particle losses will be determined (Figure A.8). The real number concentration after the critical orifice is fitted to an error function shown in Figure A.8 for 150 mbar and used for subsequent data analysis, including the other investigated pressures as the pressure independency was demonstrated in Figure A.7. The literature data shown in Figure A.8 is also fitted with an error function. The particle dilution factor in the vacuum ejector is then determined by the ratio of the two concentrations measured with the N_{UCPC} after the ejector and N_{FCE}.

Figure A.9 shows the pressure dependent particle dilution factor as a function of the selected particle mobility diameter. Also included as lines are the exponential fit functions to the particle dilution factors, based on the measured gas dilution factor, to estimate the diagram curve for larger particles. It can be seen that the dilution factor ranges from 100 to 1000, depending on the pressure, as was also found for the gas dilution

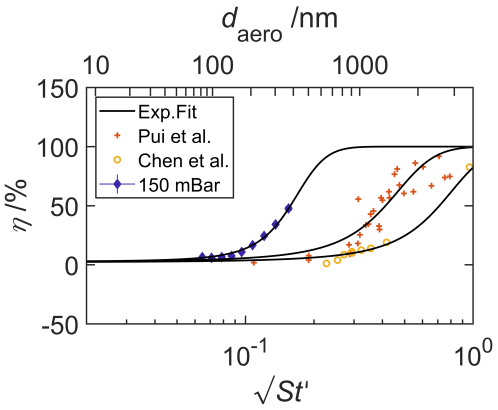

Figure A.8: Particle losses after a CO with an aspect ratio of 3 : 1 followed by a DN KF-16 tubing at different pressure as a function of $\sqrt{St'}$ and d_{aero}. Results are compared to measurements by Chen et al. (2007) and Pui, Ye, and Liu (1988)

factor. There seems to be a size-dependency of the particle dilution factor for particle diameters larger than 40 nm. This is further investigated by displaying the overall particle losses (All) compared to losses in the critical orifice (CO) and in the vacuum ejector (VIP), according to a process pressure of 150 mbar in Figure A.10. The overall particle losses in the size range from 16 nm up to 100 nm is approx. 70 %. For large particles, the particle losses increase slightly due to higher losses in the critical orifice. Whereas the critical orifice let particles smaller than 40 nm pass through without significant losses (< 10 %), the main losses of 67 % occur in the vacuum ejector.

4. CASE STUDY: SAMPLING FROM LOW-PRESSURE PLASMA REACTOR

This study is motivated by the interest in the particle morphology at a high production microwave plasma reactor in the lab scale. Knowledge about the fractal dimension and density of the particles at different positions in the synthesis reactor is necessary to optimize the process parameters. Therefore, a comprehensive parameter study of the synthesis for different silane gas concentrations, reactor pressures and different radial and vertical positions in the reactor is desirable. As an illustration of online measurements at low pressure with a vacuum ejector, we concentrate on the results at 150 mbar in the exhaust and the process condition shown in Table A.1. Size distributions are measured with a

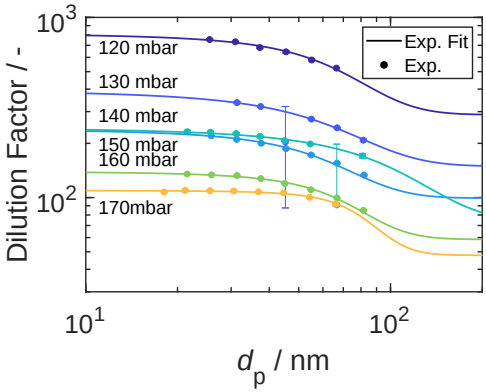

Figure A.9: Particle dilution factor as function of the diameter selected by the DMA at different pressures at the inlet of the low-pressure area.

SMPS and a ELPI+ in the exhaust where particle formation is assumed to be completed. The SMPS measures mobility based number concentrations whereas the electrical low-pressure impactor (ELPI)+ measures a current distribution as a function of the aerodynamic diameter d_{aero}. For the following measurements, a linear transfer behavior of the vacuum ejector is assumed, as a result of §3.2. To obtain the input PSD, the PSD after the vacuum ejector is multiplied by the fit function for the particle dilution factor at 150 mbar (Figure A.8).

Figure A.11a) shows the real-time measurements of the aerodynamic diameter based number distribution $\mathrm{d}N/\mathrm{d}\log(d_{\mathrm{aero}})$ with the ELPI+ at the microwave plasma reactor at 150 mbar. The particle synthesis can be monitored with 1 s time resolution. Different events can be recognized by changes in the distribution. The following events are marked in the diagram: after start-up the reactor needs 10 min to stabilize until constant conditions are reached. Clogging of the collection filter of the reactor leads to a pressure increase up to 152 mbar and thus the sampling flow rate into the ejector increases, visible by an increase of the particle number concentration. After a manual regulation of the flow control system the pressure reduces back to the set point of 150 mbar and constant conditions with no significant change in the aerodynamic diameter are found again. Figure A.11b) depicts the time averaged mobility based particle size distribution (SMPS Raw) with a median diameter of 53.87 nm and a σ_{g} of 1.67 as well as the ELPI+ size distribution with an adjusted effective density ρ_{eff}. The effective density is necessary to convert the equivalent

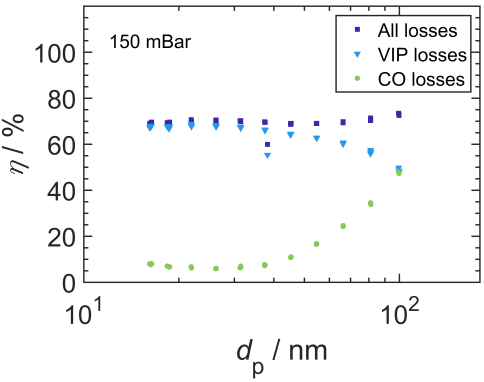

Figure A.10: Particle losses according to the critical orifice (CO) and vacuum ejector (VIP-4)

aerodynamic diameter d_{aero} measured by the ELPI+ into the mobility diameter d_{p}:

$$\frac{d_{\text{a}}^2 \cdot \rho_1}{C_{\text{C}}(d_{\text{in}})} = \frac{d_{\text{p}}^2 \cdot \rho_{\text{eff}}}{C_{\text{C}}(d_{\text{p}})} \tag{A.4}$$

The effective density ρ_{eff} is determined by a fitting procedure, which models the ELPI+ current at each stage based on the SMPS input and compares it to the measured currents as proposed for the conventional ELPI in Virtanen, Ristimäki, and Keskinen (2004). The charge probability and collection efficiency of the ELPI+ stages is modeled with the values given by Järvinen et al. (2014). In contrast to Järvinen et al. (2014), the number distribution of the ELPI+ is calculated as a function of the equivalent mobility diameter d_{p} with a constant ρ_{eff} for all stages (Stein, Kiesler, and Kruis, 2013). The effective density ρ_{eff} can be fitted by minimizing the mean square error in the current distributions between the ELPI+ and SMPS modeled values. For better comparison of the obtained size distributions after the fitting procedure, the SMPS data is rebinned into 14 channels identical to the ones of the ELPI+ (SMPS Fit) and also shown in Figure A.11.

By comparison of the mobility diameter and the aerodynamic diameter the fractal dimension can be calculated and the primary particle size, mass mobility exponent and effective density of the particles can be obtained (Stein, Kiesler, and Kruis, 2013). The primary particle diameter can be described by the Sauter diameter d_{va} as a function of mobility

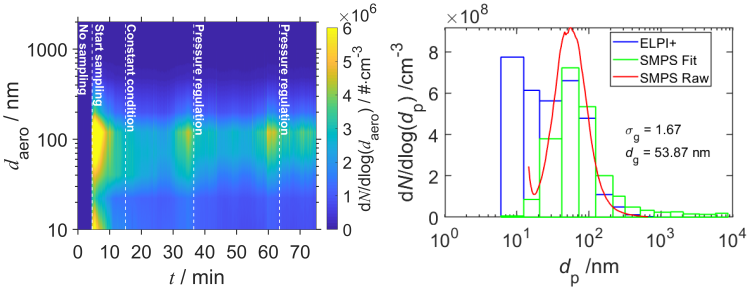

Figure A.11: a) Time resolved particle size distribution with ELPI+ in the exhaust of the microwave plasma reactor at 150 mbar and b) time averaged particle size distribution measured with ELPI+ and compared to SMPS measurements to fit the effective density.

diameter d_p, agglomerate volume v and the projected area exponent D_α (Eggersdorfer, Kadau, et al., 2012). In this work, the equation (Eq. A.5) proposed by Eggersdorfer, Kadau, et al. (2012):

$$d_{va} = \frac{6v}{a} = \left(\frac{\pi k_\alpha}{6v} (d_p)^{2D_\alpha} \right)^{\frac{1}{2D_\alpha - 3}} \tag{A.5}$$

is simplified by substitution of the agglomerate volume v with the agglomerate mass m:

$$v = m \cdot \bar{\rho_{bulk}} 1 \tag{A.6}$$

$$m = \rho_{eff} \frac{\pi}{6} d_p^3 \tag{A.7}$$

so that the primary particle diameter is determined by the mobility diameter and the relative particle densities ρ_{eff}/ρ_{bulk} A.8.

$$d_{va} = d_p \left(k_\alpha \cdot \frac{\rho_{bulk}}{\rho_{eff}} \right)^{\frac{1}{2D_\alpha - 3}} \tag{A.8}$$

The agglomerate structure descriptive parameters $k_\alpha = 0.99$ and $D_\alpha = 1.082$ are independent of the sintering mechanism and are resulting from simulations by Eggersdorfer and Pratsinis (2013).

In the work by Goudeli, Gröhn, and Pratsinis (2016) the mass mobility exponent D_{fm} is simulated for different relative particle densities ρ_{eff}/ρ_{bulk} and σ_g of the PSD. In our study an effective density ρ_{eff} of $1.4\,g/cm^3$ is obtained as best fit, leading to a D_{fm} of 2.44 for a polydisperse model ($\sigma_g = 1.5$) assuming a bulk density of $\rho_{Si} = 2.3\,g/cm^3$. Moreover, a primary particle diameter of approx. $d_{va} = 37\,nm$ is calculated by equation (Eq. A.8).

More accurate information about the particle morphology is obtained by selecting specific particle diameters from the polydisperse particle size distribution. A Long DMA (3081, TSI, Minneapolis, US) is used with an aerosol to sheath gas ratio of approx. 1 : 5 to select a mobility diameter followed by the CPMA to analyze the particle mass based number distribution.

Figure A.12 shows the normalized particle number concentration as function of the particle mass for the selected mobility diameters. The bimodal behavior of the distribution might be a result caused by recharging of the particles due to the relatively high number concentration after the DMA.

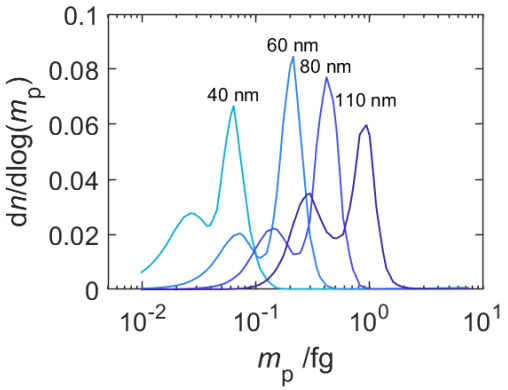

Figure A.12: Particle mass based number distribution measured with CPMA for different diameters selected by DMA after the vacuum ejector in the exhaust of the microwave plasma reactor at 150 mbar.

By assuming a monodisperse particle size distribution, the effective density of the particles of each size class can be estimated by the modal particle mass m_p given by the CPMA and modal particle diameter d_p as classified by the DMA. Thereby, an effective density can be calculated by using equation (Eq. A.7). Table A.2 indicates the selected mobility diameter besides the modal particle mass with the calculated effective density

ρ_{eff}. An effective density slightly below the bulk density for pure Si-Particles $\rho_{\text{bulk}} = 2.3\,\text{g/cm}^3$ is reached for a diameter of 40 and 60 nm. A primary diameter of $d_{\text{prim}} = 51\,\text{nm}$ is calculated using equations (Eq. A.5) and (Eq. A.6). In a diagram, $\log(m_{\text{p}} \cdot m_{\text{prim}}^{-1})$ as function of $\log(d_{\text{p}} \cdot d_{\text{va}}^{-1})$, the fractal dimension is determined as the slope of a linear fit function for diameters larger than 60 nm, expressed as the mass mobility exponent $D_{\text{fm}} = 2.276$ with a pre-factor k_{fm} of 0.942 Eggersdorfer, Gröhn, et al., 2012; Eggersdorfer, Kadau, et al., 2012. Comparing these results with those from the polydisperse measurements, it can be seen that the mean effective density and mass mobility exponent are in good agreement, but that the simpler polydisperse measurement underestimates the primary particle diameter.

d_{m} /nm	m_{mode} /fg	ρ_{eff} /g · cm^{-3}
40	0.064	1.910
60	0.21	1.857
80	0.414	1.544
110	0.973	1.396

Table A.2: Effective density of size classified particles.

An additional offline transmission electron microscope (TEM) analysis is performed with a Jeol JEM-2200FS to determine the morphology and size of the materials synthesized. The particles are sampled on the filter from the exhaust at 100 mbar and are collected in order to validate previous measurements. In Figure A.13, characteristic particle structures analyzed with the TEM are shown and the count median particle diameter was exemplary calculated by fitting a lognormal size distribution to the measured data.

The result shown in Figure A.14 indicates that the distribution profile of more than 200 examined particle diameters follows a log-normal function with a geometric mean diameter d_{g} of 37.0 nm and a geometric standard deviation of $\sigma_{\text{g}} = 1.53$. TEM counting results in a mean Sauter particle diameter of $d_{\text{va}} = 52.3\,\text{nm}$ formed at 100 mbar process pressure and is comparable to the one found by the online analysis at 150 mbar ($d_{\text{prim}} = 51\,\text{nm}$).

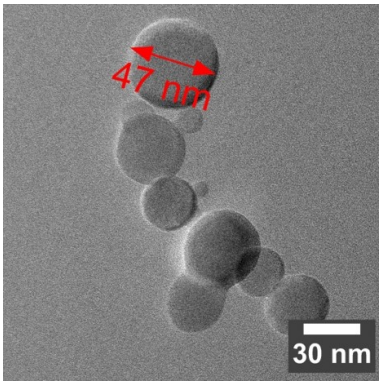

Figure A.13: TEM image of Si-NPs synthesized at 100 mbar.

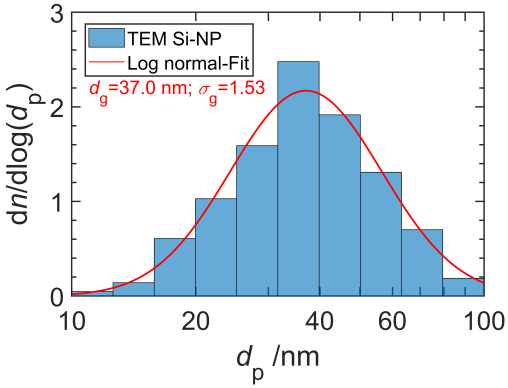

Figure A.14: Primary particle size distribution and log-normal fit of more than 200 diameters of Si-NPs recorded with TEM.

5. CONCLUSION

This study investigated a commercial vacuum ejector as a transfer system for aerosols from low-pressure processes to atmospheric conditions for particles in the size range from 10 to 100 nm. In a dedicated experimental setup, the particle (PDF) and gas dilution factor (GDF) have been determined and overall losses of 70 % have been measured for process pressures from 120 to 170 mbar. Main particle losses were found to occur inside the vacuum ejector and the critical orifice, used to transfer the aerosol from verified process conditions at atmospheric to lower pressure

regions. The size-dependent particle losses in the critical orifice were measured, allowing to determine the actual number concentration upon entering the vacuum ejector. Following this, the particle losses in the vacuum ejector could be investigated. Whereas bigger particles seem to pass through the vacuum ejector without significant losses (approx. 10 %), large losses of 67 % were determined for small particles. A change of the particle size distribution in the considered size range caused by the vacuum ejector is not observed for the spherical particles used in the experiments. The applicability of the vacuum ejector has been successfully tested with particles produced in a microwave plasma reactor in the lab scale at a process pressure of 150 mbar. Real-time online measurements have been conducted and different events during the synthesis were identified by changes in the particle size distribution. The in this study applied online measurement techniques like SMPS, ELPI+ and CPMA which require atmospheric pressures, were also compared with offline TEM analysis. The primary particle diameter, effective density as well as the fractal dimension have been calculated using different methods and are in good agreement.

ACKNOWLEDGMENT

The authors acknowledge the support by the Deutsche Forschungsgemeinschaft (DFG) in scope of the research group 2284 “Model-based scalable gas-phase synthesis of complex nanoparticles” (KR 1723/16) and the joint research program “Multi parameter characterization of functional particle based materials by innovative online measurement techniques (PAK688)” (KR 1723/14).

Chen, S.-C., Tsai, C.-J., Wu, C.-H., Pui, D. Y. H., Onischuk, A. A., and Karasev, V. V. (2007). "Particle loss in a critical orifice." In: *Journal of Aerosol Science* 38.9, pp. 935–949. ISSN: 00218502. DOI: 10.1016/j.jaerosci.2007.06.010.

Dreier, T. and Schulz, C. (2016). "Laser-based diagnostics in the gas-phase synthesis of inorganic nanoparticles." In: *Powder Technology* 287, pp. 226–238. ISSN: 0032-5910. DOI: 10.1016/j.powtec.2015.10.015.

Eggersdorfer, M. L., Gröhn, A. J., Sorensen, C. M., McMurry, P. H., and Pratsinis, S. E. (2012). "Mass-mobility characterization of flame-made ZrO_2 aerosols: Primary particle diameter and extent of aggregation." In: *Journal of Colloid and Interface Science* 387.1, pp. 12–23. ISSN: 0021-9797. DOI: 10.1016/j.jcis.2012.07.078.

Eggersdorfer, M. L., Kadau, D., Herrmann, H. J., and Pratsinis, S. E. (2012). "Aggregate morphology evolution by sintering: Number and diameter of primary particles." In: *Journal of Aerosol Science* 46, pp. 7–19. ISSN: 00218502. DOI: 10.1016/j.jaerosci.2011.11.005.

Eggersdorfer, M. L. and Pratsinis, S. E. (2013). "Restructuring of aggregates and their primary particle size distribution during sintering." In: *AIChE Journal* 59.4, pp. 1118–1126. ISSN: 0001-1541. DOI: 10.1002/aic.14043.

Ehara, K., Hagwood, C., and Coakley, K. J. (1996). "Novel method to classify aerosol particles according to their mass-to-charge ratio—Aerosol particle mass analyser." In: *Journal of Aerosol Science* 27.2, pp. 217–234. ISSN: 00218502. DOI: 10.1016/0021-8502(95)00562-5.

Eom, G. S., Park, S., Park, C. W., Choe, W., Shin, Y.-H., Chung, K. H., and Hahn, J. W. (2004). "Size Monitoring of Nanoparticles Growing in Low-Pressure Plasma using Laser-Induced Incandescence Technique." In: *Japanese Journal of Applied Physics* 43.9A, pp. 6494–6498. ISSN: 0021-4922. DOI: 10.1143/JJAP.43.6494.

Goudeli, E., Gröhn, A. J., and Pratsinis, S. E. (2016). "Sampling and dilution of nanoparticles at high temperature." In: *Aerosol Science and Technology* 50.6, pp. 591–604. ISSN: 0278-6826. DOI: 10.1080/02786826.2016.1168922.

Granqvist, C. G. and Buhrman, R. A. (1976). "Ultrafine metal particles." In: *Journal of Applied Physics* 47.5, pp. 2200–2219. ISSN: 0021-8979. DOI: 10.1063/1.322870.

Janzen, C., Kleinwechter, H., Knipping, J., Wiggers, H., and Roth, P. (2002). "Size analysis in low-pressure nanoparticle reactors: comparison of particle mass spectrometry with in situ probing transmission electron microscopy." In: *Journal of Aerosol Science* 33.6, pp. 833–841. ISSN: 00218502. DOI: 10.1016/S0021-8502(02)00048-4.

Janzen, C., Knipping, J., Rellinghaus, B., and Roth, P. (2003). "Formation of Silica-Embedded Iron-Oxide Nanoparticles in Low-Pressure Flames." In: *Journal of Nanoparticle Research* 5.5/6, pp. 589–596. ISSN: 1388-0764. DOI: 10.1023/B:NANO.0000006109.37251.fd.

Järvinen, A., Aitomaa, M., Rostedt, A., Keskinen, J., and Yli-Ojanperä, J. (2014). "Calibration of the new electrical low pressure impactor (ELPI+)." In: *Journal of Aerosol Science* 69, pp. 150–159. ISSN: 00218502. DOI: 10.1016/j.jaerosci.2013.12.006.

Münzer, A., Sellmann, J., Fortugno, P., Kempf, A., Schulz, C., and Wiggers, H. (2017). "Inline coating of silicon nanoparticles in a plasma reactor: Reactor design, simulation and experiment." In: *Materials Today: Proceedings* 4, S118–S127. ISSN: 2214-7853. DOI: 10.1016/j.matpr.2017.09.176.

Nanda, K. K. and Kruis, F. E. (2014). "A radial differential mobility analyzer for the size-classification of gas-phase synthesized nanoparticles at low pressures." In: *Measurement Science and Technology* 25.7, p. 075605. ISSN: 1361-6501. DOI: 10.1088/0957-0233/25/7/075605.

Ober, F., Mayer, M., Büttner, H., and Ebert, F. (2002). "Aerosol Measurement in Low-Pressure Systems with Standard Scanning Mobility Particle Sizers." In: *Particle & Particle Systems Characterization* 19.4, pp. 229–239. ISSN: 09340866. DOI: 10.1002/1521-4117(200208)19:4<229::AID-PPSC229>3.0.CO;2-8.

Petermann, N., Stein, N., Schierning, G., Theissmann, R., Stoib, B., Brandt, M. S., Hecht, C., Schulz, C., and Wiggers, H. (2011). "Plasma synthesis of nanostructures for improved thermoelectric properties." In: *Journal of Physics D: Applied Physics* 44.17, p. 174034. ISSN: 1361-6463. DOI: 10.1088/0022-3727/44/17/174034.

Pui, D. Y. H., Ye, Y., and Liu, B. Y. H., eds. (1988). *Sampling, transport, and deposition of particles in high purity gas supply system*. Los Angeles, CA, United States (USA). ISBN: 0-915414-37-6.

Schilling, C. and Winterer, M. (2014). "Preserving Particle Characteristics at Increasing Production Rate of ZnO Nanoparticles by Chemical Vapor Synthesis." In: *Chemical Vapor Deposition* 20.4-5-6, pp. 138–145. ISSN: 09481907. DOI: 10.1002/cvde.201307094.

Seifert, M., Tiede, R., Schnaiter, M., Linke, C., Möhler, O., Schurath, U., and Ström, J. (2004). "Operation and performance of a differential mobility particle sizer and a TSI 3010 condensation particle counter at stratospheric temperatures and pressures." In: *Journal of Aerosol Science*

35.8, pp. 981–993. ISSN: 00218502. DOI: 10.1016/j.jaerosci.2004.03.002.

Seto, T., Hirota, A., Fujimoto, T., Shimada, M., and Okuyama, K. (1997). "Sintering of Polydisperse Nanometer-Sized Agglomerates." In: *Aerosol Science and Technology* 27.3, pp. 422–438. ISSN: 0278-6826. DOI: 10.1080/02786829708965482.

Stein, M., Kiesler, D., and Kruis, F. E. (2013). "Adjustment and Online Determination of Primary Particle Size in Transferred Arc Synthesis of Copper Nanoparticles." In: *Aerosol Science and Technology* 47.11, pp. 1276–1284. ISSN: 0278-6826. DOI: 10.1080/02786826.2013.835484.

Virtanen, A., Ristimäki, J., and Keskinen, J. (2004). "Method for Measuring Effective Density and Fractal Dimension of Aerosol Agglomerates." In: *Aerosol Science and Technology* 38.5, pp. 437–446. ISSN: 0278-6826. DOI: 10.1080/02786820490445155.

Wang, X., Hafiz, J., Mukherjee, R., Renault, T., Heberlein, J., Girshick, S. L., and McMurry, P. H. (2005). "System for In Situ Characterization of Nanoparticles Synthesized in a Thermal Plasma Process." In: *Plasma Chemistry and Plasma Processing* 25.5, pp. 439–453. ISSN: 1572-8986. DOI: 10.1007/s11090-005-4991-4.

Zhao, H., Liu, X., and Tse, S. D. (2009). "Effects of pressure and precursor loading in the flame synthesis of titania nanoparticles." In: *Journal of Aerosol Science* 40.11, pp. 919–937. ISSN: 00218502. DOI: 10.1016/j.jaerosci.2009.07.004.

B

DESIGN AND OPTIMIZATION OF A MEDIUM FLOW DIFFERENTIAL MOBILITY ANALYZER (MF-DMA) FOR CLASSIFICATION OF HIGH-DENSITY PARTICLES

Thore Rosenberger[1], Dennis Kiesler[1], Esther Hontañón[1], Daniel Fuentes[2], Emilio Ramiro[2], and Frank Einar Kruis[1]

[1]*Intitute of Technology for Nanostructures (NST) and Center for Nanointegration Duisburg-Essen (CENIDE), University Duisburg-Essen, Duisburg, D-47057, Germany*

[2]*Ramem S.A., Madrid, 28027, Spain*

Published in Aerosol Science and Technology, Volume 53 - Issue 10, Pages 1172-1185 (2019)
DOI: 10.1080/02786826.2019.1642443

ABSTRACT

A new design of a differential mobility analzyer (DMA) was tested with medium aerosol flow rates ranging from 1.5 slm to 10 slm and high-density particles. The vacuum-tight construction makes it possible to classify pure metal nanoparticles from production processes. The selectable electrical mobility range is comparable to the TSI Long and Nano differential mobility analzyer (DMA) and covers the full nanometer scale from 15 to 600 nm. The medium-flow differential mobility analyzer (MF-DMA) is characterized by its transfer function, which was determined by a tandem DMA setup using a SMPS with Long DMA downstream. Silver nanoparticles with a density of 10.49 g/cm^3 were used to demonstrate the size-selecting performance of high-density particles. The transfer function was calculated for aerosol to sheath gas flow ratios of 1/10, 1/5 and 1/3 directly from the SMPS data by a new method using modeling approach and comparison to the theory. Sufficiently high resolution was reached by increasing the SMPS scan time of the classified size distribution to 300 s. During the investigation, a broadened transfer function could be attributed to an inhomogeneous flow field resulting from the aerosol inlet design. The aerosol inlet of the MF-DMA was optimized by the number of inlet drillings and the opening of the inlet slit to achieve a more homogeneous flow field. CFD simulations of the MF-DMA also confirmed this.

The modification improved the transfer function especially for medium aerosol flow rates above 5 slm.

1. INTRODUCTION

DMA are valuable instruments for classifying a polydisperse aerosol into particle size classes on the basis of their electrical mobility. The operation principle bases on the deflection of charged aerosol particles in an electrical field according to their particle size, level of electrical charge and properties of the gas environment. High-resolution classification can be performed in the submicron particle range, depending on the DMA design and the flow rates. The broad application range of nanoparticles, especially with defined sizes (Kruis, Fissan, and Peled, 1998), increases the interest in classifying these particles by means of a DMA. Cylindrical, radial and parallel plate DMA designs have been optimized for a range of applications. Since the development of the first cylindrical DMA by Hewitt (1957), many publications have focused on the optimization of its' transfer function by adapting the design of DMAs for different gas flow rates. Rosser and Fernández de la Mora (2005) have shown an approach to optimize the cylindrical DMA for small particles at high flow rates. They applied a converging flow, thus enabling classification with Reynolds numbers up to 20,000 and sheath gas flow rates up to 4000 slm The high gas flow rate leads to short residence time in the classification zone in which particles between 1 and 100 nm can be classified. A disadvantage of this approach is that ambient air is used as sheath gas flow, drawn in the DMA by a vacuum pump. Operation under a controlled gas atmosphere is sometimes required in order to avoid particle-gas interaction, such as the oxidation of pure metal nanoparticles. Steiner et al. (2010) reduced the sheath gas flow rate to 280 and 700 slm by using a closed loop arrangement in order to better control the sheath gas composition. A combination of both approaches into a single DMA is the high-flow differential mobility analyzer (HF-DMA) from Hontañón and Kruis (2009). It is designed for the lower size range of nanoparticles using high flow rates, with an aerosol flow rate up to 100 slm and a sheath flow rate up to 1000 slm, comparable to Steiner et al. (2010). A high aerosol flow rate can be useful when additional online instrumentation is needed for comprehensive aerosol characterization (Babick et al., 2018), calibration measurements are required, or monodisperse aerosols have to be provided to production processes.

One range of applications requires the classification of larger (but still submicron) and high-density particles. In particular, size-selected gold nanoparticles are required in various applications due to their good

catalytic effect. Heurlin et al. (2012) developed a method for the one-dimensional growth of GaAs nanowires onto highly crystalline gold nanoparticles in the gas phase. The gold particle size is a sensitive parameter for controlling the nanowire shape. In biomedicine, the well-studied interaction of organic functionalized groups with the gold surface is exploited to produce functionalized gold nanoparticles, e.g. for selective drug delivery and for biomedicine imaging. Functionalization of gold nanoparticles with thiol for gas-phase gene transfection has already been demonstrated by (Byeon and Roberts, 2012). The gas-phase production of gold nanoparticles has proven to be an efficient and scalable process for a wide range of functionalized nanobiomaterials.

Unfortunately, not much effort has been put into investigating and optimizing the transfer function for large and heavy particles. One reason for this might be that a compromise between selectable size range and residence time of the particles in the classification zone have to be found. A DMA prototype with longer residence time by extending the classification length to 1200 mm was demonstrated by Uin, Tamm, and Mirme (2009). As a result, PSL particles up to 1 µm in a sheath gas flow rate of 29 slm could be theoretically classified. The commercially available Long DMA (Model 3081, TSI, MN, US) can classify particle sizes up to 700 nm with an aerosol to sheath gas ratio of 0.3/3 slm. When operating this DMA with a gas flow ratio of 1.5/15 slm, the maximum achievable particle size drops to 200 nm. However, these DMAs have not been designed for particles of high density such as gold, so high particle losses by impaction can be expected. Impaction losses are dependent on the stopping distance of the particles, which is proportional to the particle density. When the stopping distance of the particles is of the same order of magnitude as a characteristic instrument dimension such as a bend or orifice size, impaction losses are expected to occur. The minimization of impaction losses places particularly high demands on the aerosol inlet and outlet geometry of the DMA, as here small orifices and bends are present.

In this work, a DMA was designed to classify particle diameters from 15 to 600 nm in an aerosol flow rate of 1.5 slm and sheath gas flow rate of 15 slm. The DMA aerosol inlet was optimized taking also possible aerosol flow rates up to 10 slm into account. The primary goal of this design is to minimize particle losses for high-density particles such as gold. Therefore, a CFD model of the DMA was used to simulate the flow field, calculate the transfer function and to compare it with experiments. Usually, the transfer function of a DMA is determined by a method which requires two DMA prototypes or at least one DMA with known transfer function in a Tandem DMA setup (Stratmann et al., 1997). In order to avoid

the fabrication of a second prototype, a new method for determining the transfer function of a DMA was developed, using two continuous scanning SMPS systems containing DMAs with known transfer function. This allowed the experimental evaluation of the transfer function of the DMA developed in this work, which is named medium-flow differential mobility analyzer (MF-DMA).

2. DESIGN CONSIDERATIONS

2.1. Size range

The MF-DMA aims at providing a monodisperse aerosol in the range 15 to 600 nm at a medium flow rate of the aerosol (up to 10 slm). A previous study of a DMA having medium flow rates focused on the lower nanometer range, especially 1 to 5 nm (Steiner et al., 2010), where diffusion losses play a major role. In contrast, as one of the applications here is to provide size-selected metallic particles, the instrument should show minimal losses of high-density particles at the upper end of the size range. For these relatively large and heavy particles, their large relaxation times can lead to particle losses due to impaction in the in- and outlet sections of the DMA, so that these sections have to be optimized. In this work, an inverted cylindrical DMA design similar to an earlier high flow DMA (Hontañón and Kruis, 2009) with an easily exchangeable classification zone was chosen. The inverted design was selected as it has been proven to be the most economical construction for large vacuum-tight components.

The inner radius of the cylindrical classification zone is set to $r_i = 36$ mm and the outer radius to $r_o = 46$ mm, resulting in a 10 mm gap. In order to avoid electrical breakdown between the inner and outer electrode or inside the high voltage plug, the maximal voltage is set to 10 kV although voltages up to 12 kV did not lead to discharges when there was no particle deposit present on the electrodes. The mean electrical mobility Z_p^* of particles exiting the aerosol outlet of this inverted cylindrical DMA can be derived in the same way as the one for the classical cylindrical DMA. It depends on the sheath gas flow Q_{sheath} and the applied voltage U_{DMA} as well as the DMA geometry:

$$Z_p = \frac{Q_{sheath} \cdot \ln(r_o/r_i)}{2\pi \cdot L \cdot U_{DMA}} \tag{B.1}$$

Designed for an aerosol flow rate of at least 1.5 slm, the MF-DMA is suitable to classify particles over a large range by expanding the

classification length L from 95 mm (Short MF-DMA) to 495 mm (Long MF-DMA). Assuming spherical particles, the mobility diameter d_B can be calculated with:

$$d_B = \frac{q \cdot e \cdot C_C(d_B)}{3\pi \cdot \eta \cdot Z_p} \tag{B.2}$$

and using the Cunningham slip correction factor C_C:

$$C_C(d_B) = 1 + \frac{2\lambda}{d_B}\left(\alpha + \beta \cdot e^{-\gamma \frac{d_B}{2\lambda}}\right) \tag{B.3}$$

with the parameters α, β, γ given by Kim et al. (2005). Here, q is the number of charges, e the elementary charge, η the dynamic gas viscosity and λ the mean free path of the surrounding gas.

As a reference, the Nano DMA (Model 3085, TSI) and Long DMA (Model 3081, TSI) are usually used in combination with a classifier with aerosol to sheath gas ratio of 0.3/3 or 1.5/15 slm. Under these sheath gas conditions, it is possible to select maximal mobility diameters $d_{B,max}$ up to 165 and 65 nm, respectively, using the Nano DMA and up to 840 and 240 nm, respectively, with the Long DMA, assuming singly charged particles. The MF-DMA was tested in this work with larger sheath gas flows rates, between 4.5 and 30 slm, which theoretically allows to provide a monodisperse aerosol up to 420 and 120 nm, respectively, with the Short version and up to 1700 and 350 nm, respectively, with the Long version. In comparison to the traditional DMA design exemplified by the TSI DMAs, the instrument dimensions of the MF-DMA can provide size-selected particles in larger quantities, having larger and high-density particles.

2.2 Technical Description

The MF-DMA consists of several parts, of which the outer parts are joined together by large vacuum flanges based on DN ISO-F 100 specifications. In this way, the DMA can easily be disassembled in smaller and lighter components for transportation and cleaning. In addition, some parts can be replaced or inserted in order to enable the conversion of the Short MF-DMA into the Long MF-DMA. The material used is stainless steel 316 L, which is for purposes of material synthesis better suited than aluminum. Figure B.1 shows the cross sections of the Short and Long MF-DMA. All gas in- and outlets are equipped with DN ISO-K 16 flanges. The sheath gas enters the DMA from the top DN ISO-KF 16 flange through

twelve ∅5 mm holes in the upper insulator tangential to the copper rod. The copper rod is used to electrically contact the hemisphere on top of the central electrode. Before the sheath gas passes the aerosol inlet and enters the classification zone, the gas flows around the hemisphere top and passes two polymer meshes. These laminarization meshes consist of fifty-four ∅50 µm fibers per centimeter and are mounted on a ring structure to provide a homogeneous flow field in the classification zone and to dampen possible flow turbulences. The mesh holder is fixed in place when screwing the hemisphere and the upper electrode together. The inner electrode consists of three parts, hemisphere, an upper and lower electrode, which are connected by threads.

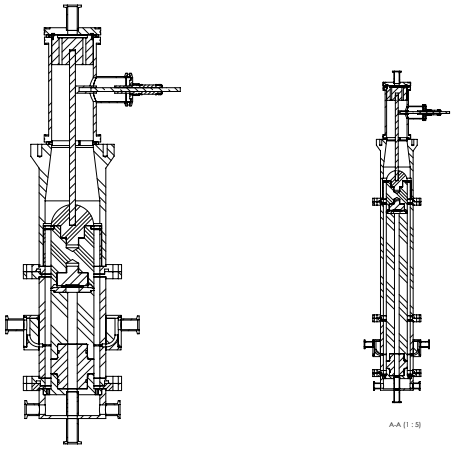

Figure B.1: Cross-sections of the Short (left) and Long MF-DMA (right).

The inner electrode is electrically isolated by two insulators at the top and bottom which are made from a ceramic material (MACOR). The polydisperse aerosol enters the DMA at the bottom and flows inside the inner electrode towards the aerosol inlet. The aerosol is led through twenty ∅3 mm drillings in the original design, which was optimized later in this work to forty ∅3 mm drillings (see discussion in in Section 2.3), and a 1 mm inlet slit in the classification zone. The opening of the inlet slit is variable in the range from 1 to 4.5 mm in 0.5 mm steps by placing distance holders between upper and lower inner electrode. The inlet slit has an angle of 39.8° (upper) and 21.8° (lower) with respect to the inner electrode.

The classification zone has an inner radius of 36 mm and an outer radius of 46 mm. The Short MF-DMA has a classification length of 95 mm. The lower part of the inner electrode can be interchanged by a longer version with a classification length of 495 mm to classify larger particles. An additional tubular part is nipped with vacuum flanges that can be inserted in the outer electrode, thereby accommodating the increased length of the inner electrode. The electrical high voltage can be applied to the inner electrode over a DN ISO-K 40 electrical feedthrough. It is connected to a copper rod and the hemisphere of the inner electrode via spring contact. The classified aerosol exits through thirty ∅0.5 mm drillings at the outer electrode in a 90° bend with an inner and outer diameter of 15 and 20 mm towards four DN ISO-K 16 flanges. The pressure drop over the small drillings is high enough so that a single aerosol outlet can be used without causing flow distortion in the classification zone. The excess aerosol leaves the annular space through ninety-six ∅1.3 mm drillings and exits the DMA sidewards over four DN ISO-KF 16 flanges.

2.3. Optimization of In- and Outlet Geometry

As the MF-DMA should be able to operate with relatively large particles of high-density up to 1.7 µm as well as with medium gas flow rates, the particle losses due to impaction have to be investigated. To this end, CFD simulations based on the finite element method were performed using a three-dimensional mesh for a radial piece of 90°, including the regions before and after the outlet, with Fluent (Version 6.2, Fluent Inc., NH, USA). The gas phase was simulated by solving the Navier-Stokes equations for an ideal gas. It was assumed that the viscosity is only temperature-dependent and can be described by the Sutherland model. Heat capacity, as well as heat conductivity, are described by the kinetic gas theory with known degrees of freedom. Particle trajectories were calculated by using the Lagrangian approach, neglecting particle-particle interactions:

$$m_{\mathrm{p}} \frac{\mathrm{d}u_{\mathrm{p}}}{\mathrm{d}t} = f_D \cdot (u - u_{\mathrm{p}}) + F_{\mathrm{B}} + F_{\mathrm{el}} \tag{B.4}$$

with u_{p} and u indicating the velocity of the particles and the gas. The particle acceleration results from several forces: the particle drag $f_D \cdot ($ *glsuserisymb* : $uv - u_{\mathrm{p}})$, a random distributed force caused by Brownian motion F_{B} and an electrical force F_{el}. The Stokes drag force was calculated using the friction coefficient f_D with the Cunningham slip correction factor C_C by Fuchs (1964) (Eq. B.3):

$$f_D = \frac{18\eta}{d_B^2 \rho_p \cdot C_C} \cdot m_p \tag{B.5}$$

The force resulting from Brownian motion was calculated with Gaussian distributed random numbers for ζ_i with a mean value of 0 (Li and Ahmadi, 1992):

$$F_B = \zeta_i \sqrt{\frac{216\eta k_B T}{\pi d_B^5 \rho_p^2 C_C \Delta t} \cdot m_p} \tag{B.6}$$

k_B is the Boltzmann constant and T the cell temperature. The time step at each iteration is set by Δt. It was assumed that the electrical force F_{el} occurs only in the radial direction and is proportional to the electrical field E and to the particle charge $q \cdot e$.

First experiments indicated that the MF-DMA with the original design of the aerosol inlet (twenty ∅3 mm drillings and 1 mm inlet slit) delivered a broadened bimodal size distribution for aerosol flows above 5 slm. Therefore, CFD simulations of the gas velocity in the classification zone of the MF-DMA were performed for analyzing the flow uniformity in the classification zone and for predicting the transfer function of the MF-DMA. For the analysis of the transfer function, 100 logarithmically distributed particle diameters in the size range 30 to 200 nm for gold particles with a density $\rho_p = 19.32\,g/cm^3$ were calculated, taking nearly 2400 different starting points each simulated trajectory into account.

Figure B.2 depicts the results of the $2.4 \cdot 10^5$ simulated trajectories based on the original (a) and the optimized inlet design (b), as well as the corresponding experimentally measured transfer functions of the Short MF-DMA (crosses). The aerosol flow rate was set to 5 slm with a sheath gas flow rate of 25 slm. Experimentally, silver particles with a diameter of 74 nm were selected by applying a voltage of 3775 V. The transport efficiency and losses are attributed to the aerosol inlet and aerosol outlet wall, the electrodes, and the aerosol outlet (i.e., the DMA transfer function). Regarding the experimental measurement of the original design, a bimodal size distribution with nodes at 65 and 80 nm can be observed, as stated earlier. The transport efficiency for the particle diameter to be classified (74 nm) is low, approx. 23 %. The corresponding simulation indicates a broadened size distribution with a flat top and a comparable low transport efficiency of 35 % (solid line), with 13 % losses in the aerosol inlet and 8 % in the outlet, and 47 % losses to inner and outer electrode. The particle losses to the outlet walls are not so significant, which can be explained by its design which

aimed at minimizing impaction losses by avoidance of sharp bends after the outlet drillings. Particles with a diameter $d_B < 65\,nm$ and $d_B > 100\,nm$ do not reach the aerosol outlet and deposit on the electrodes. The broadened transfer function, as well as the relatively high losses, necessitate a reconsideration of the inlet region design based on an analysis of the streamlines in the classification zone. The simulation with the optimized aerosol inlet (b) shows a narrower size distribution with a significant improvement of the transport efficiency up to 66 % by reducing losses to the electrodes. The predicted size distribution by the simulation is even narrower, but still in good agreement with the experiment. The transport losses to the aerosol inlet walls (9 %) are independent on the particle size and comparable to the original aerosol inlet.

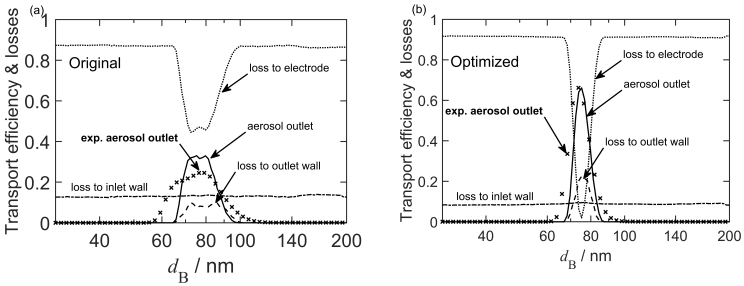

Figure B.2: Transport efficiency and losses in different regions of the MF-DMA with original aerosol inlet design (a) and optimized aerosol inlet (b) according to the simulations. The experimentally measured transfer function is also included (crosses). Short MF-DMA, with $Q_{aerosol} = 5\,slm$ and $Q_{sheath} = 25\,slm$ and an aerosol inlet gap of 1 mm.

Figure B.3 depicts the axial gas velocity in the classification zone of the CFD simulation model based on the Short MF-DMA geometry. The left part of the figure shows the streamlines in the original design of the lower inner electrode, both as a top and as a side view. The original aerosol inlet contains 20 drillings in the inner part of the inner electrode, which are necessary to spread the aerosol homogeneously in the radial direction before the aerosol enters the classification zone through the inlet slit. In the 90° top view of Figure B.3, only five of these drillings are depicted. It can be observed that this number of drillings is insufficient to reach a homogeneous gas flow field in the classification zone at these relatively high gas flow rates, as the axial velocity shows a wavy form in the top view. The mean radial velocity in the aerosol inlet slit is 0.432 m/s with a standard deviation of 0.035 m/s. The non-

uniformities in the radial flow profile lead to an inhomogeneous axial flow profile (streaks in color plot seen from the side view), which results in particles having different residence time and thus a different mobility-equivalent diameter. Consequently, the transfer function is broadened due to the simultaneous classification of particles having a different mobility-equivalent diameter. These non-uniform axial velocities are caused by the fact that the drillings are placed too far apart, so the number of drillings is doubled in the optimized design. By doubling the number of drillings, the mean radial velocity in the aerosol inlet slit does not change, but the standard deviation is reduced and becomes smaller than 0.01 m/s. That this modification leads to a much more uniform flow before and after the aerosol inlet slit can be seen on the right part of Figure B.3. Detailed experimental results and effects of the optimized aerosol inlet on the transfer function are presented in Section 4. In the following experimental setup and investigations, the optimized design of the aerosol inlet is used for the Long and Short MF-DMA.

3. EXPERIMENTAL METHODS

3.1. Experimental Setup for Determination of the Transfer Function

The performance of the MF-DMA can be assessed by means of measurement of the transfer function, which is described by its characteristic height and full width at half maximum ($FWHM$). Here, the resolution $\mathcal{R}^{-1}$ and the height α are applied to describe a diffusional broadened transfer function (Flagan, 1999). By measuring the particle size distribution before and after the MF-DMA with a reference system, the transfer function can be calculated by deconvolution (Li, Li, and Chen, 2006; Stratmann et al., 1997). The standard technique for determining the transfer function of a DMA is based on a tandem DMA setup. Generally, a first DMA provides a monodisperse aerosol with known electrical mobility and a second DMA steps through specific mobility sizes differentially. If the DMA designs are identical, the transfer function can be calculated by deconvolution, assuming that both functions are equal. If two identical DMAs are not available, it is necessary that one transfer function is known. Therefore, in a first experiment, two Long DMAs (3081, TSI) are used in a tandem DMA setup to determine the transfer function of the DMA used by the SMPS. After the completion of this measurement, the first Long DMA is exchanged by the MF-DMA.

The experimental setups for determining the transfer function of the DMAs are shown in Figure B.4. The particle generation in both setups is equal, but the supply of the aerosol flow rate for the DMAs differs

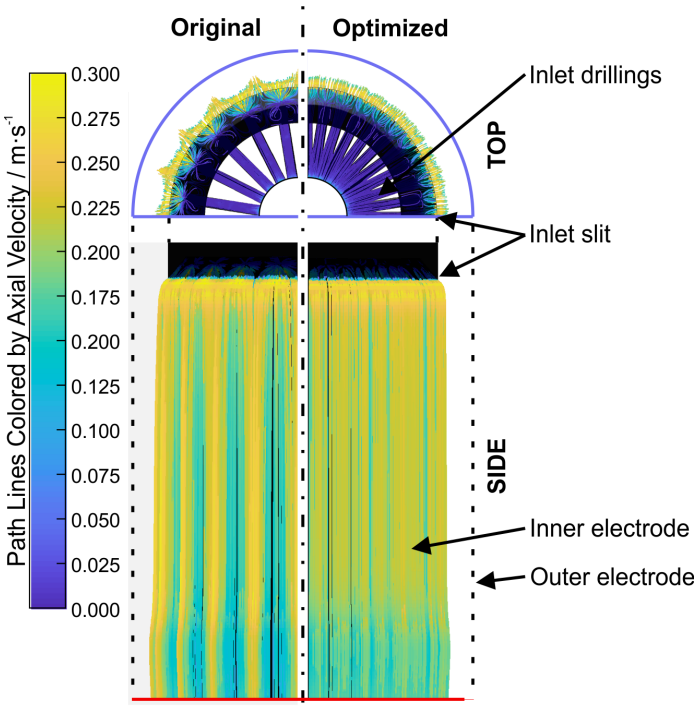

Figure B.3: Simulation of the axial gas velocity for the original aerosol inlet with 20 drillings (left) and the optimized aerosol inlet with 40 drillings (right). Shown are the top and the side view of the inner electrode. (conditions as in Figure B.2).

as represented in the setup (*a) and (*b). A first mass flow controller (Bronkhorst High-Tech B.V., Ruurlo, NL) controls a nitrogen gas flow rate of 0.8 slm (MFC 1), flowing through a furnace operated at temperatures between 1473 K and 1673 K. In the tube furnace, silver particles are synthesized by an evaporation/condensation process and are transported towards a coagulation vessel. The vessel consists of a DN ISO-F 250 tube with a total volume of 12 L. It is equipped with two DN ISO-KF 40 flanges at the top for the aerosol inlet and side flange as an outflow. After the coagulation vessel, the size of the incoming aerosol is increased to particle diameters as large as 600 nm. A custom-built Kr-85 neutralizer with an initial activity of 370 MBq is used to establish a defined equilibrium charge distribution and is required for the subsequent data inversion (Yang, Dhaniyala, and He, 2018).

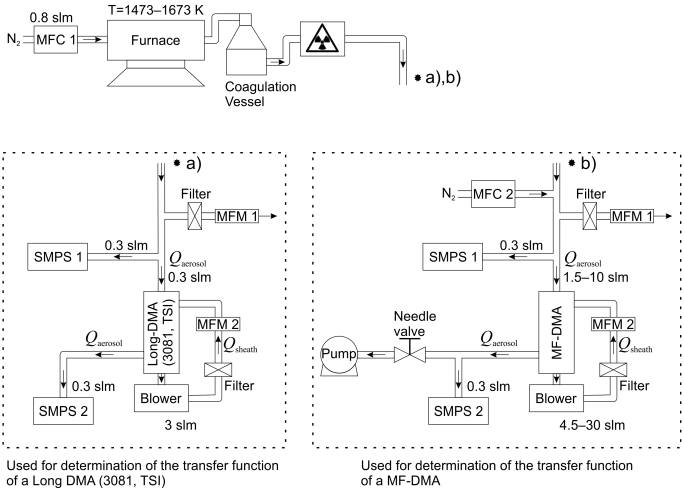

Figure B.4: Experimental setup for the determination of the transfer function of the Long DMA (3081, TSI) *a), as well as the Short and Long MF-DMA *b).

In setup (*b) only, a second mass flow controller (MFC 2) downstream of the neutralizer dilutes the aerosol to provide a total aerosol flow rate for the MF-DMA between 2 and 10.5 slm. A flow splitter directs a partial aerosol flow through a bypass with an exhaust HEPA-filter and thereby guarantees atmospheric pressure in the DMAs downstream. The flow rate in the bypass is permanently measured with a flow meter (Model 4140, TSI) to ensure constant conditions and is set to approx. 0.2 slm (MFM 1) by adjusting MFC 2. The first SMPS (Model 3936, TSI), a combination of a classifier (Model 3080, TSI), a Long DMA (Model 3081, TSI) and condensation particle counter (Model 3775, TSI), measures the polydisperse particle size distribution before entering the DMA to be characterized without additional neutralization (SMPS 1). The sample flow rate through Long DMAs to be characterized (*a) is set to 0.3 slm and a sheath gas flow rate of 3 slm is provided by a classifier (Model 3080, TSI). This configuration was chosen because it corresponds to one of the SMPS standard setups and settings. The MF-DMA is placed on top of a sheath gas closed-loop recirculation system with blower, mass flow meter (mass flow meter (MFM) 2), and HEPA-filters (*b). Thereby, the aerosol flow rate at the inlet and outlet of the DMAs are identical. A power

supply (12.5 kV, 500 µA) is connected to the MF-DMA and voltages can be applied by software, controlled via LabVIEW (National Instruments, TX, US). Another SMPS (Model 3938, TSI), a combination of a classifier (Model 3080, TSI), a Long DMA (Model 3081, TSI), condensation particle counter (Model 3775, TSI), measures the monodisperse particle size distribution at the aerosol outlet of the DMA to be characterized and also here without additional neutralization (SMPS 2). The aerosol flow rate through the MF-DMA is set by means of a needle valve and a vacuum pump placed downstream. The total aerosol flow rate provided by the two MFCs is always higher than the required gas flow rate, sucked in by the two SMPS and by the vacuum pump via the needle valve.

The transfer function of the unknown DMA is determined by selecting 14 different mobilities and measuring the fractionated mobility distribution three times each with a SMPS (SMPS 2). Preparatory measurements with this tandem DMA setup show that it is necessary to use the largest SMPS scan time, 300 s with 6 s retrace and 10 s purge, to obtain consistent results. Thereby, a better resolution for narrow distributions (Collins et al., 2004) and an enhanced particle size range from 13.6 nm to 736.5 nm is reached. In the Appendix A, the broadening of the measured geometric standard deviation of an aerosol fractionated with a Long DMA and a flow ratio of 1 : 10 in dependency of the scan times t_{scan} is shown. The largest possible scan time of 300 s was chosen for all experiments in this work. The transfer function is determined according to the method described in Section 3.2.

3.2. Determination of the Transfer Function by Data Inversion

For the determination of the transfer function by data inversion, a simulation of all steps involved in the measurement chain is implemented and utilized. Different devices can be simulated, combined and the outputs can be predicted. For the calculation of the transfer function of an unknown DMA, a full simulation of said DMA combined with a SMPS, consisting of a neutralizer, DMA and CPC is carried out and compared with experimental data. The input polydisperse size distribution for the simulation is defined by the measurement with a first SMPS (SMPS 1). Downstream of the DMA to be characterized, a second SMPS (SMPS 2) measures the classified monodisperse size distribution. A numerical fit of the SMPS 2 data and the simulation with a variety of input parameters for the DMA transfer function lead finally to the correct prediction. The numerical fit is carried out with a Nelder-Mead simplex algorithm as described in Lagarias et al. (1998) and is used to find the minimized error between measured and simulated particle size distribution. The

simulation is sufficiently accurate if the error is smaller than $\epsilon < 10^{-6}$. Thereby, the transfer function of the unknown DMA is determined by convolution with a known DMA transfer function, in this case, the Long DMA (3081, TSI).

The transfer function of the Long DMA is determined by a tandem DMA setup of two similar DMAs and the assumption that the resolution and transfer efficiency of both instruments are equal. In this case, the heights and widths of the transfer functions of the first and second DMA (SMPS 2) are coupled and the measured size distribution can be calculated by changing the $FWHM$ and α. The transfer function is calculated for an ideal non-diffusional broadened transfer function with equal aerosol flow rate into and out of the DMA. The detailed results of this measurements can be found in the Appendix B. Height and resolution are fitted with an exponential expression based on the theory for diffusional broadening as derived by Flagan (1999):

$$\alpha = -1.081e^{-0.05032 \cdot d_B} + 0.8381; \quad \mathcal{R}^{-1} = 0.2899e^{-0.0924 \cdot d_B} + 0.1133 \quad \text{(B.7)}$$

The transfer function is calculated by a mathematical toolbox (MATLAB, MathWorks, Natick, MA, USA) using a matrix-based workspace. A diffusional or non-diffusional transfer function can be calculated. The program uses direct import of the SMPS data. The imported SMPS data files (SMPS 1) are converted into a number concentration $N^{\mathrm{SMPS}}[i]$ with indexed i channels of the polydisperse aerosol. Multiple charge correction is not activated in the SMPS software (Aerosol Instrument Manager AIM, TSI) measuring the number concentration per electrical mobility. The absolute charge $Q[q] = q \cdot e$ is calculated by elementary charge e multiplied with the charge level q of the particles. The charge probability for smaller particles ($d_B < 70\,\mathrm{nm}$) is calculated by the Wiedensohler (1988) approximation formula with the given coefficients $\alpha_{q,k}$, assuming that smaller particles can only be singly, doubly or uncharged ($|q| \leqslant 2$):

$$f^{\mathrm{charge}}[i,q] = 10^{\left(\sum_{k=0}^{5} \alpha_{q,k} (\log_{10}(d_B[i]))^k\right)} \quad \text{(B.8)}$$

The Gunn-Model (Gunn and Woessner, 1956) is applied for all charges up to $q_{\max}$ and for particles larger than $d_B > 70\,\mathrm{nm}$.

$$f^{\mathrm{charge}}[i,q] = \frac{e}{\sqrt{4\pi^2 \epsilon_0 d_B[i] k_B T}} \exp\left\{ \frac{-\left[q - \frac{2\pi\epsilon_0 d_B[i] k_B T}{e^2} \cdot \ln\left(\frac{n_{I+} \cdot Z_{I+}}{n_{I-} \cdot Z_{I-}}\right)\right]^2}{2\frac{2\pi\epsilon_0 d_B[i] k_B T}{e^2}} \right\}$$

(B.9)

with dielectric constant ϵ_0, Boltzmann's constant k_B, temperature T, the ion concentration ratio $n_{I+}/n_{I-} = 1$, assuming to be in the state of equilibrium, and the ratio of ion mobility for nitrogen $Z_{I+}/Z_{I-} = 0.93$ (Wiedensohler and Fissan, 1991).

The number concentration after the neutralizer $N^{\text{neut}}[i,q]$ depends on the charge level q in the size channel i and is calculated stepwise for each size channel:

$$N^{\text{neut}}[i,q] = f^{\text{charge}}[i,q] \cdot N^{\text{SMPS}}[i] \tag{B.10}$$

Knowledge of particle charging is critical for accurate estimation of N^{neut} and affects the calculation of the number concentration after the DMA, if there is a significant fraction of multiply charged particles. Yang, Dhaniyala, and He (2018) showed that a ^{85}Kr charger with an initial activity of 41 MBq does not produce particles with steady-state charge. A higher initial activity of 221 MBq is sufficient to produce steady-state charging values at a flow rate of 0.3 slm. Increasing the aerosol flow rate (0.93 slm) leads to a less charging performance but still close to theoretically prediction. Using a charger with a higher activity with a sufficient long residence time is recommended. The channel-based charge-dependent number concentration after the DMA $N^{\text{DMA}}(d_{\text{setp}})[i,q]$ is calculated, if a DMA selects a mobility diameter d_{setp} by a component-wise multiplication of the transfer function $TF^{\text{DMA}}(d_{\text{setp}})[i,q]$ with the charge-dependent inlet concentration $N^{\text{neut}}[i,q]$:

$$N^{\text{DMA}}(d_{\text{setp}})[i,q] = TF^{\text{DMA}}(d_{\text{setp}})[i,q] \cdot N^{\text{neut}}[i,q] \tag{B.11}$$

A transfer function describes the fraction of particles per size channel of a specific particle setpoint d_{setp} which can be found in the aerosol outlet of a DMA. The mobility-based center of the transfer function $Z_{\text{setp}}(d_{\text{setp}}, q = 1)$ is calculated by Equation (B.2) using d_{setp} instead of d_B for singly charged particles.

The diffusion broadened model for cylindrical DMAs derived by Stolzenburg (1988) and given by Flagan (1999) is used for the determination of the transfer function. A new index j is introduced that covers the entire mobility range $Z_p[i,q]$ measured with the SMPS 2. The number of mobility channels $Z_p[j]$ must be higher than the number of measuring channels in order to achieve a sufficiently high resolution. Thus, a high number of mobility channels avoids aliasing effects during back conversion. The values for $Z_p[j]$ are calculated by interpolation between the mobility channels $Z_p[i,q]$.

The symmetrical flow of the aerosol flow rate is established by recirculation of the sheath gas so that the transfer function for the electrical mobility setpoint corresponding to the index [j] can be expressed by:

$$TF^{\mathrm{DMA}}[j](Z_{\mathrm{setp}}) = \frac{\alpha \cdot \tilde{\sigma}\,[j]}{\beta\sqrt{2}} \left(E(\gamma_1[j]) + E(\gamma_2\,[j]) - 2E(\gamma_3\,[j])\right) \quad \text{(B.12)}$$

Where $\beta = Q_{\mathrm{aerosol}}/Q_{\mathrm{sheath}}$ and α the transfer efficiency. The smoothed triangular function $E(\gamma[j])$ can be expressed by:

$$E(\gamma[j]) = \gamma[j] \cdot \mathrm{erf}(\gamma[j]) + \frac{1}{\sqrt{\pi}} exp\left\{-(\gamma[j])^2\right\} \quad \text{(B.13)}$$

using the error function $\mathrm{erf}(\gamma)$, and applying different equations for γ with the normalized electrical mobility $\tilde{Z}[j](Z_{\mathrm{setp}}) = Z_{\mathrm{p}}[j]/Z_{\mathrm{setp}}$:

$$\gamma_1[j] = \frac{\tilde{Z}[j] - (1+\beta)}{\sqrt{2\tilde{\sigma}\,[j]}} \quad \gamma_2[j] = \frac{\tilde{Z}[j] - (1-\beta)}{\sqrt{2\tilde{\sigma}\,[j]}} \quad \gamma_3[j] = \frac{\tilde{Z}[j] - 1}{\sqrt{2\tilde{\sigma}\,[j]}} \quad \text{(B.14)}$$

Linear interpolation is used to convert the transfer function $TF^{\mathrm{DMA}}(\tilde{Z}_{\mathrm{p}}[j])$ based on the mobility channels $Z_{\mathrm{p}}[j]$ to $TF^{\mathrm{DMA}}(Z_{\mathrm{p}}[i,q])$ based on the particle size $d_{\mathrm{p}}[i]$ and charge space q. The transfer function is only non-zero for the charge index $q > 0$. The diffusional broadening of a transfer function depends on the particle traversing time in the DMA and is expressed as the dimensionless variance $\tilde{\sigma}\,[j]$.

$$\tilde{\sigma}\,[j] = \sqrt{\frac{G_{\mathrm{c}}}{Pe} \cdot \tilde{Z}[j]} \quad \text{(B.15)}$$

The Peclet number Pe points out the dominant particle transport mechanism and is calculated by the ratio of electrophoretic to diffusive transport rate:

$$Pe = \frac{e \cdot U_{\mathrm{DMA}}\,(Z_{\mathrm{setp}})}{k_B T} \cdot f \quad \text{(B.16)}$$

The applied DMA voltage $U_{\mathrm{DMA}}(Z_{\mathrm{setp}})$ is calculated from:

$$U_{\mathrm{DMA}}(Z_{\mathrm{setp}}) = \frac{Q_{\mathrm{sheath}} \cdot \ln(\frac{r_{\mathrm{o}}}{r_{\mathrm{i}}})}{2\pi \cdot L_{\mathrm{DMA}} \cdot Z_{\mathrm{setp}}} \quad \text{(B.17)}$$

Q_{aerosol} (slm)	Q_{sheath} (slm)	β	G_c	f	Settings for
0.3	3.0	0.1	2.1401	0.707	Long DMA (3081 TSI)
1.5	15	0.1	2.5226	0.887	Short MF-DMA
1.5	15	0.1	2.5085	0.887	Long MF-DMA

Table B.1: Parameters calculated according to Flagan (1999) for a Long DMA and the two MF-DMA versions, at common DMA settings and standard conditions.

A summary of the geometry- and flow-dependent parameters: flow ratio β, the geometry parameter G_c and the parameter for non-uniformities in the electric field f calculated according to Flagan (1999) are shown in Table B.1.

The resolution of the DMA is defined by Equation (B.18) with flow ratio β and the dimensionless variance $\tilde{\sigma}$.

$$\mathcal{R}_{\text{approx}} = \frac{1}{\sqrt{\beta^2 + 6\tilde{\sigma}^2}} \tag{B.18}$$

The simulated total number concentration $N^{\text{CPC}}(d_{\text{setp}})$ for a given setpoint can be expressed as the sum of the total number concentration after the DMA multiplied by the counting efficiency η^{CPC}. Therefore, a loop with the number of i measurement channels of the SMPS is needed to calculate the number concentration of each channel. The counting efficiency is set to 100 % for particles diameters larger than 20 nm independent of their size (Hermann et al., 2007).

$$N^{\text{CPC}}(d_{\text{setp}}) = \sum_i \left(\eta^{\text{CPC}} i \cdot \sum_{-q_{\max}}^{q_{\max}} N^{\text{DMA}}(d_{\text{setp}})[i,q] \right) \tag{B.19}$$

If a DMA with an unknown transfer function is used for size selection upstream of the SMPS 2, containing a DMA with a known transfer function, initial values for the transfer efficiency and resolution of the first DMA are used to predict $N^{\text{DMA}}(d_{\text{setp}})[i,q]$ and $N^{CPC}(d_{\text{setp}})$. By comparison of the simulated number concentration with the measured number concentration by the SMPS 2 the transfer function of the first DMA will be adjusted stepwise until the error will be smaller than $\epsilon < 10^{-6}$.

4. RESULT AND DISCUSSION

The transfer function of the MF-DMA is determined and evaluated according to the procedures described in Sections 3.1 and 3.2. The aerosol flow rate is varied from 1.5 slm up to 10 slm. The maximal sheath gas flow is limited to 30 slm with the available blower and pressure drop over HEPA-filters and laminarization mesh. Therefore, aerosol flow rates above 2.5 slm are operated with an aerosol to sheath gas ratio of 1/3 or 1/5 only. The transfer function is determined by a tandem DMA setup with the MF-DMA followed by a TSI Long DMA of the SMPS 2 downstream. The MF-DMA is assembled with the improved design of the aerosol inlet design, number of 40 drillings, with an inlet slit of 1 mm. A fully characterized transfer function is determined by a data inversion procedure and delivers experimental values for the height α and the width $\mathcal{R}^{-1}$. Results are compared with theory: the width based non-diffusional theory describing the theoretical limit of the resolution, given by the aerosol to sheath gas ratio β (Knutson and Whitby, 1975), and the width according to diffusional theory as calculated from Equation (B.18). The theoretical limit of the height is 1 and indicates no particle losses in the DMA. For the experimental evaluation of the transfer function particle diameters in the full-size range from 15 to 600 nm could be tested. Higher aerosol flow rates were provided by a dilution gas so that the total number concentration was reduced, resulting in a slightly smaller size range from which a sufficiently high number concentration could be classified. An improved transfer function for smaller particle diameters can be achieved by the shortening of the classification zone. The classification length of Short MF-DMA is 95 mm and thereby approx. five times shorter than the Long MF-DMA. The measurements of the transfer function using the Long MF-DMA are presented in this section, whereas the transfer function of the Short MF-DMA can be found in Figure S1-3 (see the online supplementary information ([SI])).

Figure B.5 depicts the width $\mathcal{R}^{-1}$ (a) and the height α (b) of the transfer function of the Long MF-DMA for an aerosol to sheath flow ratio of 1/3 as a function of the setpoint particle diameter d_{setp}. Error bars indicate the standard deviation of three measurements at a given setpoint. The widths predicted by non-diffusional (β) and diffusional theory ($\mathcal{R}^{-1}_{\mathrm{approx}}$) are indicated by dashed and solid lines, respectively. A narrow size distribution is achieved with an aerosol flow rate of 1.5 slm and 2.5 slm. The width is approximately 6 % above the theoretical optimum. The transfer function becomes more broadened and is size-independent by increasing the aerosol flow rate. For higher aerosol flow rates, 8 slm and 10 slm, the width increases strongly towards smaller particle diameters.

A significant broadening of the transfer function and more particle losses are observed. Particle diameter larger than 300 nm can be still sufficiently resolved with a width of 0.45.

For the height, a value above 0.7 is obtained for aerosol flow rates below 5 slm. The height decreases towards smaller diameters due to the broadening of the transfer function. The broadening can be explained by a slightly distorted flow field which becomes more significant for higher aerosol flow rates as described in Sections 2.3. This leads to a general offset of the width from the theoretical limit β. The decrease of the resolution for smaller particle diameter could indicate higher diffusion broadening in the classification zone. Comparing with the predicted diffusional broadening (colored solid lines), it can be seen that the diffusion is not the main cause. Due to the high velocity in this classification area, diffusion broadening is only expected for setpoints below 40 nm. A higher effective diffusivity, and therefore a broadening could be a result of microturbulences at the aerosol inlet area where the aerosol and sheath gas come together. Additional particle losses can be attributed to the inner electrode wall. The multiplication of the height with the resolution gives the area of the transfer function and is equal to β without particles losses. Particle losses are higher towards smaller particle diameters and longer residence time in the inlet tube of the inner electrode. Aerosol flow rates of 1.5 and 2.5 slm lead to 28 % losses of a particle diameter of 50 nm and aerosol flow rate above 5 slm to 11 %. A shorter residence time in the inner electrode is given by the Short MF-DMA leading to less particle losses with the same settings as can be seen in SI Figure S4 (see the online supplementary information ([SI])). Particle losses of 15 % occur at an aerosol flow rate of 1.5 slm, 8 % at 2.5 slm and 2 % above 5 slm respectively.

Figure B.6 shows the transfer characteristics of the Long MF-DMA for a flow ratio of 1/5. As mentioned before, sheath gas flow rates above 30 slm cannot be supplied by the used blower. Therefore, the highest aerosol flow rate is limited to 5 slm. Similar to the flow ratio of 1/3, the width for flow rates up to 5 slm seems to be relatively independent of the setpoint diameter and increases with aerosol flow rate. The transfer function is broadened by 13 and 20 % for aerosol flow rates below and above 2.5 slm respectively. The standard deviation increases with particle size larger than 200 nm due to less concentration during the measurements. A trend of the transfer characteristic for setpoints $d_{\mathrm{setp}} > 200$ nm cannot be clearly described. The transfer efficiency increases with the particles diameter from 70 % (50 nm) to 90 % (350 mm) and is comparable to previous results with a gas ratio of 1/3.

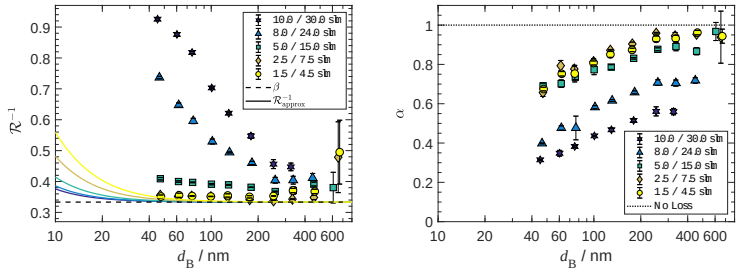

Figure B.5: Width $\mathcal{R}^{-1}$ (a) and the height α (b) of the transfer function of the Long MF-DMA for a flow ratio $\beta = 0.33$ and an aerosol inlet gap of 1 mm. The legend shows the aerosol and sheath flow rates.

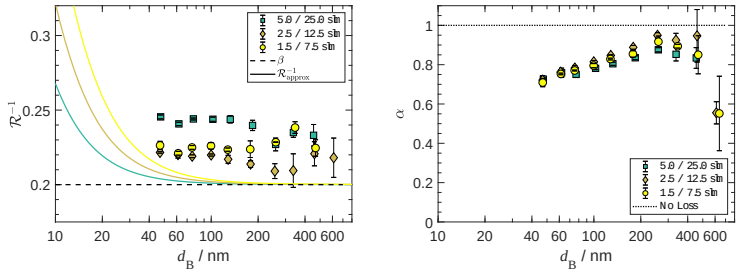

Figure B.6: Width $\mathcal{R}^{-1}$ (a) and the height α (b) of the transfer function of the Long MF-DMA for a flow ratio $\beta = 0.2$ and an aerosol inlet gap of 1 mm.

For a flow ratio of 1/10, Figure B.7 shows that the width can be found in the range of 0.125, fairly size-independent and deviating more than the ones with same aerosol flow rate but higher gas flow ratios. The height of the transfer function is between 0.6 and 0.8 and shows a less clear size-dependency compared to flow ratios of 1/3 and 1/5. This can be explained by the fairly constant and broadened width. Influence of the sheath gas flow on the broadening of the transfer function is not observed. For this reason, the formation of microturbulence resulting from the fine laminarization mesh placed at a large distance to the aerosol inlet can be excluded. In fact, the slight broadening at larger aerosol and sheath flow rates shown in Figure B.6 is mainly caused by the aerosol flow rate and can be probably related to flow inhomogeneities and turbulence at the aerosol inlet.

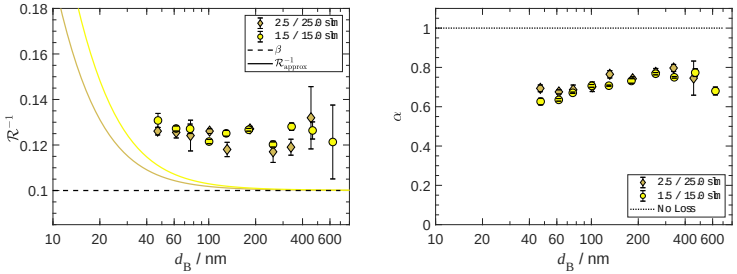

Figure B.7: Width $\mathcal{R}^{-1}$ (a) and the height α (b) of the transfer function of the Long MF-DMA for a flow ratio $\beta = 0.1$ and an aerosol inlet gap of 1 mm.

The broadening observed at higher aerosol flow rates supposedly caused by undesired mixing of aerosol and sheath gas is investigated more in detail. The aerosol inlet slit is increased stepwise by 1 mm up to 3 mm, thereby reducing the aerosol inlet velocity. Figure B.8 displays the width and height of the transfer function as a function of the aerosol flow rate for a gas ratio of 1/3, using an aerosol inlet slit opening of 1 mm, 2 mm and 3 mm and a constant setpoint diameter of 100 nm. It can be seen that the width of the transfer function increases with the aerosol flow rate, in line with the earlier findings. The width of the transfer function for a slit opening of 2 mm is reduced in comparison to an opening of 1 mm. A further enlarge of the slit opening up to 3 mm leads to a clear deterioration of the width and height characteristics.

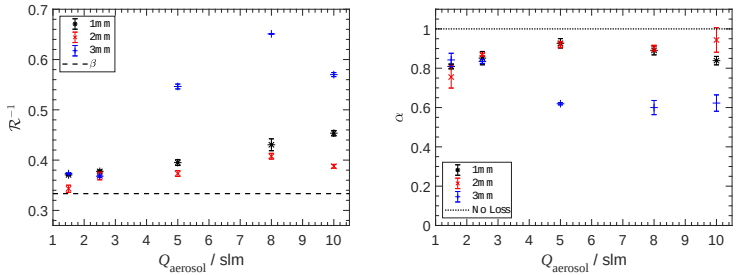

Figure B.8: Width $\mathcal{R}^{-1}$ (a) and the height α (b) of the transfer function of the Long MF-DMA for a flow ratio $\beta = 0.33$ and a variable aerosol inlet gap for a particle diameter of 100 nm.

The measurements of the transfer function were repeated using an aerosol inlet slit opening of 2 mm, as best results have been obtained with this configuration. In Figure B.9, the width and height of the transfer function for a flow ratio of 1/3 are depicted. Higher aerosol flow rates are more affected by the aerosol inlet slit so that only flow rates above 5 slm are shown. A significant improvement of the transfer characteristics can be seen in comparison to a slit opening of 1 mm (Figure B.5). The width is less broadened and the height is comparable to previous measurements: around 0.6 for the smallest particle sizes, increasing to values over 0.9 for the largest sizes.

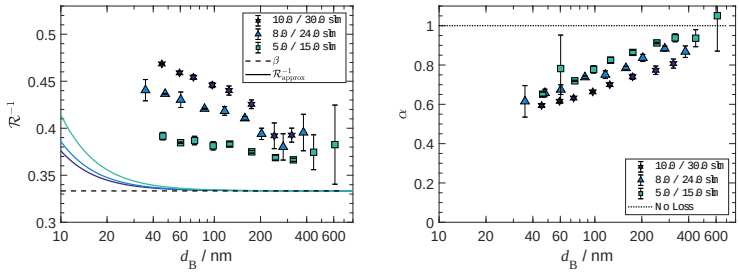

Figure B.9: Transfer function of the Long MF-DMA for a flow ratio $\beta = 0.33$ and an optimized aerosol inlet gap of 2 mm.

5. CONCLUSION

A new DMA has been designed for high-density particles in the size range from 15 to 600 nm with a flow ratio of 1.5/15 slm. The MF-DMA was developed, manufactured and optimized by comparing experimental measurements and CFD simulations. The transfer function was experimentally determined with aerosol to sheath gas ratio of 1/10, 1/5 and 1/3 and aerosol flow rates up to 10 slm. A new software tool has been introduced to calculate the transfer function directly from SMPS raw data. A significant broadening of the transfer function was observed while increasing the aerosol flow rate over 5 slm. An improvement of the transfer function, especially for higher aerosol flow rates, was achieved by the modification of the aerosol inlet and adjustment of the inlet slit which have led to a more homogeneous flow field in the classification zone. The MF-DMA is suitable for submicron particle diameters with high density, such as pure metal nanoparticles, in an aerosol flow rate up to 5 slm. This

results in a new variety of applications such as the combination of online instruments for particle structure analysis, production processes on a pilot scale, calibration of particle mass analyzers. The CFD simulations are in good agreement with the experiments so that they can be used for further investigations or for the design of different DMAs. Together with the implemented software tool, the transfer function can be easily and quickly determined and DMAs characterized without the need of two identical DMAs in a tandem setup. However, the transfer function of MF-DMA shows potential for further improvements in the area of the aerosol inlet and outlet, leading to a more homogeneous flow field, and the optimization of the design of the lower ceramic insulator for a longer operating time in production processes.

APPENDIX A

A SMPS (3938, TSI), classifier (3080), Long DMA (3081), condensation particle counter (3775) is used in Low-Flow mode with a scan time up to 300 s. Figure B.10 depicts the geometric standard deviation of a monodispersed aerosol ($d_{\mathrm{setp}} = 100\,\mathrm{nm}$) in dependency of the scan time in seconds. The scan time is increased stepwise and is limited to 300 s. Faster scan times than 180 s show a clearly increased geometric standard deviation and precise calculation of the transfer function, especially the resolution of DMAs, are not possible.

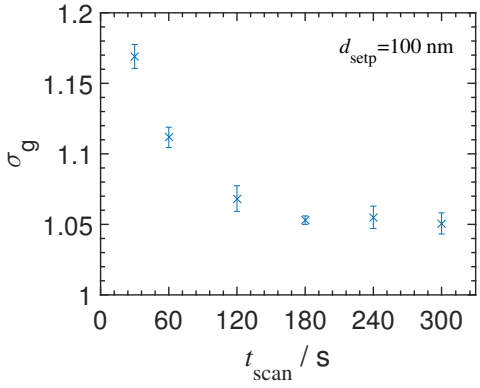

Figure B.10: Geometric standard deviation in dependency of the SMPS scan time with a flow ratio of 1 : 10.

APPENDIX B

Figure B.11 depicts the transfer function of the Long DMA (3081, TSI) which is characterized by the width $\mathcal{R}^{-1}$ and height α. The measured width of the transfer function is compared to the approximation $\mathcal{R}^{-1}_{approx}$ by Flagan (1999). The characteristics width $\mathcal{R}^{-1}$ and height α are fitted by exponential expressions to determine the transfer function of an unknown DMA in a tandem DMA setup. Particle losses occurring in the experimental setup are minimized by avoiding sharp bends and using short tube lengths. Thereby, using same tube dimensions to SMPS 1, Long DMA and SMPS 2 the particle losses are almost identical and can be neglected.

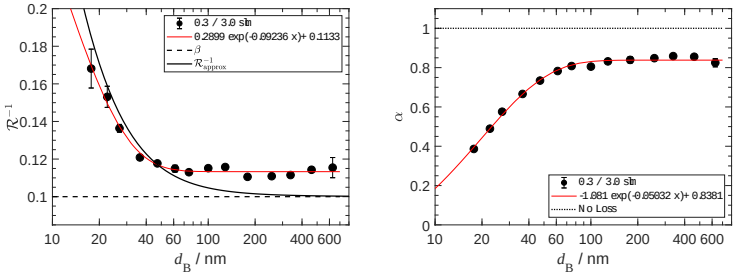

Figure B.11: Transfer function of the Long DMA (3081) for a theoretical $\beta = 0.1$.

FUNDING

The authors acknowledge the support by the European Union Seventh Framework Program (FP7/2007-2013) under Grant Agreement n°280765 (BUONAPART-E) and the Deutsche Forschungsgemeinschaft (DFG) in the scope of the research group 2284 "Model-based scalable gas-phase synthesis of complex nanoparticles" (KR 1723/16).

REFERENCES

Babick, F. et al. (2018). "Multiparameter Characterization of Aerosols." In: *Chemie Ingenieur Technik* 90.7, pp. 923–936. ISSN: 0009286X. DOI: 10.1002/cite.201700094.

Byeon, J. H. and Roberts, J. T. (2012). "Aerosol-based fabrication of biocompatible organic-inorganic nanocomposites." In: *ACS applied materials & interfaces* 4.5, pp. 2693–2698. DOI: 10.1021/am300337c.

Collins, D. R., Cocker, D. R., Flagan, R. C., and Seinfeld, J. H. (2004). "The Scanning DMA Transfer Function." In: *Aerosol Science and Technology* 38.8, pp. 833–850. ISSN: 0278-6826. DOI: 10.1080/027868290503082.

Flagan, R. C. (1999). "On Differential Mobility Analyzer Resolution." In: *Aerosol Science and Technology* 30.6, pp. 556–570. ISSN: 0278-6826. DOI: 10.1080/027868299304417.

Fuchs, N. A. (1964). "The mechanics of aerosols." In: *Quarterly Journal of the Royal Meteorological Society* 91.388, p. 249. ISSN: 00359009. DOI: 10.1002/qj.49709138822.

Gunn, R. and Woessner, R. H. (1956). "Measurements of the systematic electrification of aerosols." In: *Journal of Colloid Science* 11.3, pp. 254–259. ISSN: 00958522. DOI: 10.1016/0095-8522(56)90050-2.

Hermann, M., Wehner, B., Bischof, O., Han, H.-S., Krinke, T., Liu, W., Zerrath, A., and Wiedensohler, A. (2007). "Particle counting efficiencies of new TSI condensation particle counters." In: *Journal of Aerosol Science* 38.6, pp. 674–682. ISSN: 00218502. DOI: 10.1016/j.jaerosci.2007.05.001.

Heurlin, M., Magnusson, M. H., Lindgren, D., Ek, M., Wallenberg, L. R., Deppert, K., and Samuelson, L. (2012). "Continuous gas-phase synthesis of nanowires with tunable properties." In: *Nature* 492.7427, pp. 90–94. DOI: 10.1038/nature11652.

Hewitt, G. W. (1957). "The charging of small particles for electrostatic precipitation." In: *Transactions of the American Institute of Electrical Engineers, Part I: Communication and Electronics* 76.3, pp. 300–306. ISSN: 0097-2452. DOI: 10.1109/TCE.1957.6372672.

Hontañón, E. and Kruis, F. E. (2009). "A Differential Mobility Analyzer (DMA) for Size Selection of Nanoparticles at High Flow Rates." In: *Aerosol Science and Technology* 43.1, pp. 25–37. ISSN: 0278-6826. DOI: 10.1080/02786820802446812.

Kim, J. H., Mulholland, G. W., Kukuck, S. R., and Pui, D. Y. H. (2005). "Slip Correction Measurements of Certified PSL Nanoparticles Using a

Nanometer Differential Mobility Analyzer (Nano-DMA) for Knudsen Number From 0.5 to 83." In: *Journal of Research of the National Institute of Standards and Technology* 110.1, pp. 31–54. ISSN: 1044-677X. DOI: 10.6028/jres.110.005.

Knutson, E. O. and Whitby, Kenneth T. (1975). "Aerosol classification by electric mobility: apparatus, theory, and applications." In: *Journal of Aerosol Science* 6.6, pp. 443–451. ISSN: 00218502. DOI: 10.1016/0021-8502(75)90060-9.

Kruis, F. E., Fissan, H., and Peled, A. (1998). "Synthesis of nanoparticles in the gas phase for electronic, optical and magnetic applications—a review." In: *Journal of Aerosol Science* 29.5, pp. 511–535. ISSN: 00218502. DOI: 10.1016/S0021-8502(97)10032-5.

Lagarias, J. C., Reeds, J. A., Wright, M. H., and Wright, P. E. (1998). "Convergence Properties of the Nelder–Mead Simplex Method in Low Dimensions." In: *SIAM Journal on Optimization* 9.1, pp. 112–147. ISSN: 1052-6234. DOI: 10.1137/S1052623496303470.

Li, A. and Ahmadi, G. (1992). "Dispersion and Deposition of Spherical Particles from Point Sources in a Turbulent Channel Flow." In: *Aerosol Science and Technology* 16.4, pp. 209–226. ISSN: 0278-6826. DOI: 10.1080/02786829208959550.

Li, W., Li, L., and Chen, D.-R. (2006). "Technical Note: A New Deconvolution Scheme for the Retrieval of True DMA Transfer Function from Tandem DMA Data." In: *Aerosol Science and Technology* 40.12, pp. 1052–1057. ISSN: 0278-6826. DOI: 10.1080/02786820600944331.

Rosser, S. and Fernández de la Mora, J. (2005). "Vienna-Type DMA of High Resolution and High Flow Rate." In: *Aerosol Science and Technology* 39.12, pp. 1191–1200. ISSN: 0278-6826. DOI: 10.1080/02786820500444820.

Steiner, G., Attoui, M., Wimmer, D., and Reischl, G. P. (2010). "A Medium Flow, High-Resolution Vienna DMA Running in Recirculating Mode." In: *Aerosol Science and Technology* 44.4, pp. 308–315. ISSN: 0278-6826. DOI: 10.1080/02786821003636763.

Stolzenburg, M. R. (1988). "An Ultrafine Aerosol Size Distribution Measuring System." Ph.D. Thesis. Minneapolis, MN, USA: University of Minnesota.

Stratmann, F., Kauffeldt, T., Hummes, D., and Fissan, H. (1997). "Differential Electrical Mobility Analysis: A Theoretical Study." In: *Aerosol Science and Technology* 26.4, pp. 368–383. ISSN: 0278-6826. DOI: 10.1080/02786829708965437.

Uin, J., Tamm, E., and Mirme, A. (2009). "Electrically Produced Standard Aerosols in a Wide Size Range." In: *Aerosol Science and Technology* 43.8, pp. 847–853. ISSN: 0278-6826. DOI: 10.1080/02786820902980348.

Wiedensohler, A. (1988). "An approximation of the bipolar charge distribution for particles in the submicron size range." In: *Journal of Aerosol Science* 19.3, pp. 387–389. ISSN: 00218502. DOI: 10.1016/0021-8502(88)90278-9.

Wiedensohler, A. and Fissan, H. J. (1991). "Bipolar charge distributions of aerosol particles in high-purity argon and nitrogen." In: *Aerosol Science and Technology* 14.3, pp. 358–364. ISSN: 0278-6826. DOI: 10.1080/02786829108959498.

Yang, H., Dhaniyala, S., and He, M. (2018). "Performance of bipolar diffusion chargers: Experiments with particles in the size range of 100 to 900 nm." In: *Aerosol Science and Technology* 52.2, pp. 182–191. ISSN: 0278-6826. DOI: 10.1080/02786826.2017.1387641.

C

EJECTOR-BASED NANOPARTICLE SAMPLING FROM PRESSURES DOWN TO 20 MBAR

Thore Rosenberger, Julian Neises, Dennis Kiesler, Frank Einar Kruis
Institute of Technology for Nanostructures (NST) and Center for Nanointegration Duisburg-Essen (CENIDE), University Duisburg-Essen, Duisburg, D-47057, Germany

Published in Aerosol Science and Technology, Volume 144, Page 105531 (2020)
DOI: 10.1016/j.jaerosci.2020.105531

ABSTRACT

The application of standard online instrumentation, such as scanning mobility particle sizer (SMPS), centrifugal particle mass analyzer (CPMA) or aerosol particle mass analyzer (APM), and electrical low-pressure impactor (ELPI)+ to low-pressure processes is only possible with extensive modification of the devices and extensive calibrations. A low-pressure ejector is a suitable device to transfer aerosol nanoparticles from low-pressure regions to atmospheric pressure and allows the direct use of standard online instrumentation. In this work, a commercial low-pressure ejector is investigated in the pressure range from 20 to 180 mbar with fully-sintered and size-selected nanoparticles (15 to 80 nm) in order to extend the application range of online instruments to low-pressure processes and open up a new variety of analysis methods. Results are compared to our previous work which was limited to pressures above 120 mbar. A change in particle size during the measurements for fully-sintered silver particles was not observed. A particle dilution factor between 60 to 6500 was found. High particle losses in the ejector for large particle sizes are compensated by a lower gas dilution factor.

1. INTRODUCTION

The online measurement methods allow the characterization of aerosol particles in nearly real-time. This is especially valuable if a prompt detection of particle size/mass distribution or its change is needed. Thereby re-

actors for the synthesis of aerosol nanoparticles can be easily optimized or controlled. Most aerosol reactors for the synthesis of tailor-made aerosol nanoparticle, such as microwave plasma (Kunze et al., 2019; Münzer et al., 2017), flame reactor (Ifeacho et al., 2007) or synthesis by laser ablation (Kim, Osone, et al., 2017), are operating in the low-pressure range since the process pressure is one of the main factors for particle size distribution and production rate (Granqvist and Buhrman, 1976). Reducing the process pressure in an aerosol reactor leads to a higher gas velocity at constant gas mass flow rates and therefore to a shorter residence time of the particles. Mangolini, Thimsen, and Kortshagen (2005) showed that the size of silicon nanocrystals synthesized in a low-pressure plasma operated at $\sim$ 1.7 mbar can be tuned by the partial pressure of SiH_4, but mainly by the residence time in the reactor. If the operating pressure differs from atmospheric pressure, standard instrumentation such as scanning mobility particle sizer (SMPS), electrical low-pressure impactor (ELPI)+, and centrifugal particle mass analyzer (CPMA) or aerosol particle mass analyzer (APM) cannot be operated anymore or have to be calibrated for this specific pressure range (Seifert et al., 2004). The existing online methods for particle measurement at low pressure, such as laser-induced incandescence (LII), time of flight (TOF) and particle mass spectrometer (PMS) or particle beam mass spectrometer (PBMS) (Jayne et al., 2000; Kim, Kim, et al., 2018; Schulz et al., 2006; Ziemann et al., 1995), are often not commercially available or need substantial amount of information about the particle properties. Due to the high demand, Nanda and Kruis (2014) and Seto et al. (1997) developed low-pressure differential mobility analyzer (LP-DMA) and detected nanosized particle fractions via Faraday cup with electrometer (FCE). Chen, Seto, et al. (2019) and Seol et al. (2000) determined the transfer function of LP-DMAs and demonstrated the application down to $\sim$ 80 mbar and $\sim$ 8.67 mbar respectively by measuring the particle size/collision cross-section distribution. These studies have shown that the particle classification according to their electrical mobility under low pressure is challenging due to a shortened residence time, reduced breakdown voltage and diffusional broadening. The operation of the aerosol particle mass analyzer (APM) (Ehara, Hagwood, and Coakley, 1996) down to 650 mbar was studied by Hsiao et al., 2018 where it was found that a reduction of the pressure leads to the lowering of the detection limits or requires the improvement of the resolution. Furthermore, these instruments are rather unsuitable for low-pressure adaptation due to their intricate construction for providing very high speeds.

These problems can be solved by using online instrumentation at low-pressure aerosol reactors and to sample and to transfer the aerosol back to ambient pressure. Thereby, the online instrumentation is operating

under atmospheric pressure and time-consuming calibrations are not needed. Some of these methods do not provide continuous sampling of the particles, e.g. the low-pressure sampling device (LPSD) introduced by Ober et al. (2002), so time-resolved measurements are not possible. Holm and Roberts (2007) and Wang et al. (2005) demonstrated the in-situ characterization of nanoparticles by transferring the particles from low-pressure < 27 mbar to ambient pressure. Although they collected particles from a low-pressure reactor and showed that the application of standard online instrumentation for real-time measurements is possible, they did not study the transfer behavior of the ejector. In our previous work (Rosenberger et al., 2018) we investigated a commercial ejector (VIP-4, Landenfeld, Kassel, Germany) to establish a standard sampling procedure from low-pressure to ambient pressure for continuous real-time measurements with online methods. This low-cost ejector can be easily connected to the reactor via standard vacuum components and only needs a driver gas at high pressure (< 5 bar) to operate. Unfortunately, the low-pressure ejectors are merely applicable in a specific pressure range due to the Venturi working principle so that the minimum reachable pressure of the VIP-4 ejector (100 mbar) is only suitable for sampling in the pressure range of 120 to 170 mbar (Rosenberger et al., 2018).

In this work, a new commercial low-pressure ejector (VHP-5, Landenfeld, Kassel, Germany) is investigated in the pressure range 20 to 180 mbar and size range from 10 to 80 nm using fully-sintered and size-selected silver particles. The experimental setup is modified to yield higher particle concentrations in order to reduce the signal-to-noise ratio of the particle counters. Particle losses are determined by measuring the particle concentration in the low-pressure region via an electrometer. The particle counting is corrected by considering multiple charge correction and diffusion losses. The particle size distribution up- and downstream of the ejector is measured with a SMPS to detect changes in the particle size. Gas dilution factor (GDF) and particle dilution factor (PDF) are calculated and compared to our previous work.

2. EXPERIMENTAL

The experimental setup described in our previous paper (Rosenberger et al., 2018) is used with minor modifications to provide a higher incoming particle concentration (Figure C.1). A high particle concentration before the transition to the low-pressure region is necessary to compensate particle losses and particle dilutions in the ejector. The N_2 flow rate of 2 slm through the evaporation furnace is adjusted by a first mass flow controller (MFC) (20 slm, Bronkhorst High-Tech B.V., Ruurlo, NL).

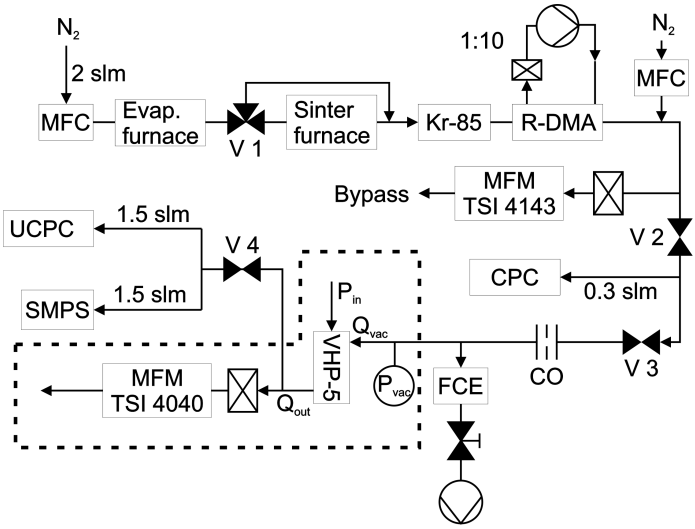

Figure C.1: Experimental setup for measuring the particle dilution factor (PDF) of the VHP-5 ejector, the part within the dashed lines are used to determine the gas dilution factor (GDF)), described in §2.2.

The temperature of the evaporation tube furnace (RoR 1.8/18.5, W.C. Heraeus GmbH, Hanau, Germany) is set to 1350 °C and is used to evaporate silver nuggets. The nuggets are filled into a ceramic boat and placed in the center of the heated zone. The coagulation vessel is removed and a 3-way valve (V 1) assembled instead so that the sintering furnace (650 °C) downstream can be bypassed. The bypass is used to measure the unsintered polydisperse aerosol and to adjust the evaporation furnace. Before the sintered particles are classified according to their electrical mobility, a defined equilibrium charge distribution is established by a custom-built Kr-85 beta charger with an initial activity of 370 MBq. A custom-built radial differential mobility analyzer (R-DMA) developed by Müschenborn (2007) for industrial gas-phase synthesis replaces the previously used L-DMA to classify particle in a higher sample flow rate with a longer runtime. The dimensions of this R-DMA are $d_o = 132$ mm, $d_i = 6$ mm and $b = 15$ mm. The sheath gas through the R-DMA is provided by a gas recirculation system, containing a blower, mass flow meter (MFM) and HEPA-filter. An additional MFC after the R-DMA is used to provide a higher aerosol flow rate up to 6 slm. The dilution of the aerosol at this point does not influence the particle synthesis or size selection in the R-DMA. A bypass downstream of a HEPA-filter and

MFM ensures atmospheric pressure, even when valve V 2 is closed to decouple the particle synthesis from the measurement instrumentation. The particle concentration of the monodisperse fraction downstream of the R-DMA is measured by a condensation particle counter (CPC) (3775, TSI, MN, USA) instead of the previously used UCPC1 (3025A, TSI). Thus the counting limit of the measurable particle concentration is increased from 10^5 to 10^7 #/cm^3. Two different critical orifices (COs) are used to separate the ambient and low-pressure region and to limit the mass flow rate into the low-pressure area. The COs consist of a 0.4 mm (1.38 slm) or a 0.8 mm (5.46 slm) copper single-hole TEM grids (Plano GmbH, Wetzlar, Germany) with a thickness of 100 µm. The single-hole TEM grids are assembled in a holder, a custom-built DN 16 KF centering ring with a diverging angle of 45° downstream. The design of the holder and the small thickness of the single-hole TEM grids reduce particle losses and charge reversal in the nozzle (Hwang et al., 2015). The pressure in the low-pressure region p_{vac} is measured with a vacuum gauge (TTR 101, Leybold, Cologne, Germany) and adjusted via a needle valve with a vacuum pump (MD 8C, vacuubrand, Wertheim, Germany) downstream of the Faraday cup with electrometer (FCE). Thus, the vacuum p_{vac} is independent from the pressure created by the low-pressure ejector. The maximal suction flow rate into the FCE is limited by a pressure drop over a small opening (4 mm) to the vacuum pump. Therefore, the pressure range 20 to 70 mbar (0.4 mm) and 100 to 180 mbar (0.8 mm) can only be covered by reducing the mass flow rate into the low-pressure region by two different COs.

A sample flow rate Q_{vac} of the aerosol is sucked in by the ejector and brought back to ambient pressure by the low-pressure ejector (VHP-5). A pressure regulator is connected to the high-pressure inlet of the VHP-5 (§2.1) allowing to set and measure the inlet pressure p_{in}. At ambient pressure downstream of the ejector, the aerosol outflow rate Q_{out}, the sum of Q_{in} and Q_{vac}, is measured with mass flow meter (Model 4040, TSI). The particle size distribution and number concentration are measured with an SMPS and a UCPC, respectively. Valves V 3 and V 4 are closed between the measurements to examine the aerosol outflow rate Q_{out} at the lowest pressure $p_{vac}(Q_{out} = 0)$ to ensure the correct operation of the ejector.

The part within the dashed lines (C.1) is detached from the setup and used to determine the (gas dilution factor (GDF)), shown in section §2.2. A needle valve is assembled to the low-pressure inlet of the ejector to adjust the sample flow rate Q_{vac} sucked in by the ejector. The sample flow rate Q_{vac} is measured by a mass flow meter (Model 4143, TSI).

2.1. Comparison of VIP-4 and VHP-5 ejectors

A low-pressure ejector is a low-cost vacuum generator based on the Venturi principle. The compressed gas flows through a narrowing Venturi nozzle and is accelerated in a diffuser up to several times of the speed of sound. The expansion of the compressed gas in a diffuser downstream of the nozzle creates a locally low-pressure area. A small opening in this area, between nozzle and diffuser, is needed to use the suction effect. In contrast to single-stage ejectors, the multi-stage ejectors used here consist of additional Venturi nozzles behind the diffuser of the first Venturi nozzle. The gas exiting the diffuser, a mixture of sucked-in gas and compressed gas from the nozzle, is thus used as the driving gas for the following stages. Each of these nozzle stages has a larger nozzle diameter in relation to the falling gas pressure difference. This configuration achieves a higher suction flow and thus a lower final pressure (Ryans and Roper, 1986). After exiting the last Venturi nozzle, the exhaust gas is slowed down to reach atmospheric pressure.

Figure C.2 depicts a schematic drawing of the inside of the VIP-4 and VHP-5 ejectors. Both multi-stage ejectors are housed in an anodized aluminum box (67x182 mm) with lid and rubber seal. The box consists of five chambers, a high-pressure stage and four stages each with a brass Venturi nozzle (indication 1-4). Stage 1-3 are separated by two elastic flaps which are closed when the downstream pressure is significantly lower. The main Venturi nozzles are glued straight aligned into the housing slightly left of center between the stages. In contrast to the VIP-4 ejector, the VHP-5 ejector applies a different nozzle design and a Venturi nozzle located parallel to the main nozzles, slightly right of center between stage 1-2. Thereby, two nozzles are supplied by the high-pressure simultaneously and the first nozzle ejects the gas into stage 2 at 172 mbar, reaches higher Mach numbers and reduces the pressure down to 12 mbar in stage 1. The pressure is stepwise increased from the lowest pressure in stage 1 to ambient conditions in stage 4.

The low-pressure inlet and aerosol outlet in stages 1 and 4, respectively, centered at the backplate are equipped with DN 16 KF screw fittings and are used to transfer the particles from a low-pressure region through the Venturi nozzles to atmospheric pressure. The standard vacuum connection allows the use of the low-pressure ejector with all common vacuum components. The high-pressure p_{in} to the first chamber is supplied via a quick coupling screw fitting.

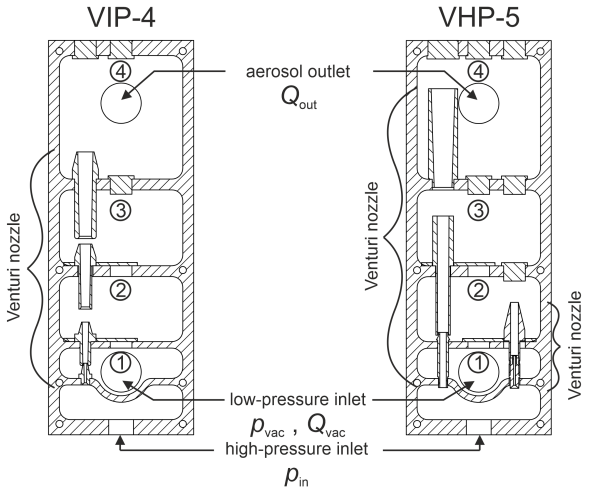

Figure C.2: Schematic drawing of the commercial vacuum ejectors VIP-4 and VHP-5.

2.2. *Gas dilution factor*

In a first experiment, the ejector is examined in a particle-free environment to determine the optimized operation condition. The used setup is shown in Figure A.1 within the dashed lines, or more detailed in our previous work (Fig.1 in Rosenberger et al., 2018). The high-pressure inlet, forming the driving gas flow with high velocity through the Venturi nozzles, is varied in the range of 1 to 6 bar (nitrogen). This accelerated gas causes a locally decreased pressure entraining a side gas, here mentioned as sample flow rate Q_{vac}. The low-pressure inlet is closed ($Q_{vac} = 0$ slm) and the pressure in stage 1 is measured dependent on the inlet pressure. Almost similar behavior is observed for both ejectors. The pressure in stage 1 decreases exponentially to a minimum pressure. A further increase of the inlet pressure leads to a small linear increase of the pressure p_{vac}. In comparison, the VIP-4 ejector reaches a minimum pressure of $p_{in} = 107$ mbar in stage 1 by applying an inlet pressure of 3.5 bar. The achieved minimum pressure of the VHP-5 ejector, resulting from an inlet pressure of 4.5 bar, is significantly lower (12 mbar) compared to the VIP-4 ejector.

In further experiments, the inlet pressure of the VHP-5 is kept constant at 4.5 bar. A needle valve is connected to the aerosol inlet and is used to control the suction flow rate Q_{vac} into the ejector. The sample flow

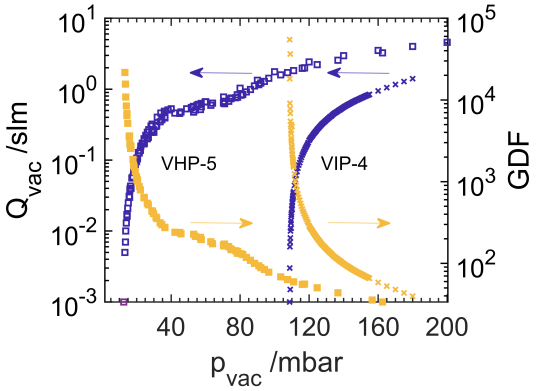

Figure C.3: Sample flow rate Q_{vac} and the GDF (Q_{out}/Q_{vac}) as a function of p_{vac} of the VIP-4 and VHP-5 ejector.

rate Q_{vac}, the aerosol outflow rate Q_{out} and the pressure p_{vac} in stage 1 are measured. Figure C.3 shows the sample flow rate (Q_{vac}) and the gas dilution factor (GDF) as a function of the pressure (p_{vac}) for the VIP-4 and VHP-5 ejector. The GDF is defined as the ratio of aerosol outflow rate Q_{out} and the sample flow rate Q_{vac}. Both ejectors show a slight increase of the pressure p_{vac}, caused by an increase of the sample flow rate (Q_{vac}). An almost linear increase of the pressure is observed by a further increase of the sample flow rate, getting closer to $Q_{vac,max}$ of approx. 7 slm for the VHP-5. The GDF determines the dilution of the sample flow rate by the driving gas and is inverse proportional to the sample flow rate. A GDF of 10^3 to 10^2 is obtained in the range $25 < p_{vac} > 100$ mbar. At higher pressures of p_{vac} the dilution factor decreases below 10^2, while lower pressures lead to a strong increase above 10^3 due to the reduction of the sample flow rate.

The curve of the sample flow of the VHP-5 is less smooth than the VIP-4 curve in the depicted pressure range, showing a change of slope at a pressure of approx. 45 and 75 mbar. This results from a low-pressure gradient between stages 1 and 2, respectively stages 3 and 4, causing the elastic flaps to open. The elastic flaps separate the different stages by covering a small opening (§2.1). Thereby, a small gas flow rate can flow through this small opening into the adjacent stage, resulting in instability in the pressure, because the Venturi nozzles are operated outside the designated pressure condition. This is also observed for the VIP-4 ejector at pressures above 180 mbar. In comparison to the VIP-4, the VHP-5

shows better performance, a higher vacuum level, and higher sample flow rates for a specific pressure p_{vac}, therefore a notably lower GDF.

3. RESULTS

The experimental assessment of the low-pressure ejector is performed with fully-sintered and size-selected silver aerosol nanoparticles, using the setup depicted in Figure C.1. As mentioned, the application of the VIP-4 is limited to a pressure of 107 mbar and the VHP-5 ejector to 12 mbar. Sampling from a low-pressure process is possible if the pressure generated locally inside the ejector is lower than the pressure of the system at the sampling inlet. Thus, the VHP-5 is tested in the pressure range from 20 to 180 mbar. Total particle losses in the experimental setup are determined by the comparison of particle number concentration measured by the CPC upstream of the orifice and the UCPC downstream of the ejector at atmospheric pressure. The deposition efficiency of the critical orifices, the particle losses and the PDF in the ejector are measured and calculated via particle concentration measurement by means of a FCE in the low-pressure region. As the FCE measures the particle concentration by means of the charge number concentration, a charge correction model by Wiedensohler and Fissan (1991) was used to take multiply charged particles into account. Particle losses by diffusion are estimated by the penetration P dependent on the dimensionless deposition parameter μ with an accuracy of 1 % (Hinds, 1999).

First, the particle losses in the two different critical orifices ($D_0 =$ 0.4 and 0.8 mm) are determined size and pressure-dependent by the ratio of CPC upstream and FCE downstream of the critical orifice as function of particle size and diameter. Particle losses in the critical orifice have to be known in order to calculate the particle losses in the ejector. Figure C.4a-c) depicts the particle losses in the critical orifices ($D_0 = 0.3,\ 0.4$ and 0.8 mm) as a function of the square root of a modified Stokes number $\sqrt{Stʹ}$ as introduced by Chen, Tsai, et al. (2007). In our previous paper, the particle losses were measured for a $D_0 = 0.3$ mm critical orifice in the size range from 10 to 100 nm (d_{mobil}), shown in Figure C.4a). $\sqrt{Stʹ}$ was defined by the Stokes number St_0 of the particles upstream of the orifice at atmospheric conditions and was compared to the literature (Chen, Tsai, et al., 2007; Pui, Ye, and Liu, 1988). The comparison allows the validation of the evaluation and the assessment of the particle losses. St_0 is calculated downstream of the orifice at low pressure using the equation for the mean free path λ_{mfp} by Jennings (1988) in Equation (C.1).

$$\lambda_{\mathrm{mfp}} = \sqrt{\frac{\pi}{8}} \cdot \frac{\eta}{u} \cdot \frac{1}{\sqrt{\rho_{\mathrm{gas}} \cdot p}} \tag{C.1}$$

Here pressure-corrected gas properties, dynamic viscosity $\eta = 18.5e-6\,\mathrm{Pa\,s}$, and the gas density $\rho_{\mathrm{gas}} = 1.204\,\mathrm{g/cm^3}$ given at standard conditions, and the numerical factor $u = 0.4987$, resulting from the calculation of the coefficient of viscosity by Pekeris and Alterman (1957) are used. In comparison to Fig. (8) in Rosenberger et al. (2018), this leads to a better agreement with the literature (Chen, Tsai, et al., 2007; Pui, Ye, and Liu, 1988). Increasing $\sqrt{St'}$ by increasing the particle size leads to higher particle losses. This is also found for the particle losses in the orifices with an opening of 0.8 mm measured in the size range from 10 to 60 nm and an opening of 0.4 mm in the size range from 15 to 80 nm. However, a minimum of 12 to 25 % is reached for a $\sqrt{St'}$ between 0.2 to 0.4 in dependency of the used opening and pressure downstream of the orifice, shown in Figure C.4b) and c). A high standard deviation is observed for the largest and smallest selected particle sizes, depicted as error bars in the figure. This results from a low signal-to-noise ratio by selecting particle sizes far from the modal value of the polydisperse size distribution. Measurements with an electrometer current $< 5\,\mathrm{pA}$ were not used for the evaluation. It can be seen that the pressure correction of the Stokes number leads to a right shift when reducing the pressure. For larger $\sqrt{St'}$, the particle losses increase due to impaction losses up to 80 % ($\sqrt{St'} = 0.64$) using the $D_0 = 0.4\,\mathrm{mm}$ and 25 to 30 % ($\sqrt{St'} = 0.428$) using the $D_0 = 0.8\,\mathrm{mm}$ orifice, respectively. Higher particle losses for small particle sizes ($d_{\mathrm{mobil}} < 25\,\mathrm{nm}$) occur at pressures $< 100\,\mathrm{mbar}$, which can be explained by the diffusional deposition of nanoparticles. This behavior is known from the measurement of impactor collection efficiencies (Liu et al., 2013; Tsai et al., 2012).

The particle losses in the VHP-5 ejector $\eta_{\mathrm{VHP-5}}(d_{\mathrm{p}}, p_{\mathrm{vac}})$ are calculated by the ratio of the entering and outflowing particle concentration $1 - N_{\mathrm{UCPC}}(d_{\mathrm{p}}) \cdot GDF(p_{\mathrm{vac}}) / N_{\mathrm{FCE}}(d_{\mathrm{p}}, p_{\mathrm{vac}})$. Figure C.5a) and b) depict the particle losses in the VHP-5 ejector dependent on the selected mobility diameter. It can be seen that the particle losses increase significantly with the mobility diameter from 50 % to approx. 90 % using the 0.4 mm orifice and the 0.8 mm orifice for pressure larger than 30 mbar. In addition, reducing pressure leads to higher losses. This can be explained by higher impaction losses in the low-pressure ejector caused by the increased stopping distance at lower pressures. Particle deposits are clearly visible on walls opposite the outflow of the Venturi nozzle in stage 2 and on sharp curves. However, the two lowest pressures (30 and 20 mbar) show

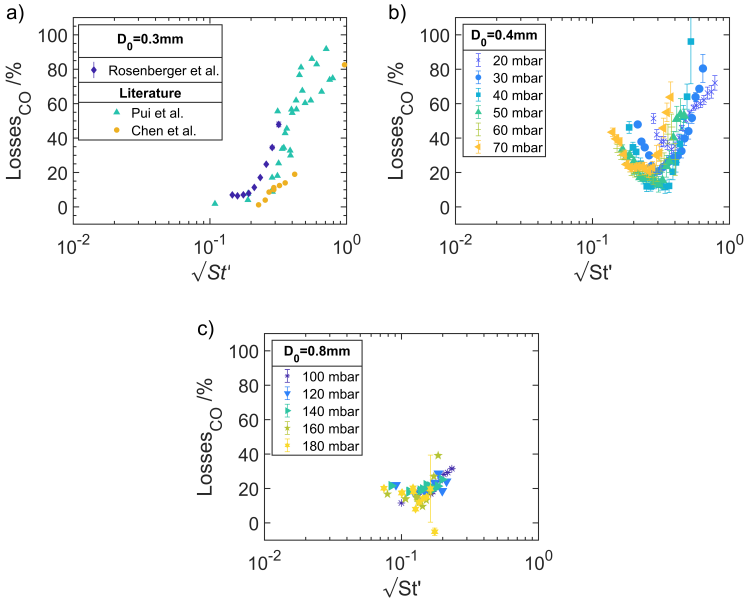

Figure C.4: Particle losses in the critical orifices (CO) used for the characterization of the low-pressure ejectors. a) $D_0 = 0.3$ mm used in the VIP-4 setup compared to Chen, Tsai, et al. (2007) and Pui, Ye, and Liu (1988). b) $D_0 = 0.4$ mm and c) $D_0 = 0.8$ mm used in the VHP-5 setup dependent on different pressures downstream of the CO.

higher particle losses for smaller particles, but lower losses for larger particles. This might be attributed to the improved operation of the first Venturi nozzle in this pressure range (§2.2), leading to an optimized flow field.

The transfer characteristic of the ejector is introduced as the particle dilution factor (PDF). The PDF is a function of the pressure p_{vac} and the selected particle diameter d_p, Equation C.2.

$$PDF(d_p, p_{vac}) = \frac{N_{FCE}(d_p, p_{vac})}{N_{UCPC}(d_p)} = \frac{GDF(p_{vac})}{1 - \eta_{VHP-5}(d_p, p_{vac})} \tag{C.2}$$

The PDF is calculated by the quotient of the number concentrations measured upstream (N_{FCE}) and downstream (N_{UCPC}) of the low-pressure ejector. The PDF is required to correct the measured number size distribution downstream of the ejector (§4 in Rosenberger et al., 2018). Figure

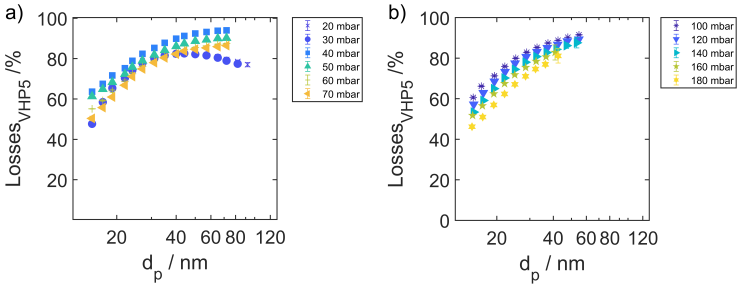

Figure C.5: Particle losses in the VHP-5 ejector, a) measured in the pressure range from 20 to 70 mbar using a 0.4 mm critical orifice and b) from 100 to 180 mbar using a 0.8 mm critical orifice.

C.6 depicts the PDF of the VIP-4 a) and VHP-5 b) as a function of the selected mobility diameter by the DMA. The particle size distribution is measured with a SMPS upstream of the critical orifice and downstream of the ejector. Each diameter was measured three times, the standard deviation was calculated and the experimental data were approximated with a spline fit as guidance to the eye. A shift of the mode diameter before and after the ejector for fully-sintered particles is not observed.

In comparison, the PDF of the VIP-4 shows an almost constant behavior with a slight decrease to larger particle diameters (Fig. 10 in Rosenberger et al., 2018), whereas the PDF of the VHP-5 shows an opposite behavior. This results from higher particle impaction losses, caused by an increase of the mobility diameter. The deposition of particles on walls is visible in the ejector. Although both ejectors are based on the same working principle, the different design and arrangement of the Venturi nozzles (§2.1) lead to different particle losses $\eta(d_\mathrm{p}, p_\mathrm{vac})$. It can be seen that the particle losses in the ejector are decisive for the course of its PDF. Therefore, the VHP-5 shows a steady increase of the PDF with particle size is observed for a pressure range from 180 to 100 mbar, starting from 60 to 200 (180 mbar) or 300 to 1000 (100 mbar), respectively. An almost size-independent behavior of the PDF is observed at the lowest pressure, where the PDF is much higher, between 5000 and 6000.

Comparing the ejectors at the same pressure, it can be found that the PDF is in the same order of magnitude. Differences occur due to the higher particle losses for larger particles in the VHP-5 by impaction. Nevertheless, the VHP-5 covers a larger pressure range and shows better performance than the VIP-4 operated close to its minimum pressure. A high particle number concentration entering the ejector is needed to reach

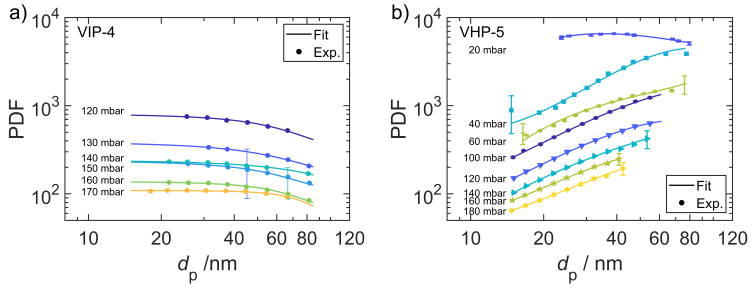

Figure C.6: particle dilution factor (PDF) as a function of the mobility diameter a) for the VIP-4 and b) for the VHP-5 ejector.

a sufficient measurement signal. Thereby, the VHP-5 ejector is suitable for low-pressure aerosol reactors with a high production rate due to the high dilution factor. The entering aerosol is directly quenched and an agglomeration of the sample is reduced.

4. CONCLUSION

The VHP-5 is a commercial low-pressure ejector that can be directly and easily used to transfer aerosol particles from aerosol reactors to atmospheric pressure. A particle dilution factor (PDF) characterizes the transfer behavior of the ejector and is required to correct the measured number size distribution. Ejector-based sampling is especially valuable when standard online instrumentation, like SMPS, APM/CPMA, etc. to applied for the analysis of low-pressure processes. The sampled aerosol is directly quenched due to the Venturi effect, reducing the agglomeration of the sample. Therefore, the PDF is high, especially at low pressures, so that a sufficiently high particle concentration is required. Impaction losses in the ejector require more extensive investigation for the detection of larger particles ($d_{\mathrm{mobil}} > 100\,\mathrm{nm}$). The VHP-5 ejector has been investigated for its suitability to transfer aerosol particles from low-pressure to atmospheric pressure. The measurements have been done with size-selected and fully-sintered silver nanoparticles in the size range from 15 to 80 nm. The gas dilution factor, particle losses in the ejector and particle dilution factor are determined in the pressure range from 20 to 180 mbar. The particle dilution factor lies in the range 60 to 6500. Changes in the size of the particles leaving the ejector were not observed. Results were

compared to our previous work with an ejector suitable for the pressure range 120 to 170 mbar.

ACKNOWLEDGMENTS

The authors acknowledge the support by the Deutsche Forschungsgemeinschaft (DFG) in the scope of the research group 2284 "Model-based scalable gas-phase synthesis of complex nanoparticles" (project number: 262219004, within KR 1723/16).

Chen, S.-C., Tsai, C.-J., Wu, C.-H., Pui, D. Y. H., Onischuk, A. A., and Karasev, V. V. (2007). "Particle loss in a critical orifice." In: *Journal of Aerosol Science* 38.9, pp. 935–949. ISSN: 00218502. DOI: 10.1016/j.jaerosci.2007.06.010.

Chen, X., Seto, T., Kortshagen, U. R., and Hogan, C. J. (2019). "Determination of nanoparticle collision cross section distribution functions in low pressure plasma synthesis reactors via ion mobility spectrometry." In: *Nano Futures* 3.1, p. 015002. ISSN: 2399-1984. DOI: 10.1088/2399-1984/aaff97.

Ehara, K., Hagwood, C., and Coakley, K. J. (1996). "Novel method to classify aerosol particles according to their mass-to-charge ratio—Aerosol particle mass analyser." In: *Journal of Aerosol Science* 27.2, pp. 217–234. ISSN: 00218502. DOI: 10.1016/0021-8502(95)00562-5.

Granqvist, C. G. and Buhrman, R. A. (1976). "Ultrafine metal particles." In: *Journal of Applied Physics* 47.5, pp. 2200–2219. ISSN: 0021-8979. DOI: 10.1063/1.322870.

Hinds, W. C. (1999). *Aerosol technology: Properties, behavior, and measurement of airborne particles*. 2. ed. A Wiley-Interscience publication. New York: Wiley. ISBN: 9780471194101.

Holm, J. and Roberts, J. T. (2007). "Surface chemistry of aerosolized silicon nanoparticles: evolution and desorption of hydrogen from 6-nm diameter particles." In: *Journal of the American Chemical Society* 129.9, pp. 2496–2503. ISSN: 0002-7863. DOI: 10.1021/ja0658970.

Hsiao, T.-C., Young, L.-H., Tai, Y.-C., and Chang, P.-K. (2018). "Effects of temperature, pressure, and carrier gases on the performance of an aerosol particle mass analyser." In: *Atmospheric Measurement Techniques* 11.8, pp. 4617–4626. DOI: 10.5194/amt-11-4617-2018.

Hwang, T.-H., Kim, S.-H., Kim, S. H., and Lee, D. (2015). "Reducing particle loss in a critical orifice and an aerodynamic lens for focusing aerosol particles in a wide size range of 30 nm — 10 μm." In: *Journal of Mechanical Science and Technology* 29.1, pp. 317–323. ISSN: 1738-494X. DOI: 10.1007/s12206-014-1238-4.

Ifeacho, P., Hülser, T., Wiggers, H., Schulz, C., and Roth, P. (2007). "Synthesis of SnO_{2-x} nanoparticles tuned between $0 \leqslant x \leqslant 1$ in a premixed low pressure H_2/O_2/Ar flame." In: *Proceedings of the Combustion Institute* 31.2, pp. 1805–1812. ISSN: 15407489. DOI: 10.1016/j.proci.2006.07.083.

Jayne, J. T., Leard, D. C., Zhang, X., Davidovits, P., Smith, K. A., Kolb, C. E., and Worsnop, D. R. (2000). "Development of an Aerosol Mass Spectrometer for Size and Composition Analysis of Submicron Particles." In: *Aerosol Science and Technology* 33.1-2, pp. 49–70. ISSN: 0278-6826. DOI: 10.1080/027868200410840.

Jennings, S.G (1988). "The mean free path in air." In: *Journal of Aerosol Science* 19.2, pp. 159–166. ISSN: 00218502. DOI: 10.1016/0021-8502(88)90219-4.

Kim, D., Kim, T. W., Park, S. H., Lim, S. K., Lee, H.-C., Kim, T., and Kang, S.-W. (2018). "Characterization of particle generated during plasma-enhanced chemical vapor deposition on amorphous carbon layer using particle beam mass spectrometer." In: *Journal of Vacuum Science & Technology A: Vacuum, Surfaces, and Films* 36.2, p. 021506. ISSN: 0734-2101. DOI: 10.1116/1.5000087.

Kim, M., Osone, S., Kim, T., Higashi, H., and Seto, T. (2017). "Synthesis of Nanoparticles by Laser Ablation: A Review." In: *KONA Powder and Particle Journal* 34.0, pp. 80–90. ISSN: 0288-4534. DOI: 10.14356/kona.2017009.

Kunze, F., Kuns, S., Spree, M., Hülser, T., Schulz, C., Wiggers, H., and Schnurre, S. M. (2019). "Synthesis of silicon nanoparticles in a pilot-plant-scale microwave plasma reactor: Impact of flow rates and precursor concentration on the nanoparticle size and aggregation." In: *Powder Technology* 342, pp. 880–886. ISSN: 0032-5910. DOI: 10.1016/j.powtec.2018.10.042.

Liu, C.-N., Awasthi, A., Hung, Y.-H., and Tsai, C.-J. (2013). "Collection efficiency and interstage loss of nanoparticles in micro-orifice-based cascade impactors." In: *Atmospheric Environment* 69, pp. 325–333. ISSN: 13522310. DOI: 10.1016/j.atmosenv.2012.12.003.

Mangolini, L., Thimsen, E., and Kortshagen, U. (2005). "High-yield plasma synthesis of luminescent silicon nanocrystals." In: *Nano letters* 5.4, pp. 655–659. ISSN: 1530-6984. DOI: 10.1021/nl050066y.

Münzer, A., Sellmann, J., Fortugno, P., Kempf, A., Schulz, C., and Wiggers, H. (2017). "Inline coating of silicon nanoparticles in a plasma reactor: Reactor design, simulation and experiment." In: *Materials Today: Proceedings* 4, S118–S127. ISSN: 2214-7853. DOI: 10.1016/j.matpr.2017.09.176.

Müschenborn, P. M. (2007). "Development of a differential mobility particle sizer applied to industrial gas phase synthesis processes for nanoscaled powders." Ph.D. Thesis. Duisburg, Germany: University of Duisburg-Essen. URL: https://duepublico2.uni-due.de/receive/duepublico_mods_00015227.

Nanda, K. K. and Kruis, F. E. (2014). "A radial differential mobility analyzer for the size-classification of gas-phase synthesized nanoparticles

at low pressures." In: *Measurement Science and Technology* 25.7, p. 075605. ISSN: 1361-6501. DOI: 10.1088/0957-0233/25/7/075605.

Ober, F., Mayer, M., Büttner, H., and Ebert, F. (2002). "Aerosol Measurement in Low-Pressure Systems with Standard Scanning Mobility Particle Sizers." In: *Particle & Particle Systems Characterization* 19.4, pp. 229–239. ISSN: 09340866. DOI: 10.1002/1521-4117(200208)19:4<229::AID-PPSC229>3.0.CO;2-8.

Pekeris, C. L. and Alterman, Z. (1957). "Solution of the Boltzmann-Hilbert Integral Equation II. The coefficients of viscosity and heat conduction." In: *Proceedings of the National Academy of Sciences of the United States of America* 43.11, pp. 998–1007. ISSN: 0027-8424. DOI: 10.1073/pnas.43.11.998.

Pui, D. Y. H., Ye, Y., and Liu, B. Y. H., eds. (1988). *Sampling, transport, and deposition of particles in high purity gas supply system*. Los Angeles, CA, United States (USA). ISBN: 0-915414-37-6.

Rosenberger, T., Münzer, A., Kiesler, D., Wiggers, H., and Kruis, F. E. (2018). "Ejector-based sampling from low-pressure aerosol reactors." In: *Journal of Aerosol Science* 123, pp. 105–115. ISSN: 00218502. DOI: 10.1016/j.jaerosci.2018.06.003.

Ryans, J. L. and Roper, D. L. (1986). *Process vacuum system design and operation*. New York: McGraw-Hill. ISBN: 0070543550.

Schulz, C., Kock, B. F., Hofmann, M., Michelsen, H., Will, S., Bougie, B., Suntz, R., and Smallwood, G. (2006). "Laser-induced incandescence: recent trends and current questions." In: *Applied Physics B* 83.3, pp. 333–354. ISSN: 0946-2171. DOI: 10.1007/s00340-006-2260-8.

Seifert, M., Tiede, R., Schnaiter, M., Linke, C., Möhler, O., Schurath, U., and Ström, J. (2004). "Operation and performance of a differential mobility particle sizer and a TSI 3010 condensation particle counter at stratospheric temperatures and pressures." In: *Journal of Aerosol Science* 35.8, pp. 981–993. ISSN: 00218502. DOI: 10.1016/j.jaerosci.2004.03.002.

Seol, K. S., Tsutatani, Y., Camata, R. P., Yabumoto, J., Isomura, S., Okada, Y., Okuyama, K., and Takeuchi, K. (2000). "A differential mobility analyzer and a Faraday cup electrometer for operation at 200–930 Pa pressure." In: *Journal of Aerosol Science* 31.12, pp. 1389–1395. ISSN: 00218502. DOI: 10.1016/S0021-8502(00)00037-9.

Seto, T., Hirota, A., Fujimoto, T., Shimada, M., and Okuyama, K. (1997). "Sintering of Polydisperse Nanometer-Sized Agglomerates." In: *Aerosol Science and Technology* 27.3, pp. 422–438. ISSN: 0278-6826. DOI: 10.1080/02786829708965482.

Tsai, C.-J., Liu, C.-N., Hung, S.-M., Chen, S.-C., Uang, S.-N., Cheng, Y.-S., and Zhou, Y (2012). "Novel active personal nanoparticle sampler for the

exposure assessment of nanoparticles in workplaces." In: *Environmental science & technology* 46.8, pp. 4546–4552. DOI: 10.1021/es204580f.

Wang, X., Hafiz, J., Mukherjee, R., Renault, T., Heberlein, J., Girshick, S. L., and McMurry, P. H. (2005). "System for In Situ Characterization of Nanoparticles Synthesized in a Thermal Plasma Process." In: *Plasma Chemistry and Plasma Processing* 25.5, pp. 439–453. ISSN: 1572-8986. DOI: 10.1007/s11090-005-4991-4.

Wiedensohler, A. and Fissan, H. J. (1991). "Bipolar charge distributions of aerosol particles in high-purity argon and nitrogen." In: *Aerosol Science and Technology* 14.3, pp. 358–364. ISSN: 0278-6826. DOI: 10.1080/02786829108959498.

Ziemann, P. J., Liu, P., Rao, N. P., Kittelson, D. B., and McMurry, P. H. (1995). "Particle beam mass spectrometry of submicron particles charged to saturation in an electron beam." In: *Journal of Aerosol Science* 26.5, pp. 745–756. ISSN: 00218502. DOI: 10.1016/0021-8502(95)00009-2.

D

A MODEL FLOW REACTOR DESIGN FOR THE STUDY OF NANOPARTICLE STRUCTURE FORMATION UNDER WELL-DEFINED CONDITIONS

Thore Rosenberger[1,2], Johannes Sellmann[2,3], Irenäus Wlokas[2,3] and Frank Einar Kruis[1,2]

[1]*Institute of Technology for Nanostructures (NST), University Duisburg-Essen, Duisburg, D-47057, Germany*

[2]*Center for Nanointegration Duisburg-Essen (CENIDE), University Duisburg-Essen, Duisburg, D-47057, Germany*

[3]*Institute for Combustion and Gasdynamics–Fluid Dynamics (IVG), University Duisburg-Essen, Duisburg, D-47057, Germany*

Published in Review of Scientific Instruments, Volume 91 - Issue 9, Page 095114 (2020)
DOI: 10.1063/5.0018880

ABSTRACT

Structure formation models describe the change of the particle structure, e.g. by sintering or coating, as a function of the residence time and temperature. For the validation of these models, precise experimental data are required. The precise determination of the required data is difficult due to simultaneously acting mechanisms leading to particle structure formation, as well as their dependency on various particle properties and process conditions in the reactor.

In this work, a model flow reactor (MFR) is designed and optimized, supported by a validated CFD simulation, to determine the structure formation of nanoparticles under well-defined conditions. Online instrumentation is used to measure the particle mass and different equivalent diameter to detect changes of the particle shape and to calculate the particle structure, defined by primary particle size, number of primary particles per agglomerate, coating thickness, effective density and fractal dimension, by means of structural models. High precision is achieved by examining size-selected particles in a low number concentration and a laminar flow field. Coagulation can be neglected due to the low particle number concentration. Structure formation is restricted to a defined re-

gion by direct particle trajectories from the water-cooled aerosol inlet to the water-cooled outlet. A preheated sheath gas is used to concentrate the aerosol on the centerline. The simulated particle trajectories exhibit a well-defined and narrow temperature residence time distribution. Residence times of at least 1 s in the temperature range from 500 to 1400 K are achieved. The operation of the MFR is demonstrated by the sintering of size-selected Fe_xO_y agglomerates with measurements of the particle size and mass distribution as a function of the temperature. An increase of the effective density, resulting from decreasing particle size at constant particle mass, is observed.

I. INTRODUCTION

Different types of aerosol synthesis reactors, e.g. hot-wall (Wiggers, Starke, and Roth, 2001), plasma or flame (Kammler, Mädler, and Pratsinis, 2001) reactors are used to produce nanoparticles with a high yield. The optimization of these reactors can be challenging and time-consuming, as the basic mechanisms leading to particle formation are not yet fully understood. To investigate the particle formation, the rapidly and simultaneously occurring mechanisms, such as chemical reactions, surface growth, coagulation, condensation, and sintering (Pratsinis, 1988) have to be separated from each other. Coagulation and sintering are the two main important mechanisms determining particle morphology and growth. Coagulation is well described in models (Davies, 1979; Lee and Chen, 1984) whereas sintering is a more complex mechanism due to its' dependency on various particle properties (e.g. size, shape, agglomerate structure), (thermodynamic) material properties, as well as on process conditions (the temperature-time history of the particles). This dependency makes it challenging to determine precise experimental data which are needed to validate sinter models (Kruis et al., 1993). A MFR can solve this problem by control of particle number concentration, simplifying the flow pattern of the aerosol and thereby providing well-defined particle trajectories with a narrow temperature-time distribution. Borgwardt (1985) constructed an MFR and studied the activation energy for calcination of limestone particles in the particle size range from 1 to 90 µm. This resolved difficulties of prior studies with small particles by providing adequate particle dispersion and high throughput of inert sweep gas. The setup of an MFR which can be operated isothermally up to 1473 K by using a preheated sheath gas is described by Gullett, Blom, and Gillis (1988). It is a high-temperature reactor (HTR) based on a vertically drop-tube. The temperature profile and the velocity of the flow field were studied and the reaction of CaO with SO_2 producing calcium sulfate ($CaSO_4$) was

investigated. The chemical conversion was limited to the HTR reaction zone between injection and collection probe by using a water-cooled inlet and outlet. A ceramic venturi nozzle at the injection probe was used for turbulent mixing of calcium hydroxide $Ca(OH)_2$ sorbent into a process gas of SO_2 and oxygen (O_2), and nitrogen (N_2). Park et al. (2001) designed two types of nanoparticle microreactor (NPMR) to study the thermal decomposition of titanium tetraisopropoxide (TTIP) in a nitrogen carrier gas. The first design of the NPMR consisted of a ∅2 mm quartz tube in a horizontal position with a constant temperature zone of about 300 mm in length. The growth of the Sauter diameter from 9 nm (773 K) to 31.7 nm (1273 K) was detected offline by TEM micrographs. After the experiment, a coated zone of matter on the upper wall inside of the horizontal quartz tube, downstream of the heated zone, was observed. The buoyancy causes the deflection of the hot gas flow towards the colder quartz tube wall, leading to the deposition of matter by condensation. Therefore, an accurate measurement of the TiO_2 particle formation by the decomposition of TTIP is difficult due to the reduction of matter on the reactor walls. A second design was introduced to reduce the surface reactions of the precursor TTIP with the quartz tube by using a centered precursor inlet (∅2 mm) surrounded by a sheath gas between precursor inlet and the increased outer quartz tube wall (∅4 mm). The coating of the wall by deposition or chemical reactions could be reduced, but not completely avoided. An elegant approach to avoid material deposition at walls is to use the thermophoresis by hot walls in a vertical tube furnace, which forces the particles back to the centerline. Seto, Shimada, and Okuyama (1995) used a vertical tube furnace with temperatures up to 1673 K and a residence time up to 9 s to study the sinter kinetics of TiO_2. The change in particle size was investigated by a tandem-differential mobility analzyer (DMA) setup, upstream and downstream of the vertical tube furnace, and TEM analysis. It turned out that controlling the particle temperature and residence time history, which is important to determine the sinter kinetics, is difficult due to the irregular flow field in the reactor, dominated by the buoyancy. Inspired by these works, Kirchhof, Schmid, and Peukert (2004) built a high-temperature and short-time flow reactor to investigate the sinter kinetics of silica nano-scaled particles in the gas phase, excluding all other mechanisms (Kirchhof, Förster, et al., 2012). Its design aims at keeping an aerosol flow at a constant high temperature by rapid heating and quenching at inlet and outlet. The reactor was operated at a pressure of 600 mbar and could be tested in the temperature range from 1533 K to 1873 K with a residence time from 3.7 to 130 ms. Rapid heating and a homogeneous temperature profile are achieved by turbulent mixing with a preheated sheath gas. A broadened residence time distribution of the

aerosol results from the turbulent flow field. A narrow residence time distribution can be achieved by injecting and sampling an aerosol onto and from the central flow axis in a laminar flow field.

Longer residence times are required when slow structure formation mechanisms, like particle coating, have to be investigated. For particle coating, the residence time and the precursor concentration are the main control parameters. Post, Jidenko, et al. (2016) and Post, Wurlitzer, et al. (2018) studied the coating process with silica from tetraethoxysilane (TEOS) and hexamethyldisiloxane (HMDSO), enhanced by a dielectric barrier discharge (DBD) on metal oxide particles. Within the used precursor concentration (< 5 ppmv), they recommend a residence time > 83 s at room temperature for achieving coating thicknesses > 1 nm as the complete conversion of the liquid coating into a solid silica coating is slow. A faster coating process within seconds is possible by increasing the temperature.

In this work, we present a model flow reactor (MFR) designed to determine the sinter and coating kinetics of aerosol nanoparticles. The MFR provides a laminar flow field in a vertical tube furnace with water-cooled inlets and outlets. Temperatures up to 1400 K can be reached and residence times in the range of seconds. The design is supported by computational fluid dynamics (CFD) simulations, which have been validated by temperature measurements. Experimental investigations of the MFR showed that a transient flow field at a temperature of ~ 773 K led to a low signal-to-noise ratio during the measurements. computational fluid dynamics (CFD) simulations confirmed that the heating of the gas is not sufficient enough to reach the buoyancy required to transport the aerosol straights from inlet to outlet. The process parameters and the reactor design have been optimized by increasing the aerosol flow rate, by shifting the heated zone towards the aerosol inlet, and by extending the heated zone at the upper end by an external trace heating. After the optimization of the flow field, the successful operation of the MFR is demonstrated by sintering size-selected Fe_xO_y agglomerates. Structural changes are measured via a combination of online instrumentation: the scanning mobility particle sizer (SMPS), centrifugal particle mass analyzer (CPMA), and differential aerodynamic particle sizer (DAPS).

II. EXPERIMENTAL FACILITY

A. Principle setup

The experimental setup is shown in Figure D.1 and is divided into four parts; a) the characterization of the particles with online and offline

instrumentation, b) the MFR for inducing a change of the structure of aerosol particles under well-defined conditions, c) the particle synthesis which provides defined particle structures (e.g. size-selected agglomerates or sintered particles), and d) the transfer of a liquid precursor into the gas phase for coating experiments.

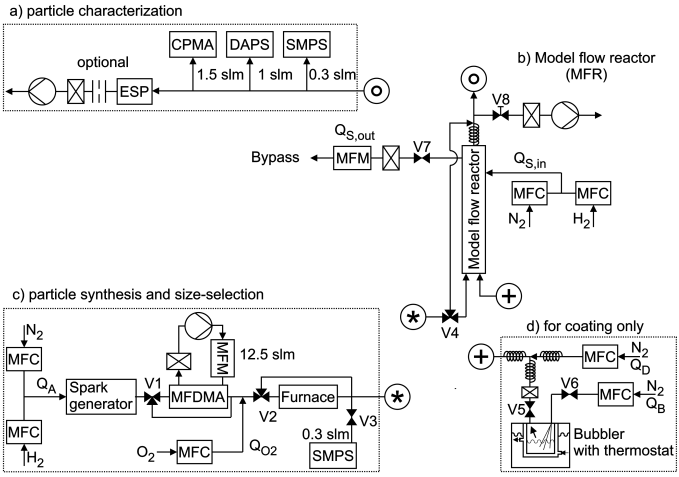

Figure D.1: Schematic representation of the experimental setup consisting of (a) particle characterization via online and offline instrumentation, (b) a model flow reactor (MFR) for providing a well-defined temperature residence time distribution, (c) particle synthesis and size-selection, and (d) a bubbler for particle coating.

Pure nitrogen or a gas mixture of up to 5 vol.% hydrogen in nitrogen is provided by two mass flow controllers (MFCs) (EL-FLOW Select, Bronkhorst High-Tech B.V., Ruurlo, NL). One MFC is connected to a liquid nitrogen tank with a gas purifier. The gas purification system is a combination of an ALPHAGAZ Purifier O2-Free (Air Liquide Deutschland GmbH, Frankfurt, DE) and Mono Torr PhaseII purifier (SAES Getters Deutschland GmbH). It is used to increase the gas purity (> 5.0) and to remove oxygen contamination. The second MFC is connected to a gas bottle (ARCAL F5, Air Liquide) filled with compressed hydrogen (5 vol.%) in nitrogen. The gas mixture Q_A, at a total flow rate of 2.5 slm, flows through $\varnothing 6x1$ mm Swagelok stainless steel tubes into the spark generator. Iron aerosol particles are synthesized by spark discharges between two $\varnothing 5$ mm iron rod electrodes (CAS 7439-89-6, Alfa Aesar by Thermo Fisher GmbH, Kandel, DE) in a custom-build spark generator.

The design of the spark generator is based on the work of Schwyn, Garwin, and Schmidt-Ott (1988), but differs in a horizontal arrangement of the aerosol inlet and outlet. The spark generator is connected in parallel to 28 capacitors with a capacity of 1 nF each and a high voltage capacitor charger (CCR10-P-750, Technix, Créteil, FR). Since the spark energy is directly proportional to the capacitance, higher capacitance results in a stronger spark and therefore in the growth of the modal diameter and increase of the particle concentration (Meuller et al., 2012; Tabrizi et al., 2009). The spark generator produces ultrafine and multiply-charged particles in an agglomerated structure. Since the particles are already charged, a monodisperse particle fraction can be extracted based on their electrical mobility using a medium-flow differential mobility analyzer (MF-DMA) (Rosenberger et al., 2019). A three-way valve (V1) located directly downstream of the spark generator can be used to bypass the MF-DMA. The MF-DMA is designed and optimized to classify high-density nanoparticles, experimentally tested with spherical silver particles up to 600 nm, and at high aerosol flow rates up to 10 slm. It is also characterized by long run times before discharges start to occur, even with relatively high particle concentrations. Thus, a time-stable monodisperse aerosol containing large agglomerates can be provided in sufficient concentration. The sheath gas flow rate for the MF-DMA is provided by a gas recirculation system. It consists of a blower with mass flow meter (AWM5104VN, Honeywell International Inc., Charlotte, NC, USA) and a high-efficiency particulate absorbing (HEPA)-filter (Ultra Filter, type H cartridge, MSA, Pittsburgh, PA, USA). A mass flow rate Q_{O2} of oxygen is set by an MFC downstream of the MF-DMA. Oxygen allows to oxidize Fe_xO_y agglomerates or to obtain a complete decomposition of the precursor used for coating experiments. The mono- or polydisperse aerosol can be pre-sintered in a tube furnace (CTF 12/450/60, Carbolite Gero GmbH & Co. KG, Neuhausen, DE) or bypassed by using a three-way valve (V2). The pre-sinter furnace is bypassed for sinter experiments and only used for coating experiments. The pre-sinter furnace is used to provide defined particle morphology, especially a spherical structure so that an increase of the particle size directly corresponds to a shell growth and the coating thickness can be determined. A tee downstream of the furnace allows taking a sample at a flow rate of 0.3 slm over a valve (V3) into an SMPS (3936, TSI, Minneapolis, US). The main aerosol flow passes over a three-way valve (V4) through the injection probe into the MFR or is fed into a bypass.

For the coating experiments (b), a custom-built glass bubbler is used to transfer a liquid precursor into the gas phase. The double-walled bubbler consists of a precursor reservoir of approx. 40 mL surrounded by heating

liquid, which can be flushed through two hose connectors. A plastic DN-25 KF centering ring with a rubber O-ring and a DN-25 KF metal lid with two $\varnothing 6x1$ mm tubes, named gas inlet and outlet, are assembled to the top of the glass body. Three syringe needles are welded to the gas inlet and extend the gas inlet shortly before the bottom of the liquid reservoir. The bubbler is immersed in the temperature-controlled oil basin of a thermostat (ECO E 3xx, Lauda, Lauda-Königshofen, DE). Two tubes are connecting the pump of the thermostat with the tube connectors of the bubbler. This allows circulating oil with a well-defined temperature through the surrounding volume between the glass walls of the bubbler, within proximity to the precursor reservoir. Thereby, the temperature of the precursor can be efficiently regulated and ensures a homogeneous temperature. The bubbler can be separated for cleaning or precursor refill from the setup by closing valves V5-6. A small nitrogen gas flow rate Q_B is set by a mass flow controller (EL-FLOW Select) flowing through the three syringe needles and the liquid precursor, creating tiny gas bubbles. The mixture of gas and precursor is directly diluted downstream of the bubbler by nitrogen gas at a flow rate Q_D set via an MFC. Additionally, the tubes from bubbler to the MFR are wrapped with a trace heating to prevent condensation caused by the oversaturation of the precursor. The trace heating is controlled by a two-point temperature regulator with thermocouple type K. Detailed setup of the MFR is described in Sec. II B. The sheath gas $Q_{S,in}$ for the MFR is adjusted by two MFCs according to the gas mixture of the aerosol. The sheath gas enters the MFR at the upper end, flows down through the outer annulus of the MFR, contacts the aerosol in the lower region, flows through the central annulus, and enters over a HEPA-filter the exhaust. The sheath gas flow rate at the exhaust $Q_{S,out}$ is measured with a volume flow meter (Gilibrator-2, Sensidyne LP, St. Petersburg, FL, USA) to check the flow conditions.

The aerosol outlet of the MFR is connected to the online instrumentation SMPS (3936, TSI), differential aerodynamic particle sizer (DAPS) (Babick et al., 2018) and CPMA (centrifugal particle mass analyzer, Cambustion Ltd., Cambridge, UK), and to an electrostatic precipitator (ESP) for optional offline analysis. A critical orifice, a HEPA-filter, and a vacuum pump downstream of the ESP are used to keep the mass flow rate into the ESP constant.

B. DESIGN OF THE MODEL FLOW REACTOR

A schematic of the MFR is shown in Figure D.2 and is based on a vertical arrangement of two concentric ceramic tubes in a tube furnace. Previous studies showed that in a horizontal tube furnace with a laminar

flow radial temperature gradients occur (Flynn and Dunlap, 1986) and that convection and condensation lead to the deposition of particle or precursor on the tube walls downstream of the heated zone (Park et al., 2001). Shrivastava, Gidwani, and Jung (2009) compared the particle trajectories in a horizontally and vertically oriented tube furnace and found out that the horizontal tube orientation leads to flow recirculation effects that result in more complex particle paths. The particles are forced by the buoyancy from the center to the hot tube walls which causes radial mixing of the particles and to a broadening of the residence time distribution.

This can be reduced and process parameters simplified by vertical alignment of the flow direction and convection. Well-defined particle trajectories, almost direct from inlet to outlet, with a narrow temperature and residence time distribution are reached in a laminar flow field. In combination with a sheathed gas flow, the formation of an unsteady flow field can be reduced (Seto, Shimada, and Okuyama, 1995). The design of the MFR is inspired by the work of Kirchhof, Schmid, and Peukert (2004), however in this work, we apply a laminar flow and a longer residence time (in seconds) in the temperature range up to 1473 K. A wire-wound tube furnace (TZF 12/75/700, Carbolite Gero GmbH & Co. KG, Neuhausen, DE) modified for vertical operation is used. The heating wire element is directly wounded onto a fixed ceramic tube, divided into three zones in length, to provide an extended uniform temperature zone in the mid-section of the heated zone (540 mm $\pm$ 5 K). The furnace temperature set by a two-segment controller is continuously monitored with a multimeter (180 Series, Fluke Deutschland GmbH, Glottertal, DE). A $\varnothing 70x5$ mm Alsint (99.7 % Al_2O_3) ceramic work tube with a total length of 1500 mm (Type C 799, Buntenkötter Technische Keramik GmbH, Neuss, DE) is inserted into the wire-wound ceramic tube of the TZF. Protruding tube parts are covered by a ceramic fiber blanket (FIRETEK EAF-Blanket, R.A. Schmidt-Feuerfest GmbH, Norderstedt, DE) and aluminum foil to reduce heat losses. The open ends of the tube are grounded to a diameter of 68 mm over a length of 80 mm for the precise fitting of custom-built adapters from ceramic tube to standard vacuum components.

The ceramic-to-CF adapters allow the vacuum-tight connection of the ceramic tube with DN-63 CF standard vacuum components by the squeezing of two FPM O-rings (Viton). An additional DN-63 CF adapter is mounted on the upper ceramic-to-CF adapter and is equipped with four radially distributed openings ($\varnothing$8 mm), drilled at an axial angle of 145°, with DN-16 KF flanges as sheath gas inlets. This adapter fixes and centers an inner ceramic ($\sim$ 60 % Al_2O_3) tube, $\varnothing 50x5x1370$ mm (Pythagoras, Type C 610, Buntenkötter Technische Keramik GmbH) in the outer work tube.

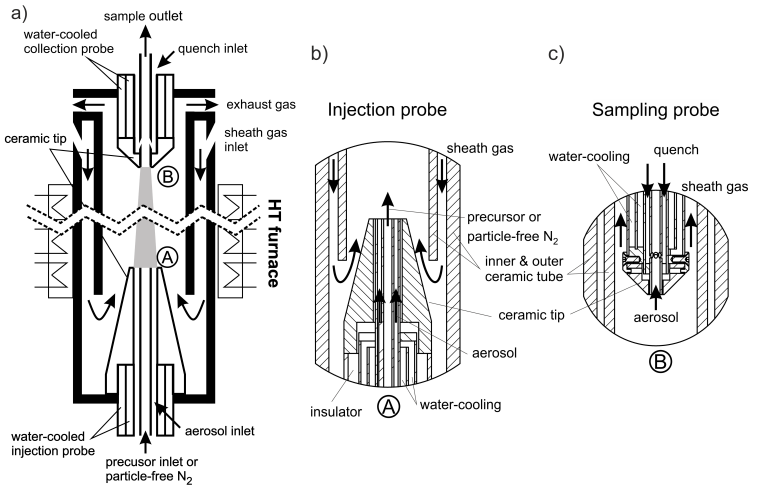

Figure D.2: (a) Schematic representation of model flow reactor (MFR), the reaction zone is indicated by a gray-colored area (∅10 mm to ∅6x750 mm), with a detailed drawing of (b) the injection probe (A) and (c) the sampling probe (B).

The inner tube is slightly shorter than the outer tube and hangs freely at the lower end. Ceramic root faces/filaments are glued to the lower end and are also used for centering.

A DN-63 CF double cross with four DN-40 KF flanges is assembled between the injection probe and the lower ceramic-to-CF adapter and another double-cross is mounted between the sampling probe and the upper DN-63 CF adapter. Vacuum pump, pressure gauge, and safety overpressure valve are assembled to lower DN-40 KF flanges of the double-cross. A vacuum pump and two symmetrical sheath gas exhausts are connected to the upper DN-40 KF flanges. Figure D.2b) and c) depict a detail of the injection and sampling probe, consisting of the concentric arrangement of stainless-steel tubes (316 Ti), ∅6x1 mm and ∅12x1 mm for gas inlets and outlets, covered by water-cooling (between ∅12x1 mm, ∅20x1 mm, ∅28x1 mm), a 6 mm thick ceramic fiber blanket (FIRETEK EAF-Blanket) and a ∅42.4x2 mm heat resistant stainless-steel tube (314). The probe tips are manufactured from a machinable calcium silicate-based ceramic (Duratec 750, Goodfellow Cambridge Ltd, Huntingdon, UK) and converge with smooth surfaces towards the reaction zone. Thereby, the formation of unsteady flow fields at the aerosol inlet and outlet is minimized and the heat loss from the heated zone is reduced due to the low thermal

conductivity of the ceramic parts. Thus, cold aerosol gas and precursor or particle-free gas entering through the injection probe are mixed with a preheated sheath gas. The sheath gas flows through the inlet drillings in the upper DN-63 CF adapter downwards and is preheated by flowing through the heated zone between the inner tube and outer ceramic tube. It is redirected at the end of the inner tube for sheathing and stabilizing the aerosol and precursor flow to the centerline. The total gas flow, preheated sheath gas, and gas mixture of aerosol and precursor flow upwards through the sintering zone inside of the inner ceramic tube. The total reaction volume is a conical cylinder with a diameter of ∅10 mm to ∅6 mm over a length of 750 mm and is indicated by the gray-colored area in Figure D.2a). The aerosol is sucked in through the sampling probe and can be quenched at the probe tip. The sheath gas flows in the exhaust.

C. Characterization of the model flow reactor

1. Temperature measurement

The CFD simulations are required to calculate the particle trajectories in the reactor to determine the residence time and temperature distribution. Figure D.3 depicts a drawing of the temperature measurement with thermocouples in the reaction zone and along the heated outer tube. Temperature measurements along the outer ceramic tube are used to define the boundary conditions of the CFD simulations, whereas the measurements inside of the reaction zone are used to validate the CFD simulations. The temperature is measured via insulated thermocouples with a diameter of ∅1 mm and a length of 2 m with stainless steel sheath (type K sensor, RS Components GmbH, Mörfelden-Walldorf, DE). The stainless-steel sheath together with the thickness of the sensor gives the thermocouple sufficient flexibility and stability to pull it through the reactor zone without damage to the sensor but requires longer dwell time for precise measurements (Xu, Tian, and Zhao, 2017). The temperature along the outer tube is measured in small ceramic tubes, which are attached to the wire-wound tube by the manufacturer for temperature measurement using thermocouples. The measurement of the temperature in the reaction zone ($0.24\,\mathrm{m} < z_{\mathrm{axial}} < 0.99\,\mathrm{m}$, $0\,\mathrm{mm} < r_{\mathrm{radial}} < 20\,\mathrm{mm}$) is done with a stainless-steel cross (outer diameter ∅39.4 mm and 4x4 mm spokes) as a position holder. It contains nine holes in a radial distance ($r_{\mathrm{radial}} = 0$, 2.5, 5.0, 7.0, 9.0, 11.0, 13.0, 15.0 and 17.0 mm), which hold the thermocouples in position. A material with sufficient mechanical stability is required due to the thin construction and not perfectly round ceramic tube, which can cause the cross to jam. A taut wire (∅1 mm,

titanium) is connected to the center of the metal cross to pull it through the ceramic tube and to keep it in position. Additionally, the taut wire is needed to release the jamming of the metal cross in the ceramic tube. The metal surface of the cross absorbs thermal radiation, especially when oxidized, and changes the temperature and flow field in the reaction zone. In order to minimize this perturbation on the temperature measurement, the thermocouples stick out by 10 mm from the cross's surface in the upstream direction (Figure D.3). The temperature is measured every 10 mm in the axial direction. Figure D.4 depicts the temperature measurement via thermocouples of the outer ceramic tube (dots), inside the center of the reaction zone (crosses), and the simulated temperature (solid line) as a function of the vertical position. Position 0 m defines the transition point of the ceramic tube in the lower ceramic-to-CF adapter and position 1.4 m to the upper ceramic-to-CF adapter, respectively. The reaction zone, starting with the end of the injection probe (aerosol and precursor inlet) and ending with the beginning of the sampling probe (aerosol outlet), are marked by dashed lines (0.24 m and 0.99 m).

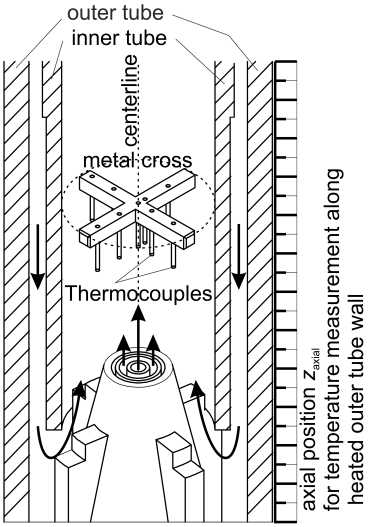

Figure D.3: Drawing of the temperature measurement by thermocouples in the reaction zone using a metal cross as a position holder and along the heated outer tube wall.

The sheath gas flow rate is set to 8 slm (0.167 g/s) and the aerosol flow rate to 1.25 slm ($2.61 \cdot 10^{-2}$ g/s) nitrogen. Fixed temperatures are set to the tube furnace (773, 1023 and 1273 K) and after a constant temperature

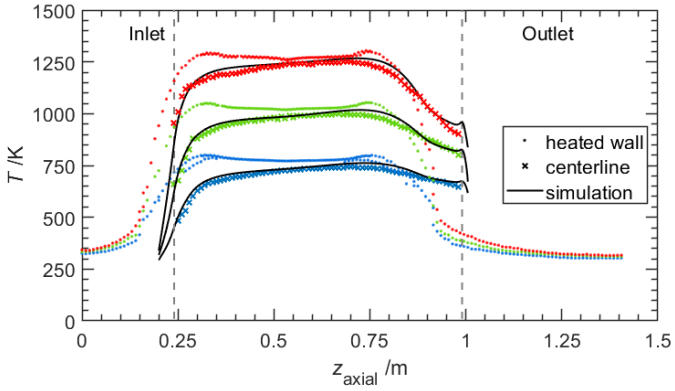

Figure D.4: Temperature measurement at three tube furnace temperatures (773, 1023 and 1273 K) with thermocouples at the outer tube (heated wall, dots) and inside the reaction zone on the centerline (crosses). Results of the CFD simulation of the centerline temperature as a function of the axial position (solid lines) are also shown.

profile is achieved the temperature is measured at the outer tube and inside the reaction zone. For each furnace temperature set, the measured temperature at the outer tube shows two maxima close to the end of the heated zone at approx. 0.32 and 0.75 m, respectively, and in between almost a plateau with a minimum at 0.55 m. The average temperature of the plateau corresponds to ± 5 K of the temperature set by the furnace temperature controller. The two maxima result from the temperature set to the first and the third zone by the controller, whereby a higher power is applied to extend the homogenous temperature profile along the outer tube. Away from the heated zone, the temperature decreases strongly with increasing distance to the heated zone and reaches room temperature (300 K). The edges of the temperature profile are fitted by exponential functions and the middle part by a polynomial function allowing to set the measured temperature as wall boundary conditions in the CFD simulation.

The temperature in the reaction zone (crosses) slightly increases with increasing distance from the injection probe due to the mixing of the cooled gas leaving the injection probe and the preheated sheath gas. In the laminar flow, heat conduction is the main transport mechanism of heat crosswise to the flow direction, thus it takes several hundred milliseconds to equalize the temperature of the aerosol and the sheath gas. From position 0.3 to 0.75 m, the slope decreases and an almost constant heating

rate ($\sim$ 2 to 2.5 K/cm) is observed. The aerosol is extracted through the sampling probe downstream of the heated zone at 0.99 m, where the temperature is already reduced by heat conduction to the outer ceramic tube. The simulated and measured temperature on the radial center in the reaction zone are in good agreement. A detailed description of the CFD simulation can be found in Sec. II C 2.

2. CFD analysis

The flow field inside the reactor has been calculated by two different types of CFD simulations with the fluid mechanic's code ANSYS Fluent (v.19.2, ANSYS, Inc., Canonsburg, PA, USA). The first simulation (A) is adapted to the experimental measurement procedure, whereby the taut wire is represented in the simulation as a metal body with a diameter of 1 mm. Thus, the simulated temperature distribution can be validated with the experimental measurement.

The validated temperature fields were then used as boundary conditions for the second type of simulation (B), which was used to optimize and determine the undisturbed flow field (without metal cross with thermocouples). The gas flow velocity in the inner ceramic tube is calculated as $v_{\max} \sim 0.7\,\mathrm{m/s}$ at ($T = 773\,\mathrm{K}$) and the corresponding Reynolds number is $Re = 364$. Further heating increases the gas velocity, but at same time the viscosity and mass density decreases, leading to a further decrease of the Reynolds number. The critical Reynolds-number of $Re \approx 2300$ for circular pipes is never exceeded, the flow remains laminar. Due to the rotationally symmetric geometry of the reactor, the vertical orientation of the setup, and the laminar flow, a two-dimensional computation domain was utilized, discretized by 47,000 cells. The transport equations are solved with the second-order upwind scheme for a steady-state simulation. For simulation type (A), the experimentally measured values at the outer ceramic tube were used as the temperature boundary condition for the outer boundary of the reactor tube in a so-called conjugate heat transfer model. Radiation was computed using a discrete ordinate (DO) model with the emissivity values ($\epsilon_{\mathrm{alsint}} = 0.9$, $\epsilon_{\mathrm{pythagoras}} = 0.6$, $\epsilon_{\mathrm{steel}} = 0.3$) for the relevant materials, obtained sources (Chemical Rubber Company Cleveland, 1979; Pissanetzky et al., 1981). Sheath gas and aerosol flow rate are set according to the experiment described in Sec. II C 1.

Figure D.5 depicts the comparison of the experimental measurement (left half) with the simulation (type A, right half) in the reaction zone for the three temperatures a) 773 K, b) 1023 K, and c) 1273 K. The normalized temperature gradient $\mathrm{d}T/\mathrm{d}r_{\mathrm{radial}}$ at five fixed axial positions

(z_{axial} = 0.25, 0.4, 0.55, 0.7 and 0.85 m) is shown by white lines at the corresponding axial position z_{axial}. Overall, a good agreement between simulation and experiment is achieved.

For all temperatures, almost parabolic temperature profiles are observed, which become more flattened in the flow direction. Deviations from an ideal parabolic profile are caused by the metal body in simulations and the taut wire in the experiment. The metal body in the simulations absorbs radiation and creates a thermal bridge between the water-cooled inlet/outlet and the heated zone. This results in a higher heating rate at the inlet and higher cooling rate at the outlet, as the heated zone already ends below the outlet. This becomes evident by showing the normalized temperature gradient in Figure D.5a-c) (white lines). A negative temperature gradient around $r_{radial} = 0$ and adjacent cells can be seen close to the injection probe and a positive gradient close to the sampling probe, respectively.

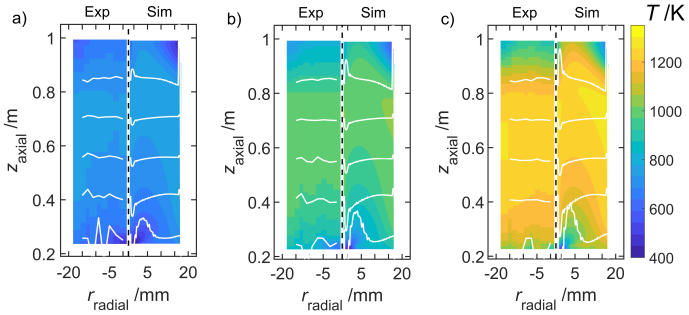

Figure D.5: Comparison of the measured (left half) and simulated (type A, right half) temperature in the reaction zone for the furnace temperatures a) 773 K, b) 1023 K, and c) 1273 K. Temperature gradient dT/dr_{radial} at five axial positions (z_{axial} = 0.25, 0.4, 0.55, 0.7 and 0.85 m) is indicated by white lines.

Changes in the temperature gradient are more apparent in the simulation due to the higher resolution. This is attributed to the metal cross used as a thermocouple position holder in the experiment which is neglected in the rotational symmetric 2-D simulation. On the one hand, the thermal conductivity of the cross could lead to a smoothing of the temperature measurement in the experiment, and on the other hand, the thermocouples have certain thermal inertia so that a transient flow cannot be resolved. It is assumed that the simulation accurately represents the flow and temperature conditions in the reaction zone and that deviations

from the experiment are due to the measurement inaccuracy of the used methods.

3. Sintering of Fe_xO_y size-selected agglomerates

For sinter experiments, the metal cross with taut wire and thermocouples are removed and size-selected agglomerates are sintered while the furnace temperature is linearly increased by 0.3 K/min from 673 to 1073 K. Figure D.6a) depicts the continuous measurement with two SMPSs of the entering ($d_{\mathrm{m,input}}$) and outflowing ($d_{\mathrm{m,output}}$) mobility diameter into/out of the MFR as a function of the temperature ramp. The particle size distribution (PSD) is shown on the y-axis with the normalized number concentration as color bar. The modal particle diameter of the PSD is indicated by a black line. On the upper half of this figure, it can be seen that a constant PSD at the input of the MFR is given over the entire temperature range. The PSD is size-selected by means of a DMA consisting of high number concentration (yellow) with a diameter of $\sim$ 90 nm (+1/1 charge) and a slightly lower concentration (light blue) with a particle diameter of 135 nm (+2/1 charges). The second light blue area at a particle size of 61 nm (+1/2) is to be evaluated as a measurement artifact and is not a part of the input aerosol. This can be confirmed, as this particle size is not measured at the outlet (lower half). It results from the neutralization of an already charged aerosol downstream of the MF-DMA. The recharging of the particles from +1 to +2 charges leads to higher electrical mobility and consequently to a smaller particle diameter in the SMPS measurements. Compared to the output aerosol downstream of the MFR (lower half), it can be seen that the mobility diameter decreases with increasing the temperature and the PSD becomes narrower due to the sintering to a more compact structure. In the temperature range from 840 to 960 K, in which a significant reduction of the mobility diameter from 70 to 45 nm occurs, is not resolved because of a low signal-to-noise ratio. The simulations show that strong buoyancy effects with the set parameters occur, which lead to a slowing down of the flow and result in a further dilution of the aerosol concentration. In order to avoid this effect and obtain a better signal-noise ratio, the aerosol flow rate is increased from 1.25 slm to 2.2 slm ($4.59 \cdot 10^{-2}$ g/s) and the heated zone of the furnace is shifted by 50 mm towards the injection probe and additionally extended at the upper end using a trace heating ($T = 673$ K).

CFD simulations, which are required for the determination of the particle residence time distribution in the reaction zone during the sintering experiments, are adapted to the new experimental conditions without taut wire on the centerline and to the improvements made. The tempera-

ture profile in the reaction zone changes due to the absence of the metal body. An ideal parabolic temperature profile with a shorter heating and cooling rate on the centerline ($r_{\text{radial}} = 0$) results, leading to an elongation of the temperature profile in the flow direction. Figure D.6b) depicts the adapted CFD simulation of the temperature profile and gas velocity (arrows) in the reaction zone (∅40 mm, 750 mm) of the original (left half) and an optimized flow field (right half) at a fixed furnace temperature of $T = 773\,\text{K}$. The temperature in the reaction zone is indicated by the color bar and the gas velocity by the direction and length of the arrow vectors. In both simulations, the aerosol enters into the reaction zone at $z_{\text{axial}} = 0.24\,\text{m}$ and $r_{\text{radial}} < 5\,\text{mm}$ with a gas temperature of 300 K. At the injection, the gas velocity for the optimized flow field is faster due to the higher aerosol flow rate and causes a larger area of a colder gas indicated by the blue area at the injection probe. The temperature difference between the aerosol carrier-gas and the sheath-gas (both nitrogen) results in a density gradient and thus significant buoyancy effects, driving instability of the steady flow. A stable and steady flow field could only be maintained by reducing the density gradient by careful temperature control of the aerosol carrier and the sheath gas. The idea to adjust the densities by changing the gas composition (admixture of lighter gases) was discarded as it would require a re-calibration of the online instrumentation. Figure D.6 indicates that the heating rate of the aerosol laden gas at the injection probe might not be sufficient enough to transport the aerosol with a constant axial gas velocity to the sampling probe ($z_{\text{axial}} = 0.99\,\text{m}$ and $r_{\text{radial}} < 2\,\text{mm}$). The aerosol flows a small distance into the reaction zone, reduces its axial velocity (original at $z_{\text{axial}} = 0.35\,\text{m}$ or optimized at $z_{\text{axial}} = 0.42\,\text{m}$), and increases its axial velocity again due to the increase in buoyancy after getting heated. An unsteady flow field or an expansion of the aerosol from the centerline is not observed. The sampling probe is located above the end of the third heated zone of the furnace, where the temperature at the outer tube ($z_{\text{axial}} > 0.85\,\text{m}$ and $r_{\text{radial}} > 10\,\text{mm}$) is already decreasing (Figure D.6). A transient flow field occurs due to the cooling down of the sheath gas near the ceramic tube wall and thus creating backflow regions. In the simulation, the aerosol flow on the centerline is not affected by the backflow region. Nevertheless, additional external trace heating with a fixed temperature of 673 K, covered with a ceramic fiber blanket and an aluminum foil, wrapped around the ceramic tube is used to extend the heated zone and to prevent the observed backflow. Comparing original with optimized simulation, it can be seen that the temperature is only slightly decreased and the gas velocity vector is almost constant near the ceramic wall. At higher furnace temperatures, the temperature of the

heated zone deviates more from that of the trace heating, but this does not lead to a transient flow field, as the buoyancy of the gas increases with rising temperatures.

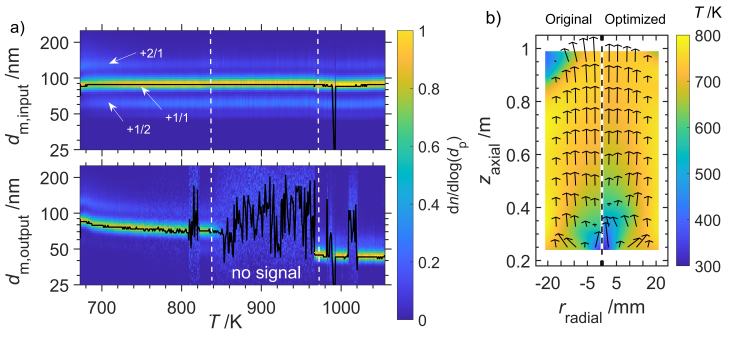

Figure D.6: a) Comparison of the normalized particle size distribution of the input and output mobility diameter as a function of the temperature in the range from 673 to 1073 K, and b) CFD simulation of the temperature profile and gas velocity (arrows) in the reaction zone of the original (left half) and the optimized flow field (right half) at a fixed furnace temperature of $T = 773$ K.

III. EXEMPLARY RESULTS

The development of the structure of the aerosol particles is determined by the measurement of particle properties (e.g. equivalent diameters, particle mass) downstream and upstream of the MFR. Different online and offline instrumentation, like SMPS, CPMA, DAPS (online), and TEM with energy-dispersive X-ray (EDX) and EELS, XRD, XAFS, Brunauer, Emmett and Teller (BET) (offline) are combined to describe the particle structure based on primary particle size, number of primary particles per agglomerate, effective density, and fractal dimension (Eggersdorfer et al., 2012). The activation energy and structure formation rate can then be determined using suitable kinetic models (Buesser and Pratsinis, 2010; Kruis et al., 1993; Schmidt-Ott, 1988) of sinter and coating. For sinter experiments, a polydisperse aerosol of iron oxide particles is generated by spark discharge, operated with a charge current of 5 mA and a discharge voltage of 4 kV. The lognormal particle size distribution has a geometric mean diameter d_g of 110 nm with a standard deviation σ_g of 1.6 and a number concentration of $\sim 10^7$ #/cm^3. The particles are highly agglomerated with a mean primary particle diameter of 4 nm (BET, Gemini VII,

Micromeretics GmbH, Aachen, DE) and a fractal dimension of 2.23. The powder for BET measurements is sampled from the spark housing after several hours of synthesis, purged with nitrogen and annealed overnight before analysis. Due to the large surface area, the agglomerates are partly oxidized. A MF-DMA is used to select an agglomerate size based on its electrical mobility. Two SMPSs are used to measure the particle size distribution of this size-selected aerosol by means of the electrical mobility particle diameter downstream and upstream of the MFR. Input and output size distributions are directly comparable and allow the detection of structure formation by changes in size. The DAPS measures the aerodynamic behavior of the particles upstream of a critical lens and is used to calculate the aerodynamic diameter or Stokes diameter, respectively, and to determine the primary particle size. Evaporation and coagulation of the particles can be excluded as long as the particle mass remains unchanged during sintering. Operating the MFR at room temperature does not lead to changes in size and mass distribution. Thus, the structure formation can be directly attributed to the changes in operating conditions of the MFR. Continuous operation of the online instrumentation ensures a known particle size distribution at inlet and outlet and the precise determination of the structure formation.

In a first experiment, agglomerates with a diameter of 100 nm are classified using the MF-DMA, operated with a sheath gas flow rate of 12.5 L/min and a voltage of 3.2 kV. The mean number concentration downstream of the DMA is $\sim 1.1 \cdot 10^5$ #/cm^3 and almost constant, decreases slightly with during the experiments. The temperature of the MFR is linearly increased with a heating rate of 2 K/min from 573 to 1373 K, held constant at 1373 K for 60 min and then let drop down to 523 K. The subsequent cooling rate cannot be controlled and decreases from 8 to 0.2 K/min. Measurands during heating are indicated by filled squares and during cooling by unfilled squares. The measurements are correlated to the temperature in the mid-section of the heated zone, monitored by the furnace temperature controller. Figure D.7a) depicts the continuous measurements with SMPS, CPMA, and DAPS downstream of the MFR as a function of the temperature. The mean number concentration of $1.95 \cdot 10^4$ #/cm^3 is measured with the SMPS and a mean yield of 16.5 % is determined. The yield decreases with temperature from 22 % to 10 % due to particle losses by thermophoresis to the water-cooled injection and sampling probe. It can be seen that the initial mobility particle diameter ($\sim$ 100 nm) decreases with the temperature, whereas the primary diameter increases. The particle mass is measured with a mass resolution of 5.6 mass class/decade to keep the measurement time short. A particle mass change during sintering is not observed and is constant (0.176 fg).

At low temperatures $< 600\,\mathrm{K}$, the mobility diameters of the upstream and downstream SMPS do not differ from each other, thus no sintering occurs. The primary particle size is calculated from the Stokes diameter measured by the DAPS and is initially 7.5 nm. Large changes in size are observed in the temperature range 800 to 1050 K resulting in a final primary diameter of 37 nm and a mobility diameter of 40 nm. This can be explained by the change in the aerodynamic behavior of the particles. The primary particle size increase while the number of primary particles per agglomerate decreases (Schmidt-Ott, 1988). This results in a more compact structure, which can be described by an increasing effective density and fractal dimension. A further increase of the temperature ($> 1100\,\mathrm{K}$) does not lead to any further size changes.

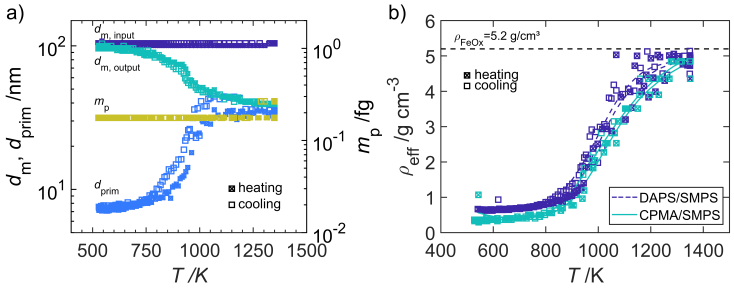

Figure D.7: a) Sintering of Fe_xO_y agglomerates measured by the change of the modal particle mass m_p, mobility d_m, and primary diameter d_{prim} as a function of a temperature ramp and b) calculated from these values the change of the effective density. Heating and cooling the furnace is indicated by filled and unfilled squares.

For fully sintered particles, primary and mobility particle diameter should be equal. Here, a small difference in size at temperature $> 1100\,\mathrm{K}$ is observed. This results from a small signal-to-noise ratio at the DAPS detector, a Faraday cup electrometer, after the classification via the aerodynamic particle diameter. At low temperatures $< 600\,\mathrm{K}$, the primary particle size is small and the lower size limit of the DAPS is reached, leading to a mismatch of DAPS ($d_{prim} = 7.5\,\mathrm{nm}$) and BET ($d_{prim} = 4\,\mathrm{nm}$) measurement at room temperature. The hysteresis is caused by the thermal load of the parts with high thermal capacity, e.g. ceramic parts, in the MFR. This leads to a temperature gradient between temperature, measured at the outer tube wall, and the temperature on the centerline. The effective density ρ_{eff} as a function of the furnace temperature is shown in Figure D.7b) and is determined in two ways from the CPMA/SMPS and

DAPS/SMPS measurands. The effective density is calculated from the particle mass (m_p) and particle volume $v_m = \pi/6 \cdot d^3_{m,output}$, respectively, fitted by the size distribution of Stokes diameter d_s and mobility diameter ($d_{m,output}$). The effective density increases with temperature from $\rho_{eff} = 0.3$ to $4.8\,g/cm^3$ calculated from CPMA/SMPS data and from $\rho_{eff} = 0.6$ to $5.0\,g/cm^3$ fitted from DAPS/SMPS data. Here, a spherical shape is assumed as the final structure after sintering. The differences between these data are caused by the set resolution of the CPMA to reduce measurement time and the measuring limits of the DAPS with a low noise-to-signal ratio as mentioned earlier. For small primary particle diameters ($< 7\,nm$), the fit between Stokes and mobility diameter distribution is difficult because the DAPS measurement provides only the descending part of the Gaussian distribution. For fully sintered particles ($T > 1300\,K$) the effective density approximates the bulk density of Fe_xO_y ($\sim 5.2\,g/cm^3$) shown as a dashed line.

IV. SUMMARY

A model flow reactor (MFR) has been designed for the investigation of particle structure formation, e.g. sintering or coating, under well-defined conditions in a laminar flow field. Precise kinetic data can be determined in a narrow temperature residence time distribution by measuring the particle structure formation with a combination of online instrumentation. The structure formation is verified by online measurements of different equivalent diameters and the calculation of the primary particle size, number of primary particles per agglomerate, and changes of the effective density by means of structural models. Comprehensive temperature measurements at the inside and outside parts of the MFR were conducted for validation of the CFD simulations. Thereby, the severe buoyancy-driven transient flow effects could be found and counter-measures could be developed in order to optimize the operating conditions of the MFR. The operation of the MFR was demonstrated by sinter experiments of size-selected Fe_xO_y nanoparticles and measurement of the structural changes with different online and offline instrumentation.

ACKNOWLEDGMENT

The authors acknowledge the support by the Deutsche Forschungsgemeinschaft (DFG) in the scope of the research group 2284 "Model-based scalable gas-phase synthesis of complex nanoparticles" (project number: 262219004, within TP5 and TP9).

DATA AVAILABILITY

The data that support the findings of this study are available from the corresponding author upon reasonable request.

REFERENCES

Babick, F. et al. (2018). "Multiparameter Characterization of Aerosols." In: *Chemie Ingenieur Technik* 90.7, pp. 923–936. ISSN: 0009286X. DOI: 10.1002/cite.201700094.

Borgwardt, R. H. (1985). "Calcination kinetics and surface area of dispersed limestone particles." In: *AIChE Journal* 31.1, pp. 103–111. ISSN: 0001-1541. DOI: 10.1002/aic.690310112.

Buesser, B. and Pratsinis, S. E. (2010). "Design of Aerosol Particle Coating: Thickness, Texture and Efficiency." In: *ACS applied materials & interfaces* 4.5, pp. 2693–2698. ISSN: 0009-2509. DOI: 10.1021/am300337c.

Chemical Rubber Company Cleveland, Ohio (1979). *CRC handbook of chemistry and physics : a ready-reference book of chemical and physical data. 60. 1979 - 1980*. Handbook of chemistry and physics. Boca Raton, Fla. [u.a.]: Taylor & Francis.

Davies, C. N. (1979). "Coagulation of aerosols by brownian motion." In: *Journal of Aerosol Science* 10.2, pp. 151–161. ISSN: 00218502. DOI: 10.1016/0021-8502(79)90064-8.

Eggersdorfer, M. L., Kadau, D., Herrmann, H. J., and Pratsinis, S. E. (2012). "Aggregate morphology evolution by sintering: Number and diameter of primary particles." In: *Journal of Aerosol Science* 46, pp. 7–19. ISSN: 00218502. DOI: 10.1016/j.jaerosci.2011.11.005.

Flynn, J. H. and Dunlap, L. A. (1986). "Temperature gradients in horizontal tube furnaces." In: *Thermochimica Acta* 105, pp. 215–218. ISSN: 00406031. DOI: 10.1016/0040-6031(86)85238-8.

Gullett, B. K., Blom, J. A., and Gillis, G. R. (1988). "Design and characterization of a 1200 °C entrained flow, gas/solid reactor." In: *Review of Scientific Instruments* 59.9, pp. 1980–1984. ISSN: 0001-1452. DOI: 10.1063/1.1140062.

Kammler, H. K., Mädler, L., and Pratsinis, S. E. (2001). "Flame Synthesis of Nanoparticles." In: *Chemical Engineering & Technology* 24.6, pp. 583–596. ISSN: 0930-7516. DOI: 10.1002/1521-4125(200106)24:6<583::AID-CEAT583>3.0.CO;2-H.

Kirchhof, M. J., Förster, H., Schmid, H.-J., and Peukert, W. (2012). "Sintering kinetics and mechanism of vitreous nanoparticles." In: *Journal of Aerosol Science* 45, pp. 26–39. ISSN: 00218502. DOI: 10.1016/j.jaerosci.2011.10.006.

Kirchhof, M. J., Schmid, H.-J., and Peukert, W. (2004). "Reactor system for the study of high-temperature short-time sintering of nanoparticles."

In: *Review of Scientific Instruments* 75.11, pp. 4833–4840. ISSN: 0001-1452. DOI: 10.1063/1.1809258.

Kruis, F. E., Kusters, K. A., Pratsinis, S. E., and Scarlett, B. (1993). "A Simple Model for the Evolution of the Characteristics of Aggregate Particles Undergoing Coagulation and Sintering." In: *Aerosol Science and Technology* 19.4, pp. 514–526. ISSN: 0278-6826. DOI: 10.1080/02786829308959656.

Lee, K. W. and Chen, H. (1984). "Coagulation Rate of Polydisperse Particles." In: *Aerosol Science and Technology* 3.3, pp. 327–334. ISSN: 0278-6826. DOI: 10.1080/02786828408959020.

Meuller, B. O., Messing, M. E., Engberg, D. L. J., Jansson, A. M., Johansson, L. I. M., Norlén, S. M., Tureson, N., and Deppert, K. (2012). "Review of Spark Discharge Generators for Production of Nanoparticle Aerosols." In: *Aerosol Science and Technology* 46.11, pp. 1256–1270. ISSN: 0278-6826. DOI: 10.1080/02786826.2012.705448.

Park, K. Y., Ullmann, M., Suh, Y. J., and Friedlander, S. K. (2001). "Nanoparticle microreactor: Application to synthesis of titania by thermal decomposition of titanium tetraisopropoxide." In: *Journal of Nanoparticle Research* 3.4, pp. 309–319. ISSN: 1388-0764. DOI: 10.1023/A:1017906916427.

Pissanetzky, S., Cingolani, H., Volpi, R., and Almagro, J. C. (1981). "Numerical simulation of the transient temperature distribution within the cladding material during annealing in a high vacuum furnace." In: *Nuclear Engineering and Design* 65.1, pp. 141–150. ISSN: 00295493. DOI: 10.1016/0029-5493(81)90127-8.

Post, P., Jidenko, N., Weber, A. P., and Borra, J.-P. (2016). "Post-Plasma SiOx Coatings of Metal and Metal Oxide Nanoparticles for Enhanced Thermal Stability and Tunable Photoactivity Applications." In: *Nanomaterials (Basel, Switzerland)* 6.5. ISSN: 2079-4991. DOI: 10.3390/nano6050091.

Post, P., Wurlitzer, L., Maus-Friedrichs, W., and Weber, A. P. (2018). "Characterization and Applications of Nanoparticles Modified in-Flight with Silica or Silica-Organic Coatings." In: *Nanomaterials (Basel, Switzerland)* 8.7. ISSN: 2079-4991. DOI: 10.3390/nano8070530.

Pratsinis, S. E. (1988). "Simultaneous nucleation, condensation, and coagulation in aerosol reactors." In: *Journal of Colloid and Interface Science* 124.2, pp. 416–427. ISSN: 0021-9797. DOI: 10.1016/0021-9797(88)90180-4.

Rosenberger, T., Kiesler, D., Hontañón, E., Fuentes, D., Ramiro, E., and Kruis, F. E. (2019). "Design and optimization of a medium flow differential mobility analyzer (MF-DMA) for classification of high-density particles." In: *Aerosol Science and Technology* 53.10, pp. 1172–1185. ISSN: 0278-6826. DOI: 10.1080/02786826.2019.1642443.

Schmidt-Ott, A. (1988). "New approaches to in situ characterization of ultrafine agglomerates." In: *Journal of Aerosol Science* 19.5, pp. 553–563. ISSN: 00218502. DOI: 10.1016/0021-8502(88)90207-8.

Schwyn, S., Garwin, E., and Schmidt-Ott, A. (1988). "Aerosol generation by spark discharge." In: *Journal of Aerosol Science* 19.5, pp. 639–642. ISSN: 00218502. DOI: 10.1016/0021-8502(88)90215-7.

Seto, T., Shimada, M., and Okuyama, K. (1995). "Evaluation of Sintering of Nanometer-Sized Titania Using Aerosol Method." In: *Aerosol Science and Technology* 23.2, pp. 183–200. ISSN: 0278-6826. DOI: 10.1080/02786829508965303.

Shrivastava, M., Gidwani, A., and Jung, H. S. (2009). "Modeling Oxidation of Soot Particles Within a Laminar Aerosol Flow Reactor Using Computational Fluid Dynamics." In: *Aerosol Science and Technology* 43.12, pp. 1218–1229. ISSN: 0278-6826. DOI: 10.1080/02786820903321716.

Tabrizi, N. S., Ullmann, M., Vons, V. A., Lafont, U., and Schmidt-Ott, A. (2009). "Generation of nanoparticles by spark discharge." In: *Journal of Nanoparticle Research* 11.2, pp. 315–332. ISSN: 1388-0764. DOI: 10.1007/s11051-008-9407-y.

Wiggers, H., Starke, R., and Roth, P. (2001). "Silicon Particle Formation by Pyrolysis of Silane in a Hot Wall Gasphase Reactor." In: *Chemical Engineering & Technology* 24.3, pp. 261–264. ISSN: 0930-7516. DOI: 10.1002/1521-4125(200103)24:3<261::AID-CEAT261>3.0.CO;2-K.

Xu, Z., Tian, X., and Zhao, H. (2017). "Tailor-making thermocouple junction for flame temperature measurement via dynamic transient method." In: *Proceedings of the Combustion Institute* 36.3, pp. 4443–4451. ISSN: 15407489. DOI: 10.1016/j.proci.2016.08.071.

E

ATMOSPHERIC-PRESSURE PARTICLE MASS SPECTROMETER FOR INVESTIGATING PARTICLE GROWTH IN SPRAY FLAMES

Samer Suleiman[a], Monika Nanjaiah[b], Ivan Skenderović[c], Thore Rosenberger[c], Frederik Kunze[d], Irenaeus Wlokas[b,e], Frank Einar Kruis[c,e], Hartmut Wiggers[a,e,*], Christof Schulz[a,e]

[a] *IVG, Institute for Combustion and Gas Dynamics – Reactive Fluids, University of Duisburg-Essen, 47048, Duisburg, Germany*

[b] *IVG, Institute for Combustion and Gas Dynamics – Fluid Dynamics, University of Duisburg-Essen, 47048, Duisburg, Germany*

[c] *NST, Institute of Technology for Nanostructures, University of Duisburg-Essen, 47057, Duisburg, Germany*

[d] *IUTA, Institut für Energie- und Umwelttechnik e.V, 47229, Duisburg, Germany*

[e] *Center for Nanointegration Duisburg-Essen (CENIDE), University of Duisburg-Essen, Duisburg, Germany*

Published in Journal of Aerosol Science, Volume 158, Page 105827 (2021)
DOI: 10.1016/j.jaerosci.2021.105827

ABSTRACT

In this work, we introduce a new ambient-pressure particle mass spectrometer (AP-PMS) that is able to detect particle-size distributions at ambient pressure using a three-stage pumping design. This device is demonstrated for direct sampling from the particle formation in spray-flame synthesis of iron oxide nanoparticles. Aerosol sampling is performed by a probe with integrated dilution that has been characterized and configured by computational fluid dynamics simulations and the chamber-skimmer system has been investigated by schlieren imaging. The system was validated by detailed characterization of a standardized sooting flame and by iron oxide nanoparticles generated in the SpraySyn burner from iron nitrate dissolved in a mixture of ethanol and 2-ethylhexanoic acid. The PMS results are compared to additional inline measurements with SMPS and ELPI+ as well as with TEM measurements of thermophoretically sampled materials from the same location in the spray flame.

1. INTRODUCTION

Gas-phase synthesis enables the continuous production of tailor-made nanoparticles (Li, Ren, et al., 2016). In such a process, a precursor is decomposed to form gas-phase species in a supersaturated environment that then give rise to particle nucleation and growth (Schulz, Dreier, et al., 2019). The energy required for the initiation of the precursor reaction can be provided by external heating, e.g., by a furnace, a plasma, or a flame. Particle synthesis processes are mainly used to produce specific materials and the materials characteristics are usually investigated by analyzing the final materials produced. This is insufficient for gaining detailed understanding of the underlying processes including precursor delivery and reaction, particle nucleation and growth, especially when using complex, potentially turbulent flow fields (Rittler et al., 2017). This understanding, however, requires as much information as possible directly out of the reaction zone to enable tailoring of research conditions as well as scale-up of processes. In ideal circumstances, flow fields, gas-phase temperature, species concentration, as well as droplet and particle size information are accessible with high spatial resolution to fully support model development and to generate databases that are suitable for validating simulation results. Such data are mainly generated via in situ optical diagnostics (Dreier and Schulz, 2016) or probe techniques. Additionally, particle sampling from hot, reactive zones for subsequent ex situ analysis is possible via thermophoretic sampling with fast-acting probes (Köylü et al., 1997).

Established measurement equipment using probe techniques such as scanning mobility particle sizer (SMPS) require comparably long sampling lines and agglomerate formation and water condensation in the sampling lines must be suppressed. With cooled-probe sampling (Goudeli, Gröhn, and Pratsinis, 2016; Gröhn et al., 2014), the sampled aerosols are typically thermally quenched and diluted with inert gas directly at the sampling probe inlet.

Sampling-induced effects and subsequent reactions can also be suppressed by molecular-beam sampling, where the sampled gases rapidly expand into high vacuum which in turn minimizes further collisions that could lead to reactions or particle interaction. This method is well established for analyzing molecular species (Taatjes et al., 2005), and has also been successfully used for analyzing particles sampled from pre-mixed flames with particle mass spectrometer (PMS). The conventional PMS consists of a two-stage skimmer-nozzle system and can be directly adopted to low-pressure reactors operating at a few ten mbar. In an electrical field, the charged particles are deflected from the underlying molecular beam as described by Roth and Hospital (1994). Due to its high

mass-to-charge ratio sensitivity, this technique is able to detect particles in the sub-10 nm range (Hospital and Roth, 1991). Information about the particle growth kinetics is thus accessible when moving the sampling nozzle relative to the reaction front. This method has also been successfully combined with time-of-flight mass spectrometry for gaseous species to cover the entire size range from atomic species, molecules and clusters to primary particles (Kluge, Wiggers, and Schulz, 2017). Molecular-beam mass-spectrometry techniques need to transfer gas (here: aerosol) samples from the reacting medium to high vacuum. Because of the limitations of the capacity of vacuum pump, in the conventional two-stage systems the pressure in gas of interest is limited to below $\sim$ 100 mbar. For several applications, assessing reactive media at atmospheric pressure, however, would be of high interest. In this paper, we present a PMS approach capable for this application.

With conventional PMS systems, nanoparticle synthesis has been systematically studied in low-pressure flames and plasmas where single gaseous or pre-vaporized precursors are used. The information gained from these experiments led to the development of reaction mechanisms that can then be applied to atmospheric-pressure production environments (Rahinov et al., 2021). In such processes, for materials, that contain two elements from two different precursors, in most cases core-shell particles will form, only in specific cases the decomposition and particle nucleation characteristics match well enough to form mixed phases (Bywalez et al., 2013). Utilizing spray flames in combustion synthesis has the advantage that a variety of inexpensive non-volatile precursors can be used and combined, e.g., for the generation of multinary oxides with a wide variability in composition. This opens up pathways to a wide range of materials and potential to industrial applications (Angel et al., 2020; Cho et al., 2009; Kammler, Mädler, and Pratsinis, 2001; Mädler et al., 2002; Tricoli and Elmøe, 2012; Weise et al., 2015). The precursors including salts are dissolved in combustible liquids and solvent mixtures that are atomized and burned (Teoh, Amal, and Mädler, 2010) in a piloted flame. To prevent premature evaporation of the spray and provide high production rates, spray flames for nanoparticle synthesis are usually operated at around atmospheric pressure (Hardt et al., 2015). This, however, prevents the use of the previously established conventional PMS. Because changing the pressure fundamentally changes the process, also fundamental studies need to be carried out at atmospheric pressure. To enable the generation of comprehensive data sets regarding the spray-flame synthesis of nanoparticles, a standardized burner geometry, the so-called SpraySyn burner (Schneider et al., 2019) has been defined. Its standardized design is used in a multitude of labs (Aßmann et al., 2020; Martins, Costelha,

and Neves, 2020; Stodt, Liu, et al., 2021; Tischendorf et al., 2021) with a variety of measurement approaches and is the basis for the experiments presented in this paper.

This paper deals with the development and characterization of an AP-PMS that is then used for the investigation of the growth process of nanoparticles in a spray-flame reactor. In this paper, the design and functionality of the newly developed ambient-pressure particle mass spectrometer (AP-PMS) including a sampling system suitable for the spray-flame processes is presented. The system is characterized by simulations and comparative experimental studies based on thermophoretic sampling with TEM, and probe sampling with SMPS.

1.1 EXPERIMENT

1.1.1. Spray-flame reactor

The SpraySyn burner is a standardized and characterized burner which serves as a reference system in the spray flame synthesis under standardized operating conditions as described before (Schneider et al., 2019) and is used without any modifications. The particle synthesis takes place at 940 mbar in a closed reactor chamber as illustrated in Figure E.1 and the flame reactor is operated under the conditions given in Table E.1. For the spatially-resolved investigations of the particle generation, the spray-flame reactor and the PMS are connected via a system that enables the exact positioning of the sampling probe via translation stages. Horizontal positioning of the sampling probe enables addressing exact radial positions with respect to the spray flame while vertical positioning is done by an adjustment of the vertical burner position inside the burner chamber. The material system considered for the measurements presented in this work is iron oxide nanoparticle formation from a solution of iron nitrate in a mixture of ethanol and 2-ethyl hexanoic acid.

The combustible precursor solution is atomized by a two-fluid nozzle with external mixing that leads to atomization of the precursor solution due to the different relative velocities between the liquid and the oxygen that is used as dispersion gas. The generated spray passes through a premixed methane/oxygen flame and ignites into a spray flame. Within the spray flame, the precursor decomposes leading to small molecular species that form the desired particles by nucleation, surface growth, coalescence, and coagulation. A nitrogen co-flow stabilizes the spray flame, shields the flame from the environment, and ensures fast transport of the particles from the reactor to the downstream filter unit. To protect

Flow channel	Specifications	Flow rate
Pilot O_2	Gas, purity $\geqslant$ 99.5 mol.%	16 slm
Pilot CH_4	Gas, purity $\geqslant$ 99.5 mol.%	2 slm
Co-flow N_2	Gas, purity $\geqslant$ 99.9 vol.%	120 slm
Dispersion gas O_2	Gas, purity $\geqslant$ 99.5 mol.%	10 slm
Quenching gas compressed air	Gas, purity $\geqslant$ 99.9 vol.%	145 slm
	Iron(III)-nitrate-nonahydrate $\geqslant$ 98 %	
Precursor solution	in 35 vol.% ethanol and	2 mL/min
	65 vol.% 2-ethylhexanoic acid	
Precursor concentration	0.05 mol/L, 0.1 mol/L, 0.2 mol/L, 0.5 mol/L	

Table E.1: Materials and flow rates for iron oxide particle synthesis with the SpraySyn burner (Schneider et al., 2019).

the filter from overheating and to prevent further particle interaction, the aerosol is quenched by an additional compressed air gas flow.

1.2. Sampling probe

Continuous sampling from particle-forming flows requires small-diameter probes to minimize the perturbation of the flow. At the same time, a sufficiently large probe orifice is required to prevent clogging. Common capillaries with inner diameters between 0.8 and 1.7 mm would be large enough to prevent clogging but they would also promote particle growth by condensation and coagulation along the flow path (Fissan and Schwientek, 1987) when applied without dilution/quenching. To prevent further growth after sampling, the aerosol sample must be quenched as early as possible to reduce temperature and particle number concentration. For this purpose, a sampling probe described by Goertz et al. (2011) was used that consists of a concentric arrangement of capillaries and tubes (schematics shown in Figure E.2). The particles are sampled directly from the flame through a 0.8 mm nozzle inlet and directed to the center capillary. Through a coaxial tube, nitrogen is fed for dilution and typical dilution ratios nitrogen/sampling gas are in the range between 4 and 10 as will be discussed later. The expected particle number concentration can be estimated from the precursor concentration and the mean particle diameter and is in the order of $1 \cdot 10\,\#/\mathrm{cm}^3$ for the smallest particles. The sampling probe is surrounded by a cooling jacket to prevent heat damage. The probe's tip is inclined towards the flow to prevent recirculation at the nozzle.

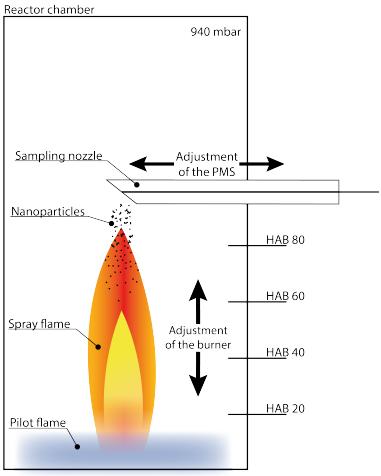

Figure E.1: Illustration of the reactor chamber with height-adjustable spray flame and sample probe movable in radial direction. Chamber pressure: 940 mbar. The height above burner (HAB) defines the distance between the burner outlet and the inlet of the sample probe and is adjusted with the vertical position of the burner related to the sampling probe.

1.3. Fluid dynamics simulation

Particle characterization via online sampling provides high accuracy and good resolution of the particle-size distribution. The sampling influences the measurement by perturbation of the flow. This is unavoidable if the outer design of the probe is fixed, but needs to be quantified in complementary experiments or simulations for possible correction of the measurement. In this work, the effect of the sampling nozzle is investigated by computational fluid dynamics (CFD) simulations in addition to the experimental investigations to (i) estimate the effective sampling volume, which determines the spatial resolution of the sampling. The sampling volume is defined as the area surrounding the probe inlet orifice in which the gas is accelerated due to suction towards the probe's orifice. (ii) Additionally, simulations are used to examine the further fate of the particle-laden gas after entering the probe and the effect of dilution.

The computational domain is the volume of the probe itself (referred to as 'inner' section), immersed into a sufficiently large section of the reactor volume (referred to as 'outer' section). The dilution gas is nitrogen at a prescribed mass flow rate and at an inlet temperature of 300 K. The state of sampled gas was estimated representative from the simulations

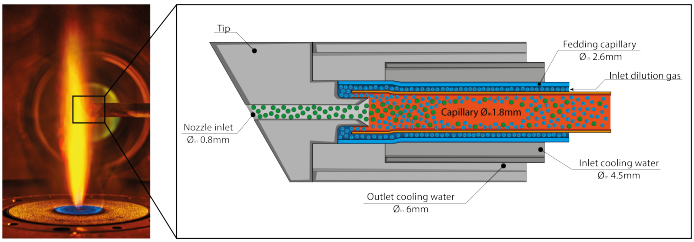

Figure E.2: Left: Image of the sampling from a spray flame. Right: Cross-section of the sampling probe consisting of several concentrically arranged capillaries and tubes for the rapid dilution of the aerosol after sampling. The tip is inclined by 30° to prevent the sampling of recirculated aerosol.

of by Rittler et al. (2017) and Schneider et al. (2019). The cold sampled gas was set to be nitrogen in order to match the setup of sampled flux measurements (cases 1a and 2a in Table E.2). The hot sampled gas was assumed to have the composition of major components of burned process gases at a temperature of 2300 K. The mole fractions were $X_{O2} = 0.66$, $X_{H2O} = 0.21$ and $X_{CO2} = 0.13$, and the specific heat ratio at this temperature was $\gamma = 1.235$. The thermodynamic properties of the gases were represented as NASA polynomials, the diffusive mixing was computed under the assumption of a unity Lewis number. The gas in the outer section was at rest or flowing at $u = 20\,\mathrm{m/s}$ crosswise to the probe (cases 1c and 2c in Table E.2).

The nature of the modeling study is quantitative but with several restrictions: The probe itself is just a part of the complex particle-size detection system. It is connected via a series of narrow tubes with the vacuum section of the PMS. The wall roughness of the tubes and the geometry of the connectors are not well known, implying large uncertainty in fluid mechanical loss characteristics. The geometrical uncertainty of the piping between the probe and the vacuum system makes a sufficiently accurate calculation of the pressure at the intersection of probe-piping an intractable problem. A computation of the flow state at the interface between the probe and the piping using the assumption of a choked Fanno-flow provided a plausible estimate, but was not sufficiently accurate to reproduce the relation between the sampled mass and the dilution-gas flow rate. At least the total mass flow rate should be independent of the down-stream state in the vacuum section (PMS), as the flow is chocked due to the large pressure ratio.

All simulations were performed with the open-source CFD software OpenFOAM, extended for the detailed computation of the molecular

transport properties of gas mixtures. An exhaustive description of the implemented models was provided by Deng et al. (2015). The sampling was investigated for two different dilution flow rates, for the cold sampling of resting gas, and for hot sampling of resting and moving gas in the outer section. The temperature of the water-cooled probe was assumed to be constant at $T = 300\,\mathrm{K}$. The assumption of isothermal, cold walls is very strong, thus future investigations will include a conjugate heat transfer model. The boundary conditions are summarized in Table E.2. The simulation-grid was adapted to the geometric details with cell sizes ranging from 0.025 mm inside the probe, to 0.4 mm in the far field of the outer section. The total number of computational cells was approx. $1.5 \cdot 10^6$. To ensure sufficient grid resolution, different computational meshes were compared, from which the economical variant was chosen for all production simulations. The Reynolds numbers inside the orifice ranged from $Re = 350$ in the hot sampling, to $Re = 2000$ in the cold sampling. The Reynolds number inside mixing section ranged from $Re = 2000$ in hot sampling, to $Re = 3600$ in cold sampling. This regime of Reynolds numbers is problematic for most turbulence models based on the Reynolds-averaged Navier-Stokes equations (RANS), especially, as the density also varies notably. Because the Re numbers during sampling of hot gas remained smaller than the critical limit for transition to turbulence in circular pipes ($Re_{Cr} < 2300$), we decided to perform the simulations without turbulence modeling under acceptance of possible deviations for the simulation of the cold sampling. The cold sampling was simulated to verify the reliability of the simulation by comparison to measurements of the mass flow rates. In the reference-experiment, the sampled gas was nitrogen – like the dilution gas. In the reference-simulation, the outer domain was filled with a gas of identical thermodynamic and transport properties, but allocated to a different label in order to be distinguishable. The total pressure of the outer domain was set to 100.000 Pa.

We decided to simulate the sampling at just a single hot condition, as the temperature at the sampling positions (Figure E.1) ranges from 2000 to 2500 K. In this temperature regime, the flow inside the orifice and inside the mixing section of the probe will remain laminar. In order to cover a wider range of sampling conditions, especially to identify the transition regime of the flow, would require a separate simulation study and is planned for the future.

1.4. Thermophoretic sampling and TEM analysis

For the thermophoretic particle sampling, a proprietary system (Kunze et al., 2019) was used as shown in Figure E.3. A TEM grid is placed

Case	Dilution gas mass flow /slm	Outlet pressure /kPa	Temperature /K	Sampled flux (simulation) /slm	Sampled flux (measurement) /slm
1a, cold	3	92.7	300	2.012	2.016
1b, hot	3	92.7	2300	0.524	-
1c, hot	3	92.7	2300	0.464	-
2a, cold	7	96.2	300	1.617	1.600
2b, hot	7	96.2	2300	0.397	-
2c, hot	7	96.2	2300	0.383	-

Table E.2: Summary of boundary conditions for the investigated cases. The ambient pressure was set to 1 bar for all simulations. The cases 1c and 2c refer to sampling from hot gas flowing at $u = 20\,\mathrm{m/s}$.

on a holder that is weighted with defined weights inside the sampling system. The sampling system is accelerated into the reaction chamber by a double-acting pneumatic cylinder. Shortly before the center axis of the spray flame is reached, the sampling system is stopped abruptly while the holder further moves up to the center axis due to its inertia. With this movement, the previously covered TEM grid is exposed for a short time while a spring inside the sampling system is expanded and accelerates the holder back into the sampling system. The combination of the weights and the spring constant determine the displacement and the exposure time of the TEM grid, so that the integral thermophoretic deposition time as well as the sampling position of the grid can be defined.

The exact position and the residence time were verified with a high-repetition-rate camera and is 14 ms for the used configuration. Due to the low particle number concentration within the spray flame, a simple exposure of the grid is not sufficient for a representative analysis for the spray flame. For this reason and in contrast to the sooting flame (Santoro burner, as described in the results section), the exposure was repeated several times resulting in a total residence time of 210 ms for the spray flame and 140 ms for the Santoro flame.

1.5. Particle mass spectrometer

The particle mass spectrometer (PMS) used in this work is based on the conventional design for low-pressure operation (Roth and Hospital, 1994), which has been extended with an additional pumping stage for operation under ambient pressure conditions (Figure E.4). The first pumping stage is equipped with a rotary vane pump with a pumping capacity of $100\,\mathrm{m^3/h}$, while the second and third stages are each supplied with tur-

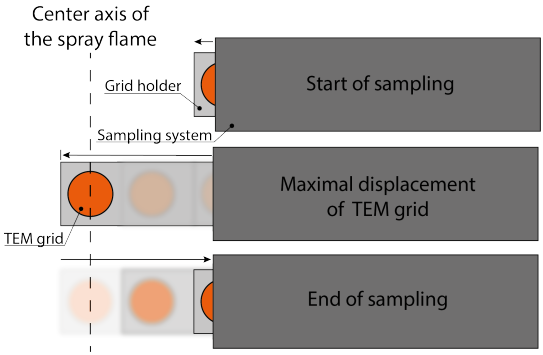

Figure E.3: Illustration of the thermophoretic particle sampling system. A TEM grid is placed into a weighted grid holder which is hidden in the sampling system. The accelerated system is stopped in front of the spray flame and the inertia of the grid holder moves the TEM grid into the flame. A spring inside the sampling system stops the TEM grid at the centerline of the spray flame and accelerates it back into the sampling system.

bomolecular pumps (2200 and 450 L/s, respectively). Aerosol sampling is done via the probe described above that is used as an inlet to chamber 1 with a pressure of 1 to 10 mbar (cf. Figure E.9). The expanded gas is guided through two skimmers (orifice diameter 0.5 mm) into chamber 2 (10^{-5} to 10^{-3} mbar) and 3 (10^{-6} to 10^{-5} mbar). In the latter, the particle mass is measured based on particle deflection in an electric field and particle velocity and the relative contribution of each particle-size class is determined from the charges of the respective particles by a Faraday cup connected to an electrometer. Depending on the deflection voltage, the particle current is a measure for the number concentration of a specific mass range. Details regarding the measurement with the PMS and the determination of particle sizes can be found in literature (Hospital and Roth, 1991; Roth and Hospital, 1994) as well as in the supplementary material.

1.6. Conventional aerosol measurement techniques

Conventional aerosol instrumentation is used in parallel to the PMS to determine particle-size and -mass distributions, and to compare to the PMS measurements (Figure E.5). A sample flow rate of 0.72 slm was sucked-in by the same sampling probe mentioned above and directly quenched

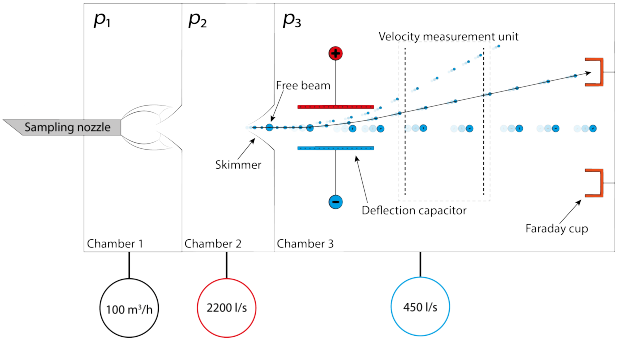

Figure E.4: Principle of the three-stage particle mass spectrometer. The gas exiting the sampling probe (left) passes the two subsequent skimmers connecting chambers 1 and 2, and 2 and 3, respectively. Charged particles in the free aerosol jet are deflected in a variable electric field and detected with a Faraday cup. With a known particle velocity, a measurement of the particle-mass distribution is possible by variation of the deflection voltage, which can be converted to particle-size distributions based on the density of the respective material.

with 10 slm of N_2 at the probe tip. The pressure p_{vac} in the sampling line is kept constant at 150 mbar by adjusting the flow rate via a needle valve V1 with a HEPA-filter upstream of the vacuum pump. While the PMS is suitable for high particle number concentrations sampled from a wide pressure range, most of the conventional aerosol instrumentation require atmospheric pressure and a particle number concentration below 10^7 #/cm^3. The aerosol is transferred back to atmospheric pressure from low-pressure and directly diluted by a VIP-4 low-pressure ejector (VIP-4, Landenfeld, Kassel, GER) based on the Venturi principle (Rosenberger et al., 2018). The Venturi nozzle is operated with a driving gas pressure $p_{in} = 3.45$ bar (a flow rate of 55 slm) entraining a sample flow rate of 0.75 slm at 150 mbar. For maintenance, the VIP-4 with aerosol instrumentation can be disassembled from the spray flame reactor by closing valve V2. The sample flow is diluted and transferred to atmospheric pressure by the driving gas, forming the outflow rate of approx. 56 slm. Atmospheric pressure downstream of the VIP-4 is ensured by a bypass with a HEPA-filter. The outflow of the VIP-4 is connected to a scanning mobility particle sizer (SMPS, 3938, TSI, Minneapolis, US), and an electrical low-pressure impactor (ELPI+, Dekati Ltd., Kangasala, FIN) with sample flow rates of 1.5 slm (SMPS) and 9.4 slm (ELPI+), respectively. The residence time in the measuring line from VIP-4 to a first classifier with Long DMA (3082 and 3081, TSI) upstream of the SMPS is reduced

by sucking an additional mass flow rate of 40 slm via a needle valve V4 and a pump. A HEPA-filter with needle valve V5 and pump is used in parallel to the SMPS and increases the sample flow rate by 1.5 slm to a total of 3 slm. The first classifier within the dashed box in Figure E.5 is used to determine the particle-charge distribution by selecting a defined particle mobility and measurement of the mobility-size distribution with a SMPS downstream. The L-DMA is operated with an aerosol to sheath gas ratio of 3/15 ($\beta = 0.2$). This classifier with DMA is not needed for the measurements of the particle size and mass distribution and can be bypassed. The aerosol is neutralized with an x-ray neutralizer (3088, TSI) upstream of the SMPS. The ELPI+, measuring the distribution of aerodynamic diameters, is connected in parallel to the SMPS. A needle valve V3 downstream of the junction to SMPS enables additional dilution of the aerosol for ELPI+ measurements, but is not needed in this setup.

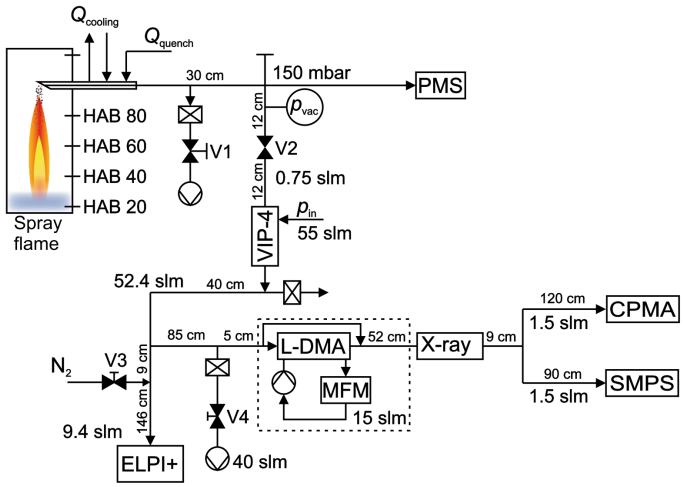

Figure E.5: Setup of the online instrumentation connected to the spray-flame reactor to measure the particle size distribution. The setup is modified by L-DMA with classifier, within the dashed box, to determine the charging probability as a function of the particle size.

2. RESULTS

2.1. Aerosol sampling

To ensure reproducible aerosol sampling, characterization of the sampling probe is required. Figure E.6 shows the sampled volume flow rate at room temperature as a function of the dilution mass flow. It can be seen that the maximum sampled volume flow of 2.14 slm slowly decreases with the addition of the dilution gas up to a volume flow of 3 slm and decreases very strongly thereafter until the sampling stops at 11.6 slm of dilution gas. The dilution factor shows a linear increase up to a factor of about 3 until a dilution gas flow of 6 slm and begins to increase very strongly afterwards. The maximum determinable dilution of the sample probe is 11 slm of dilution gas and has a factor of about 37. For the most efficient sample collection, it is important to have the highest possible sample volume flow at the highest possible dilution. Therefore, the working range of the sample probe shown here was defined for a dilution gas flow between 3 and 7 slm.

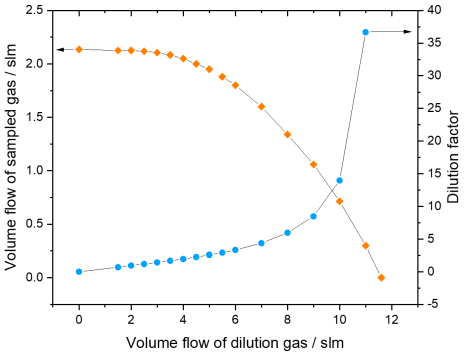

Figure E.6: Characterization of the sampling probe at room temperature and ambient pressure. Mass flow of sampled gas (left) and the related dilution factor (right) as function of the nitrogen dilution gas volume flow.

These results give information about the characteristics of the sampling probe at room temperature and do not draw any conclusions about sampling directly from the flame. It is also not clear, which volume in front of the probe is involved in the sampling process and how the transfer time is until the dilution is successful. These questions are addressed via the simulations below.

2.2. *Simulation results*

The simulations revealed a compact sampling volume with a diameter of approximately three times the probe inlet diameter. This finding is in accordance with the previous experience with molecular beam sampling nozzles (Deng et al., 2015), where the diameter of the sampling volume was also estimated to three times the orifice diameter. The gas velocity in the inlet tube is highly affected by the temperature-dependent viscosity resulting in small Reynolds numbers and high velocities at high temperature. The total mass-flow rate at flame temperature is roughly four times smaller compared to cold-gas sampling due to the lower density of the hot gas. Figure E.7 shows the velocity magnitude and quench-gas concentration contour plots in the vertical slice through the probe. The hot sampled gas (Figure E.7, case 1c) is accelerated much stronger in the probe compared to the room-temperature one (Figure E.7, case 1a) but due to its lower density and therefore smaller momentum, the gas jet inside the probe is shielded completely from the walls. This applies to hot sampling from flowing or resting gas. The sampling volume is indicated by the white dashed line in the velocity-contour plot in Figure E.7. The size of this zone is independent of the temperature of the sampled gas, but its shape is strongly affected by the external flow. At the acute angled side of the inlet, the flow strongly detaches and does not re-attach in the cold sampling case because of the smaller viscosity and higher momentum. This detachment causes strong deflection of the sampled gases in the dilution section of the probe. Such detachment must always be expected at sharp inlets and is usually minimized by a 'well-rounded' design of the inlet. In the present case, the required rounding of the inlet would have been large due to the inclination of the probe towards the sampled gas flow, resulting in a strongly enlarged sampling volume. Therefore, no further design measures were taken, but the operator of the probe needs to be aware of this behavior that can cause that particles accumulate and deposit at the wall in the wake of such detached flows. When the sampled gas enters the inside of the probe, it is shielded from its wall by the dilution gas. This shielding fails at small flow rates but is sufficient in case 2a at a dilution of 7 slm. This problem does not appear in sampling from hot atmosphere. Due to the nearly constant Prandtl and Lewis numbers, the temperature distribution due to the mixing shows similar contour as the concentration distribution in both cases (Figure E.7).

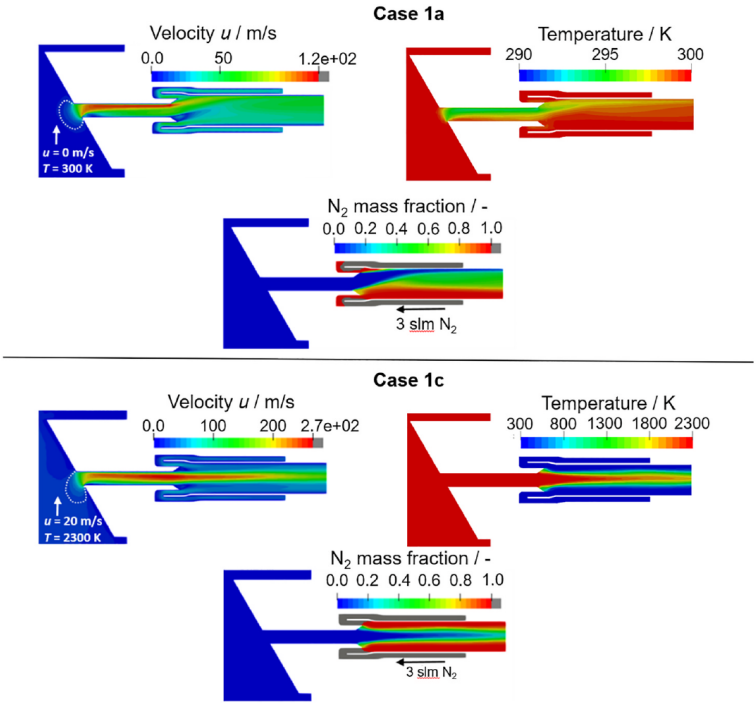

Figure E.7: Gas velocity (absolute values), temperature and dilution gas mass fraction for the sampling of cold (case 1a) and hot (case 1c) gases with 3 slm dilution mass flow rate. The sampling volume is indicated by the white-dashed line. The hot case is shown for the probe placed cross-wise in a flow at 20 m/s.

2.3. Experimental results

Based on the previous characterizations, the sampling probe was checked for correct operation by using a co-flow-stabilized standardized non-premixed sooting jet burner (so-called Santoro burner, Schulz, Kock, et al., 2006) that is operated with ethylene/air (0.231 slm ethylene with a 43 slm air co-flow). As shown in Figure E.8, a sample for characterization was taken at the height above burner (HAB) of 50 mm using the TEM sampling system (orange) and then repeated at the same height with the sampling system (blue) in combination with the vacuum system of the PMS. After sampling into the PMS, the particles are expanded into a particle free jet and deposited directly onto a TEM grid in the analyses

chamber. In order to achieve the desired combination of a shielding the sample flow from the walls inside the probe and a preferably high sample mass flow, a N_2 mass flow of 6 slm was chosen as dilution gas. In addition to the types of sampling, the procedure was repeated using a capillary (inner diameter 0.8 mm) without dilution. The PMS measurements of the particle-size distribution after sampling with the sampling system described above directly from the flame at $HAB = 50$ mm shows a count median diameter (CMD) of 29 nm, which agrees well with literature data (Schulz, Kock, et al., 2006). As expected, sampling with a simple capillary without quenching results in a significant increase in CMD to 34 nm. The preservation of the particle size distribution after sampling with our sampling system enables representative measurements with the PMS, which is essential for the subsequent measurements in the nanoparticle generating flame.

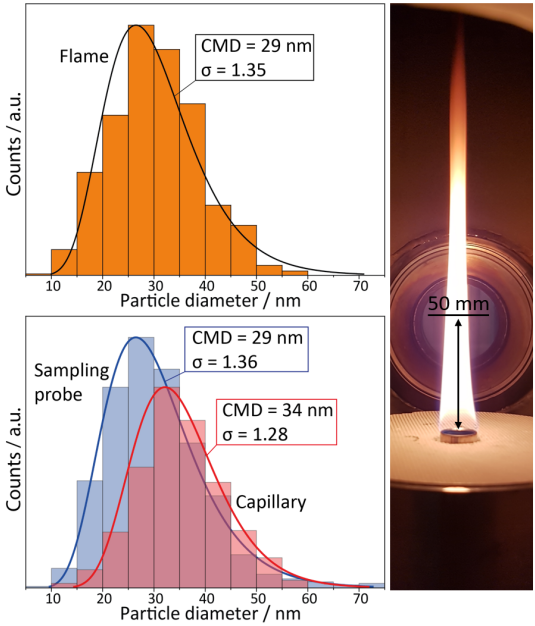

Figure E.8: Right: Photo of the Santoro burner with the on-axis measurement location at $HAB = 50$ mm indicated. Left: Histogram of TEM particle sizes from thermophoretic sampling from the flame (orange) and for sampling from the aerosol behind the simple capillary (red) and the sampling tool with N_2 dilution (blue).

2.4. Pressure measurement in the AP-PMS

The PMS measurement technique requires a strong pressure drop enabling supersonic expansion as well as an independently constant low pressure in the analysis chamber of less than around 10^{-4} mbar. Therefore, pressures for all three chambers were recorded as a function of the reactor pressure p_0 for the newly developed three-stage AP-PMS (Figure E.9). With increasing p_0, the pressure in the respective chambers also increases up to 13 mbar for the first (black squares), $1 \cdot 10^{-3}$ mbar for the second (red circles), and $3 \cdot 10^{-5}$ mbar for the third chamber (blue triangles). The strong increase of the respective chamber pressures with increasing reactor pressure (low initial pressure followed by a leveling-off in the higher-pressure ranges in chamber 1 and 2 and the only moderate increase of p in chamber 3) is due to the pressure-dependent pumping capacity of the individual pumps and the flow conditions in the individual chambers. The minor pressure increases in chamber 3 (blue) is typically observed for turbomolecular pumps operating in the free molecular regime while the conditions in the chamber 2 (red, also turbomolecular pump) changes between 100 and 200 mbar reactor pressure from free molecular to Knudsen regime. As a result, viscous properties of the gas change and the pumping speed of the respective turbomolecular pump is reduced. The conditions in the first chamber are in the continuum regime and show the typical pressure-dependent behavior of a rotary vane pump.

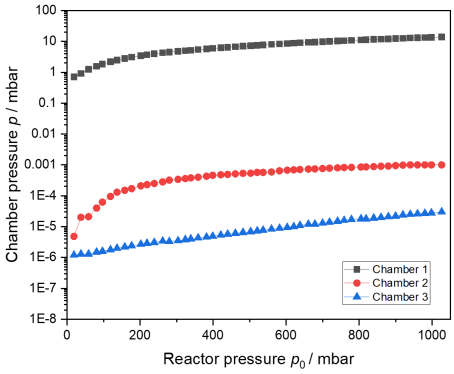

Figure E.9: Pressures p_1, p_2, and p_3 in the three vacuum chambers of the atmospheric-pressure PMS as a function of the reactor pressure p_0.

It was confirmed that the pressure conditions in the analysis chamber 3 match the high-vacuum requirements for PMS measurements. However,

initial experiments to determine particle size measurements with this setup failed. The analysis of possible reasons led to the assumption that problems occurred in chamber 1 since measurements at reduced pressure (without chamber 1) were successful.

The main difference between the new AP-PMS and the conventional low-pressure PMS is the extension of the pressure gradient by an additional chamber and the longer path for the sampled gas. While in the low-pressure PMS the samples are taken by a skimmer from the zone of interest, in the AP-PMS the samples are taken by a modified capillary with a certain length. This indicates that the desired supersonic expansion may differ between the two systems and thus might prevent a successful measurement with the AP-PMS. The formation of a supersonic expansion is a basic requirement for the generation of a free jet. The extracted aerosol is expanded into a low-pressure chamber, which accelerates the particles from the continuum into the free-molecular flow region. The supersonic expansion simultaneously forms a rotationally symmetric structure of compression shocks (frame C in Figure E.10), which is closed by a vertical compression shock (Mach disc) as a shock cell (Bier and Schmidt, 1961). The length of the shock cell is determined by the length x_M (frame B in Figure E.10)

$$x_M = \frac{2}{3} d_{S0} \sqrt{\frac{p_0}{p_1}} \tag{E.1}$$

between the exit of the sampling and the position of the Mach disc and can be determined theoretically by Equation (E.1) for nozzles and short tube as sampling probe (Ashkenas and Sherman, 1964). In Equation (E.1), d_{S0} describes the orifice diameter, p_0 is the pressure in front of the nozzle and p_1 the pressure in chamber 1. Inside the shock cell there is an area that is completely free of compression shocks (so-called zone of silence, frame A in Figure E.10) and the particles are accelerated without obstruction into the free molecular range. In order to maintain the free molecular flow condition, the particles must be extracted in the zone of silence by a skimmer before they pass through the Mach disc. Particles that pass through the Mach disc are decelerated back into the continuum region and must be re-accelerated. In addition, the particles can interact more strongly with each other due to the strong reduction of the mean free path and may change or lose their imposed charge (Chambers et al., 1991).

The estimation of x_M applies to nozzles or short tubes and can be used for low-pressure reactors, but differs for longer tubes such as the sampling probe and therefore cannot be reliable applied to AP-PMS. The

influence of the sampling probe on x_M was investigated with a double-lens schlieren setup according to Toepler (Settles and Hargather, 2017; Weinstein, 2010). Figure E.10 shows the change of x_M as a function of p_1 for a capillary (red) with an inner diameter of 1.7 mm and a length of 400 mm and x_M calculated from Equation (E.1) for a nozzle (black) with the same diameter.

Both curves show an identical decrease with increasing chamber pressure, whereby the values of the capillary are clearly below the calculated values of the nozzle expansion. This indicates that the supersonic expansion with a capillary follows the known theory, but is additionally influenced by the length of the capillary. With increasing length, the flow resistance inside the capillary increases and the pressure pexit at the outlet of the capillary decreases with the length (Jousten, 2004). As for the same orifice diameter, the distance between the Mach disc and the outlet depends only on the difference between p_{exit} and p_1. With decreasing p_{exit}, the pressure difference also decreases and x_M is therefore generally smaller than for expansion through a nozzle.

As the chamber pressure increases, the zone of silence decreases as shown in frames A–C in Figure E.10 and the Mach disc moves closer to the capillary exit. In addition, with higher chamber pressure, crossing compression shocks (shock diamonds) form behind the Mach disc. These additional compression shocks can further intensify the interaction between particles or the surrounding gas when they leave the zone of silence (Panda and Seasholtz, 1999). Therefore, not only the distance to the capillary outlet but also the back pressure is important for maintaining free-molecular conditions. Due to the high values of x_M for low pressures and the decrease in x_M as shown in Figure E.10, pressures below 25 mbar can enlarge the zone of silence sufficiently and distances between the sampling outlet and the skimmer inlet below 5 mm ensure a safe placement of the skimmer in the zone of silence. For the AP-PMS, a distance of 4.5 mm was chosen, which maintains the flow conditions and allows the particles to enter the analysis chamber without disturbance under free-molecular conditions.

Figure E.11 right shows PMS particle-size measurements on inline-sampled (orange) and TEM measurements of thermophoretically-sampled iron oxide nanoparticles (red) generated in the spray-flame. For all flame heights, the CMD for both measuring systems agrees well. This indicates that the PMS enables reliable inline measurements of particle formation and growth in the spray flame. As an example, Figure E.11 shows the normalized probability density function (PDF) as a function of the particle diameter d_{p} and is a typical PMS signal at different HAB for a 0.05 M iron(III)-nitrate-nonahydrate spray flame as described in Table E.1.

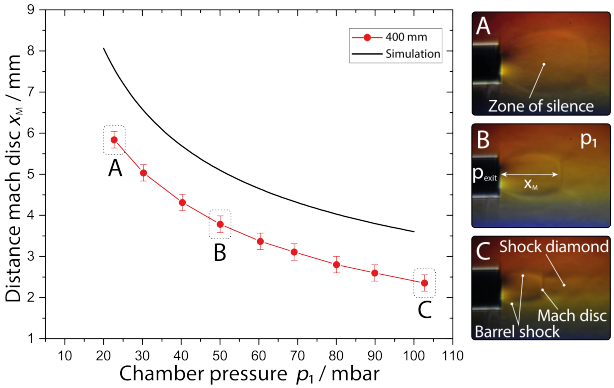

Figure E.10: Left: Distance x_M from the capillary exit to the Mach disc as a function of the chamber pressure p_1. Right: Schlieren images of shock cells at 23 mbar (A), 50 mbar (B) and 103 mbar (C). Due to the higher flow resistance inside the capillary, the pressure difference required for supersonic expansion decreases and results in smaller values for x_M compared to a nozzle. PMS measurements of spray-flame generated iron oxide nanoparticles.

The strongest signal is to be detected at the lowest height (HAB= 40 mm), which decreases in intensity and widens with increasing height. This height-dependent pattern shows the particle formation with a high particle number concentration occurred at lower heights and that the distribution subsequently decreases in particle number along the flame. The reduction of the left shoulder from HAB= 40 to 50 mm and the complete disappearance on HAB= 60 mm with a simultaneous shift of the whole distribution to larger particle diameters indicates that the nucleation process already occurred at lower heights and the system had already started growing earlier at the expanse of smaller particles. It is noticeable that the CMD of the particle size distribution remains constant regardless of the height and does not shift to larger particle diameters with increasing height, as would expected (Hospital and Roth, 1991). Only on the basis of the data presented, a valid conclusion cannot be made. However, it can be assumed that micro explosions induced during the synthesis by the use of 2-ethylhexanoic acid (Li, Pokhrel, et al., 2020; Rosebrock et al., 2016) could lead to this shown behavior.

Figure E.12 illustrates the measured particle-size distribution for different molar concentrations of iron nitrate for a constant HAB= 70 mm as described in Table E.1 while on the right side the corresponding CMD is plotted as a function of the precursor concentration. With the increase

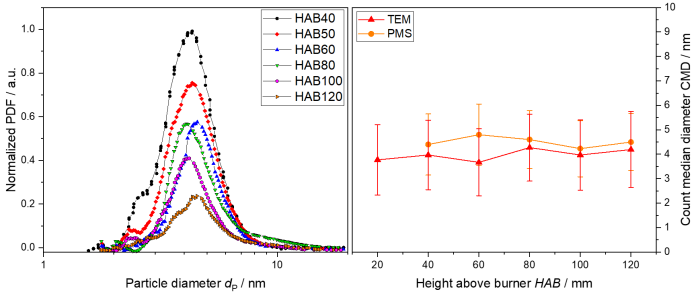

Figure E.11: Left: Normalized particle size distribution for different HAB measured with AP-PMS for iron oxide particles in a 0.05 M iron nitrate spray flame as described in Table E.1. Right: Comparison of the CMD of iron oxide particles in a 0.05 M iron nitrate spray flame (Table E.1) as function of HAB for TEM (red) and PMS (orange).

of the precursor concentration, the CMD of the lowest molar concentration (green) of 0.05 mol/L $Fe(NO_3)_3 \cdot 9\,H_2O$ is shifted from 4.4 to 5.6 nm (blue), 7 nm (red) and 7.8 nm (black) for the maximum concentration of 0.5 mol/L $Fe(NO_3)_3 \cdot 9\,H_2O$.

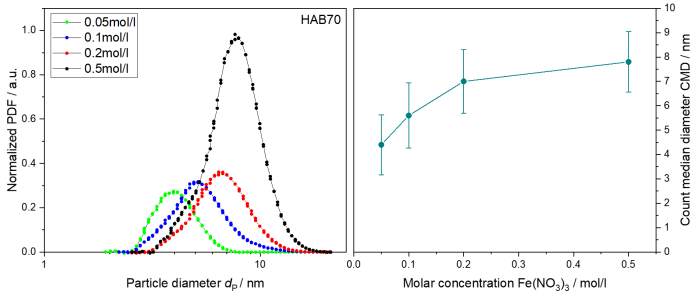

Figure E.12: Left: PMS-Signal as function of the molar precursor concentration for a spray flame on $HAB = 70$ mm as described in Table E.1. Right: Resulting dependence of the CMD of the measured particle-size distribution on the precursor concentration.

The strong shift of the CMD with increasing precursor concentration indicates an earlier start of the particle formation. This is caused by a concentration-dependent shift of the zone of supersaturation required for particle nucleation in the direction of the burner outlet. Due to the shifted point of nucleation, the particles have a longer time for growth by coagulation and coalescence and the particle diameter can increase

more with increasing concentration. Furthermore, an increase of the detector current with increasing concentration can be observed. Because the detection current is proportional to the particle number in the free jet, the increase shows that the particle number concentration in the spray flame increases with increasing precursor concentration. This indicates that most of the injected precursor is transferred from the droplet into the gas phase and is actively involved in the particle formation in dependence of concentration.

2.5. Comparison with conventional aerosol measurement techniques

The opportunity to operate the new AP-PMS at atmospheric pressures enables the comparative investigation with various aerosol analysis techniques. The AP-PMS is more robust against higher particle number concentrations with the transfer of the particles into free molecular region by supersonic expansion (Gröhn et al., 2014), compared to the established particle mass measurement techniques like APM or CPMA. For reliable CPMA measurements, atmospheric pressure needs to be ensured and the particle number concentration should be below 10^7 #/cm^3. Several groups studied the particle-size evolution along the spray-flame centerline by combining particle mobility measurements (SMPS) and thermophoretic sampling (Goudeli, Gröhn, and Pratsinis, 2016; Gröhn et al., 2014). They showed conventional aerosol measurement techniques to be well suited to study the particle-size evolution and morphology in the upper flame region, while thermophoretic sampling was applied in the lower flame region. However, no explicit reason was stated for this preference. One possible explanation might be to prevent droplets being sucked into the sampling probe and therefore interfere with the measurement. To our knowledge, there are no publications describing the usage of conventional aerosol measurement techniques in the lower flame region in spray-flame synthesis of nanoparticles. For better understanding of the particle formation mechanisms however, size information from the lower flame region is important as here particles are initially formed. Often these particles are smaller than 10 nm and therefore at the lower size limit of conventional aerosol measurement setups. As will be discussed in this chapter a conventional SMPS setup can be well utilized to measure particles in the lower flame region if technical limitations of the tandem PMS-SMPS setup (Figure E.5) are accounted for.

The operation of the standard instrumentation, SMPS, CPMA, and ELPI+, at the spray-flame reactor is complicated due to the high particle number concentration, small particle size and mass, as well as the low pressure of 150 mbar downstream of the sampling probe. The use

of the VIP-4 low pressure allows the direct use of standard instrumentation downstream of the sampling probe by diluting and transferring the aerosol back to atmospheric pressure. Thereby, the measurement of particle size distribution using SMPS was possible, or conditionally possible with ELPI+ due to the measurement range. The final stage of the ELPI+ consist of a back-up filter and measures aerodynamic particle in the size range of 6 to 17 nm. Reliable measurements of the particle mass by means of the CPMA could not be performed due to the small particle mass ($m_p < 0.5$ ag) and low charge state of the particles.

To interpret the differences between the two measuring techniques, the spray flame was studied under the same conditions with the SMPS and was compared with the TEM and AP-PMS in Figure E.13. The direct comparison shows that the CMD of the SMPS over the entire height of the flame is significantly higher than the values of the other measuring techniques. Furthermore, it can be seen that the CMD starts to rise strongly with increasing height at HAB= 60 mm and suggests an increased agglomeration process.

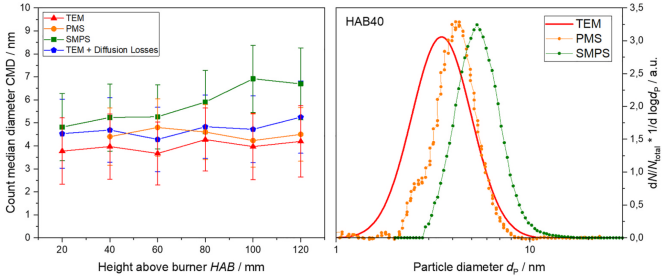

Figure E.13: Left: Comparison of the CMD as a function of HAB for TEM (red triangles), PMS (orange points), SMPS (green squares), and SMPS with the correction of diffusion losses (blue pentagons) for iron oxide particles in a 0.05 M iron nitrate spray flame as described in Table E.1. Right: Comparison of the area-normalized particle size distribution at HAB= 40 mm measured by TEM (red), PMS (orange points) and SMPS (green points) for iron oxide particles in a 0.05 M iron nitrate spray flame as described in Table E.1.

Deviations between SMPS and TEM results can be largely attributed to limitations of the tandem PMS-SMPS measurement setup. The main source of error in the combined setup are particle wall losses caused by turbulent flow and diffusion in the tube connecting VIP-4 ejector and V4. The combined effect of very small particle size, small tube diameter and turbulent flow leads to preferential deposition of small particles

onto tube walls. The original particle size distribution can be recalculated by applying the theory of Lee and Gieseke (1994) and Wells and Chamberlain (1967) for deposition of particles in turbulent pipe flows to the reference TEM measurement. The results are shown in Figure E.13. In conventional measurements the VIP4 ejector is not required as the reactor already operates near standard conditions and thus eliminating this source of error. Additionally, the counting efficiency of condensation particle counter (CPC) 3775 model by TSI is 4.0 nm (50 %) with lowest detectable size limit between 2.5 to 2.9 nm causing a shift towards larger mean diameters. These two phenomena can largely explain the CMD difference between SMPS and TEM measurements. In contrast to PMS results the SMPS graph shows a slight increase of CMD over HAB especially after 60 mm. This can be attributed to particle coagulation in the connecting tubes. Particle residence time for SMPS is longer than for PMS due to higher length of connecting tubes. Additionally, as flame temperature along HAB drops, the gas containing particles contracts which increases the particle concentration leading to increased coagulation in the connecting tubes. Stodt, Kiefer, and Fritsching (2020) measured in a similar experiment that flame temperature approximately halves after lower flame region. Similar conditions can be expected in this experiment.

3. CONCLUSIONS

The detailed understanding of particle growth in spray flames allows the tailor-made synthesis of particles in the sub-10 nm range and requires suitable measurement techniques. In this work a new developed ambient-pressure particle mass spectrometer (AP-PMS) is presented which is able to detect particle size distributions in spray flames at ambient pressure. For this purpose, a low-pressure PMS was expanded with an additional pressure stage and a sampling probe with integrated dilution gas supply. computational fluid dynamics (CFD) simulations of the sampling probe were able to provide information about the sampling volume, the volume flow taken from the flame and the transfer time into the sampling probe until dilution. In addition, the simulations showed significant reductions in the volume flow during hot sampling and that it becomes almost independent of the dilution gas flow. Experimental results using the Santoro flame as a reference source and TEM sampling showed the successful preservation of the sampled particles by sampling probe with integrated dilution.

With Schlieren imaging, it was possible to determine the position of Mach disc in the necessary free beam formation and to determine a suitable positioning of the sampling probe in front of the skimmer. The

results showed that the use of a capillary affects the supersonic expansion and the position of the Mach disc deviates from the known theory.

Successful validation of the performance of the AP-PMS was achieved by TEM sampling of iron oxide nanoparticles spray-flame synthesized from a solution of iron nitrate in a mixture of ethanol and 2-ethyl hexanoic acid with the SpraySyn burner under standardized conditions. Particle growth in the spray flame was studied using conventional aerosol measurement techniques such as TEM, SMPS and ELPI+ at heights ranging from 20 to 120 mm above the burner. The direct comparison of the AP-PMS with the conventional measurement techniques shows that the AP-PMS is more robust to higher particle number concentrations and pressures due to the use of a particle free beam and is therefore an attractive alternative for the investigation of particle growth processes in spray flames.

DECLARATION OF COMPETING INTEREST

The authors declare no conflict of interest.

ACKNOWLEDGMENT

The authors gratefully acknowledge funding by the German Research Foundation (DFG) with in the priority program "Nanoparticle Synthesis in Spray Flames" SPP1980 (No.375857056 and 375692188) and the Research Unit "Model-based scalable gas-phase synthesis of complex nanoparticles" FOR2284 (No.262219004)

APPENDIX A. SUPPLEMENTARY DATA

Supplementary data to this article can be found online at https://doi.org/10.1016/j.jaerosci.2021.105827.

REFERENCES

Angel, S., Neises, J., Dreyer, M., Friedel Ortega, K., Behrens, M., Wang, Y., Arandiyan, H., Schulz, C., and Wiggers, H. (2020). "Spray–flame synthesis of La(Fe, Co)O 3 nano–perovskites from metal nitrates." In: *AIChE Journal* 66.1. ISSN: 0001-1541. DOI: 10.1002/aic.16748.

Ashkenas, H. and Sherman, F. S. (1964). "Structure and utilization of supersonic free jets in low density wind tunnels: Rarefied Gas Dynamics." In: *Proc. 4th RGD Symposium* Volume 2, pp. 84–105.

Aßmann, S., Münsterjohann, B., Huber, F. J. T., and Will, S. (2020). "Droplet sizing in spray flame synthesis using wide-angle light scattering (WALS)." In: *Applied Physics B* 126.5. ISSN: 0946-2171. DOI: 10.1007/s00340-020-07443-2.

Bier, K. and Schmidt, B. (1961). "Zur Form der Verdichtungsstibe in frei expandierenden Gasstrahlen." In: *Z. Angew. Phys.* 13.11, pp. 493–500.

Bywalez, R., Orthner, H., Mehmedovic, E., Imlau, R., Kovacs, A., Luysberg, M., and Wiggers, H. (2013). "Direct gas-phase synthesis of single-phase β-FeSi2 nanoparticles." In: *Journal of Nanoparticle Research* 15.9. ISSN: 1388-0764. DOI: 10.1007/s11051-013-1878-9.

Chambers, D. M., Poehlman, J., Yang, P., and Hieftje, G. M. (1991). "Fundamental studies of the sampling process in an inductively coupled plasma mass spectrometer-I." In: *Spectrochimica Acta Part B: Atomic Spectroscopy* 46.6-7, pp. 741–760. ISSN: 05848547. DOI: 10.1016/0584-8547(91)80079-I.

Cho, K., Chang, H., Kil, D. S., Park, J., Jang, H. D., and Sohn, H. Y. (2009). "Mechanisms of the Formation of Silica Particles from Precursors with Different Volatilities by Flame Spray Pyrolysis." In: *Aerosol Science and Technology* 43.9, pp. 911–920. ISSN: 0278-6826. DOI: 10.1080/02786820903025986.

Deng, L., Kempf, A., Hasemann, O., Korobeinichev, O. P., and Wlokas, I. (2015). "Investigation of the sampling nozzle effect on laminar flat flames." In: *Combustion and Flame* 162.5, pp. 1737–1747. ISSN: 00102180. DOI: 10.1016/j.combustflame.2014.11.035.

Dreier, T. and Schulz, C. (2016). "Laser-based diagnostics in the gas-phase synthesis of inorganic nanoparticles." In: *Powder Technology* 287, pp. 226–238. ISSN: 0032-5910. DOI: 10.1016/j.powtec.2015.10.015.

Fissan, H. and Schwientek, G. (1987). "Sampling and transport of aerosols." In: *TSI Journal of Particle Instrumentation* 2.2, pp. 3–10.

Goertz, V., Korp, D., Al-Hasan, N., Giglmaier, M., and Nirschl, H. (2011). "Experimental study of gas-dynamically induced nanoparticle synthesis by use of adapted sampling probes." In: *Chemical Engineering and Processing: Process Intensification* 50.8, pp. 836–845. ISSN: 02552701. DOI: 10.1016/j.cep.2011.05.007.

Goudeli, E., Gröhn, A. J., and Pratsinis, S. E. (2016). "Sampling and dilution of nanoparticles at high temperature." In: *Aerosol Science and Technology* 50.6, pp. 591–604. ISSN: 0278-6826. DOI: 10.1080/02786826.2016.1168922.

Gröhn, A. J., Eggersdorfer, M. L., Pratsinis, S. E., and Wegner, K. (2014). "On-line monitoring of primary and agglomerate particle dynamics." In: *Journal of Aerosol Science* 73, pp. 1–13. ISSN: 00218502. DOI: 10.1016/j.jaerosci.2014.03.001.

Hardt, S., Wlokas, I., Schulz, C., and Wiggers, H. (2015). "Impact of Ambient Pressure on Titania Nanoparticle Formation During Spray-Flame Synthesis." In: *Journal of nanoscience and nanotechnology* 15.12, pp. 9449–9456. DOI: 10.1166/jnn.2015.10607.

Hospital, A. and Roth, P. (1991). "In-situ mass growth measurements of charged soot particles from low pressure flames." In: *Symposium (International) on Combustion* 23.1, pp. 1573–1579. ISSN: 00820784. DOI: 10.1016/S0082-0784(06)80428-5.

Jousten, K. (2004). *Wutz Handbuch Vakuumtechnik: Theroie und Praxis*. 8th ed. Vol. I. Wiesbaden: Vieweg+Teubner Verlag. ISBN: 978-3-322-96972-9. DOI: 10.1007/978-3-322-96971-2.

Kammler, H. K., Mädler, L., and Pratsinis, S. E. (2001). "Flame Synthesis of Nanoparticles." In: *Chemical Engineering & Technology* 24.6, pp. 583–596. ISSN: 0930-7516. DOI: 10.1002/1521-4125(200106)24:6<583::AID-CEAT583>3.0.CO;2-H.

Kluge, S., Wiggers, H., and Schulz, C. (2017). "Mass spectrometric analysis of clusters and nanoparticles during the gas-phase synthesis of tungsten oxide." In: *Proceedings of the Combustion Institute* 36.1, pp. 1037–1044. ISSN: 15407489. DOI: 10.1016/j.proci.2016.06.165.

Köylü, Ü.Ö., McEnally, C. S., Rosner, D. E., and Pfefferle, L. D. (1997). "Simultaneous measurements of soot volume fraction and particle size / microstructure in flames using a thermophoretic sampling technique." In: *Combustion and Flame* 110.4, pp. 494–507. ISSN: 00102180. DOI: 10.1016/S0010-2180(97)00089-8.

Kunze, F., Kuns, S., Spree, M., Hülser, T., Schulz, C., Wiggers, H., and Schnurre, S. M. (2019). "Synthesis of silicon nanoparticles in a pilot-plant-scale microwave plasma reactor: Impact of flow rates and precursor concentration on the nanoparticle size and aggregation." In: *Powder*

Technology 342, pp. 880–886. ISSN: 0032-5910. DOI: 10.1016/j.powtec.2018.10.042.

Lee, K. W. and Gieseke, J. A. (1994). "Deposition of particles in turbulent pipe flows." In: *Journal of Aerosol Science* 25.4, pp. 699–709. ISSN: 00218502. DOI: 10.1016/0021-8502(94)90011-6.

Li, H., Pokhrel, S., Schowalter, M., Rosenauer, A., Kiefer, J., and Mädler, L. (2020). "The gas-phase formation of tin dioxide nanoparticles in single droplet combustion and flame spray pyrolysis." In: *Combustion and Flame* 215, pp. 389–400. ISSN: 00102180. DOI: 10.1016/j.combustflame.2020.02.004.

Li, S., Ren, Y., Biswas, P., and Tse, S. D. (2016). "Flame aerosol synthesis of nanostructured materials and functional devices: Processing, modeling, and diagnostics." In: *Progress in Energy and Combustion Science* 55, pp. 1–59. ISSN: 03601285. DOI: 10.1016/j.pecs.2016.04.002.

Mädler, L., Kammler, H. K., Mueller, R., and Pratsinis, S. E. (2002). "Controlled synthesis of nanostructured particles by flame spray pyrolysis." In: *Journal of Aerosol Science* 33.2, pp. 369–389. ISSN: 00218502. DOI: 10.1016/S0021-8502(01)00159-8.

Martins, A., Costelha, H., and Neves, C. (2020). "Supporting the Design, Commissioning and Supervision of Smart Factory Components through their Digital Twin." In: *2020 IEEE International Conference on Autonomous Robot Systems and Competitions (ICARSC)*. IEEE, pp. 114–119. ISBN: 978-1-7281-7078-7. DOI: 10.1109/ICARSC49921.2020.9096072.

Panda, J. and Seasholtz, R. G. (1999). "Measurement of shock structure and shock–vortex interaction in underexpanded jets using Rayleigh scattering." In: *Physics of Fluids* 11.12, pp. 3761–3777. ISSN: 1070-6631. DOI: 10.1063/1.870247.

Rahinov, I., Sellmann, J., Lalanne, M. R., Nanjaiah, M., Dreier, T., Cheskis, S., and Wlokas, I. (2021). "Insights into the Mechanism of Combustion Synthesis of Iron Oxide Nanoparticles Gained by Laser Diagnostics, Mass Spectrometry, and Numerical Simulations: A Mini-Review." In: *Energy & Fuels* 35.1, pp. 137–160. ISSN: 0887-0624. DOI: 10.1021/acs.energyfuels.0c03561.

Rittler, A., Deng, L., Wlokas, I., and Kempf, A. M. (2017). "Large eddy simulations of nanoparticle synthesis from flame spray pyrolysis." In: *Proceedings of the Combustion Institute* 36.1, pp. 1077–1087. ISSN: 15407489. DOI: 10.1016/j.proci.2016.08.005.

Rosebrock, C. D., Wriedt, T., Mädler, L., and Wegner, K. (2016). "The role of microexplosions in flame spray synthesis for homogeneous nanopowders from low-cost metal precursors." In: *AIChE Journal* 62.2, pp. 381–391. ISSN: 0001-1541. DOI: 10.1002/aic.15056.

Rosenberger, T., Münzer, A., Kiesler, D., Wiggers, H., and Kruis, F. E. (2018). "Ejector-based sampling from low-pressure aerosol reactors." In: *Journal of Aerosol Science* 123, pp. 105–115. ISSN: 00218502. DOI: 10.1016/j.jaerosci.2018.06.003.

Roth, P. and Hospital, A. (1994). "Design and test of a particle mass spectrometer (PMS)." In: *Journal of Aerosol Science* 25.1, pp. 61–73. ISSN: 00218502. DOI: 10.1016/0021-8502(94)90182-1.

Schneider, F., Suleiman, S., Menser, J., Borukhovich, E., Wlokas, I., Kempf, A., Wiggers, H., and Schulz, C. (2019). "SpraySyn-A standardized burner configuration for nanoparticle synthesis in spray flames." In: *Review of Scientific Instruments* 90.8, p. 085108. ISSN: 0001-1452. DOI: 10.1063/1.5090232.

Schulz, C., Dreier, T., Fikri, M., and Wiggers, H. (2019). "Gas-phase synthesis of functional nanomaterials: Challenges to kinetics, diagnostics, and process development." In: *Proceedings of the Combustion Institute* 37.1, pp. 83–108. ISSN: 15407489. DOI: 10.1016/j.proci.2018.06.231.

Schulz, C., Kock, B. F., Hofmann, M., Michelsen, H., Will, S., Bougie, B., Suntz, R., and Smallwood, G. (2006). "Laser-induced incandescence: recent trends and current questions." In: *Applied Physics B* 83.3, pp. 333–354. ISSN: 0946-2171. DOI: 10.1007/s00340-006-2260-8.

Settles, G. S. and Hargather, M. J. (2017). "A review of recent developments in schlieren and shadowgraph techniques." In: *Measurement Science and Technology* 28.4, p. 042001. ISSN: 1361-6501. DOI: 10.1088/1361-6501/aa5748.

Stodt, M. F. B., Kiefer, J., and Fritsching, U. (2020). "Drop dynamics in heterogeneous spray flames for nanoparticle synthesis." In: *Atomization and Sprays* 30.11, pp. 779–797. ISSN: 1044-5110. DOI: 10.1615/AtomizSpr.2020034819.

Stodt, M. F.B., Liu, C., Li, S., Mädler, L., Fritsching, U., and Kiefer, J. (2021). "Phase-selective laser–induced breakdown spectroscopy in flame spray pyrolysis for iron oxide nanoparticle synthesis." In: *Proceedings of the Combustion Institute* 38.1, pp. 1711–1718. ISSN: 15407489. DOI: 10.1016/j.proci.2020.06.092.

Taatjes, C. A., Hansen, N., McIlroy, A., Miller, J. A., Senosiain, J. P., Klippenstein, S. J., Qi, F., Sheng, L., Zhang, Y., Cool, T. A., Wang, J., Westmoreland, P. R., Law, M. E., Kasper, T., and Kohse-Höinghaus, K. (2005). "Enols are common intermediates in hydrocarbon oxidation." In: *Science (New York, N.Y.)* 308.5730, pp. 1887–1889. DOI: 10.1126/science.1112532.

Teoh, W. Y., Amal, R., and Mädler, L. (2010). "Flame spray pyrolysis: An enabling technology for nanoparticles design and fabrication." In: *Nanoscale* 2.8, pp. 1324–1347. DOI: 10.1039/C0NR00017E.

Tischendorf, R., Simmler, M., Weinberger, C., Bieber, M., Reddemann, M., Fröde, F., Lindner, J., Pitsch, H., Kneer, R., Tiemann, M., Nirschl, H., and Schmid, H.-J. (2021). "Examination of the evolution of iron oxide nanoparticles in flame spray pyrolysis by tailored in situ particle sampling techniques." In: *Journal of Aerosol Science* 154, p. 105722. ISSN: 00218502. DOI: 10.1016/j.jaerosci.2020.105722.

Tricoli, A. and Elmøe, T. D. (2012). "Flame spray pyrolysis synthesis and aerosol deposition of nanoparticle films." In: *AIChE Journal* 58.11, pp. 3578–3588. ISSN: 0001-1541. DOI: 10.1002/aic.13739.

Weinstein, L. M. (2010). "Review and update of lens and grid schlieren and motion camera schlieren." In: *The European Physical Journal Special Topics* 182.1, pp. 65–95. ISSN: 1951-6355. DOI: 10.1140/epjst/e2010-01226-y.

Weise, C., Menser, J., Kaiser, S. A., Kempf, A., and Wlokas, I. (2015). "Numerical investigation of the process steps in a spray flame reactor for nanoparticle synthesis." In: *Proceedings of the Combustion Institute* 35.2, pp. 2259–2266. ISSN: 15407489. DOI: 10.1016/j.proci.2014.05.037.

Wells, A. C. and Chamberlain, A. C. (1967). "Transport of small particles to vertical surfaces." In: *British Journal of Applied Physics* 18.12, pp. 1793–1799. ISSN: 0508-3443. DOI: 10.1088/0508-3443/18/12/317.

F

DETERMINING THE SINTERING KINETICS OF FE AND FE_XO_Y-NANOPARTICLES IN A WELL-DEFINED MODEL FLOW REACTOR

Thore Rosenberger[a,b], Ivan Skenderović[a,b], Johannes Sellmann[b,c], Patrick Wollny[b,c], Alexander Levish[b,d], Irenäus Wlokas[b,c], Andreas Kempf[b,c], Markus Winterer[b,d] and Frank Einar Kruis[a,b]

[a] *Institute of Technology for Nanostructures (NST) and Center for Nanointegration Duisburg-Essen (CENIDE), Faculty of Engineering Science, University Duisburg-Essen, Duisburg, Germany*

[b] *Center for Nanointegration Duisburg-Essen (CENIDE), University of Duisburg-Essen, Duisburg, Germany*

[c] *Institute for Combustion and Gas Dynamics, Chair of Fluid Dynamics, University Duisburg-Essen, Duisburg, Germany*

[d] *Nanoparticle Process Technology (NPPT), University Duisburg-Essen, Duisburg, Germany*

Published in Aerosol Science and Technology, Volume 56 - Issue 9, Pages 833-846 (2022)
DOI: 10.1080/02786826.2022.2089011

ABSTRACT

A model flow reactor provides a narrow particle temperature-residence time distribution with well-defined conditions and is mandatory to measure changes of the particle structure precisely. The experimental data of iron and iron oxide agglomerates are used to determine the sintering kinetics considering the temperature-time history of the particles. Thousand particle trajectories are tracked in a validated CFD model at three different furnace temperatures each. Strongly agglomerated particles with a small primary particle size ($\sim$ 4 nm) are synthesized by spark discharge and are size-selected (25 to 250 nm) before sintering. The structure development is measured simultaneously with different online instrumentations and the structure calculated by means of structure models. A simple sintering model, based on the reduction of surface energy, is numerically quantified with the experimental results. The surface of the particles is strongly dependent on the primary particle size and the

agglomerate structure. The chemical phase is analyzed using the offline techniques XANES, XRD, and EELS. It is observed that the addition of hydrogen led to a reduction of iron oxide to iron nanoparticles and to changes of the sintering kinetics. The sintering exponent $m = 1$ was found to be optimal. For Fe, an activation energy E_a of 59.15 kJ/mol and a pre-exponential factor A_s of $1.57 \cdot 10^4$ s/m were found, for Fe_3O_4 an activation energy E_a of 55.22 kJ/mol and a pre-exponential factor A_s of $2.54 \cdot 10^4$ s/m.

INTRODUCTION

The synthesis of functionalized particles with defined structures and material properties is challenging due to rapidly and simultaneously occurring mechanisms, such as chemical reactions, surface growth, coagulation, condensation, and sintering (Pratsinis, 1988). Besides coagulation, sintering is one of the most important mechanisms that determine particle morphology but also one of the most complex mechanisms (German, 1996). It is dependent on various particle properties (e.g., size, shape, agglomerate structure), on material properties as well as on the process conditions, especially the temperature-time history of the particles. Sintering models can be used to describe the sintering process as a function of characteristic values, and thus contribute to a better understanding.

The sintering process can be investigated by different methods. Using imaging techniques, individual macroscopic particles/objects can be precisely examined. For this purpose, the objects are heated in a controlled atmosphere at different temperatures and time periods and structural changes (e.g., shrinkage, growth of sintering necks) are documented (Kuczynski, 1949). This method was used by Matsumura (1971) to study the sintering mechanism and diffusion coefficient of iron wires. He found an activation energy of 242 kJ/mol and concluded that the predominant sintering mechanism for iron is dependent on the temperature as well as on the ratio of the neck and particle radii. Knight et al. (2000) and Mikami, Kamiya, and Horio (1996) used a fluidized bed with iron powder (reduced steel shot powder) to investigate the mechanism of de-fluidization and particle-to-particle neck growth. They determined an activation energy of 221 kJ/mol by assuming surface diffusion for particles sizes of 200 µm. The sintering mechanism of two submicron iron oxide (Fe_3O_4) powders at low temperature (773 to 843 K) was examined by Kramer and German (1978) with offline measurement techniques, like scanning electron microscopy, gas adsorption, and X-ray diffraction. They identified surface diffusion as the dominant sinter transport mechanism

by the linear dependence of the logarithmic reduction of the specific surface area on time.

The use of these earlier kinetic data in sintering models of aerosol reactors is questionable due to the different size and temperature ranges. Also, small differences in the environment or the morphology of the structure to be sintered can strongly influence the sintering process. Therefore, reliable kinetic data are necessary when applying sintering models for aerosol reactor optimization (Kruis et al., 1993). The determination of precise kinetic data by using experimental data from a complex aerosol reactor, in which different processes take place simultaneously, is difficult. Therefore, the mechanisms have to be isolated from each other and well-defined conditions have to be provided. Model flow reactor (MFR) are designed to provide a well-defined particle temperature-time history and to exclude undesired processes by controlling the number concentration and the monodispersity of the aerosol. The probability of agglomerate formation by coagulation can be avoided by using a low number concentration. Kirchhof, Förster, et al. (2012) designed a MFR to study the sintering kinetics of silica nanodoublets, i.e., two connected spherical primary particles, as function of different primary particle sizes in the temperature range 1533 to 1873 K with residence times from 3.7 to 130 ms. A turbulent flow field was used to achieve a nearly constant temperature in the reaction zone and to characterize the structural change of the nanodoublets by offline TEM analysis. A less tedious measurement of the structure development was carried out by Cho, Hogan, and Biswas (2007). They measured the sintering of polystyrene latex (PSL) agglomerates at different temperatures and residence times online with a tandem differential mobility analzyer (DMA) setup. A reasonable agreement with the sintering model of Koch and Friedlander (1990) was demonstrated.

In this work, the sintering of Fe_xO_y-NPs is studied in a model flow reactor previously developed (Rosenberger, Sellmann, et al., 2020). Iron or iron oxide agglomerates are synthesized in the size range from 25 to 250 nm by spark discharge, size-selected by means of a DMA and sintered having a well-defined temperaturetime history. A CFD model is validated and used to calculate the particle trajectories in the sintering zone for different furnace temperatures and thereby provide the necessary temperature-time histories. Online in strumentation is used to monitor the changes of the mobility diameter, Stokes diameter and particle mass during the sintering process. The change of the chemical phase from iron oxide to iron by the addition of hydrogen during sintering is analyzed by electron energy loss spectroscopy (EELS) and X-ray absorption near edge structure (XANES) measurements. The sintering kinetics is determined applying

different furnace temperatures and initial agglomerate sizes, with the number of primary particles per agglomerate up to a few thousand.

THEORY

Determining the particle structure

It is necessary to characterize the initial particle structure to determine structural changes. An aerosol generated by spark discharge is strongly agglomerated containing a large number of small primary particles due to the steep temperature gradient after the spark pulse. The structure of the agglomerates can be described by the fractal dimension together with the primary particle size. Here, the fractal dimension is expressed by the mass–mobility exponent D_{fm} (Kim et al., 2009; Scheckman, McMurry, and Pratsinis, 2009) which ranges from 1.8 to 2.9 for an open structured agglomerate generated by diffusion-limited (DLCA, Kolb and Herrmann, 1987) or by ballistic cluster–cluster agglomeration (BCCA, Tence, Chevalier, and Jullien, 1986). D_{fm} is defined by Equation (F.1) (Park, Kittelson, and McMurry, 2004) and can be determined by a linear fit of the logarithm particle mass $\log(m_{\mathrm{p}})$ as function of the logarithm mobility diameter $\log(d_{\mathrm{m}})$. It is assumed that the fractal prefactor k_{fm} is constant and the primary particle diameter d_{prim} does not change over the size range.

$$m_{\mathrm{p}} = k_{\mathrm{fm}} \left(\frac{d_{\mathrm{m}}}{d_{\mathrm{prim}}} \right)^{D_{\mathrm{fm}}} \tag{F.1}$$

The primary particle diameter d_{prim} can then be determined by applying the structure model by Eggersdorfer, Kadau, et al. (2012), leading to Equation (F.2) (Rosenberger, Münzer, et al., 2018).

$$d_{\mathrm{prim}} = d_{\mathrm{m}} \left(k_{\alpha} \cdot \frac{\rho_{\mathrm{bulk}}}{\rho_{\mathrm{eff}}} \right)^{\frac{1}{2D_{\alpha}-3}} \tag{F.2}$$

The agglomerate structure descriptive parameters $k_{\alpha} = 0.99$ and $D_{\alpha} = D_{\mathrm{fm}}/2 = 1.082$ are independent of the sintering mechanism and remain constant during sintering (Eggersdorfer and Pratsinis, 2013).

The effective density ρ_{eff} is found from the mobility diameter d_{m} and the particle mass m_{p} respectively the bulk density ρ_{bulk} from the ratio of the mass to the volume of a full sintered sphere, Equation (F.3).

$$\rho_{\text{eff}} = \frac{6 m_{\text{p}}}{\pi {d_{\text{m}}}^3} \tag{F.3}$$

An alternative method for determining primary particle size that is less dependent on the charge state and more sensitive to particle structure is based on the comparison of the Stokes diameter d_{s} with the mobility diameter d_{m}. The DAPS measurements used here are based on aerodynamic focusing of a narrow size fraction, generated by the classification with respect to relaxation time (Babick et al., 2018). The measured value by the DAPS is the aerodynamic diameter d_{a} in the free-molecular regime which can be expressed as the Stokes diameter $d_{\text{s}} = d_{\text{a}} \cdot \sqrt{\rho_0/\rho_{\text{eff}} \cdot C_C(d_{\text{a}})/C_C(d_{\text{s}})}$ with the standard-density ρ_0=1 g/cm^3 (DeCarlo et al., 2004). Measuring a narrow particle size distribution simultaneously with the DAPS and SMPS allows the determination of ρ_{eff} by adapting the number weighted Stokes diameter distribution $\mathrm{d}N = \mathrm{d}\log(d_{\text{s}})$ to the number weighted mobility diameter distribution $\mathrm{d}N = \mathrm{d}\log(d_{\text{m}})$ The mass–mobility exponent can then be calculated from the ratio of the effective density to the bulk, $D_{\text{fm}} = 2.2 + 0.8(\rho_{\text{eff}}/\rho_{\text{bulk}})^5$ (Goudeli, Gröhn, and Pratsinis, 2016) and finally the primary particle diameter d_{prim} by Equation (F.4), introduced by Stein, Kiesler, and Kruis (2013).

$$d_{\text{prim}} = d_{\text{m}} \left(\frac{\rho_{\text{eff}}}{\rho_{\text{bulk}}} \right)^{\frac{1}{3-D_{\text{fm}}}} \tag{F.4}$$

Model to determine the sintering kinetics

The sintering kinetics of the structure-forming mechanisms is determined using the sintering model of Koch and Friedlander (1990), which poses that the change of the surface area as function of time $\mathrm{d}A/\mathrm{d}t$ of a single agglomerate is proportional to the deviation from the surface area of the same coalesced particle A_{sph} as shown in Equation (F.5).

$$\frac{\mathrm{d}A}{\mathrm{d}t} = -\frac{1}{\tau_{\text{s}}} \cdot \left(A - A_{\text{sph}} \right) \tag{F.5}$$

The surface area is calculated by $A = \pi \cdot {d^2}_{\text{prim}} \cdot N_{\text{agglo}}$ for an agglomerate consisting of N_{agglo} primary particles with the constant primary particle surface area. The driving force for the coalescence is the reduction in surface energy. The proportionality factor $1/\tau_{\text{s}}$ is defined as the inverse

of the characteristic sintering time (Friedlander and Wu, 1994). According to the Arrhenius type expression, the characteristic sintering time is a function of the temperature of the particles T and activation energy E_a as well as the pre-exponential factors A_s and d_{prim} to the power of m, Equation (F.6).

$$\tau_s = A_s d_{prim}^m \cdot \exp\left(\frac{E_a}{k_B T}\right) \tag{F.6}$$

The exponent m describes the dominant transport mechanism of the sintering process. The sintering mechanism, such as grain boundary diffusion, surface diffusion or volume diffusion, strongly influences the kinetics and is usually not precisely known or changes with temperature. For the specific case of sintering of iron particles, one report suggests the surface or grain boundary diffusion mechanism ($m = 4$) to be dominant at temperatures below 1323 K (Mikami, Kamiya, and Horio, 1996).

Since the activation energy and the pre-exponential factor might not be independent from each other and will depend on the sintering mechanism, a global minimum from the combination of all three parameters is searched for in order to determine the sintering kinetics. The mathematical problem can be simplified by assuming a dominant sintering mechanism (i.e., exponent m) and obtaining the best fitting combination of E_a and A_s by error minimization between experiment and sintering model, Equations (F.5)–(F.7). The numerical solution by a MATLAB routine (Version 2020a, MathWorks, Natick, MA, USA) is based on the Nelder-Mead simplex algorithm for solving strictly convex functions with two dimensions (Lagarias et al., 1998). Equation (F.5) is solved by integration with a variable step size and variable order (VSVO) solver, based on the numerical differentiation formulas (NDFs), and calculates the evolution of the surface area according to the temperature-time history and combination of E_a and A_s. The quality of the determined kinetic parameters is evaluated by comparing the measured primary particle size $d_{prim,exp}$ and the calculated particle size $d_{prim,calc}$ considering the temperature-time histories for a given combination of E_a and A_s. The ΣSQR is defined as the sum of the quadratic errors of the primary particle diameter and is normalized $d_{prim,exp}^2$, Equation (F.7).

$$\sum SQR = \frac{\sum \left[d_{prim,exp} - d_{prim,calc}\right]^2}{d_{prim,exp}^2} \tag{F.7}$$

EXPERIMENTAL SETUP

The setup used for the sintering experiments is depicted in Figure F.1 and consists of three main parts: (a) the particle synthesis, which provides defined particle structures (e.g. size-selected agglomerates), (b) the model flow reactor to induce the structure formation of aerosol particles under well-defined conditions, and (c) the characterization of the particles with online and offline instrumentation. A detailed description of this setup with design of the MFR is described in our previous work (Rosenberger, Sellmann, et al., 2020).

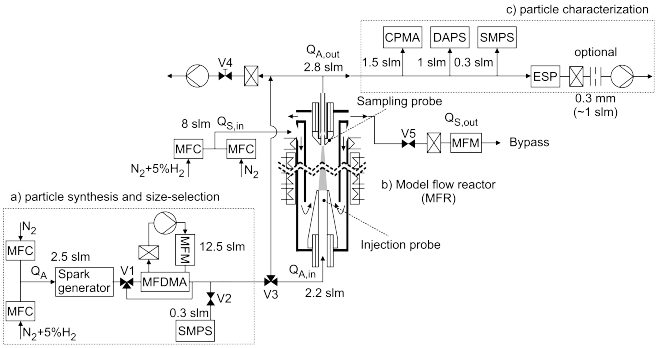

Figure F.1: Experimental setup for determining the sintering kinetics: (a) the particle synthesis, which provides defined particle structures, (b) the model flow reactor (MFR) to induce structure formation of aerosol particles under well-defined conditions, and (c) characterization of the particles with online and offline instrumentation.

Two mass flow controllers (MFC, EL-FLOW Select, Bronkhorst High-Tech B.V., Ruurlo, NL) are used to provide a gas mixture Q_A of purified nitrogen and up to 5 vol.% hydrogen. The gas purification system is a combination of an adsorber (ALPHAGAZ Purifier O_2-Free Air, Liquide Deutschland GmbH, Frankfurt, DE) and a getter (Mono Torr Phase II purifier, SAES Getters Deutschland GmbH). It is used to increase the gas purity (better than 5.0) and to remove oxygen contamination. The second MFC is connected to a gas bottle (ARCAL F5, Air Liquide) filled with compressed hydrogen (5 vol.%) in nitrogen. A gas with a total flow rate of 2.5 slm enters through Swagelok tubes into a custom-built spark generator where iron oxide agglomerates with a small primary particle size are formed by spark discharge (Schwyn, Garwin, and Schmidt-Ott, 1988). The charge current of the 28 capacitors (each having a capacitance of 1 nF) is set to 5 mA when nitrogen or 1 vol.% H_2 is used and 10 mA with

5 vol.% H_2. A broad particle size distribution (PSD) based on mobility diameter is obtained, with a geometric diameter around 100 nm and standard deviation of 1.6. The breakdown voltage (approx. 4 kV) is kept constant and can be controlled by the gap distance between two ∅5 mm iron rod electrodes (CAS 7439-89-6, Alfa Aesar by Thermo Fisher GmbH, Kandel, DE). The spark discharge energy is directly proportional to the capacitance, increasing it leads to an increase of the particle concentration and to growth of the modal diameter (Tabrizi et al., 2009). A monomobile size fraction of the aerosol is provided by a custom-built DMA which can handle larger flow rates due its larger size (Medium Flow-DMA/MF-DMA, Rosenberger, Kiesler, et al., 2019) or remains polydisperse when bypassing it by using valve V1. Agglomerates are not neutralized before the mobility selection and show multiple charges as a result from the spark discharge. A recirculation pump provides a constant sheath and exhaust gas flow through the DMA. A first SMPS is connected via a valve V2 downstream of the MF-DMA and samples a flow of 0.3 slm in order to measure the PSD before the particle laden enters the MFR. The valve V3 can be used to bypass the MFR. The total sheath gas flow rate $Q_{S,in}$ of the MFR is set constant to 8 slm by two MFCs. The sheath gas mixture corresponds to the aerosol Q_A. The sheath exhaust is connected to a valve V5, a HEPA-filter and a mass flow meter (MFM, 4041 TSI) to the bypass. The mass flow rate of the exhaust is measured to check whether it is equal to $Q_{S,in} - (Q_{A,out} - Q_{A,in})$, with $Q_{A,in} = 2.2$ slm, and $Q_{S,out} = 7.4$ slm. The flow rate $Q_{A,out}$ of 2.8 slm is sampled from the MFR by the online instrumentation: 0.3 slm by theSMPS (3936, TSI, Minneapolis, US), 1 slm by the differential aerodynamic particle sizer (DAPS) (Babick et al., 2018) and 1.5 slm by the centrifugal particle mass analyzer (CPMA Mk1, Cambustion Ltd., Cambridge, UK). An electrostatic precipitator (ESP) can be used to sample particles on a substrate, such as a TEM grids, for offline analysis. For sampling, the pump of the DAPS is turned off and the aerosol is drawn in by a critical orifice upstream of a HEPA-filter and external pump of the ESP. The diameter of the critical orifice of 0.3 mm limits the mass flow to approx. 1 slm, so that SMPS and CPMA can be used simultaneously without changing the sample flow rate as compared to previous measurements. The needle valve V4 with HEPA-filter and vacuum pump are used to keep the sample flow rate through the MFR constant when the online instrumentation is not in use.

The model flow reactor uses a wire-wound tube furnace (TZF 12/75/700, Carbolite Gero GmbH & Co. KG, Neuhausen, DE), modified for vertical application. The working tube consists of a coaxial arrangement of two ceramic tubes and water-cooled injection (bottom) and sampling probes (top) projecting into the heating zone. The ceramic tube ends are

connected to the probes with vacuum-tight adapters applying DN-63 CF standard components. The aerosol enters the reaction zone through the injection probe at room temperature ($T = 300\,\mathrm{K}$) and is drawn in and cooled down by the sample probe at the upper end. In a laminar flow field, the particle trajectories starting from the inlet and ending in the outlet are almost straight from inlet to outlet and lead to a conical reaction zone with a volume of ∅10 to ∅6x750 mm, indicated by the gray-colored area. In addition, a preheated sheath gas stabilizes and heats up the cold aerosol on the radial centerline. The sheath gas enters at the upper end of the MFR, between the outer and inner ceramic tube, and flows downwards through the heated zone of the furnace. It can be seen that the inner ceramic tube is slightly shorter than the outer tube and hangs freely at the lower end. This allows the sheath gas to be redirected below the injection probe tip and to flow upwards with the aerosol to the exhaust, respectively to sample outlet. The sample flow can be quenched at the probe tip by flowing a dilution gas through the annular space between the water cooling and sampling pipe at the sample probe. However, the dilution gas in combination with the water cooling leads to significant thermophoretic losses. Particle deposits and a significant decrease in a particle concentration was observed, which enhances the statistical uncertainties, in some cases even the detection limit of the instrumentation was reached. Therefore, no quenching gas was used and the temperature of the water cooling was raised to constant 300 K.

PRELIMINARY INVESTIGATIONS

CFD simulation

Knowledge of the temperature-time history $T(t)$ of the particles during sintering is essential to determine precise sintering kinetics from the experimental data. In our previous work (Rosenberger, Sellmann, et al., 2020), we introduced and validated a CFD simulation against experiments. The CFD simulations were performed using a two-dimensional, axial symmetric grid, where a mesh for the reactor walls was added with the objective to resolve the heat flux directly. Here, the resulting temperatures from previous simulations were used as boundary conditions for a three-dimensional simulation in which single-particle trajectories were calculated. From these trajectories, times (t) and temperatures (T) histories of individual particles could then be extracted and combined into mean profiles. The simulations were performed on a three-dimensional grid using OpenFOAM (v.2.1). The flow field is assumed to be non-reactive and laminar ($Re \leqslant 364$), and the Navier-Stokes equations were solved in

the Eulererian frame, while the particle trajectories were calculated in the Lagrangian frame. Three different simulations were performed for N_2 as carrier gas, for furnace temperatures of 773, 1023, 1273 K.

The trajectories are computed by numerically tracking particles injected at the inlet. The particles are transported passively in the flow field, except for the drift due to thermophoresis. The thermophoretic velocity is calculated applying an extended Waldmann equation (Li and Wang, 2004). Brownian motion is neglected assuming small particle diffusivity in respect to the thermophoretic drift.

In each simulation, 1000 particles were released at the inlet, randomly distributed over the radius $\left(\sqrt{y_{\text{radial}}^2 + z_{\text{radial}}^2} < 5\,\text{mm}\right)$ of the aerosol inlet tube (z_{axial}= 0.2 m). After traveling through the domain, they were then either collected by the sampling probe (at z_{axial} = 1.05 m), or they left the domain through the outlet. In the latter case, the particle time history was withdrawn and not considered for the analysis. To capture the reaction zone, the trajectories start 40 mm upstream and end 60 mm downstream from the reaction zone. Whereas the residence time τ is defined as the time, in which the particles reach the sampling probe after passing the axial position $z_{\text{axial}} > 0.24\,\text{m}$ ($t = 0$).

Figure F.2a) and b) depicts the mean temperature-time history $T(t)$ of the particle trajectories and the residence time distribution as function of the furnace temperatures 773, 1023, 1273 K. The mean $T(t)$ of the particle trajectories resulting from CFD simulations at the three furnace temperatures are marked by solid lines with the standard deviation in the gray areas. The intermediate temperature-time histories are determined by linear interpolation, shown and described in the Supplementary Information S2. It can be seen that the temperature of the particles increases and the total residence time shortens with rising furnace temperature. Whereas the gas mass flow rate is kept constant, an increase in temperature results in an expansion of the gas volume and thereby to a higher gas velocity, thus to a shorter residence time. A plateau of the particle temperature as function of the time is not reached and a slight slope is always noticeable. The slope is steeper at high furnace temperatures due to the higher temperature gradient and the shorter residence times in the reaction zone. The significant temperature gradients at t_{min} and t_{max} are due to the water-cooled injection and sample probe. Kirchhof, Schmid, and Peukert (2004) achieved an almost constant temperature in the reaction zone by turbulent mixing of the cold aerosol with the preheated sheath gas but at the disadvantage of a broadener residence time distribution. Figure F.2b) shows that the particle trajectories have little residence time scatter and are narrowly distributed. The mean absolute

deviation is 15 ms at 1273 K, 18 ms at 1073 K, and broadens to 31 ms at the lowest furnace temperature 773 K.

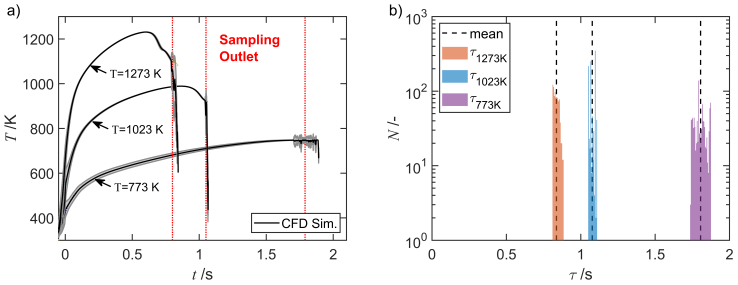

Figure F.2: a) Mean temperature-time history $T(t)$ and b) residence time distribution τ for a number of trajectories N at three different furnace temperatures. Solid lines indicate the mean calculated from CFD simulation for furnace temperatures of 773, 1023, 1273 K. The standard deviation of $T(t)$ in a) is shown as gray area.

OFFLINE INVESTIGATION OF THE CHEMICAL PHASES

XRD analysis

A first indication of the synthesized particle structure and phase composition can be obtained by X-ray diffraction (XRD). The powder for the analysis has been sampled from the spark generator housing after several hours of synthesis at constant conditions in nitrogen. It is used for the analysis which are found directly in the reactor before further processing. It is analyzed by XRD using a diffractometer equipped with Ni-filtered copper Kα radiation (X'pert Pro, PANalytical B.V., Almelo, NL). Alteration of the sample due to the exposure to oxygen cannot be excluded, so the crystallographic data may not be fully representative for the sintered nanoparticles. The powder is pressed into a powder holder for the measurement. Figure F.3 depicts the X-ray diffractogram of the powder with individually contributing components weighted according to the refined phase composition. The analysis was performed with the reference crystal structures (ICSD Fe_2O_3 15840 (Blake et al., 1966), Fe_3O_4 26410 (Fleet, 1981), Fe_3O_4* 50271 (Okudera, 1997) and α-Fe 53802 (Hull, 1917)) and Rietveld refinement using the software MAUD (Lutterotti, 2010). The adaption of the reference data is challenging due to the low signal-to-noise ratio. It is assumed that the crystal structures of the sample consist

mainly of the elements iron (Fe) and oxygen (O). A good agreement with the experimental data (R_{wp} = 8.74 %) is achieved by adapting the crystalline phases magnetite Fe_3O_4 (68 wt.%), hematite Fe_2O_3 (31 wt.%) and α-iron Fe (1 wt.%). The large amount of the crystal phase magnetite and hematite is a result of the ultrafine primary particles and the fast oxidation of iron due to the large specific particle surface. The crystallite size for hematite is 7.2 ± 1.3 nm. For the magnetite phase two different crystallite sizes are obtained, 41.2 wt.% of a non-stoichiometric magnetite ($Fe_{2.96}O_4$) with 2.5 ± 0.2 nm and 26.8 wt.% with 6.3 ± 0.4 nm. All oxide phase crystallites were also found to have relatively high microstrain, 0.015 ± 0.001 for hematite, 0.002 ± 0.001 for the larger fraction of magnetite and 0.047 ± 0.003 for the smaller fraction. This can be attributed to the small size of the nanoparticles as well as to the method used to generate them. The metallic iron phase is present in form of micron-sized particles (> 1 µm), indicated by the large and narrow reflection at 2Θ= 45° in the diffractogram, which can be formed by splashing of molten material from the cathode surface during the spark discharge (Hontañón et al., 2013).

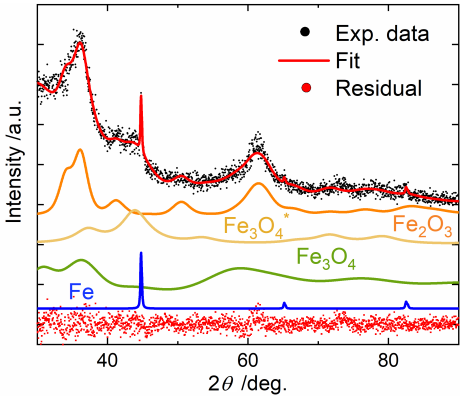

Figure F.3: Rietveld refinement of Cu-Kα XRD data of a powder sampled from the spark generator housing after several hours of synthesis in pure nitrogen. Diffractograms for the separate phases magnetite Fe_3O_4 (27 wt.%), iron-deficient magnetite Fe_3O_4* (41 wt.%), hematite Fe_2O_3 (31 wt.%) and iron Fe (1 wt.%) as refined together with original data, total refined profile (fit) and residual (difference between data and refinement) are displayed.

XRD analysis provided no clear indication if pure iron nanoparticles can be synthesized in a nitrogen atmosphere. The high amount of iron oxide particles suggests that the particles are completely oxidized during

synthesis or sampling. A higher amount of metallic iron can be obtained by adding a reducing agent to the particle generation process. Hallberg et al. (2018) investigated the production of single crystalline and non-oxidized metal nanoparticles in a spark discharge. The addition of 5 vol.% hydrogen to the nitrogen carrier gas as reducing agent already during particle generation prevents the formation of the oxide phase and thus improves the sintering properties of the nanoparticles, forming compact and monocrystalline metals. Furthermore, the addition of hydrogen during sintering leads to a reduction of the oxide phase (Seipenbusch et al., 2003). Therefore, the particles in this work are synthesized and sintered in purified nitrogen, in 1 vol.% H_2 and 5 vol.% H_2 in nitrogen to investigate the sintering kinetics of iron and iron oxide nanoparticles.

XANES and EELS analysis

The investigation of the chemical composition of the sintered particles is difficult due to the low number concentration and the rapid oxidation of pure iron when exposed to air. Two different offline techniques, (I) X-ray absorption fine structure (XAFS) at the near-edge XANES and (II) transmission electron microscope (TEM) with electron energy loss spectroscopy (EELS), are used to analyze the chemical composition and phase. A representative sample is taken by electrostatic precipitator (ESP) under the specific process gas environment (purified N_2, 1 vol.% H_2 or 5 vol.% H_2 in N_2). A constant sample flow rate of 1 slm is ensured by a critical orifice downstream of the ESP. The suction gas flow rate from the MFR of 2.8 slm is kept unchanged to the sintering experiments by switching off the pump of the DAPS. The suction gas flow rate is then divided over SMPS (0.3 slm), CPMA (1.5 slm), and ESP (1 slm). The coverage of particles on the substrate is controlled by the deposition voltage and time. After sampling, the ESP is sealed gas-tight and transferred to a nitrogen glove box, where the sample is prepared for analysis and packed for transport. Sampling, preparation and analysis are carried out promptly to avoid reaction of modifying the sample.

XANES measurements at the iron *K*-edge (7112 eV) are performed with a Si-passivated implanted planar silicon (Si-PIPS) single-channel fluorescence detector at the P65 beamline (PETRA III, Deutsches Elektronen-Synchrotron DESY, Germany). The energy resolution at the iron absorption edge of the P65 beamline with the beamline optics is about 0.99 eV. The XANES analysis requires a high degree of substrate coverage for an adequate signal. This could only be achieved within a deposition time of about $\sim$ 24 h by sampling a polydisperse aerosol and applying a high voltage of -8 kV to the ESP. The high electric field together with the slow

gas velocity tangential to the substrate surface creates a small deposition spot of positively charged particles. The particles are deposited between two polyimide foils (Kapton, DuPont de Nemours Inc., Wilmington, DE, USA) with a thickness of 25 µm each. The films are adhered together in an inert gas atmosphere to avoid altering of the sample.

Figure F.4 depicts the XANES spectra at the Fe-*K* edge of the polydisperse samples after sintering at 1373 K in pure nitrogen and in 5 vol.% hydrogen in nitrogen. The highest operation temperature of the MFR was used to ensure spherical particles with bulk density. The spectra were analyzed using linear combination fitting (LCF) with Fe, FeO, Fe_3O_4 and Fe_2O_3 standards and the red lines represent best fit combinations. The experimental data are indicated by black dots and the corresponding reference data are marked in color. Iron foil (25 µm, 99,99+ %; Goodfellow GmbH, Hamburg, DE) and Fe_3O_4 powder in starch (Alfa Aesar, Thermo Fisher Scientific GmbH, Kandel, DE) are used as reference standards. In case of the oxide samples the iron foil is used as internal standard to calibrate the energy scale. Data were also fitted using pseudo-voigt function for the pre-edge and white line features and a step function for the edge. Comparing both spectra, it can be seen that the white line of the *K*-edge occurs at about 7130.2 ± 0.3 eV in both cases, however, the peak intensity of the Fe phase is smaller. The pre-edge can be described in the form of a shoulder in both cases with a higher intensity in the $N_2 + 5\%H_2$ atmosphere. Fe_3O_4 shows a pre-edge peak of lower intensity well separated in front of the absorption edge and therefore cannot be considered as the only phase for N_2 atmosphere. A significant shift of the pre-edge (7114.3 ± 0.5 eV) due to iron oxidation state Fe^{3+} or Fe^{2+} is not observed. Nevertheless, a shift in the *K*-edge step from 7120.2 ± 0.3 eV in the case of $N_2 + 5\%H_2$ atmosphere to 7122.6 ± 0.3 eV in the case of pure N_2 atmosphere. This so-called chemical energy shift is an indicator of the increase in the valence of iron in the corresponding sample Zhao et al., 1993 and is in good agreement with the LCF fit results. Differences in intensity and shape are also observed. The LCF fitting of the samples with standards resulted in a best fit for $N_2 + 5\%H_2$ atmosphere using pure α-iron and in N_2 for the 72.8 % magnetite phase and 27.2 % iron. Minor deviations between the Fe reference and sample in pure $N_2 + 5\%H_2$ may be due to the nano scaled morphology of the samples which may also lead to crystallographic defects and thus a broadening of the features compared to the standard, a bulk metallic foil. The deviations of the N_2 atmospheric sample can also be attributed to the crystallographic defects, Fe^{2+}/Fe^{3+} ratio and the vacancy distribution or due to the small size of the particles (Krishnan, 1990).

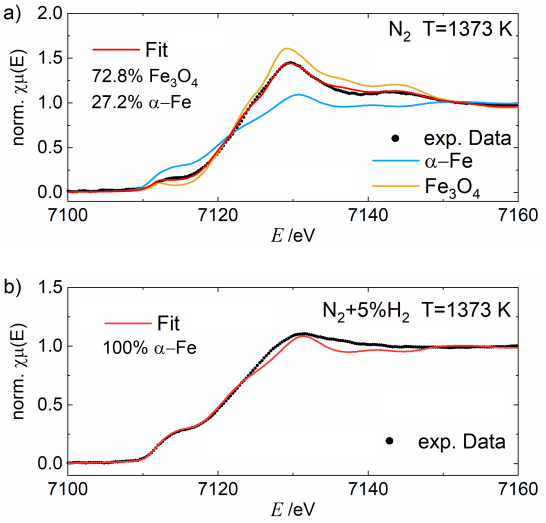

Figure F.4: LCF fitting of the Fe-*K* edge XANES spectra of polydisperse Fe_xO_y nanoparticles after sintering at 1373 K (black line) in purified nitrogen (N_2) a) and reducing gas mixture of nitrogen and hydrogen (95 vol.% H_2) b) with corresponding Fe and Fe_3O_4 references.

An examination of single particles is performed with TEM (2200FS, JEOL GmbH, Freising, DE) and the analysis of the electron energy loss spectroscopy (EELS) in cooperation with the ICAN (Interdisciplinary Center for Analytics on the Nanoscale, Duisburg, Germany). Agglomeration on the substrate is prevented by keeping the particle coverage low in order to study the particle morphology and the chemical composition resulting from the sintering. A monodisperse aerosol is precipitated for about 10 min on TEM copper grids covered with a lacey carbon film. A voltage of 95 V or 1570 V is applied to the MF-DMA for classifying agglomerates with a mobility diameter of 30 nm or 145 nm, respectively. After sintering in pure nitrogen or 5 vol.% hydrogen in nitrogen at the highest temperature of 1373 K, the particles show a spherical structure with a diameter of 20 nm, and 60 nm, respectively.

Figure F.5 shows the EEL spectra of spherical Fe_xO_y nanoparticles after sintering at 1373 K with a diameter of 20 nm and 60 nm in a) purified nitrogen or b) in 5 vol.% hydrogen in nitrogen. The backgrounds of the EELS spectra are removed by adapting a power law equation. The oxygen O *K*-edge, and iron Fe L_3, and Fe L_2-edges are marked with arrows according to literature (Feldhoff et al., 2009). It is difficult to distinguish

between the different iron species because the general spectral shapes are almost similar for Fe^0, Fe^{2+} and Fe^{3+}. All these spectra show a main peak at around 708 to 710 eV (L_3) and a less intense peak at 721 to 723 eV (L_2) and do not differ significantly in terms of energy. The iron spectra with higher oxidation state are more shifted to higher energy and show a broadened L_2 peak. Hematite (Fe_2O_3) shows an energetically lower shoulder in relation to magnetite (Fe_3O_4) and differs in the peak intensity at E_{loss}= 722 eV and E_{loss} = 724 eV. The reference phases iron (Fe), hematite (Fe_2O_3) and magnetite (Fe_3O_4) from EELS Database (Ewels et al., 2016) are initialized by 30 % each and adapted to the spectra. According to previous XANES analysis, it is assumed that the phase maghemite (γ-Fe_2O_3) is not present in this sample and only forms when the sample is exposed to an oxygen-rich atmosphere. The maximum L_3 and L_2 line of the reference is observed at an energy about 1.8 ± 0.1 eV lower than that of the sample. It can be seen that the spectra of 20 nm and 60 nm particles do not differ much and that magnetite (59 %) is the dominant phase in pure nitrogen and iron (87 %) in 5 vol.% H_2 in N_2. The hematite phase content is in all measurements less than 1 %. The fitting procedure is strongly dependent on the background removal and the determined energy shift. Even better agreement to previous XANES measurements is achieved by fitting a higher proportion of magnetite phase to the spectra in Figure F.5a). Regarding the O-*K* absorption edge, it is observed that the intensity ratio of the O-*K* and Fe-L_3 peak increases with decreasing particle diameter. Adding hydrogen reduces this ratio and leads to a higher iron content which is also observed in the XANES analysis.

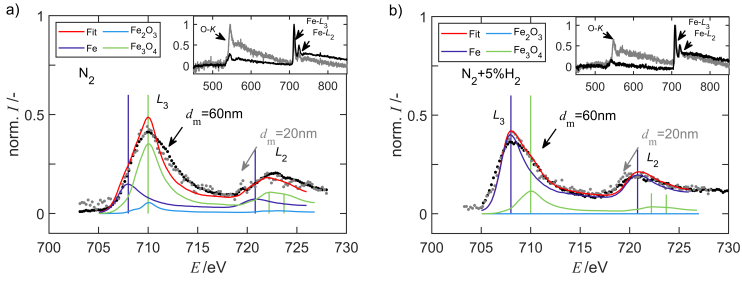

Figure F.5: Electron energy loss spectroscopy (EELS) of spherical Fe_xO_y nanoparticles after sintering at 1373 K with a diameter of 20 nm and 60 nm a) in purified nitrogen and b) in 5 vol.% hydrogen.

RESULTS AND DISCUSSION

Online measurement of particle morphology changes during sintering of Fe and Fe_xO_y

A monodisperse aerosol is provided by selecting a mobility diameter between 25 and 250 nm via the MF-DMA downstream of the spark synthesis. A logarithmic distributed voltage ranging from 30 V to 3 kV is applied to the DMA with a sheath gas flow rate of 12.5 L/min. The combination of the different online instrumentation allows the prompt measurement of different particle properties and the determination of the particle morphology. The particle structure can be described by different parameters, such as the effective density and fractal dimension (Tavakoli and Olfert, 2014) which allows to determine the diameter of the primary particles and number of particles per agglomerate.

The particle mass and diameter distribution of the size-selected aerosol is measured for 20 different mobility diameters at room temperature downstream of the MF-DMA with a CPMA and an SMPS. The particle mass measured with the CPMA is corrected with the mass correction function (S1) introduced by Liao et al. (2019). The doubly charged agglomerates lead to a bimodal PSD containing two maxima at a selected size (± 1 charge) and in lower concentration (not more than 20 %) at a larger particle diameter (± 2 charges). Determining the mass-mobility exponent with Equation (F.1) by linear fits of the logarithm modal particle mass as function of the logarithm modal mobility particle diameter over the size range 25 to 250 nm for the three gas compositions, pure nitrogen, 1 vol.% hydrogen, and 5 vol.% hydrogen in nitrogen, leads to an almost constant of 2.2 ± 0.03 which is in good agreement with theory for open structured agglomerates. The primary particle diameter is determined by different methods, as it is essential for the calculation of the sintering kinetics.

The two methods applied to the experimental data described above result in a primary particle diameter of 4 ± 0.5 nm for pure nitrogen. In our previous work (Rosenberger, Sellmann, et al., 2020), we reached the lower detection limit of the DAPS, so that the mode value of the particle size distribution could not be measured. This led to an overestimation of d_{prim} (7.5 nm instead of 4 nm) during the fit procedure from $\mathrm{d}N = \mathrm{d}\log(d_{\mathrm{s}})$ to $\mathrm{d}N = \mathrm{d}\log(d_{\mathrm{m}})$ with help of the effective density. Therefore, the sheath gas of the DAPS was changed from nitrogen to helium, thereby shifting the measuring range toward smaller particle diameters.

An alternative method for determining the primary particle diameter is the Brunauer, Emmett and Teller (BET) method. The sampled powder for XRD analysis is also used for the BET analysis (Gemini VII, Micromeritics

GmbH, Aachen, Germany). The measurement of the adsorbed gas volume allows to determine the BET-equivalent diameter d_{BET} from the specific surface area (SSA) by assuming spherical primary particles in an open agglomerate structure, Equation (F.8). The SSA is defined as the surface area per unit mass of the powder.

$$d_{\mathrm{BET}} = \frac{6}{\rho_{\mathrm{p}}} \cdot \frac{v_0}{V_{\mathrm{m}} N_A a_0} \tag{F.8}$$

with the surface area of a single adsorbed gas molecule a_0, the molar volume of the adsorbate v_0, the bulk density of the particles ρ_{p}, the volume of the adsorbate V_{m} required for monolayer coverage on unit mass of the particle and the Avogadro constant N_A. As it is surface-based, d_{BET} can be seen as an estimation of the primary particle diameter. For pure iron particles with a density of $7.874\,\mathrm{g/cm^3}$ the diameter is about 4 nm and for iron oxide particle with a density of $5.2\,\mathrm{g/cm^3}$ approx. 6 nm. This is in excellent agreement with the primary particle diameter determined from the online measurements.

The size-selected agglomerates are injected in the reaction zone and are sintered at fixed temperatures, as set by to the MFR parameters. The effective density is calculated from the particle mass (CPMA) and mobility diameter (SMPS), using Equation (F.3). The primary particle diameter is determined from combined SMPS and DAPS measurement, applying Equation (F.4). Figure F.6a) and c) depict the effective density ρ_{eff} and Figure F.6b) and d) the primary particle diameter d_{prim} as function of the mobility diameter d_{m} at various furnace temperatures, indicated by colored symbols. The effective density and primary particle size of fully sintered particles is indicated by a dashed line. The slope of the dashed line is a result of the sphericity of the particles, and can be expressed in the mass-mobility exponent D_{fm}.

Observing m_{p} and d_{m} down- and upstream of the MFR, a change in structure cannot be detected when the MFR is bypassed or operated with temperatures $< 500\,\mathrm{K}$. The initial effective density and primary particle diameter of the agglomerates can be extracted from the measurements at room temperature $T = 293\,\mathrm{K}$ for b) N_2 and d) $N_2 + 5\%H_2$ atmosphere. At room temperature, it is observed that the effective density ρ_{eff} decreases from 1 to $0.25\,\mathrm{g/cm^3}$ with increasing the agglomerate size, thus a more compact structure of smaller agglomerates.

The primary particle size is almost constant ($d_{\mathrm{prim}} = 4\,\mathrm{nm}$; $D_{\mathrm{fm}} = 2.2 \pm 0.03$) for the selected agglomerate sizes and significant differences between the pure N_2 and 5 vol.% H_2 are not visible. Increasing the furnace temperature leads to a shift of the mobility diameter toward smaller sizes

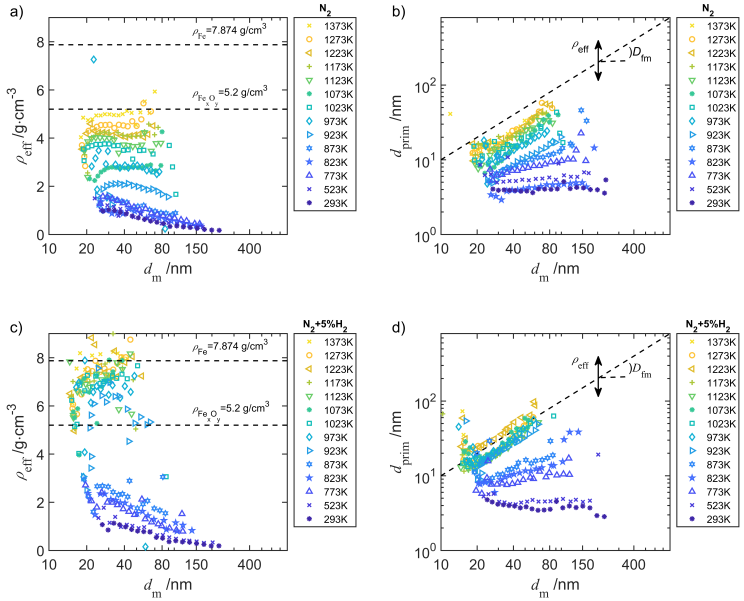

Figure F.6: a) and c) Effective density ρ_{eff} and b) and d) primary particle diameter d_{prim} as function of the mobility diameter d_{m} for different furnace temperatures in a) and b) N_2 and c) and d) in $N_2 + 5\%H_2$.

due to the compaction of the structure, thus to a higher effective density and an increase of the fractal dimension. In nitrogen, the agglomerate density increases steadily with temperature, whereas in 5 vol.% H_2 a significant increase of the effective density can be seen from approx. $2\,\text{g/cm}^3$ (873 K) to $7\,\text{g/cm}^3$ (923 K). This results from particle mass loss during sintering (shown in S_4) caused by the reduction of Fe_xO_y to Fe with hydrogen (Manchili et al., 2020). At the highest furnace temperature of 1373 K, the sintered agglomerates show a spherical structure ($D_{\text{fm}} = 3$) and a density close to the bulk density of iron oxide ($5.2\,\text{g/cm}^3$) and pure iron (to $7.874\,\text{g/cm}^3$).

Obtaining the sintering kinetics from the measured morphology changes

The primary particle size and number per agglomerate are calculated from SMPS and CPMA measurands. These properties can also be obtained from the combination of DAPS and SMPS, but lead to a lower

accuracy due to the detection limit of the DAPS, smaller primary particles at low temperatures and low number concentration at high temperatures. Figure F.7 depicts the increase of d_{prim} (circles) and the reduction of N_{agglo} (crosses) of different agglomerate sizes and as a function the furnace temperature in a) N_2 and b) in $N_2 + 5\%H_2$ atmosphere.

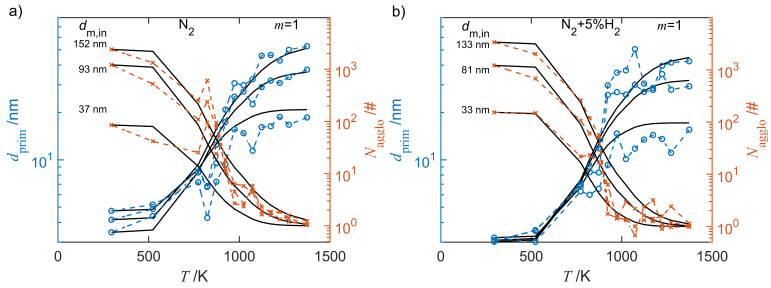

Figure F.7: Morphology change due to sintering according to the experimental data (symbols, connected by dashed lines) and results of the sintering model using the best fitting combination of and assuming $m = 1$ (solid lines). Shown are the primary particle diameter (circles) and number of primary particles per agglomerate (crosses) of different sized agglomerates as function the furnace temperature-time histories in a) pure nitrogen (N_2) and b) in nitrogen with 5 vol.% hydrogen ($N_2 + 5\%H_2$).

For the optimization procedure, 14 representative measurements, differing by aggregate sizes, at 4 temperatures (298, 773, 1023 and 1273 K) were used from the experimental data. The results of the optimization procedure are also shown in Figure F.7, for an assumed value $m = 1$. The solid line represents the results from the sintering model with the optimal combination of E_a and A_s. In N_2 atmosphere, the particle mass remains constant during sintering for the respective size-selected agglomerate so that coagulation, evaporation or condensation can be excluded. In addition, the particle synthesis in N_2 and $N_2 + 5\%H_2$ has no significant influence on the initial primary particle diameter (approx. 4 nm), nor does the mean primary particle size of the size-selected agglomerates differ. Large changes, increase of d_{prim} and decrease of N_{agglo} are observed at approx. 900 K leading to a more compact structure (Schmidt-Ott, 1988). Comparing the Figure F.7a) and b), it can be seen that in $N_2 + 5\%H_2$ atmosphere the sintering is slightly shifted to lower temperatures of approx. 30 K, the slope is much steeper and no further changes of N_{agglo} are observed for $T > 1100$ K. This procedure is followed for the three

different gas atmospheres and values for the exponent m between 1 and 4, shown detailed in S3. Table F.1 summarizes the results.

Gas N_2 (particle density 5.2 g/cm^3)			
m	E_a	A_s	ΣSQR
1	55.22 kJ/mol	$2.54 \cdot 10^{04}$ s/m	0.52
2	77.22 kJ/mol	$1.01 \cdot 10^{11}$ s/m^2	0.59
3	101.68 kJ/mol	$2.68 \cdot 10^{17}$ s/m^3	0.66
4	127.24 kJ/mol	$5.90 \cdot 10^{23}$ s/m^4	0.72
Gas $N_2 + 5\%H_2$ (particle density 7.874 g/cm^3)			
m	E_a	A_s	ΣSQR
1	59.15 kJ/mol	$1.57 \cdot 10^{04}$ s/m	1.09
2	83.85 kJ/mol	$5.08 \cdot 10^{10}$ s/m^2	1.20
3	111.04 kJ/mol	$1.10 \cdot 10^{17}$ s/m^3	1.29
4	185.61 kJ/mol	$1.12 \cdot 10^{20}$ s/m^4	1.50
Gas $N_2 + 1\%H_2$ (particle density 6.02 g/cm^3)			
m	E_a	A_s	ΣSQR
1	57.00 kJ/mol	$4.92 \cdot 10^{04}$ s/m	2.49
2	75.43 kJ/mol	$4.92 \cdot 10^{11}$ s/m^2	2.93
3	234.89 kJ/mol	$2.50 \cdot 10^{11}$ s/m^3	4.00
4	320.12 kJ/mol	$8.49 \cdot 10^{14}$ s/m^4	4.06

Table F.1: Sintering parameters E_a and A_s determined using error minimization of the residuals sum of squares (ΣSQR), for three different gas atmospheres and four sintering exponents m.

It can be seen that the differences in the residual's sums of squares are not very large, so that a very clear preference for one of the values of m does not appear, but lower values of m seem to lead to better fitting results. The fit results are significantly worse for 1 vol.% H_2 than for 5 vol.% H_2 or pure N_2, presumably because the particle density changes during sintering and this density cannot be determined exactly as also a morphology change takes place.

It also has to be stressed that although a minimum is found, another combination of E_a and A_s might also lead to well-fitting results. Figure F.8 depicts the quadratic error (ΣSQR) as function of the activation energy and the sintering rate in N_2, assuming plastic and viscous flow

as dominant transport mechanism for which $m = 1$. It can be seen that combinations of E_a and A_s lead to a valley of minima.

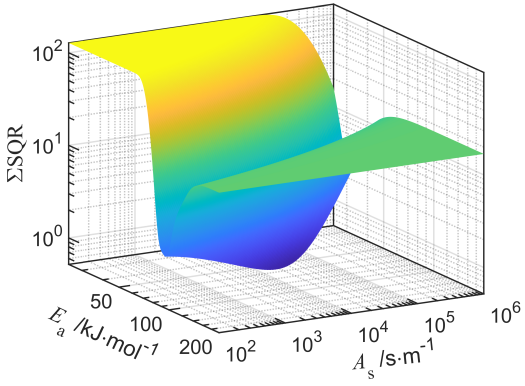

Figure F.8: Numerical solution as sum of squares error (ΣSQR) as function of the activation energy E_a and the sinter rate A_s of iron oxide in N_2, assuming $m = 1$. The global minimum is numerically calculated by the deviation to experimental primary particles.

It is interesting to note that although a minimum is found for the residual sum of squares, for each activation energy E_a between approx. 50 and 150 kJ/mol there is a value of the kinetic pre-factor A_s which gives almost similar good results. The same is true for the exponent m describing the particular sintering mechanism - both with 3 and 4 good residuals sums of squares are obtained. The experimental data and numerical evaluation do not allow reliable conclusions about the sintering mechanism. In the case of the surface or grain boundary diffusion mechanism, which is expected to be the dominant sintering mechanism for iron and iron oxide, the combination of E_a and A_s shifts to higher values. A comparison to the literature is limited, since often only values for E_a are given, but this value is only meaningful in combination with a value for A_s. A shift toward lower activation energies due to the addition of hydrogen, as described in the literature, is not observed. The parameter pair, together with the exponent m, represent precise values for the description of the sintering kinetics.

CONCLUSIONS

The sintering kinetics of iron oxide and iron nanoparticles have been determined numerically from experimental data using the model flow

reactor. The MFR provides a narrow temperature-residence time distribution in a laminar flow field which is needed for the precise determination of the sintering kinetics. Other structure formation mechanisms, such as nucleation or coagulation, can be excluded by a low number concentration and the monitoring of particle mass and size during sintering. The structure formation of size-selected agglomerates is limited to the reaction zone by water-cooled injection and sampling probe and was measured with different online instrumentation. Particle trajectories were simulated based on a validated CFD model and used to calculate the temperature-time history of the particles. Structure models based on the effective density were used to measure the change in morphology during sintering, yielding the primary particle size and number of primary particles in the agglomerate. The sintering model by Koch and Friedlander (1990) was used to model the morphology change. The chemical phase was analyzed by different offline methods, and showed that depending on the gas atmosphere a higher amount of either Fe ($N_2 + 5\%H_2$) or Fe_3O_4 (N_2) is present. For size-selected agglomerates having a broad range of initial sizes, and for varying sintering temperatures and gas atmospheres the agglomerate morphology was determined, and the sintering parameters were obtained by error minimization of the primary particle diameter. The sintering exponent $m = 1$ was found to be optimal. For Fe, an activation energy E_a of 59.15 kJ/mol and a pre-exponential factor A_s of $1.57 \cdot 10^4$ s/m were found, for Fe_3O_4 an activation energy E_a of 55.22 kJ/mol and a pre-exponential factor A_s of $2.54 \cdot 10^4$ s/m. A shift of the sintering kinetics of iron toward lower activation energies by the addition of hydrogen is not observed. This could be due to the fact that, on the one hand, iron oxide particles are already present before sintering and are reduced by the addition of hydrogen and, on the other hand, only the three validated temperature residence time histories (at 773, 1023 and 1273 K) are used to calculate the sintering kinetics.

A more accurate fit to the measured data is possible by adding further temperature profiles, as well as the separate evaluation of the preclassified particle sizes. Furthermore, an investigation of the sintering in certain temperature ranges, e.g., before and after the reduction iron oxide, would be interesting. The use of the interpolated temperature residence time histories, shown in S2, calculated from the validated temperature residence time profiles might be too inaccurate for this purpose.

ACKNOWLEDGMENT

We acknowledge DESY (Hamburg, Germany), a member of the Helmholtz Association HGF, for the provision of experimental facilities. Parts of

this research were carried out at the Beamline P65 and we would like to thank the beamline staff for assistance. TEM with EELS analysis by Dr. M. Heidelmann (Interdisciplinary Center for Analytics on the Nanoscale (ICAN), University of Duisburg-Essen) are gratefully acknowledged.

FUNDING

The authors acknowledge the support by the Deutsche Forschungsgemeinschaft (DFG) in the scope of the research group 2284 (project number: 262219004, within TP4, TP5 and TP9) and priority program SPP1980 (project number: 375692188), the European Union's Horizon 2020 research and innovation program under grant agreement No. 646121.

Babick, F. et al. (2018). "Multiparameter Characterization of Aerosols." In: *Chemie Ingenieur Technik* 90.7, pp. 923–936. ISSN: 0009286X. DOI: 10.1002/cite.201700094.

Blake, R. L., Hessevick, R. E., Zoltai, T., and Finger, L. W. (1966). "Refinement of the hematite structure." In: *American Mineralogist* 51.1-2, pp. 123–129. ISSN: 0003-004X.

Cho, K., Hogan, C. J., and Biswas, P. (2007). "Study of the mobility, surface area, and sintering behavior of agglomerates in the transition regime by tandem differential mobility analysis." In: *Journal of Nanoparticle Research* 9.6, pp. 1003–1012. ISSN: 1388-0764. DOI: 10.1007/s11051-007-9243-5.

DeCarlo, P., Slowik, J., Worsnop, D., Davidovits, P., and Jimenez, J. (2004). "Particle Morphology and Density Characterization by Combined Mobility and Aerodynamic Diameter Measurements. Part 1: Theory." In: *Aerosol Science and Technology* 38.12, pp. 1185–1205. ISSN: 0278-6826. DOI: 10.1080/027868290903907.

Eggersdorfer, M. L., Kadau, D., Herrmann, H. J., and Pratsinis, S. E. (2012). "Aggregate morphology evolution by sintering: Number and diameter of primary particles." In: *Journal of Aerosol Science* 46, pp. 7–19. ISSN: 00218502. DOI: 10.1016/j.jaerosci.2011.11.005.

Eggersdorfer, M. L. and Pratsinis, S. E. (2013). "Restructuring of aggregates and their primary particle size distribution during sintering." In: *AIChE Journal* 59.4, pp. 1118–1126. ISSN: 0001-1541. DOI: 10.1002/aic.14043.

Ewels, P., Sikora, T., Serin, V., Ewels, C. P., and Lajaunie, L. (2016). "A Complete Overhaul of the Electron Energy-Loss Spectroscopy and X-Ray Absorption Spectroscopy Database: eelsdb.eu." In: *Microscopy and microanalysis : the official journal of Microscopy Society of America, Microbeam Analysis Society, Microscopical Society of Canada* 22.3, pp. 717–724. DOI: 10.1017/S1431927616000179..

Feldhoff, A., Martynczuk, J., Arnold, M., Myndyk, M., Bergmann, I., Šepelák, V., Gruner, W., Vogt, U., Hähnel, A., and Woltersdorf, J. (2009). "Spin-state transition of iron in $(Ba_{0.5}Sr_{0.5})(Fe_{0.8}Zn_{0.2})O_{3-\delta}$ perovskite." In: *Journal of Solid State Chemistry* 182.11, pp. 2961–2971. ISSN: 00224596. DOI: 10.1016/j.jssc.2009.07.058.

Fleet, M. E. (1981). "The structure of magnetite." In: *Acta Crystallographica Section B Structural Crystallography and Crystal Chemistry* 37.4, pp. 917–920. ISSN: 05677408. DOI: 10.1107/S0567740881004597.

Friedlander, S. K. and Wu, M. K. (1994). "Linear rate law for the decay of the excess surface area of a coalescing solid particle." In: *Physical review. B, Condensed matter* 49.5, pp. 3622–3624. ISSN: 0163-1829. DOI: 10.1103/PhysRevB.49.3622.

German, R. M. (1996). *Sintering theory and practice*. A Wiley-Interscience publication. New York [u.a.]: Wiley. ISBN: 047105786X.

Goudeli, E., Gröhn, A. J., and Pratsinis, S. E. (2016). "Sampling and dilution of nanoparticles at high temperature." In: *Aerosol Science and Technology* 50.6, pp. 591–604. ISSN: 0278-6826. DOI: 10.1080/02786826.2016.1168922.

Hallberg, R. T., Ludvigsson, L., Preger, C., Meuller, B. O., Dick, K. A., and Messing, M. E. (2018). "Hydrogen-assisted spark discharge generated metal nanoparticles to prevent oxide formation." In: *Aerosol Science and Technology* 52.3, pp. 347–358. ISSN: 0278-6826. DOI: 10.1080/02786826.2017.1411580.

Hontañón, E., Palomares, J. M., Stein, M., Guo, X., Engeln, R., Nirschl, H., and Kruis, F. E. (2013). "The transition from spark to arc discharge and its implications with respect to nanoparticle production." In: *Journal of Nanoparticle Research* 15.9, p. 1957. ISSN: 1388-0764. DOI: 10.1007/s11051-013-1957-y.

Hull, A. W. (1917). "A New Method of X-Ray Crystal Analysis." In: *Physical Review* 10.6, pp. 661–696. ISSN: 0031-899X. DOI: 10.1103/PhysRev.10.661.

Kim, S. C., Wang, J., Emery, M. S., Shin, W. G., Mulholland, G. W., and Pui, D. Y. H. (2009). "Structural Property Effect of Nanoparticle Agglomerates on Particle Penetration through Fibrous Filter." In: *Aerosol Science and Technology* 43.4, pp. 344–355. ISSN: 0278-6826. DOI: 10.1080/02786820802653763.

Kirchhof, M. J., Förster, H., Schmid, H.-J., and Peukert, W. (2012). "Sintering kinetics and mechanism of vitreous nanoparticles." In: *Journal of Aerosol Science* 45, pp. 26–39. ISSN: 00218502. DOI: 10.1016/j.jaerosci.2011.10.006.

Kirchhof, M. J., Schmid, H.-J., and Peukert, W. (2004). "Reactor system for the study of high-temperature short-time sintering of nanoparticles." In: *Review of Scientific Instruments* 75.11, pp. 4833–4840. ISSN: 0001-1452. DOI: 10.1063/1.1809258.

Knight, P. C., Seville, J. P. K., Kamiya, H., and Horio, M. (2000). "Modelling of sintering of iron particles in high-temperature gas fluidisation."

In: *Chemical engineering science* 55.20, pp. 4783–4787. ISSN: 0009-2509. DOI: 10.1016/S0009-2509(00)00055-5.

Koch, W. and Friedlander, S. K. (1990). "The effect of particle coalescence on the surface area of a coagulating aerosol." In: *Journal of Colloid and Interface Science* 140.2, pp. 419–427. ISSN: 0021-9797. DOI: 10.1016/0021-9797(90)90362-R.

Kolb, M. and Herrmann, H. J. (1987). "Surface fractals in irreversible aggregation." In: *Physical review letters* 59.4, pp. 454–457. DOI: 10.1103/PhysRevLett.59.454.

Kramer, C. M. and German, R. M. (1978). "Low-Temperature Sintering of Iron Oxides." In: *Journal of the American Ceramic Society* 61.7-8, pp. 340–342. ISSN: 0002-7820. DOI: 10.1111/j.1151-2916.1978.tb09324.x.

Krishnan, K. M. (1990). "Iron L3,2 near-edge fine structure studies." In: *Ultramicroscopy* 32.4, pp. 309–311. ISSN: 03043991. DOI: 10.1016/0304-3991(90)90076-X.

Kruis, F. E., Kusters, K. A., Pratsinis, S. E., and Scarlett, B. (1993). "A Simple Model for the Evolution of the Characteristics of Aggregate Particles Undergoing Coagulation and Sintering." In: *Aerosol Science and Technology* 19.4, pp. 514–526. ISSN: 0278-6826. DOI: 10.1080/02786829308959656.

Kuczynski, G. C. (1949). "Self-diffusion in sintering of metallic particles." In: *JOM* 1.2, pp. 169–178. ISSN: 1047-4838. DOI: 10.1007/BF03398090.

Lagarias, J. C., Reeds, J. A., Wright, M. H., and Wright, P. E. (1998). "Convergence Properties of the Nelder–Mead Simplex Method in Low Dimensions." In: *SIAM Journal on Optimization* 9.1, pp. 112–147. ISSN: 1052-6234. DOI: 10.1137/S1052623496303470.

Li, Z. and Wang, H. (2004). "Thermophoretic force and velocity of nanoparticles in the free molecule regime." In: *Physical review. E, Statistical, nonlinear, and soft matter physics* 70.2 Pt 1, p. 021205. ISSN: 1539-3755. DOI: 10.1103/PhysRevE.70.021205).

Liao, B.-X., Gong, W.-C., Li, Z., and Tsai, C.-J. (2019). "A mass correction method for the aerosol particle mass analyzer to measure the particle mass of sub-50 nm nanoparticles." In: *Aerosol Science and Technology* 53.9, pp. 1056–1066. ISSN: 0278-6826. DOI: 10.1080/02786826.2019.1626345.

Lutterotti, L. (2010). "Total pattern fitting for the combined size–strain–stress–texture determination in thin film diffraction." In: *Nuclear Instruments and Methods in Physics Research Section B: Beam Interactions with Materials and Atoms* 268.3-4, pp. 334–340. ISSN: 0168583X. DOI: 10.1016/j.nimb.2009.09.053.

Manchili, S. K., Wendel, J., Hryha, E., and Nyborg, L. (2020). "Analysis of Iron Oxide Reduction Kinetics in the Nanometric Scale Using Hydrogen." In: *Nanomaterials (Basel, Switzerland)* 10.7. ISSN: 2079-4991. DOI: 10.3390/nano10071276.

Matsumura, G. (1971). "Sintering of iron wires." In: *Acta Metallurgica* 19.8, pp. 851–855. ISSN: 00016160. DOI: 10.1016/0001-6160(71)90141-6.

Mikami, T., Kamiya, H., and Horio, M. (1996). "The mechanism of defluidization of iron particles in a fluidized bed." In: *Powder Technology* 89.3, pp. 231–238. ISSN: 0032-5910. DOI: 10.1016/S0032-5910(96)03187-7.

Okudera, H. (1997). "Single crystal X-ray studies of cation-deficient magnetite." In: *Zeitschrift für Kristallographie - Crystalline Materials* 212.6, pp. 458–461. ISSN: 2194-4946. DOI: 10.1524/zkri.1997.212.6.458.

Park, K., Kittelson, D., and McMurry, P. (2004). "Structural Properties of Diesel Exhaust Particles Measured by Transmission Electron Microscopy (TEM): Relationships to Particle Mass and Mobility." In: *Aerosol Science and Technology* 38.9, pp. 881–889. ISSN: 0278-6826. DOI: 10.1080/027868290505189.

Pratsinis, S. E. (1988). "Simultaneous nucleation, condensation, and coagulation in aerosol reactors." In: *Journal of Colloid and Interface Science* 124.2, pp. 416–427. ISSN: 0021-9797. DOI: 10.1016/0021-9797(88)90180-4.

Rosenberger, T., Kiesler, D., Hontañón, E., Fuentes, D., Ramiro, E., and Kruis, F. E. (2019). "Design and optimization of a medium flow differential mobility analyzer (MF-DMA) for classification of high-density particles." In: *Aerosol Science and Technology* 53.10, pp. 1172–1185. ISSN: 0278-6826. DOI: 10.1080/02786826.2019.1642443.

Rosenberger, T., Münzer, A., Kiesler, D., Wiggers, H., and Kruis, F. E. (2018). "Ejector-based sampling from low-pressure aerosol reactors." In: *Journal of Aerosol Science* 123, pp. 105–115. ISSN: 00218502. DOI: 10.1016/j.jaerosci.2018.06.003.

Rosenberger, T., Sellmann, J., Wlokas, I., and Kruis, F. E. (2020). "A model flow reactor design for the study of nanoparticle structure formation under well-defined conditions." In: *Review of Scientific Instruments* 91.9, p. 095114. ISSN: 0001-1452. DOI: 10.1063/5.0018880.

Scheckman, J. H., McMurry, P. H., and Pratsinis, S. E. (2009). "Rapid Characterization of Agglomerate Aerosols by In Situ Mass−Mobility Measurements." In: *Langmuir* 25.14, pp. 8248–8254. ISSN: 0743-7463. DOI: 10.1021/la900441e.

Schmidt-Ott, A. (1988). "New approaches to in situ characterization of ultrafine agglomerates." In: *Journal of Aerosol Science* 19.5, pp. 553–563. ISSN: 00218502. DOI: 10.1016/0021-8502(88)90207-8.

Schwyn, S., Garwin, E., and Schmidt-Ott, A. (1988). "Aerosol generation by spark discharge." In: *Journal of Aerosol Science* 19.5, pp. 639–642. ISSN: 00218502. DOI: 10.1016/0021-8502(88)90215-7.

Seipenbusch, M., Weber, A. P., Schiel, A., and Kasper, G. (2003). "Influence of the gas atmosphere on restructuring and sintering kinetics of nickel and platinum aerosol nanoparticle agglomerates." In: *Journal of Aerosol*

Science 34.12, pp. 1699–1709. ISSN: 00218502. DOI: 10.1016/S0021-8502(03)00355-0.

Stein, M., Kiesler, D., and Kruis, F. E. (2013). "Adjustment and Online Determination of Primary Particle Size in Transferred Arc Synthesis of Copper Nanoparticles." In: *Aerosol Science and Technology* 47.11, pp. 1276–1284. ISSN: 0278-6826. DOI: 10.1080/02786826.2013.835484.

Tabrizi, N. S., Ullmann, M., Vons, V. A., Lafont, U., and Schmidt-Ott, A. (2009). "Generation of nanoparticles by spark discharge." In: *Journal of Nanoparticle Research* 11.2, pp. 315–332. ISSN: 1388-0764. DOI: 10.1007/s11051-008-9407-y.

Tavakoli, F. and Olfert, J. S. (2014). "Determination of particle mass, effective density, mass–mobility exponent, and dynamic shape factor using an aerodynamic aerosol classifier and a differential mobility analyzer in tandem." In: *Journal of Aerosol Science* 75, pp. 35–42. ISSN: 00218502. DOI: 10.1016/j.jaerosci.2014.04.010.

Tence, M., Chevalier, J. P., and Jullien, R. (1986). "On the measurement of the fractal dimension of aggregated particles by electron microscopy: experimental method, corrections and comparison with numerical models." In: *Journal de Physique* 47.11, pp. 1989–1998. ISSN: 0302-0738. DOI: 10.1051/jphys:0198600470110198900.

Zhao, J., Huggins, F. E., Feng, Z., Lu, F. L., Shah, N., and Huffman, G. P. (1993). "Structure of a Nanophase Iron Oxide Catalyst." In: *Journal of Catalysis* 143.2, pp. 499–509. ISSN: 0021-9517. DOI: 10.1006/jcat.1993.1293.

DOI: 10.17185/duepublico/78277
URN: urn:nbn:de:hbz:465-20230420-123127-9